

Newcastle University  
Faculty of Science, Agriculture and Engineering  
School of Engineering



**Morphology-based landslide monitoring  
with an Unmanned Aerial Vehicle**

**Maria Valasia Peppia**

Thesis submitted for the degree of  
Doctor of Philosophy

March 2018



*For Tasia and Angelo*



# Abstract

---

Landslides represent major natural phenomena with often disastrous consequences. Monitoring landslides with time-series surface observations can help mitigate such hazards. Unmanned aerial vehicles (UAVs) employing compact digital cameras, and in conjunction with Structure-from-Motion (SfM) and modern Multi-View Stereo (MVS) image matching approaches, have become commonplace in the geoscience research community. These methods offer a relatively low-cost and flexible solution for many geomorphological applications. The SfM-MVS pipeline has expedited the generation of digital elevation models at high spatio-temporal resolution. Conventionally ground control points (GCPs) are required for co-registration. This task is often expensive and impracticable considering hazardous terrain.

This research has developed a strategy for processing UAV visible wavelength imagery that can provide multi-temporal surface morphological information for landslide monitoring, in an attempt to overcome the reliance on GCPs. This morphological-based strategy applies the attribute of *curvature* in combination with the scale-invariant feature transform algorithm, to generate pseudo GCPs. *Openness* is applied to extract relatively stable regions whereby pseudo GCPs are selected. Image cross-correlation functions integrated with *openness* and *slope* are employed to track landslide motion with subsequent elevation differences and planimetric surface displacements produced. Accuracy assessment evaluates unresolved biases with the aid of benchmark datasets.

This approach was tested in the UK, in two sites, first in Sandford with artificial surface change and then in an active landslide at Hollin Hill. In Sandford, the strategy detected a  $\pm 0.120$  m 3D surface change from three-epoch SfM-MVS products derived from a consumer-grade UAV. For the Hollin Hill landslide six-epoch datasets spanning an eighteen-month duration period were used, providing a  $\pm 0.221$  m minimum change. Annual displacement rates of dm-level were estimated with optimal results over winter periods. Levels of accuracy and spatial resolution comparable to previous studies demonstrated the potential of the morphology-based strategy for a time-efficient and cost-effective monitoring at inaccessible areas.



# Acknowledgements

---

First and foremost, I would like to express my gratitude to my supervisory team for giving me the opportunity to conduct research at Newcastle University. This research was jointly funded by a Natural Environment Research Council (NERC) BGS BUFI award (S241) and an Engineering and Physical Sciences Research Council (EPSRC) DTA award (EP/L504828/1)

I am very grateful to Prof Jon Mills for his immense knowledge and valuable advice. His guidance helped me widen my research horizon and kept me motivated during the last four years. Besides my primary supervisor, I would like to thank Prof Phil Moore for his patience and support especially during the writing-up process. He was able to sense delicate situations and was happy to offer endless encouragement. The research would not have been possible without the valuable guidance I was fortunate to get from Dr Pauline Miller especially in the first PhD stage. Her belief in my potential together with her insightful comments and constructive criticism until the end helped me improve my study. My special thanks go to Dr Jon Chambers for his advice about landslides. He also provided me the opportunity to get access to the British Geological Survey facilities and datasets.

The fieldwork would have never been so successful and enjoyable without the great assistance from the “UAV team”, including Martin Robertson, Elias Berra, Magda Smigaj, Ben Grayson and Polpreecha Chidburee (Aun) as well as Dr Rachel Gaulton, Dr Paul Sallis and Dr Sarah Owen. I am very grateful to Martin for his endless support during long hours of fieldwork and his enthusiasm to respond to my technical requests. Special thanks to Paul for his guidance with UAV flying and his willingness to help with aircraft’s technical issues. Elias, Magda, Ben and Aun were always happy to encourage me during tough periods and share scientific ideas. Endless mornings and nights in G19 at Geomatics would not be so pleasant without the great atmosphere created by colleagues and friends, such as Ciprian, Ahmed, Kaizer, Zheng, Tom, Yasir, Jiajun, Miles, Chris, Pippa, Craig, Katarina. I will not forget the lovely lunch and coffee times I had with many peers in the School of Engineering, especially Panagiota, Shadman, Reza, David, Amelie, Marcos, Fei, Edmond, Kishor, Carolina, Alex.

Outside University, my PhD life in Newcastle upon Tyne became colourful, despite the cloudy weather. This is due to amazing people I met from every corner of the world, my great salsa moments, plus Greek and Romanian friendships that added happy memories full of smiles, laughing and love. My final special thanks go to my parents and family for their warm support and genuine affection and love they offered me even from far away.

# Contents

---

<b>Abstract</b> .....	<b>i</b>
<b>Acknowledgements</b> .....	<b>iii</b>
<b>Contents</b> .....	<b>v</b>
<b>List of Figures</b> .....	<b>ix</b>
<b>List of Tables</b> .....	<b>xiii</b>
<b>List of Abbreviations</b> .....	<b>xv</b>
<b>Chapter 1. Introduction</b> .....	<b>1</b>
1.1 Research background .....	1
1.1.1 Overview .....	1
1.1.2 Landslide processes.....	2
1.1.3 Landslide monitoring .....	5
1.1.4 Monitoring studies .....	6
1.2 Aims and objectives .....	10
1.3 Thesis outline .....	10
<b>Chapter 2. Geomatics monitoring techniques</b> .....	<b>13</b>
2.1 Ground-based techniques .....	13
2.1.1 Geotechnical and geophysical investigations .....	13
2.1.2 Total station and GNSS.....	15
2.2 Remote sensing techniques .....	17
2.2.1 Photogrammetric techniques.....	18
2.2.2 Airborne and terrestrial laser scanning .....	20
2.3 UAV-based approaches.....	21
2.3.1 UAV systems .....	21
2.3.2 Transition from classical to UAV-based photogrammetry .....	25
2.3.3 Applications to morphological monitoring, UAV-case studies .....	29
2.4 Summary .....	34
<b>Chapter 3. Morphology-based monitoring strategy</b> .....	<b>35</b>
3.1 Strategy overview.....	35
3.2 UAV-derived SfM-MVS products.....	36
3.2.1 Typical SfM-MVS pipeline .....	36
3.2.2 DSM/DEM generation .....	37
3.2.3 Orthophotomosaic generation .....	40

3.2.4 SfM-MVS software description .....	41
3.2.5 SfM-MVS pipeline in PhotoScan .....	43
3.2.6 Error sources in SfM-MVS derived products .....	49
3.3 Surface morphological attributes .....	53
3.3.1 Morphological attributes derived from elevation variations.....	54
3.3.2 Secondary morphological attributes .....	58
3.4 Morphology-Based co-Registration (MBR) workflow .....	63
3.4.1 Related work on co-registration.....	64
3.4.2 Implementation and development.....	68
3.4.3 Statistical measures .....	74
3.5 3D sensitivity and estimation of surface change.....	75
3.5.1 Related work on error assessment.....	75
3.5.2 Related work on surface change estimation.....	78
3.5.3 Computational aspects .....	81
3.6 Summary .....	84
<b>Chapter 4. Study sites, ground-based data acquisition and equipment.....</b>	<b>85</b>
4.1 Cockle Park test site .....	85
4.1.1 Site overview and ground-based control data.....	85
4.2 Sandford Industrial Park test site .....	87
4.2.1 Site overview .....	87
4.2.2 Ground-based control data.....	89
4.3 Hollin Hill landslide.....	91
4.3.1 Geological and geomorphological overview .....	91
4.3.2 GNSS and total station observations.....	95
4.3.3 Terrestrial laser scanning observations.....	98
4.4 UAV system.....	99
4.4.1 Platform overview.....	99
4.4.2 On-board sensors .....	100
<b>Chapter 5. Control testing of morphology-based strategy.....</b>	<b>105</b>
5.1 Experiment description .....	105
5.1.1 UAV image acquisition and processing.....	106
5.1.2 Experimental results and analysis.....	108
5.2 Morphology-based co-registration experiments at Sandford Industrial Park.....	112
5.2.1 UAV image acquisition and DPC pre-processing .....	112
5.2.2 MBR-based implementation and analysis .....	114
5.2.3 Assessment of co-registration solutions.....	125
5.3 Assessment of surface change estimations at Sandford Industrial Park .....	128
5.3.1 3D sensitivity estimations .....	128
5.3.2 Elevation and volume differences.....	128
5.4 Summary .....	135

<b>Chapter 6. Real world assessment at Hollin Hill landslide .....</b>	<b>137</b>
6.1 Description of experiments, data acquisition and data cleaning .....	138
6.1.1 Experiment description .....	138
6.1.2 UAV imaging network configurations.....	138
6.1.3 DPC pre-processing and vegetation filtering .....	141
6.2 Co-registration solutions .....	143
6.2.1 MBR-based implementation and analysis.....	143
6.2.2 Assessment of co-registration solutions.....	151
6.3 3D sensitivity and estimation of elevation change.....	163
6.3.1 3D sensitivity estimations .....	163
6.3.2 Estimation of elevation and volume change .....	166
6.4 Evaluation of the NCC function.....	171
6.4.1 NCC implementation with synthetic datasets .....	171
6.4.2 Sensitivity analysis of the NCC function with real datasets .....	175
6.5 2D landslide motion and validation .....	179
6.5.1 GCP-based and MBR-GCP estimations of 2D displacements.....	179
6.5.2 Comparison with GNSS and rainfall observations .....	183
6.5.3 Camera stability checks .....	189
6.6 Summary .....	192
<b>Chapter 7. Discussion and Conclusions .....</b>	<b>195</b>
7.1 Discussion of research outcomes .....	195
7.1.1 Performance of the MBR workflow.....	195
7.1.2 Performance of the image cross-correlation function .....	200
7.1.3 Implications for landslide monitoring.....	202
7.2 Revisiting research objectives.....	203
7.3 Future work and outlook .....	206
<b>Appendix A .....</b>	<b>209</b>
<b>Appendix B .....</b>	<b>219</b>
<b>References .....</b>	<b>227</b>



# List of Figures

---

Figure 1.1: Landslide classification scheme (BGS, 2017).....	3
Figure 3.1: Morphology-based monitoring strategy overview .....	36
Figure 3.2: Number of published studies processing UAV imagery with <i>PhotoScan</i> , <i>Pix4D</i> and <i>MicMac</i> in the last six years, as extracted from <i>Scopus</i> .....	42
Figure 3.3: Schematic representation of normal vectors mapped in two DEMs visualising a rough and smooth terrain. The variations of vector orientation indicate surface roughness. Reproduced from McKean and Roering (2004) and Hobson (1972). .....	56
Figure 3.4: Illustration of positive (a) and negative (b) openness at a particular point of a DEM with $L$ denoting the spatial limit. Extracted and modified from Yokoyama et al. (2002) and Chen et al. (2015). .....	61
Figure 3.5: Example of two distributions of points projected on a spherical surface; a) cluster distribution where one large eigenvalue ( $\lambda_1$ ) is observed and b) girdle where two comparable eigenvalues ( $\lambda_1, \lambda_2$ ) are dominant. Modified from Baek and Kim (2015)...	63
Figure 3.6: Workflow of the MBR approach to generate a UAV-derived DEM time series. ....	68
Figure 4.1: Overview of the Cockle Park farm. Inset map locates the site within the UK. ....	86
Figure 4.2: A black and white circular target.....	86
Figure 4.3: Overview of the experimental site at Sandford. Inset map locates the site within the UK. The UAV derived orthophotomosaic at epoch E0 (prior to excavations) is displayed in the background.....	88
Figure 4.4: (a) Excavation of ground material for slope failure performed by the Hawk Group. (b) Overview of the epoch E2 excavations with the GNSS receiver at station S2 in the background.....	88
Figure 4.5: Perspective view of TLS point clouds at the three observed epochs over slope failure. ....	90
Figure 4.6: (a) Breaks in slope superimposed over <i>Shaded relief</i> grid derived from 2011 ALS with (b) geomorphological and geological properties of Hollin Hill landslide. Inset map locates the site within the UK. Modified from Merritt et al. (2014) and Uhlemann et al. (2017). ....	91
Figure 4.7: (a) Overview of the back scarp at the top of the slope captured on 01/14 during reconnaissance with (b) a closer view taken on 09/15. (c) Surface cracks observed across the site. (d) Formed lobes at the west part of the site, as seen from the foot of the slope (taken on 01/14). (e) A closer view of the eastern lobe captured on 03/15. (f) A weather station installed in the centre of the site together with other sensors and pegs shown in (g).....	93

Figure 4.8: Location of surveyed spot heights per campaign. ....	97
Figure 4.9: Rotational failure at the top of the slope, as observed with TLS (a) in 02/16 and (b) in 05/16. ....	99
Figure 4.10: (a) Overview of Quest-300 UAV. (b) Payload setup inside the main UAV body. (c) AutoCAD 3D model and (d) 3D printed version of a camera case to hold the Sony A6000 camera. ....	100
Figure 4.11: Illustration of (a) the calibration board used in <i>PhotoModeler</i> and (b) the calibration test field used in <i>PhotoScan</i> . ....	102
Figure 5.1: The 250 ft post-flight trajectory (in white), with the number of overlapping images (in colour), the camera exposure positions after post-processing together with the distribution of targets. ....	106
Figure 5.2: Average RMSEs at 21 CPs under different scenarios of flying height and number of GCPs. ....	109
Figure 5.3: Planimetric error vectors and errors in elevation after interpolation at GCPs and CPs. ....	111
Figure 5.4: Values of (a) camera's focal length and (b) $K_1$ lens distortion parameter estimated after the SfM-MVS self-calibrating bundle adjustment. ....	111
Figure 5.5: Profile of UAV and TLS-derived DPCs. Inset map locates profile AB within the study area. ....	113
Figure 5.6: Mean <i>curvature</i> grids of (a) E0 and (b) E2 epochs with their corresponding candidate pseudo GCPs. (c) Distribution of GCPs and CPs, used for the GCP-based experiment. (d) Overview of <i>openness</i> grids together with the detected pseudo GCPs. ....	115
Figure 5.7: Histograms of EVR values for epoch E2. ....	117
Figure 5.8: Example of EVR grid for epoch E2. ....	117
Figure 5.9: E2 <i>Openness</i> (a) before and (b) after applying a threshold of $84^\circ$ over slope failure. ....	117
Figure 5.10: Histograms of pseudo GCPs with respect to (a) different <i>curvature</i> kernel sizes and (b) errors derived from the MBR workflow. ....	119
Figure 5.11: Candidate pseudo GCPs detected on (a) epoch E1 and (b) epoch E2. ....	122
Figure 5.12: (a) Planimetric error vectors at pseudo GCPs of the MBR-UAV experiment with (b) their directional distribution. ....	124
Figure 5.13: Elevation differences between GCP-based and MBR-GCP DEMs, before (a, b) and after (c, d) removal of pseudo points with systematic error. ....	126
Figure 5.14: Elevation differences of E2-E0 epoch pair derived from (a) the GCP-based and (b) the MBR-GCP experiments. ....	133

Figure 5.15: 3D RMSEs at (a) 102 pseudo GCPs and (b) 15 ICPs for E2 of MBR-GCP experiment.....	134
Figure 6.1: Image overlap and post flight trajectories for (a) 05/14 and (b) 05/16 campaigns.....	140
Figure 6.2: Profile of a DPC reconstructed with three disparity options (Peppas et al., 2016). .....	141
Figure 6.3: (a) Polygons of DEM standard deviation for masking out (b) erroneously classified vegetated regions.....	143
Figure 6.4: <i>Openness</i> grids for stable terrain extraction from the GCP-based Panasonic experiment.....	145
Figure 6.5: Mean <i>curvature</i> grids of (a) E0 and (b) E4 epochs with their corresponding pseudo GCPs over stable terrain. ....	146
Figure 6.6: Key-points as derived from the SIFT implementation with (a) E0 and (b) E4 orthophotomosaics using exactly the same settings described in Section 3.4.2. ....	147
Figure 6.7: Planimetric error vectors and errors in elevation after interpolation at CPs in the GCP-based Panasonic experiment. For (a) and (b) interpolation performed at both GCPs and CPs due to a limited number of CPs (Table 6.4). ....	152
Figure 6.8: Planimetric error vectors and errors in elevation at CPs of the GCP-based Sony experiment. ....	154
Figure 6.9: Planimetric error vectors of pseudo GCPs and CPs with elevation differences between GCP-based and MBR-GCP based Panasonic experiments.....	157
Figure 6.10: (a) Elevation differences between GCP-based and MBR-GCP Sony experiment with planimetric error vectors in E5. (b) Planimetric error vectors at pseudo GCPs of the MBR-UAV Sony result. ....	158
Figure 6.11: 3D RMSEs of MBR-GCP processing at (a) 1096 pseudo GCPs, (b) 11 CPs of E1, also at (c) 1298 pseudo GCPs and (d) 20 CPs of E4.....	160
Figure 6.12: Implementation of the M3C2 algorithm for various scale settings. ....	161
Figure 6.13: Elevation differences of three successive epoch pairs derived from GCP-based and MBR-based experiments .....	168
Figure 6.14: Perspective 3D views of (a) E0 and (c) E5 textured surface models with their corresponding (b) E0 and (d) E5 slope maps over back scarp derived from GCP-based experiment.....	169
Figure 6.15: Volume change over (a) back scarp and (b) eastern lobe for three successive epoch pairs computed by GCP-based and MBR-GCP elevation differences. ....	171
Figure 6.16: SNR maps derived from Cosi-Corr with (a) positive openness and (b) shaded relief generated from synthetic datasets of E0 Panasonic GCP-based DEM (Peppas et al., 2017). ....	174

Figure 6.17: Box plots for stable terrain, Regions A and B, as derived from the implementation of COSI-Corr with <i>shaded relief</i> , <i>slope</i> , positive <i>openness</i> and <i>curvature</i> applied to synthetic datasets. The median is displayed as a red line, the mean as a red rectangle, the whiskers as black horizontal lines and the outliers as black crosses (Peppas et al., 2017).....	174
Figure 6.18: Scatterplots of estimated surface displacements determined by COSI-Corr with (a) positive <i>openness</i> and (b) <i>slope</i> plotted against manual observation per epoch pair (Peppas et al., 2017). .....	176
Figure 6.19: COSI-Corr results over eastern lobe for E4-E5 epoch pair derived with morphological attributes of (a) positive <i>openness</i> and (b) <i>slope</i> . .....	177
Figure 6.20: RMSEs computed from the differences between manually observed displacements and COSI-Corr displacements derived with various kernel sizes for morphological attributes of E4-E5 epoch pair. ....	178
Figure 6.21: Maps of surface displacements of (a and d) E0-E1, (b and e) E1-E4 and (c and f) E4-E5 epoch pairs from GCP-based and MBR-GCP datasets. Manually derived planimetric vectors at sample points are also superimposed. ....	180
Figure 6.22: Scatterplots of 2D displacements between GCP-based and MBR-GCP results for three consecutive epoch pairs.....	181
Figure 6.23: Detailed view of E0 and E4 positive <i>openness</i> maps over (a) eastern lobe and (b) back scarp with elevation and <i>openness</i> plotted along (c) Profile AB from Panasonic GCP-based datasets (Peppas et al., 2017). .....	183
Figure 6.24: Elevation differences and planimetric vectors indicating the horizontal 2D incremental displacement rate of E0-E4 and E0-E5 epoch pairs derived from GNSS, total station, GCP-based and MBR-GCP observations.....	184
Figure 6.25: 2D incremental displacements and elevation differences from GNSS, GCP-based and MBR-GCP datasets over peg 8 and point 100. Effective rainfall is superimposed. ....	187
Figure 6.26: Focal lengths estimated by different workflows across all epochs for (a) the Panasonic DMC-LX5 and (b) the Sony A6000. ....	189
Figure 6.27: Radial distortion curves of the on-board Quest-300 UAV used cameras.	191

# List of Tables

---

Table 1.1: Velocity classes for landslides (Cruden and Varnes, 1996). .....	4
Table 2.1: Summary of major innovations in image matching from photogrammetry and computer vision contributed to SfM-MVS evolution. ....	28
Table 2.2: Reported vertical errors and estimated relative error ratios per study. ....	33
Table 3.1: List of software produced to-date that adopts (partially or fully) the SfM-MVS pipeline. ....	41
Table 4.1: Data processing details of surveyed base stations, circular targets and spot heights. ....	96
Table 4.2: Calibration results prior to UAV flights for Panasonic DMC-LX5 and Sony A6000, as derived from <i>PhotoModeler</i> , <i>PhotoScan</i> and <i>DBAT</i> . ....	103
Table 5.1: Processing details of four UAV projects used in the Cockle Park experiment. ....	107
Table 5.2: UAV image acquisition over Sandford Industrial Park. ....	112
Table 5.3: Statistics of M3C2 comparison between UAV and TLS DPCs. ....	114
Table 5.4: Statistics of the pseudo GCPs before and after the removal of points with error vectors showing systematic pattern (MBR-GCP experiment). ....	121
Table 5.5: Statistics of the final pseudo GCPs for E1 (MBR-UAV experiment). ....	124
Table 5.6: Statistics at CPs derived from the MBR-GCP and GCP-based experiment. ....	126
Table 5.7: Statistics of M3C2 comparison against TLS and after ICP per experiment. ....	127
Table 5.8: Statistics of M3C2 comparison after ICP of the MBR-UAV experiment. ...	127
Table 5.9: 3D Sensitivity estimations per experiment. ....	128
Table 5.10: Statistics following DEM subtraction of the epoch pair E1-E0 per experiment. ....	129
Table 5.11: Statistics of elevation differences of epoch pair E2-E0 over area of slope failure. ....	130
Table 5.12: Area and volume of detected changes of epoch pair E2-E0. ....	130
Table 6.1: Details of SfM-MVS processing of UAV imagery. ....	139
Table 6.2: Statistics of the coordinate residuals of the MBR-derived pseudo GCPs from Panasonic experiment. ....	150

Table 6.3: Statistics of the coordinate residuals of the MBR-derived pseudo GCPs from Sony experiments.....	150
Table 6.4: Statistics at CPs from the GCP-based Panasonic experiment.....	151
Table 6.5: Statistics at CPs from the GCP-based Sony experiment.....	154
Table 6.6: Statistics of elevation differences derived from the comparison of the GCP-based Panasonic outputs against independently observed elevations at sample points. ....	155
Table 6.7: Statistics at CPs from the MBR-GCP based Panasonic experiment.....	155
Table 6.8: Statistics at CPs from the MBR-GCP Sony experiment.....	158
Table 6.9: Statistics of M3C2 after epoch to epoch comparison with TLS datasets. ...	162
Table 6.10: Statistics of M3C2 comparison after ICP implemented with respect to E0 over stable terrain, for Panasonic datasets. ....	164
Table 6.11: Statistics of M3C2 comparison after ICP implemented with respect to E4 over stable terrain, for Sony datasets. ....	164
Table 6.12: Sensitivities estimated for Panasonic experiments. ....	165
Table 6.13: Sensitivities estimated for Sony experiments. ....	165
Table 7.1: Relative error ratios per experiment. ....	196

# List of Abbreviations

---

ALS	Airborne Laser Scanning
BGS	British Geological Survey
C/A	Coarse/Acquisition
CP	Control Point
DEM	Digital Elevation Model
DG	Direct Georeferencing
DPC	Dense Point Cloud
DSLR	Digital Single Lens Reflex
DSM	Dense Surface Model
EOP	Exterior Orientation Parameter
EVR	Eigenvalue ratio
EXIF	Exchangeable Image File Format
GCP	Ground Control Point
GLONASS	GLobal NAVigation Satellite System
GNSS	Global Navigation Satellite System
GPR	Ground Penetrating Radar
GPS	Global Positioning System
GSD	Ground Sampling Distance
ICP	Iterative Closest Point
IDW	Inverse Distance Weighted
IG	Indirect Georeferencing
IMU	Inertial Measurement Unit
IOP	Interior Orientation Parameter
LGO	Leica Geo Office software
LIDAR	Light Detection and Ranging
M3C2	Multiscale Model to Model Cloud Comparison
MBR	Morphology-based co-Registration
MEMS	Micro-Electro Mechanical System
MVS	Multi-View Stereo
NCC	Normalised Cross Correlation
OSGB36	Ordnance Survey Great Britain 1936
RANSAC	RANdom SAMpling Consensus
RMSE	Root Mean Square Error
RTK	Real Time Kinematic
SE	Standard Error

SfM	Structure-from-Motion
SGM	Semi Global Matching
SIFT	Scale-Invariant Feature Transform
TIN	Triangulated Irregular Network
TLS	Terrestrial Laser Scanning
WGS84	World Geodetic System 1984

# Chapter 1. Introduction

---

## 1.1 Research background

### *1.1.1 Overview*

Landslides represent hazardous natural phenomena that can have disastrous impact on society (Schuster, 1996; Haque et al., 2016). Catastrophic landslides often involve loss of life, damage to infrastructure and communities yielding significant economic implications worldwide (Schuster, 1996; Klose et al., 2014; Haque et al., 2016). It has been reported that thousands of landslides triggered by the 7.8-strength earthquake in Nepal on 25<sup>th</sup> of April 2015 caused more than 8.5 thousand human losses and more than US\$5 billion in damages (Chaulagain et al., 2016; USGS, 2016). However, earthquakes are not the only landslide trigger factor. Other causes include natural erosion, volcanic processes, subsidence, snowmelt, hydrogeological processes, human activities (e.g. slope undercutting, excavation, mining), prolonged and intense rainfall, as well as combinations of these (Clague and Stead, 2012; Haque et al., 2016). In the UK context, the British Geological Survey (BGS) reported a significant increase in landslide events during 2012 due to the increase in extreme rainfall events that year (BGS Landslides Team, 2013). A potential increase in the number of landslides in the future due to climate change has also been investigated (Uhlemann et al., 2015; Gariano and Guzzetti, 2016). Reliable approaches to interpret, monitor and mitigate landslide hazards are therefore crucial.

Time-series surface observations can improve understanding of a landslide's complex behaviour and aid quantification of its geometry and kinematics (Lu et al., 2004). To derive suitable time-series of morphological change an appropriate monitoring strategy must be implemented. This choice depends on various factors, including: a) the type of the landslide, its movement mechanism and velocity (Cruden and Varnes, 1996); b) required spatio-temporal resolution to derive the magnitude of the surface change; c) constraints such as site extent, accessibility, vegetation and weather conditions; and d) operational costs for monitoring equipment and logistics (Mantovani et al., 1996; Borgatti et al., 2010; Scaioni et al., 2014; Dall'Asta et al., 2017). Traditionally, geotechnical and geophysical investigations have been used to monitor the internal structure of landslides (Franklin, 1984; Walstra et al., 2007; Uhlemann et al., 2016). Land surveying equipment

constitute conventional tools for quantification of surface movement (Franklin, 1984; Walstra et al., 2007; Jaboyedoff et al., 2012). However, the aforementioned approaches require physical access to the site that can be impractical and potentially hazardous in steep or mountainous terrain. Thus, scientists have been investigating the potential of remotely-sensed multi-temporal surface observations with the ultimate scope of developing time-efficient and cost-effective reliable landslide monitoring approaches (Lee, 2004; Scaioni et al., 2014). Not only can these approaches measure the extent, the horizontal and vertical change of a surface spatially and temporally, but also can complement traditional methods thereby accelerating the landslide investigation and model prediction.

### ***1.1.2 Landslide processes***

A landslide is “*a movement of a mass rock, earth or debris down a slope*” as defined by Cruden (1991). Any type of sliding movement of material influenced by gravity and/or water is considered as a landslide (Cruden and Varnes, 1996; Clague and Stead, 2012). The gravitational and the hydrological forces constitute the disturbing forces that act upon a slope (Lee, 2004). When the disturbing forces exceed the resisting forces of the material (i.e. the strength of the material), landslides develop as a result of a slope failure (Lee, 2004). The factors that contribute to a slope failure either increase the disturbing forces or decrease the strength of the materials (Varnes, 1978). For instance, the removal of underlying support material due to running water or the increase of loading due to vegetation can increase the shear stress. Moreover, loose soil materials are more vulnerable to weathering which can decrease their strength (Varnes, 1978). Many more examples can indicate the numerous factors involved in a landslide development, illustrating its complex mechanism. The most common factors are material characteristics, geological structure, pore water pressures, topography, slope angle, river and coastal erosion, weathering, seepage erosion and high groundwater levels (Lee, 2004).

Landslides are primarily classified based on the type of movement and the properties of the materials, as defined by Varnes (1978) and Cruden and Varnes (1996). An updated classification scheme was recently introduced by Hungr et al. (2014). Figure 1.1 illustrates the different categories as a combination of the movement and material type.

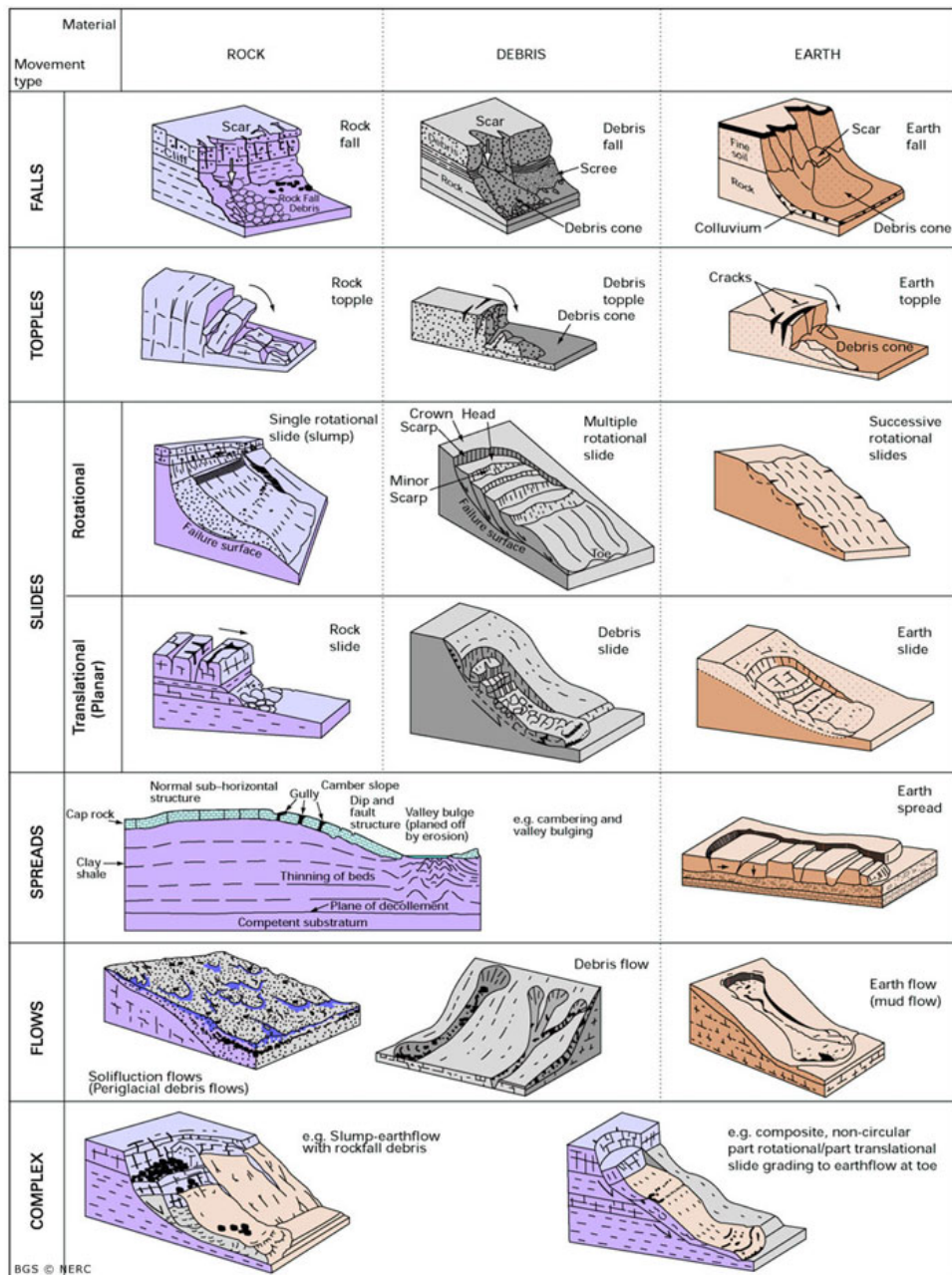


Figure 1.1: Landslide classification scheme (BGS, 2017).

Usually, a combination of the different types shown in Figure 1.1 occur in nature (BGS, 2017). A secondary landslide classification scheme, designed by Cruden and Varnes (1996), is based on the velocity magnitude, as seen in Table 1.1. According to Lee (2004) this classification scheme designates the level of expected risks and potential damages that need to be taken into consideration for a proper response, especially when human life is threatened. In addition, landslides are differentiated depending on their activity state as active, suspended, dormant, abandoned, stabilised and relict (Cruden and Varnes, 1996). The activity state is a vital attribute of a landslide as it shows temporal patterns of behavior. For instance, reactivation or acceleration of a landslide can occur after variations of external forces such as an intensive rainfall event and/or an increase of groundwater level (Lee, 2004; Stumpf et al., 2017). All aforementioned classification schemes set a common terminology for Earth scientists and engineers to support investigation of landslide behavior and motion.

Table 1.1: Velocity classes for landslides (Cruden and Varnes, 1996).

Velocity class	Description	Typical velocity	Response
7	Extremely rapid	5 m/s	Nil
6	Very rapid	3 m/min	Nil
5	Rapid	1.8 m/h	Evacuation
4	Moderate	13 m/month	Evacuation
3	Slow	1.6 m/yr	Maintenance
2	Very slow	16 mm/yr	Maintenance
1	Extremely slow	<16 mm/yr	Nil

A landslide event directly deforms the Earth's surface topography, as can be seen in Figure 1.1 (Clague and Stead, 2012). For instance a rotational failure followed by transitional slide to earthflow (complex type in Figure 1.1) causes ground subsidence forming a scarp at the top and transverse cracks over the accumulated material at the toe of a slope (Lee, 2004). This shows that a spatial change of surface morphology occurs during landslide development. The surface morphology becomes generally rough when surface discontinuities are formed (McKean and Roering, 2004). Quantification of this change can reveal important information related to landslide nature (i.e. activity state, type, velocity etc.) and triggering factors (Scaioni et al., 2014).

### ***1.1.3 Landslide monitoring***

Landslide monitoring is defined by Mantovani et al. (1996) as *the comparison of conditions relevant to a landslide (i.e. spatial extent, velocity, surface topography, soil moisture etc.) over time to assess the landslide activity*. Hence, quantitative observations of morphological surface changes across space and time of a slope prone to failure constitute the basis of landslide monitoring (Scaioni et al., 2014). Assessment of surface deformations can provide an early indicator of instability (Scaioni et al., 2014). Observations of morphological changes in combination with invasive observations of the internal landslide body acquired with geotechnical and geophysical ground-based investigations installed on site can further support landslide investigation. Therefore, monitoring is crucial as it directly enhances the understanding of landslide mechanisms, which in turn facilitates the modelling, prediction and mitigation of hazards (Lee, 2004).

In the context of a monitoring strategy, many factors need to be considered, specifically, spatial and temporal scale, accuracy level and spatial resolution (Lane et al., 1998; Lu et al., 2004; Dall'Asta et al., 2017). These parameters are related to selection of the equipment, the measuring technique and the algorithms required by the monitoring strategy. They are also strongly correlated to the nature of the landslide, such as spatial extent, type and motion rate. To account for the uncertainties associated with the technological framework, a minimum detectable surface change must be estimated (Lane et al., 2003; James et al., 2017b). A European research program, SafeLand<sup>1</sup>, raised the awareness of landslide risks and consequences and delivered guidelines for monitoring and assessment (SafeLand, 2011). These guidelines described a series of remote sensing techniques suitable for landslide monitoring and discussed their advantages and limitations in relation to the aforementioned factors. Of particular importance were the costs of data collection and post-processing (SafeLand, 2011). When it comes to the development of a monitoring strategy, the ratio between costs and performance of a technique requires consideration.

Overall, a landslide event involves numerous parameters which need to be investigated to enable a comprehensive understanding of its complex behavior. Identifying these parameters within a holistic monitoring strategy is a challenging task, even though modern techniques and state-of-the-art algorithms have improved the technological performance and capabilities.

---

<sup>1</sup> [www.esdac.jrc.ec.europa.eu/projects/safeland](http://www.esdac.jrc.ec.europa.eu/projects/safeland)

#### *1.1.4 Monitoring studies*

Traditionally, inclinometers, tiltmeters and extensometers have been used to monitor the internal structure of landslides (Franklin, 1984; Walstra et al., 2007; Uhlemann et al., 2016). However, these devices need to be installed within the ground across a landslide to provide invasive subsurface observations (Chambers et al., 2011). Point-based monitoring techniques, based on Global Navigation Satellite Systems (GNSS) and total stations, plus aerial photogrammetric surveys, are complementary approaches to derive surface displacements (Malet et al., 2002; Walstra et al., 2007; Borgatti et al., 2010). In the last two decades, airborne laser scanning (ALS) and terrestrial laser scanning (TLS) have become attractive alternatives, enabling generation of high quality digital elevation models (DEMs) (Ackermann, 1999; Jaboyedoff et al., 2012). Although laser scanning offers higher spatial resolution than point-based approaches, both ALS and TLS require relatively high cost investment (Stumpf et al., 2011; Travelletti et al., 2012). Further, with TLS, occlusions can occur due to oblique incidence angles which necessitate the establishment of numerous scanning positions (Jaboyedoff et al., 2012), increasing operational cost. The emergence of unmanned aerial vehicles (UAVs) equipped with off-the-shelf compact cameras, alongside the Structure-from-Motion (SfM) and Multi-View Stereo (MVS) processing pipeline, has expedited the automatic generation of high spatio-temporal resolution dense point clouds (DPCs) (Snavely et al., 2008; Remondino et al., 2014), in a time-efficient, cost-effective and user-friendly manner (Fonstad et al., 2013).

The SfM-MVS pipeline is capable of generating a point cloud of tie points (i.e. image observations), after pixel-based matching, via a self-calibrating bundle adjustment without any a priori information about the camera interior orientation parameters (IOP) (i.e. focal length, sensor size, radial and tangential distortion coefficients). An initial estimate of the focal length is extracted from the exchangeable image file format (EXIF) (Fonstad et al., 2013; Remondino et al., 2014). Control information, necessary to scale and orientate the resultant point cloud, is usually provided in the form of surveyed ground control points (GCPs), (in the case of indirect georeferencing, IG), or obtained from the positions of the camera exposures (in the case of direct georeferencing, DG). This information, incorporated into a seven-parameter Helmert transformation, determines the reconstructed point cloud and exterior orientation camera parameters (EOPs), in a fixed reference frame (James and Robson, 2014; Remondino et al., 2014; Carbonneau and Dietrich, 2016). The SfM-MVS pipeline usually results in (red green blue; RGB) coloured

DPC, a digital surface model (DSM), a digital elevation model (DEM), an orthophotomosaic, a 3D mesh and texture.

The suitability of the UAV-based SfM-MVS pipeline utilising compact cameras to detect morphological changes in dynamic Earth surface environments has been presented in various studies, for example: landslide monitoring (Niethammer et al., 2012); fluvial dynamics (Woodget et al., 2015; Cook, 2017); soil erosion (d'Oleire-Oltmanns et al., 2012; Eltner et al., 2015); coastal dynamics (Gonçalves and Henriques, 2015; Turner et al., 2016); glacier monitoring (Immerzeel et al., 2014; Dall'Asta et al., 2017). These studies demonstrated the flexibility of the SfM-MVS pipeline for monitoring hazardous phenomena, enabling dense point clouds to be generated from several centimetres ground sample distance (GSD). UAV-based DEMs and orthophotomosaics of cm-level spatial resolution covering study sites with km-length and hundreds of metres width can be derived. Datasets can be acquired with high temporal frequency, as UAVs are easily deployable and can be launched at short notice (Eisenbeiss and Sauerbier, 2011). These studies also report the variability of the estimated uncertainty (i.e. relevant root mean square errors, RMSEs) of the derived products over stable terrain. Reported relative error ratios (average UAV flying height divided by the estimated uncertainty, see Eltner et al. (2016)) range from 1: 150 to 1: 3000, indicating the wide spectrum of precision with respect to flying height. In addition, the studies report errors from 1-10 times the DEM spatial resolution derived from the SfM-MVS pipeline, with largest errors typically caused primarily by vegetation presence.

Regardless of the geo-referencing approach, IG or DG, SfM-MVS studies invariably report the presence of DEM deformations, such as doming or dishing, causing uncertainties in derived products. A number of recent studies (James and Robson, 2014; Eltner and Schneider, 2015; Carbonneau and Dietrich, 2016; James et al., 2017a; James et al., 2017b) have investigated the error sources of these deformations. These include: a) poor imaging networks (i.e. parallel flight lines with low percentage overlap); b) low number and poor distribution of GCPs; c) GCPs of low measurement uncertainty included as weighting information in the self-calibrating bundle adjustment; d) non-rigorous camera models in the employed SfM-MVS software that were unable to resolve the IOPs and EOPs. Carbonneau and Dietrich (2016) demonstrated that these deformations, if unsolved, can be propagated into rotational, translational and vertical offsets in the SfM-MVS derived products, creating systematic tilt and/or radial patterns that adversely affect the time-series observations. An additional error source is the presence of vegetation,

which creates high surface roughness, affecting the photogrammetric outcome (Lane et al., 2000; Cook, 2017). In the context of morphological monitoring, it is crucial to account for these errors and estimate the real terrain change (James et al., 2017b).

The aforementioned studies employed a wide spectrum of UAV platforms, from in-house manufactured systems equipped with a consumer-grade single frequency GNSS receiver and Micro-Electro Mechanical System-Inertial Measurement Unit (MEMS-IMU), to more expensive, survey-grade UAVs integrated with dual frequency GNSS and multiple MEMS-IMU sensors or augmented with RTK-GNSS (Carbonneau and Dietrich, 2016; Rehak and Skaloud, 2017b). Consumer-grade platforms typically deliver precision of a few meters and degrees for position and orientation of the camera exposure stations respectively, whereas survey-grade instrumentation is capable of dm-level measurement precision with 1° angular precision (Chiang et al., 2012; Carbonneau and Dietrich, 2016; Gerke and Przybilla, 2016; James et al., 2017b). This makes survey-grade more reliable than consumer-grade platforms, especially when DG approaches are employed. Nonetheless, for repeated surveys with RTK-integrated UAVs, systematic errors associated with erroneously fixed ambiguity solutions can be propagated into the UAV camera exposure stations (Dall'Asta et al., 2017) and lead to co-registration discrepancies between epochs in reconstructed DEM time-series. Therefore, augmentation of the SfM-MVS pipeline through the inclusion of a few well distributed GCPs is still considered an essential step to simultaneously reduce biases and derive detectable surface changes at the cm-level (Carbonneau and Dietrich, 2016). However, the installation and maintenance of GCP networks for long-term observations is a labour intensive and costly task, as well as potentially hazardous in steep or mountainous terrain.

Of great importance for landslide investigation is the motion tracking of characteristic surface features related to the landslide mechanism together with the estimation of a continuous surface displacement map. Surface morphological attributes, derived from DEMs (e.g. *slope*, *shaded relief*, *curvature*, etc.), can provide additional information for landslide investigation (McKean and Roering, 2004; Glenn et al., 2006). Traditionally, to detect the landslide motion, discrete locations at natural or artificial features were either monitored through stereoscopic images or surveyed with GNSS/total station (Brückl et al., 2006). A recent study on glacier monitoring (Dall'Asta et al., 2017) reported that a manual detection of about 1000 characteristic surface features on multi-epoch UAV derived orthophotomosaics required eight hours effort from an experienced operator. Thus, apart from the risks related to site accessibility, as previously discussed, these

approaches are labour intensive and time consuming with high operational costs and low spatial resolution. Only a few studies have exploited the high resolution of morphological attributes, generated from UAV-based DEMs, to determine surface displacements (Lucieer et al., 2014; Turner et al., 2015). To achieve this, they utilised the morphological attribute of *shaded relief* in combination with image cross-correlation functions. The latter is a well-established technique in monitoring studies (Leprince et al., 2007a; Ayoub et al., 2009a; Heid and Kääb, 2012). However, there are many morphological attributes, as presented in Favalli and Fornaciai (2017), yet to be investigated for the purpose of landslide monitoring.

Through this discussion the research motivation and gaps are highlighted. Firstly, an investigation to overcome the reliance on GCPs in the SfM-MVS pipeline for landslide monitoring is presented in this research. An automatic workflow to generate “pseudo GCPs” over relatively “stable” terrain for the effective co-registration of time-series DEMs derived from a consumer-grade, fixed-wing mini UAV and SfM-MVS is introduced. This automatic solution can potentially bridge the gap between the expensive task of physically establishing and repetitively surveying GCPs using an IG strategy, and the use of survey-grade UAVs in DG. Secondly, to meet the need for additional analysis with high-resolution morphological datasets, this research examines the implementation of image cross-correlation functions with various UAV survey derivatives. The research blends different analytical methods within a monitoring strategy to deliver an overview of horizontal and vertical surface deformation patterns.

## 1.2 Aims and objectives

This research aims *to develop a strategy for handling UAV imagery that can provide multi-temporal surface morphological information for landslide monitoring*. A particular focus is co-registration for aligning time-series of SfM-MVS products in the absence of physically established GCPs. It is anticipated that this core component can increase the time-efficiency and cost-effectiveness of the strategy, thereby enabling landslide investigation at inaccessible and/or hazardous areas. Ultimately, the research will directly facilitate effective surface morphological change estimation beneficial to landslide assessment. The main objectives to achieve the aim are:

1. To evaluate the suitability of current UAV-based approaches for morphological monitoring;
2. To investigate the uncertainties associated with SfM-MVS processing of UAV imagery;
3. To propose and develop a monitoring strategy that establishes the rigorous alignment of spatio-temporal UAV-derived observations and quantifies landslide kinematics;
4. To implement the monitoring strategy at appropriate test sites and undertake quantitative evaluation with the aid of benchmark observations;
5. To evaluate the capabilities and uncertainties of the strategy, thereby ensuring its applicability for landslide monitoring.

## 1.3 Thesis outline

The thesis comprises seven chapters, as outlined below.

**Chapter 1** sets the research context and provides relevant background information to landslide monitoring. It highlights the research gaps and specifies the aims and objectives of the research.

**Chapter 2** provides a review of both traditional and state-of-the-art research geomatics techniques for morphological monitoring. First, the well-established techniques are presented and then the emerging UAV-based remote sensing approaches are investigated in terms of accuracy, performance and suitability for morphological monitoring.

**Chapter 3** details the methodological steps of the morphology-based monitoring strategy. It explains the SfM-MVS pipeline, which constitutes the core process of the UAV image processing, and highlights associated errors. This chapter sets the fundamental co-

registration aspect of the strategy, the Morphology-Based co-Registration (MBR) workflow. A review of various relevant algorithms, alongside their integration within the monitoring strategy, are presented.

**Chapter 4** describes the three study sites used in the research: Cockle Park Farm near Morpeth; an experimental site with artificial surface change at Sandford, Prees; an active landslide at Hollin Hill, Yorkshire. The ground-based control observations acquired at each site are also presented. These constitute the benchmark datasets for quantitative assessment of the monitoring strategy. The Quest-300 fixed-wing UAV that was used, together with the on-board off-the-shelf cameras employed for imagery acquisition, are described.

**Chapter 5** firstly examines the typical SfM-MVS workflow, performed with the inclusion of a minimum number of GCPs at Cockle Park. It then describes the implementation of the MBR workflow to the experimental site at Sandford. Co-registration solutions, performed both with and without GCPs, are used to assess the MBR workflow performance. Results of the estimated surface change are presented. Accuracy assessment at each stage of the workflow is carried out with the aid of benchmark datasets.

**Chapter 6** describes the implementation of the morphology-based monitoring strategy at the Hollin Hill landslide, evaluating its performance with ground-based control datasets under different scenarios with and without GCPs. Results of co-registration solutions, horizontal, vertical and volumetric changes from observations of the two utilised cameras are presented. Minimum detectable surface changes are quantified within the morphology-based monitoring strategy under each scenario. Accuracy considerations are discussed.

**Chapter 7** brings together the findings from Chapters 5 and 6 and addresses the advantages, limitations, challenges and opportunities related to the morphology-based monitoring strategy and its efficiency for landslide monitoring. Objectives are revisited and future research recommendations are proposed.



# Chapter 2. Geomatics monitoring techniques

---

Chapter 1 introduced the landslide phenomenon and highlighted the importance of monitoring and assessment. The level of landslide deformation that can be monitored with a particular strategy is regulated by the spatiotemporal resolution and the accuracy of the adopted technique. Chapter 2 presents the techniques that are used in morphological studies with a particular focus on landslide monitoring. Ground-based and remote sensing techniques are reviewed in relation to accuracy considerations and cost-effectiveness. The review is completed with a presentation of current UAV-based approaches highlighting their suitability for morphological monitoring.

## 2.1 Ground-based techniques

### 2.1.1 *Geotechnical and geophysical investigations*

Geotechnical and geophysical investigations are well-established techniques for landslide monitoring (Baum and Reid, 1995; Corominas et al., 2000; Chambers et al., 2011; Uhlemann et al., 2017). Geotechnical investigations involve invasive subsurface observations that provide direct metrics of the internal structure of unstable bodies (Dunncliff, 1988). They also observe environmental conditions vital to understand landslide trigger factors (Borgatti et al., 2010). Conversely, geophysical investigations are non-invasive and provide information about physical properties of the ground material (e.g. electric and elastic materials behavior etc.), not directly related to geological characteristics (Jongmans and Garambois, 2007).

#### *Geotechnical investigations*

Traditional geotechnical techniques include: a) borehole and penetration tests utilising extensometers, inclinometers etc.; b) hydrogeological and hydraulic sensors such as piezometers and tensiometers, and c) sensors for climatic observations such as rainfall and temperature (Baum and Reid, 1995; Abbiate and Lovisolo, 2010; Borgatti et al., 2010; Uhlemann et al., 2016).

For example, extensometers measure the distance changes between two points. Extensometers are vertically installed in stable and unstable parts of the ground. Typically, extensometers are installed within boreholes by means of a rod or a wire with

the latter considered a low-cost solution (Corominas et al., 2000; Abbiate and Lovisolo, 2010). Sub-mm level accuracies of relative displacement have been reported in Corominas et al. (2000) and (Malet et al., 2002). Inclinerometers are used to detect the depth of the shear surface (Uhlemann et al., 2016). A typical installation involves multiple probes fixed within a borehole at various depths, along a guided casing, which tracks changes of orientation (Abbiate and Lovisolo, 2010). Inclinerometers give low spatial resolution, due to limited observations only around the boreholes (Uhlemann et al., 2016). Piezometers observe the water level and pore water pressure within the ground providing valuable information for landslide triggering parameters (Abbiate and Lovisolo, 2010). The aforementioned sensors can be installed in boreholes, providing simple and cost-effective long-term monitoring (Abbiate and Lovisolo, 2010). However, geotechnical methods offer limited spatial resolution across a landslide body due to discrete observations. Installation of geotechnical sensors require physical access to steep slopes and hazardous terrain (Chambers et al., 2011; Merritt et al., 2014). Nevertheless, modern sensors provide remote control and automatic data recording, suitable for real time monitoring (Abbiate and Lovisolo, 2010). Refer to Dunnycliff (1988) for further reading.

### ***Geophysical investigations***

Unlike geotechnical investigations, geophysical investigations provide observations of the subsurface across a landslide body and can be easily conducted on steep terrain (Jongmans and Garambois, 2007; Lecomte et al., 2010). Geophysical observations can be obtained along 1D vertical/horizontal profiles, 2D vertical sections providing 2D maps and multiple 2D sections generating 3D maps (Jongmans and Garambois, 2007).

There is a wide range of geophysical methods, including seismic and geoelectrical methods, and ground penetrating radar (GPR) (Jongmans and Garambois, 2007; Lecomte et al., 2010; Chambers et al., 2011; Uhlemann et al., 2017). In seismic methods, the velocity of seismic waves is measured providing, amongst other, insight into the shear strength of the ground material (Jongmans and Garambois, 2007). In geoelectrical methods, electrical currents are introduced to the ground from pairs of electrodes. The geoelectrical measurements are assessed to produce spatial information about the nature, conductivity, water content and other attributes of the ground material (Jongmans and Garambois, 2007; Chambers et al., 2011). The GPR systems consist of two antennas for emitting and receiving electromagnetic waves through the ground. The antennas are typically set at a fixed distance and can be moved along a profile on the surface. Measurements of the velocity and attenuation of the electromagnetic waves can provide

useful information about the electrical properties of the ground material (e.g. electric permittivity), indicating, amongst other, fractures, voids and ground water content (Lecomte et al., 2010). Interpreting geophysical observations to provide intuitive information about a landslide body is a challenging task which requires the cooperation of many scientists (Lecomte et al., 2010). Moreover, calibration and cross-validation from geotechnical observations and observations of higher spatial resolution are essential to derive time-series observations (Chambers et al., 2011; Merritt et al., 2014).

### ***2.1.2 Total station and GNSS***

In addition to sub-surface landslide investigation, conventional land survey-based techniques include total station and GNSS measurements (Gili et al., 2000; Malet et al., 2002; Borgatti et al., 2010; Giordan et al., 2013).

#### ***Total station***

A total station, consisting of an electronic theodolite augmented with electronic distance measurement, can record angles and distances to derive the 3D position of a point. In the context of landslide monitoring, total station measurements are used to detect the movement of significant surface features (i.e. fissures, cracks, faults etc.) on a slope over space and time. To achieve that, a network of points (retro-reflective micro prisms) is usually established on the unstable landslide body and at least two fixed stations are established on the stable part of the area (Giordan et al., 2013). The installation of a total station is simple, and easy, providing a low-cost solution (Stumpf et al., 2011). Modern robotic total stations allow for observations of high temporal frequency (Giordan et al., 2013; Salvini et al., 2015). The main advantage of total station measurements is their mm-level 3D accuracy (Gili et al., 2000; Malet et al., 2002; Stumpf et al., 2011; Giordan et al., 2013; Salvini et al., 2015). Due to this, total station measurements are considered benchmark observations and used for assessing positional accuracies of other geomatics techniques.

Tsai et al. (2012) utilised a reflectorless total station to quantify surface and volumetric changes after a landslide event in Taiwan. The authors surveyed sample points with an average density of 1.5 point/m<sup>2</sup> and reported a maximum relative range error of 0.003 %. They also noted that expertise is required for the selection of the surveyed point location in order to achieve high point density across rugged terrain. However, they did not investigate to what extent the estimated changes were affected by the reported point densities, as observations of higher spatial resolution were unavailable. Giordan et al.

(2013) observed planimetric displacements of prisms installed on a landslide in Italy, with the aid of robotic total stations which could handle remote data recording. With a maximum observed distance of 1 km relative to base stations, they estimated minimum surface velocities of mm per day. However, total station observations do not provide a complete image of the deformation across the landslide site due to spatial low resolution (Merritt et al., 2014). With repeated measurements over several hours and high positional accuracies, these techniques give relatively reliable results offering the potential for early warning and real-time monitoring (Stumpf et al., 2011; Giordan et al., 2013).

## **GNSS**

The term global navigation satellite systems (GNSS) encompasses all satellite-based positioning systems, namely, the Global Positioning System (GPS) operated by the United States, the Global Navigation Satellite System (GLONASS) operated by Russia, the Galileo system operated by the European Union and the Beidou system operated by China (Hofmann-Wellenhof, 2008). Currently, 24 to 30 GPS satellites have been deployed ~ 20,000 km altitude above the Earth's surface in various orbital planes (Hofmann-Wellenhof, 2008). GNSS typically carrier signals at L-band frequencies, e.g. the L1 and L2 for GPS satellites. The coarse/acquisition (C/A) GPS code is modulated on L1 (used for civilian purposes, e.g. handheld receivers with m-level accuracy) and precision (P) code modulated on both carrier signals. These codes are emitted from each satellite. The receiver measures the travel time of the signal and determines the distance to the satellite. The distance determination is affected by multiple errors such as the ionospheric and tropospheric errors, clock bias, orbital errors, multipath etc. Observations from at least four or more satellites are used to determine the position of a point. Refer to Hofmann-Wellenhof (2008) and Groves (2013) for GNSS principles.

Static and rapid static are two common post-processing techniques for position determination of an observed point. Static includes observations over longer periods than rapid static (observations of few minutes). The post-processing is performed with dedicated software that account for biases and can derive positions with cm-level accuracy. Typically, simultaneous observations from stations of known positions are also included in the post-processing (relative positioning). In kinematic positioning, the position of a second (rover) moving receiver is determined with respect to a base station. Real time kinematic (RTK) GNSS provides instantaneous (real-time) solutions with the aid of pseudorange differential GPS, whereby corrections from a base station of known

position are transmitted to the rover via a data link. Refer to Gili et al. (2000) for further reading in relation to landslide monitoring.

GNSS is a well established land survey-based technique and has long been used for morphological monitoring, such as crustal deformation (Prescott et al., 1989), glacier monitoring (Sjöberg et al., 2000), landslide monitoring (Gili et al., 2000; Malet et al., 2002; Brückl et al., 2006; Baldi et al., 2008), coastal monitoring (Mills et al., 2005; Teatini et al., 2005) etc. These studies demonstrated that GNSS technology can derive mm-level 3D accuracies at individual points.

Similar to total station observations, GNSS provide discrete measurements unsuitable for a holistic overview of landslide deformation (Stumpf et al., 2011; Merritt et al., 2014). However, surface features can be tracked with GNSS over long distances without the requirement of a visible line of sight and at any desirable time interval. High temporal frequency GNSS observations are possible for monitoring any type of landslide (Table 1.1), and also suitable for supporting an early warning system (Malet et al., 2002; Stumpf et al., 2011; Giordan et al., 2013). In the context of a monitoring strategy, the installation and cost of multiple GNSS receivers over steep and hazardous terrain should be considered (Stumpf et al., 2011; Giordan et al., 2013).

In recent monitoring studies, total station/GNSS observations were used for three main purposes: a) to assess DEM accuracies derived from remote sensing techniques (e.g. Giordan et al. (2013) and Stumpf et al. (2017)); b) to provide control information for UAV-based monitoring approaches (e.g. Dall'Asta et al. (2017), Section 2.3.3); and c) to integrate subsurface with surface movements (e.g. Uhlemann et al. (2015)) providing a complete image of landslide deformation.

## **2.2 Remote sensing techniques**

Remote sensing techniques, for landslide monitoring utilise terrestrial, airborne and spaceborne optical and microwave images as well as airborne (ALS) and terrestrial laser scanning (TLS) datasets (Scaioni et al., 2014). ALS, TLS and techniques using optical observations are discussed in the following section. Techniques using microwave observations (e.g. synthetic aperture radar) are outside the interest of this research. As synthetic aperture radar systems typically measure signal phase differences through time, require other than morphology-based approaches in order to generate surface deformations (e.g. interferometry, Colesanti and Wasowski (2006)).

### **2.2.1 Photogrammetric techniques**

Photogrammetric techniques involve observations from optical images acquired with terrestrial, airborne and spaceborne sensors (Mikhail et al., 2001; Kraus, 2007; Wolf et al., 2014). Photogrammetry, originating from the Greek word “*φωτογραμμετρία*”, implies the derivation of metric information from photographs.

The fundamental mathematical concept to derive metric information is based on the collinearity condition; an optical ray is defined by three points, the image point, the camera perspective centre and the object point, forming a straight line. In stereo photogrammetry with the use of image pairs, two optical rays, representing conjugate image points, ideally intersect at an object point (spatial intersection). The collinearity condition establishes the geometric relationship between 2D image coordinates and 3D object space position. To reconstruct this relationship, interior, relative and absolute orientations are involved (Kraus, 2007; Wolf et al., 2014).

Interior orientation establishes the camera geometry determining the camera’s interior orientation parameters (IOP). These are focal length (the distance between the lens centre and the point where the lens focuses), principal point (the intersection of fiducial lines), symmetrical radial lens and decentring distortion parameters (see Section 3.2.5). With known camera geometry (i.e. interior orientation), relative orientation can be established. This determines the position and orientation between two images, relative to each other, generating a stereo model. In a stereo model, two optical rays of image points intersecting at an object point, together with the baseline between their camera perspective centres, form a plane (coplanarity condition). Absolute orientation defines the 3D position of control points of a stereo model in the required coordinate system, via a 3D conformal coordinate transformation using at least two horizontal and three vertical control points. Then, the camera’s exterior orientation parameters (EOPs i.e. three translations, in each coordinate direction and three rotations around each coordinate axis) are determined (spatial resection). When multiple images are acquired, the orientations of all images are determined simultaneously (aerial triangulation). Bundle block adjustment then establishes the position and orientation of each bundle of optical rays. For redundancy, multiple GCPs are utilised. In the case of self-calibrating bundle adjustment both IOP and EOP are re-optimised simultaneously in a least-squares sense but initial values are essential for the solution convergence. Refer to Mikhail et al. (2001), Kraus (2007) and Wolf et al. (2014) for additional reading.

Photogrammetry is a well-established technique for landslide investigations. For example, in large photoscale ( $>1:10.000$ , Mantovani et al. (1996)) applications, satellite derived DEMs have been used for monitoring (Delacourt et al., 2009; Debella-Gilo and Käab, 2011; Barazzetti et al., 2014; Stumpf et al., 2017). Depending on the resolution of the recording system, ground sampling distance (GSD) values between 1- 30 m were reported in Stumpf et al. (2011). The quality of the derived DEM depends on the satellite sensor characteristics, the image quality and the post-processing algorithms (Stumpf et al., 2011).

In addition, studies with archival aerial photographs have been conducted since the 1990s with the use of analogue metric cameras (Chandler and Brunsten, 1995; Walstra et al., 2007; Baldi et al., 2008; Dewitte et al., 2008; Prokešová et al., 2010; Achilli et al., 2015). Archival photographs can illustrate the evolution of landslide phenomena up to the present day. Malet et al. (2002) reported dm-level typical positional accuracy for average flying height of 500 m. In principle, the accuracy is influenced by the flying height, the focal length and the distance between camera exposure stations of a stereo pair (Kraus, 2007).

With the transition from analogue metric to digital single lens reflex (DSLR) and low-cost compact cameras, terrestrial observations for close range landslide monitoring became more affordable (Barazzetti et al., 2010; Gance et al., 2014). Stumpf et al. (2011) noted that DSLR and compact cameras cost €1.000-2.000 and  $<€500$  respectively. In terrestrial applications, as images are mainly oblique, corrections for topographic effects and camera distortions are essential to derive high quality DEMs (Travelletti et al., 2012). A major difficulty is the identification of well-defined surface features in the natural environment for use as GCPs and/or for derivation of motion vectors from subsequent acquisitions. Image cross-correlation algorithms have been applied to derive displacement vectors in the absence of GCPs (Travelletti et al., 2012; Gance et al., 2014; Stumpf et al., 2015). Moreover, environmental conditions (e.g. fog, rain, night etc.) can limit image acquisitions and affect the accuracy of the photogrammetric outcome (Stumpf et al., 2011). However, terrestrial techniques offer higher spatial resolution than point-based techniques and deliver cm-level positional accuracies, as shown in (Travelletti et al., 2012) for points located at 100 m distance from the camera station.

### ***2.2.2 Airborne and terrestrial laser scanning***

Laser scanning technology is based on the light detection and ranging sensors (LIDAR) which emit pulses of light (infrared region of electromagnetic spectrum) with much greater thousands of pulses per second. Distances from a scanner position to a surface are measured by computing the travel time needed for the pulse (i.e. laser beam) to return (Baltsavias, 1999). In ALS technology, laser sensors are mounted on fixed-wing or rotary manned aircrafts. The position and orientation of the scanner are derived with the aid of GNSS/IMU sensors of high accuracy. In TLS technology, the laser sensors are fixed on a base platform. ALS and TLS generate point clouds of high density representing a 3D model of a surface. Further description of LIDAR technology can be found in Baltsavias (1999) and Lichti and Jamtsho (2006). A detailed review of laser technology in relation to landslides is presented in Jaboyedoff et al. (2012). A variety of recent laser scanning sensors with ALS and TLS for landslide monitoring is presented in Stumpf et al. (2011).

Numerous studies have applied ALS and TLS to generate DEMs for landslide detection, characterisation and monitoring (McKean and Roering, 2004; Glenn et al., 2006; Monserrat and Crosetto, 2008; Teza et al., 2008; Abellán et al., 2009; Ghuffar et al., 2013; Kenner et al., 2014; Fey et al., 2015). These studies showed that ALS observations can cover thousand km<sup>2</sup> with cm to dm-level vertical accuracies. ALS produce point clouds with density of 0.1-30 points/m<sup>2</sup>, as reported in Stumpf et al. (2011). According to Baltsavias (1999), the accuracy of a ALS derived DEM is affected by various factors such as uncertainties associated with the scanning sensor and the GNSS-IMU sensors, flying height, mechanical and systematic errors of the laser beam etc. Recent investigations apply ALS strip matching with ICP algorithms to minimise systematic errors (Glira et al., 2015).

Compared to ALS, the accuracy of TLS derived DEMs is one order of magnitude higher (Jaboyedoff et al., 2012; Scaioni et al., 2014). Due to portability, simple setup and high spatial resolution, TLS has become more popular than ALS (Stumpf et al., 2011). However, both techniques have drawbacks; firstly, unlike imagery, they do not provide textural information and secondly, both require relatively high cost investment (Stumpf et al., 2011; Travelletti et al., 2012). In particular, ALS entails high costs associated with airborne surveys and requires relatively good weather conditions. James and Robson (2012) reported TLS costs of US\$10<sup>4</sup>-10<sup>5</sup> magnitude. Additionally, in the case of TLS, several scan stations are required in order to cover a large study area and occlusions can occur in point clouds due to oblique incident angles (Eisenbeiß, 2009).

## **2.3 UAV-based approaches**

### ***2.3.1 UAV systems***

Parallel to the advance of satellite/airborne remote sensing platforms, UAV technology has been developed over the last decade (Eisenbeiß, 2009; Watts et al., 2012; Toth and Józków, 2016). UAVs are also known as aerial robots, drones, unmanned aerial systems and remotely piloted aircraft systems (Colomina and Molina, 2014; Toth and Józków, 2016). Although they were initially designed for military purposes (Watts et al., 2012), interest for commercial and research applications has grown due to their affordability and flexibility (Colomina and Molina, 2014). A UAV system includes a platform, imaging sensors, GNSS and IMU sensors, an autopilot unit, a ground control station and a communication data link (Colomina and Molina, 2014).

#### ***UAV platforms***

A variety of UAV platforms exist. For instance, there are flexible wing UAVs such as gliders and kites, fixed-wing UAVs with propeller or jet engines as well as rotary-wing UAVs including single rotors, coaxial, quad-rotors, hexacopters and octocopters (Eisenbeiß, 2009). The use of each platform depends on the nature of the application and the environmental conditions (i.e. weather and wind velocity). For example, fixed-wing UAVs can fly over larger areas compared to rotary-wing UAVs. Conversely, multi-rotors are manoeuvrable and easy to take off and land in challenging environments such as forests, steep slopes etc. (Eisenbeiß, 2009; Toth and Józków, 2016). Images acquired with rotary-wing UAVs can also be captured obliquely and/or on near-vertical surfaces. UAV platforms can be launched at short notice and fly at low altitudes and being limited by cloudy conditions. Due to this, they are more cost-effective than manned photogrammetric surveys for large areas. For further information about various UAV platforms refer to Eisenbeiß (2009) and Colomina and Molina (2014).

According to the United Kingdom Civil Aviation Authority, UAV platforms are classified as micro and mini with total mass  $< 5$  kg and  $< 30$  kg respectively (CAP, 2012). UAVs heavier than these are considered tactical. An operational licence is not required for a UAV platform of total mass  $\leq 7$  kg. Typically, micro and mini UAVs have been adopted for morphological monitoring in research communities, as presented in Section 2.3.3. The UAV system used in this research is described in Section 4.4.

UAVs are also classified into consumer and survey-grade with respect to accuracy levels of the on-board sensors (Eisenbeiß, 2009; Carbonneau and Dietrich, 2016; Toth and Józków, 2016; Rehak and Skaloud, 2017b).

In a consumer-grade UAV the on-board GNSS receiver is normally limited to single frequency and provides positional accuracy to 5 m or better (Rehak et al., 2013; Turner et al., 2013). The autopilot unit contains a small, low-grade MEMS-IMU comprising accelerometers, gyroscopes and magnetometers (Groves, 2013). As these sensors are small in size, lightweight and inexpensive they are prone to errors (gyro drift and accelerometer bias) that accumulate rapidly over time, as detailed by Groves (2013). A study by Woodman (2007) shows that when MEMS-IMU sensors operate in a stand-alone mode the average error in position grows to more than 150 m after 60 seconds. To reduce these errors the commercial autopilot units of mini-UAVs incorporate a Kalman filter that refines the flight trajectory in real-time when the UAV is operating. More specifically, the Kalman filter combines IMU with GNSS observations and provides a best estimate of the new aircraft position based on the previous position (Woodman, 2007; Groves, 2013). Additionally, it describes the variation of errors with respect to time (Woodman, 2007; Groves, 2013). Various Kalman filters have been developed to improve the integration of low-cost UAV components (Weiss and Siegwart, 2011; Hajiyev and Soken, 2013). However, Rehak et al. (2013) noted that, compared to conventional airborne photogrammetric approaches with metric cameras, mini-UAV approaches still cannot provide better than cm-level positional and arc-minute orientational accuracy, independently of direct or indirect georeferencing approach.

Survey-grade UAVs consist of high performance IMU (Eisenbeiß, 2009) or multiple MEMS-IMU sensors (Rehak and Skaloud, 2017b) alongside dual frequency GNSS and/or augmentation with RTK-GNSS receivers (Carbonneau and Dietrich, 2016).

RTK-GNSS can deliver cm-level positional accuracies with the use of differential positioning, as long as the satellite signal is transmitted without interruption and the ambiguity<sup>2</sup> is fixed (Hofmann-Wellenhof, 2008). UAVs augmented with RTK-GNSS receivers rely on a base ground control GNSS station (with known coordinates) which send corrections to the on-board GNSS receiver (Dall'Asta et al., 2017). The RTK-integrated UAV allows for direct georeferencing with the aid of the on-the-fly GNSS

---

<sup>2</sup> Ambiguity is the unknown integer number of the full wavelength of the carrier phase signal. It can be fixed for example with initial static observations of a GNSS receiver over a known point. (Hofmann-Wellenhof, 2008).

coordinates of the camera exposures, thereby enabling an automatic orientation of the photogrammetric block (Section 2.3.2). In principle, the positional accuracy is influenced by several errors such as noise in the GNSS phase observations, multipath, satellite availability etc. (Hofmann-Wellenhof, 2008). Additional noise can be generated due to electromagnetic interference and vibrations during flying, increasing the risk for erroneous ambiguity resolution (Rehak and Skaloud, 2017a). To minimise erroneous solutions, at least one GCP is recommended to be incorporated into the SfM-MVS pipeline when processing RTK-UAV images (Benassi et al., 2017).

Shi et al. (2017) investigated the integration of precise point positioning into RTK-UAVs. Precise point positioning methods do not rely on corrections from a ground control station, but on the precise satellite orbit and clock data provided, for example, by the International GNSS Service (Hofmann-Wellenhof, 2008; Shi et al., 2017). Shi et al. (2017) demonstrated the potential of precise point positioning solutions to derive the aircraft trajectory with accuracies comparable to conventional airborne photogrammetry. Although such UAV systems are still under development, this is a new and potentially high accuracy opportunity for mapping.

According to Rehak and Skaloud (2017b) a critical aspect of a UAV system is time synchronization between the GNSS logged timestamp with the real image acquisition time. Typically, this is achieved with the installation of a time pulse counter device on the camera. Such installations are not usually provided in consumer-grade UAVs. In addition, the time delay between the activation of the mechanical shutter and the recorded trigger time can propagate into positional error of the camera exposure stations (e.g. 0.05 m error for a 5 ms delay with a UAV speed of 10 m/s, Rehak and Skaloud (2017b)). This in turn can adversely affect the accuracy of direct georeferencing with survey-grade UAVs.

In recent morphological studies (Gonçalves and Henriques, 2015; Woodget et al., 2015; Carbonneau and Dietrich, 2016; Cook, 2017) the costs of UAV systems have been reported. Draganflyer X6 together with the Panasonic Lumix DMC-LX3 and relevant accessories cost £ 29,500 in 2010 (Woodget et al., 2015). According to Gonçalves and Henriques (2015) the cost of consumer-grade UAVs with payload within 0.5-3.5 kg lies in the range of US\$ 5,000-60,000. Cook (2017) reported that a total expense of \$ 1000 was required to purchase the DJI Phantom 2 quadcopter equipped with the Canon IXUS 135 and Powershot 4000IS compact cameras with an in-house manufactured camera case.

Costs of US\$ 1,200 -2,400 for consumer-grade DJI<sup>3</sup> UAVs were also reported by Carbonneau and Dietrich (2016). On the other hand, Carbonneau and Dietrich (2016) reported cost exceeding £ 10,000 for RTK integrated UAVs. It is noteworthy that, due to the emerging technology and demanding market, the costs fluctuate continuously. However, UAV cost is an important parameter in monitoring studies.

The reported costs showed that typical commercial UAV systems with consumer-grade GNSS/IMU sensors and off-the-shelf digital cameras are generally affordable. However, raw GNSS/IMU observations are not available from the manufacturers (Toth and Józków, 2016). This limits control of further post-processing and potential for refining the aircraft trajectory, thereby improving the initial camera exposure positions.

### *Camera settings for UAV surveys*

UAV survey planning involves specification of forward/lateral overlap and flying height based on the camera's nominal focal length and pixel resolution. It is common practice to set the flight plan assuming that images are acquired along parallel axes and that they are vertical. The theoretical GSD is denoted by:

$$GSD = \frac{H \times S_{pix}}{f} \quad (2.1)$$

where  $H$  is the flying height,  $S_{pix}$  the camera's nominal pixel size and  $f$  the focal length. By decreasing the flying height, the GSD is increased yielding higher spatial resolution. It is recommended to set up the focus (which is a function of aperture) to infinity in order to achieve the full depth of field of the camera under any height variation (Shahbazi et al., 2015).

With regard to camera settings, automatic stabilization options and automatic focus are deactivated so that the internal camera geometry remains stable (Eltner et al., 2016). Conversely, systematic errors might be produced see (Section 3.2.6). Shutter speed defines the exposure time and regulates the motion blur (Sieberth et al., 2014; O'Connor et al., 2017). Increased exposure time (i.e. low shutter speed) allows more light to reach the sensor, thereby improving dark images. However, it can overexpose bright ones increase blur. High shutter speed reduces the errors due to UAV forward motion. ISO indicates the sensor's noise and is generally set at low values. In order to generate sharp

---

<sup>3</sup>[www.dji.com/](http://www.dji.com/)

images, camera settings should be taken into account. Important considerations related to optimal camera settings can be found in O'Connor et al. (2017).

### ***2.3.2 Transition from classical to UAV-based photogrammetry***

Early studies with medium format digital cameras employed on microlight aircrafts represent an important advance in airborne photogrammetry providing affordable to that time survey mapping solutions (Graham, 1988; Mills et al., 1996). Recently, mini UAVs with off-the-shelf digital cameras have become even more attractive over expensive manned photogrammetric platforms and heavy metric cameras respectively (Toth and Józków, 2016). Together with the continuously emerging UAV technology, as discussed previously, contemporary processing approaches have been developed blending classical photogrammetric and computer vision algorithms. An overview and history of the SfM-MVS pipeline evolution is presented here.

The SfM-MVS pipeline has facilitated and expedited the photogrammetric process using image-based feature matching approaches (Seitz et al., 2006; James and Robson, 2012; Remondino et al., 2014). SfM-MVS is related to the 3D geometry of an object or a scene (structure) viewed from multiple positions (multi-view) of a moving camera (motion) (Ullman, 1979; Snavely et al., 2008; Granshaw, 2016a). SfM-MVS involves a self-calibrating bundle adjustment together with two image-based matching approaches: a) feature-based and b) area-based. The feature-based approaches establish the detection of corresponding points or features (such as edges, lines, corners etc.). This has also been named image correspondences (Lowe, 2004; Remondino et al., 2014). The area-based approaches utilise local or global window templates to measure the per-pixel intensity values (e.g normalized cross-correlation (NCC) function, gradient-based algorithms, energy minimization algorithms etc.) (Hirschmüller, 2008; Szeliski, 2011; Gruen, 2012; Remondino et al., 2012; Scaioni et al., 2015). These approaches enable the generation of disparity or depth map, known in photogrammetry as parallax, which corresponds to the object's height perception from overlapping stereo pairs (Remondino et al., 2014; Wolf et al., 2014). The current state of the SfM-MVS pipeline results from a blend of developments in bundle adjustment and image-based matching algorithms from both the photogrammetry and computer vision community (Remondino et al., 2014; Granshaw and Fraser, 2015; Eltner et al., 2016).

According to published reviews (Snavely et al., 2008; Westoby et al., 2012; Nex and Remondino, 2014; Remondino et al., 2014; Granshaw and Fraser, 2015; Scaioni et al.,

2015; Eltner et al., 2016), the major contributions from the two communities that supported the evolution of the SfM-MVS concept, are listed in Table 2.1. More studies could be reported, but Table 2.1 constitutes the core of the SfM-MVS concept. As evidenced in Table 2.1, the transition from analogue to analytic and digital photogrammetry from 1950 to 1990 gave more automated and precise techniques that were incorporated within least squares adjustment for image matching. The transition also included the extension of a stereo pair from two images to multiple stereo pairs. In parallel, computer vision algorithms emerged through robotic applications. These focused on developing fast algorithms thereby decreasing the computational effort for matching multiple images. This was beneficial for the era of close range photogrammetry, in the 1990s and later, when convergent imagery was included into the photogrammetric blocks. Moreover, the development of computer vision algorithms supported reconstruction of 3D surfaces from convergent imagery, which traditional aerial photogrammetric algorithms could not handle. This is because traditional algorithms were designed to cope with 100% nadir imagery from calibrated cameras. The computer vision approaches provide automation with the potential to overcome the reliance on a priori information such as the camera's IOPs or surveyed GCPs (Nex and Remondino, 2014; Remondino et al., 2014; Granshaw and Fraser, 2015).

Over the last decade, novel feature detection algorithms and linear optimization approaches from computer vision (Table 2.1), have been adopted into the self-calibrating bundle adjustment and applied to close-range images (Fonstad et al., 2013; Nex and Remondino, 2014; Granshaw and Fraser, 2015). These, together with the innovative image matching approaches (Table 2.1), enabling a dense surface representation, have led to the maturity of the SfM-MVS matching concept (Remondino et al., 2014).

The SfM-MVS pipeline has become a standard workflow for processing UAV imagery (James et al., 2017a), as it can handle mixed image block geometries of non-vertical, unordered and marker-less images (Fonstad et al., 2013; Nex and Remondino, 2014). This is mainly attributable to the feature-based image matching algorithms, which are able to generate a high number of image correspondences (usually >1000) regardless of the different image rotations, scales and baselines within the photogrammetric block (Fonstad et al., 2013; Nex and Remondino, 2014). The adaptation of random sampling consensus "(RANSAC)-type" algorithms (e.g. maximum a posterior sample consensus, least median of squares etc.), into the feature-based matching algorithms, has aided in removing erroneous image correspondences (i.e. outliers) and simultaneously estimating the

relative orientations in a fast and robust manner (Snavely et al., 2008; Barazzetti et al., 2010; Granshaw and Fraser, 2015). Conversely, in the classical photogrammetric procedure, a smaller number of high quality points (i.e. tie points and GCPs), compared to SfM-MVS, can solve for the collinearity condition (Fonstad et al., 2013; Granshaw and Fraser, 2015).

In classical photogrammetry the self-calibrating bundle adjustment relies on the inclusion of redundant GCPs to re-estimate the camera's IOPs and EOPs (Nex and Remondino, 2014). Their initial values are usually obtained by laboratory or field calibration methods performed in advance (Wolf et al., 2014). In the SfM-MVS pipeline, initial values of camera's IOPs are not essential as only an approximate estimate of the focal length is typically extracted from the exchangeable image file format (EXIF, Snavely et al. (2008)). Then, a self-calibrating bundle adjustment re-estimates the focal length and determines all other interior parameters per image based on specified camera calibration models with the aid of linearised formulations adapted from computer vision (Pierrot Deseilligny and Clery, 2011; Fonstad et al., 2013; Granshaw, 2016b).

In the past heavy and expensive metric cameras were designed and calibrated to be used in the classical airborne photogrammetry for mapping purposes (Clarke and Fryer, 1998). The geometric stability of those cameras was well defined by manufacturers. With the advance of consumer-grade, lightweight digital cameras, as not being designed for the derivation of metric information, the stability of their interior orientation was and still is a crucial consideration. A large body of literature has investigated the geometric internal consistency of consumer-grade digital cameras since late 90s (Fraser, 1997; Clarke and Fryer, 1998; Shortis et al., 1998; Mills et al., 2003b; Habib et al., 2006; Wackrow et al., 2007). Their investigations including development of camera calibration methods and assessment of interior parameters behavior have improved our understanding of errors propagated into any type of photogrammetric products, with the more recent ones derived from the SfM-MVS pipeline (Section 3.2.6).

Table 2.1: Summary of major innovations in image matching from photogrammetry and computer vision contributed to SfM-MVS evolution.

Studies	Contribution	Community
Hobrough (1959);	Introduction of image cross correlation for identification of image correspondences.	Photogrammetry
Marr and Poggio (1976); Longuet-Higgins (1981)	Stereo disparity determination and implementation on biological applications of neuroscience.	Computer Vision
Helava (1978);	Implementation of image cross correlation on stereoscopic plotting systems.	Photogrammetry
Granshaw (1980); Fraser (1982); Dermanis (1994); Fraser (1997);	Self-calibration and free network bundle adjustment techniques.	Photogrammetry
Lucas and Kanade (1981); Moravec (1981);	Early work for feature tracking and image registration with applications in robotics.	Computer Vision
Fischler and Bolles (1981);	Random sampling consensus algorithm (RANSAC) for outlier detection in image observations.	Computer Vision
Förstner (1982); Ackermann (1984);	Image to image least squares correlation, parallax determination and implementation in analytical plotter.	Photogrammetry
Rosenfeld and Kak (1982);	Introduction to similarity correlation measures.	Computer Vision
Gruen (1985); Gruen and Baltsavias (1988);	Geometrical constraints for multi-photo least squares matching.	Photogrammetry
Förstner (1986); Förstner and Gülch (1987);	Detecting distinctive points with precise localisation for image matching.	Photogrammetry
Wrobel (1987); Heipke (1992);	Least squares image matching in object space.	Photogrammetry
Harris and Stephens (1988);	Interest operator for identifying image correspondences based on gradient-based algorithms.	Computer Vision
Spetsakis and Aloimonos (1991); Collins (1996);	Geometric relationships between object and image space from multiple images.	Computer Vision
Tomasi and Kanade (1992); Shi and Tomasi (1994);	Matrix formations of image observations including affine transformation for feature tracking.	Computer Vision
Förstner (1993);	Feature extraction from multiple images and geometrical relationship between object and image space.	Photogrammetry
Maas (1996);	Combination of previous image matching approaches for DEM reconstruction from multiple images.	Photogrammetry
Roy and Cox (1998);	Global energy minimisation cost routine for matching multiple epipolar line pairs.	Computer Vision
Birchfield and Tomasi (1999);	Per-pixel measurements for disparity computation.	Computer Vision
Triggs et al. (2000);	Linear numerical formulations for bundle adjustment.	Computer Vision
Lowe (2004); Ke and Sukthankar (2004); Rosten and Drummond (2006); Bay et al. (2008);	Interest operators for detection and description of distinctive features on images.	Computer Vision
Pierrot-Deseilligny and Paparoditis (2006)	Extension of Roy and Cox (1998) algorithm with satellite imagery.	Photogrammetry
Vogiatzis et al. (2007); Furukawa and Ponce (2010); Vu et al. (2012)	MVS algorithms including patch-based and global optimisation routines.	Computer Vision
Hirschmüller (2008); Gehrke et al. (2010)	Semi global matching (SGM) algorithms for dense representation of a surface.	Computer Vision Photogrammetry

In conventional airborne photogrammetry, approximate camera EOPs are estimated from on-board survey-grade GNSS/IMU sensors facilitating the aerial triangulation solutions (Schenk, 1997). Consumer-grade UAVs carry miniature GNSS/INS sensors of low positional accuracy (Section 2.3.1), consequently the inclusion of GCPs in the SfM-MVS pipeline is recommended (James and Robson, 2014). However, researchers are currently investigating automated solutions as a tradeoff between accuracy and cost, critical parameters of a monitoring strategy (Carbonneau and Dietrich, 2016; James et al., 2017b). A description of the SfM-MVS pipeline as implemented in current commercial software is presented in Section 3.2.

### ***2.3.3 Applications to morphological monitoring, UAV-case studies***

Recent morphological monitoring case studies with UAV systems, as discussed in Section 2.3.1, are introduced here.

Niethammer et al. (2012) monitored the Super-Sauze landslide in the southern French Alps. They generated a SfM-MVS derived DEM of 0.06 m spatial resolution, using a quad-rotor UAV equipped with a Praktica Luxmedia 8213 compact camera, manually flying 100-250 m above ground level. They established 199 GCPs, which were included into the SfM-MVS pipeline (e.g. as a combination of three software: a) Vision Measurement System<sup>4</sup> for close range photogrammetric process, b) Gruen Otto–Chau image matching algorithm; Otto and Chau (1989) and c) an image blending algorithm included in OrthoVista<sup>5</sup>). They achieved a 0.20 m planimetric and vertical RMSE after comparing the SfM-MVS estimation with the GNSS surveyed GCP coordinates. To cross-validate the results, the SfM-MVS DEM was compared with a TLS DEM at the toe of the landslide, delivering a 0.310 m vertical RMSE. Due to high uncertainty, the authors acknowledged that this study was suitable for displacement analysis at an annual basis, as smaller displacement magnitudes could not be resolved from observations of higher temporal frequency.

d'Oleire-Oltmanns et al. (2012) extracted a DEM of 0.05 m spatial resolution with a Sirius I MAVinci fixed-wing UAV fitted with a Panasonic Lumix GF1 compact camera, flying at approximately 70 m above ground level. They surveyed 30 GCPs with total station delivering a 0.03 m planimetric and 0.01 m vertical precision and achieved a cm-level 3D RMSE at GCPs after including them in the SfM-MVS bundle adjustment (e.g. Leica

---

<sup>4</sup> [www.geomsoft.com/](http://www.geomsoft.com/)

<sup>5</sup> [www.orthovista.com/](http://www.orthovista.com/)

Photogrammetric Suite). They demonstrated the capability of their system to identify high spatial resolution gully edges, which aided in monitoring gully development in Morocco. However, there were no independent observations to cross-validate their results.

Turner et al. (2015) presented the continuation of a monitoring study of an active landslide in southern Tasmania firstly commenced by Lucieer et al. (2014). This landslide is moving with a rate of approximately 0.01-0.038 m per day (Lucieer et al., 2014). Turner et al. (2015) generated seven DEMs of 0.02 m spatial resolution when flying with a multi-rotor OktoKopter equipped with a Canon 550D Digital Single Lens Reflex (DSLR) camera at 40 m height. SfM-MVS processing (e.g. PhotoScan; see Table 3.1) was adopted with the inclusion of 16-66 GCPs, with a different number per campaign. To evaluate the SfM-MVS results, RMSEs at independent check points (CPs) were calculated by comparing the CP coordinates, surveyed with RTK GNSS, at the estimated SfM-MVS. Planimetric and vertical RMSEs were estimated in the range 0.031-0.076 m and 0.031-0.090 m respectively. They also reported that a 0.07 m mean vertical RMSE was calculated over stable terrain after comparing subsequent DEMs. The authors noted that UAV acquisitions with higher frequency than a few-months duration would be necessary in order to resolve the actual displacement rate.

Eltner et al. (2015) generated dense point clouds of 0.002 m and 0.004 m GSD with Panasonic Lumix DMC-LX3 and Sony NEX 5N cameras respectively, mounted on an octo-rotor Falcon 8 UAV flying within 8-11 m above ground level. They validated the SfM-MVS derived data (processed in Pix4D; see Table 3.1) against TLS-derived observations through point cloud comparisons, delivering an average 0.005 m 3D standard deviation for the differences. They reported that the lowest detectable change was 0.01 m from their multi-temporal SfM-MVS observations, by applying typical error propagation approach to the 0.005 m standard deviation with a 90% confidence level (Wolf and Ghilani, 2010). Eltner et al. (2015) demonstrated the high spatial and temporal resolution of SfM-MVS outputs and the capability to quantify soil erosion with precision of  $10^{-2} \text{ m}^3$  and detect surface ridges of 0.02 m width.

Woodget et al. (2015) investigated the quantification of fluvial geomorphology with the use of a SfM-MVS pipeline from images obtained with the consumer-grade Draganflyer X6 UAV. This was equipped with a Panasonic Lumix DMC-LX3 compact camera. Four DEMs of average 0.02 m spatial resolution were generated when the UAV was flying at approximately 27 m. From 16 to 25 GCPs were incorporated into the SfM-MVS pipeline

(e.g. PhotoScan) and hundreds of independent CPs were observed with total station/GNSS for validation. After comparing the SfM-MVS derived CP coordinates with the surveyed CP coordinates, vertical standard deviations outside the submerged areas were estimated in the range 0.019-0.203 m. High vertical standard deviations were attributed to tall and dense vegetation.

Gonçalves and Henriques (2015) evaluated the SfM-MVS pipeline in monitoring of coastal dynamics at sandy beaches of the Portuguese coast. They used a SwingletCAM<sup>6</sup> fixed-wing UAV equipped with a Canon IXUS 220 HS compact camera. A 0.045 m and a 0.032 m GSD were estimated when the UAV flew at 131 m and 93 m above ground level respectively at two different sites. 12 and 13 GCPs were incorporated into the SfM-MVS processing (e.g. PhotoScan) of the two UAV flights. 114 and 71 independent CPs were distributed on the sand at the first site and outside the GCP-coverage at the second site respectively and surveyed with RTK GNSS. A 0.046 m and a 0.107 m vertical RMSEs were estimated at CPs indicating the overall accuracy of the SfM-MVS outputs. Gonçalves and Henriques (2015) explained that poor accuracy was caused by sand movement which might have occurred below the targets while surveying with the GNSS poles.

Dall'Asta et al. (2017) utilised a SwingletCAM fixed-wing UAV to monitor a rock alpine glacier in Italy with an expected motion of 0.10 m per month. This UAV flew twice fitted with a Canon IXUS 220 HS and a Canon IXUS 125 HS compact camera in 2012 and 2014 respectively, at an average flying height of 150 m above the ground. A 0.05 m GSD was achieved from both cameras and both flights. With the use of 10 to 16 GCPs in the SfM-MVS pipeline (e.g. PhotoScan), a 0.110 m and a 0.156 m standard deviations in elevation were calculated after comparing the coordinates from GNSS observations at CPs. In the same study, a senseFly eBee<sup>7</sup> RTK UAV flew at 140 m with a Sony Cyber-shot DSC-WX220, which has better pixel resolution than the other two cameras, delivering a 0.04 m GSD. A 0.05 m 2D RMSE and a 0.072 m vertical RMSE was computed after comparing the RTK-UAV derived and GNSS surveyed coordinates at 12 CPs. The RTK-UAV derived point cloud was compared against a GCP-UAV derived point cloud after co-registering the two point clouds with an Iterative Closest Point (ICP) algorithm. The point-to-point comparison delivered a 0.136 RMSE, indicating the overall uncertainty of the RTK-UAV direct georeferencing. From the multi-epoch UAV-derived

---

<sup>6</sup> [www.sensefly.com/fileadmin/user\\_upload/sensefly/images/BROCHURE-swingletCAM.pdf](http://www.sensefly.com/fileadmin/user_upload/sensefly/images/BROCHURE-swingletCAM.pdf)

<sup>7</sup> [www.sensefly.com/drones/overview.html](http://www.sensefly.com/drones/overview.html)

orthophotomosaics Dall'Asta et al. (2017) identified the displacement of 48 markers and compared against GNSS observations, achieving a 0.16 m 3D RMSE. This study demonstrated that comparable accuracies can be derived from the GCP and RTK-UAV based solutions. However, they did not explicitly derived minimum detectable thresholds that can be estimated from the various solutions to confirm their suitability for glacier monitoring of a dm-level motion per month.

Cook (2017) utilised a DJI Phantom 2 quadcopter customised with a Canon IXUS 135 and Powershot 4000IS compact cameras of 16 Mb resolution to monitor the erosion of the Daan River Gorge in Taiwan. They manually flew the quadcopter at an average height of 73 m and generated SfM-MVS point clouds of an average 0.022 m GSD. They incorporated 8 -14 GCPs into the SfM-MVS pipeline (e.g. PhotoScan) during two UAV campaigns. After comparing the two point clouds with TLS derived point clouds, generated at the same epochs, 3D RMSEs of an order of 0.30 m were computed from the point-to-point differences. They suggested that 0.30 m is the lowest detectable threshold of 3D surface change with their methodology.

The aforementioned case studies demonstrated variations of SfM-MVS outputs in spatial resolution and uncertainties, delivered from a wide spectrum of UAV systems with GNSS/IMU and imaging sensors of different performance and spatial resolution respectively. According to James and Robson (2012) and Eltner et al. (2016) a relative error ratio ( $e_r$ ) can be computed to compare the reported uncertainties as follows:

$$e_r = \frac{\sigma_e}{H} \quad (2.2)$$

where  $\sigma_e$  is a reported vertical error representing either an RMSE or standard deviation value after comparing SfM-MVS results against benchmark datasets (e.g. TLS or independent CPs) and  $H$  corresponds to the average flying UAV height. Based on Equation (2.2) relative error ratios of the aforementioned studies are listed in Table 2.2. Equation (2.2) was also applied to compare results from this research (see Chapters 5 and 6) with the results of the aforementioned studies and presented in Section 7.1.1.

Table 2.2: Reported vertical errors and estimated relative error ratios per study.

Study	Inclusion of GCPs	Reported vertical errors [m]	Average flying height [m]	Relative error ratio	Highest/lowest error
Niethammer et al. (2012)	Yes	0.310	175	1:565	
Turner et al. (2015)	Yes	0.044	40	1:909	Lowest
Turner et al. (2015)	Yes	0.090	40	1:444	Highest
Eltner et al. (2015)	Yes	0.005	9.5	1:1900	
Woodget et al. (2015)	Yes	0.019	26.89	1:1415	Lowest
Woodget et al. (2015)	Yes	0.203	28.39	1:140	Highest
Gonçalves and Henriques (2015)	Yes	0.046	131	1:2848	Lowest
Gonçalves and Henriques (2015)	Yes	0.107	93	1:869	Highest
Gerke and Przybilla, (2016)	No (RTK-UAV)	0.065	105	1:1615	
Cook (2017)	Yes	0.307	73	1:238	
Dall'Asta et al. (2017)	No (RTK-UAV)	0.072	140	1:1944	Lowest
Dall'Asta et al. (2017)	Yes	0.110	150	1:1364	Highest

For studies with numerous experiments, Table 2.2 reports the results with the highest and lowest errors. Relative error ratios are in the region of 1:140-1944 with the lowest caused primarily by vegetation presence (Woodget et al., 2015). Overall, ratios are at the lower end of the 1:1080-9400 which were estimated from the use of DSLR cameras and conventional photogrammetric procedures by James and Robson (2012). In addition, in the absence of GCPs, the ratios are comparable giving confidence to the performance of the recent RTK-UAV. However, in the context of morphological monitoring, investigation of the error distribution is also required. It is noteworthy that, regardless of the UAV system and/or camera types, SfM-MVS processing can generate uncertainties that influence the level of the minimum detectable surface change (Section 3.2). The review of these case studies demonstrated that consumer-grade UAVs equipped with off-the-shelf cameras can offer cm-level spatial resolution and can constitute a suitable cost-effective monitoring approach. However, examination of resultant uncertainties is a necessity (Mantovani et al., 1996), which can be achieved with the aid of total station, GNSS and/or TLS observations as they provide up to mm-level accuracies.

## 2.4 Summary

Chapter 2 demonstrated the wide range of geomatics monitoring techniques and discussed their performance in relation to accuracy and cost-effectiveness. Firstly, conventional geotechnical and geophysical investigations, used to observe subsurface structure, were introduced. These are generally complemented by total station and GNSS observations to derive surface displacement and movement rates. These techniques can quantify landslide deformations with high accuracy but low spatial resolution. Previous monitoring studies with photogrammetric, ALS and TLS observations demonstrated the capability for high spatial and temporal resolutions with high performance. Although these techniques are still popular in landslide monitoring, they are relatively costly. Chapter 2 also reviewed current UAV-based approaches which bridge the gap between terrestrial, manned airborne and spaceborne techniques. The flexibility of mini UAVs with compact and low-cost off-the-shelf digital cameras alongside the ease of contemporary SfM-MVS processing workflow have become attractive in monitoring studies. The review showed that consumer-grade UAV-based approaches could deliver cost-effective monitoring solutions with acceptable accuracies and spatial resolutions for landslide monitoring. However, to quantify the landslide deformation that each approach can observe, errors inherited in the SfM-MVS process and UAV systems must be investigated. As a continuation of this review, Chapter 3 details the associated uncertainties and proposes a morphology-based monitoring strategy.

## **Chapter 3.**

# **Morphology-based monitoring strategy**

---

Chapter 2 reviewed existing geomatics techniques for landslide monitoring and highlighted some relevant differences between them. Discussion related to different spatial and temporal resolutions, operational costs for repeated surveys and the level of landslide movement each technique can estimate. The chapter also presented the evolution and emergence of UAV technology, in combination with the SfM workflow, as a modern and affordable airborne photogrammetric approach. Through the discussion, it was concluded that mini consumer-grade UAVs are suitable for monitoring purposes, enabling point clouds of high density with relatively low operational costs. This chapter presents a monitoring strategy that can be applied to UAV imagery acquired over inaccessible hazardous terrain accounting for the variations of surface morphology over time. The chapter commences with an introduction of the proposed monitoring strategy and then describes the generation of DEM, orthophotomosaic and surface morphological attributes, which are the core input datasets, also highlighting associated errors. Finally, every step of the proposed strategy is explained, while the various algorithms involved in the process are reviewed.

### **3.1 Strategy overview**

The proposed morphology-based monitoring strategy links together three prime aspects of surface monitoring, namely a) co-registration for aligning time-series of 3D surfaces; b) 3D sensitivity to set the error boundaries through statistics; and c) estimation of 3D surface change to support landslide mechanism investigation (Figure 3.1).

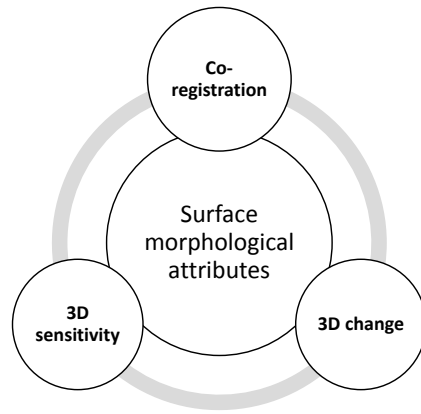


Figure 3.1: Morphology-based monitoring strategy overview

Co-registration constitutes the core step of the proposed monitoring strategy. Unresolved misalignment errors and other possible biases from the co-registration step are expressed in the 3D sensitivity. This quantifies the minimum detectable change and constitutes a quality index of co-registration. Cross-validation of the estimations is performed with independent benchmark datasets and is integrated into every phase of the monitoring strategy. The fundamental element of the proposed monitoring strategy that distinguishes it from other approaches is the bond between landslides and surface morphology. This bond is developed through the integration of surface morphological attributes into the adopted workflows for co-registration and surface estimation. This integration involves an automatic generation of pseudo GCPs incorporated into the SfM-MVS pipeline, eliminating the requirement for surveyed GCPs. Moreover, it involves the combination of morphological attributes with image cross-correlation functions to automatically quantify landslide kinematics.

## 3.2 UAV-derived SfM-MVS products

### 3.2.1 Typical SfM-MVS pipeline

According to recent published studies and reviews (Snavely et al., 2008; Haala and Rothermel, 2012; Fonstad et al., 2013; James and Robson, 2014; Remondino et al., 2014; Eltner and Schneider, 2015; Eltner et al., 2016; James et al., 2017a), the standard SfM-MVS pipeline can be summarized into three main phases, as follows:

Sparse point cloud reconstruction: Firstly, the generation of a point cloud of tie points (i.e. image observations, internal constraints, sparse point cloud) is performed, with feature-based matching, via a self-calibrating bundle adjustment without any a priori information of the camera's IOPs. This step aligns acquired images and establishes a

multi-stereo pair reconstruction based on epipolar geometry<sup>8</sup>. In particular, a feature-based algorithm detects and matches corresponding points lying on epipolar lines across images. Subsets of images are incrementally aligned until the complete photogrammetric block is orientated. Outlier detection is recursively performed to eliminate erroneous point matches. The camera's IOPs and EOPs are simultaneously determined through iterations in a least squares sense by minimizing a global reprojection error. This quantifies the pixel differences between the initially detected corresponding points and those estimated and back-projected into all overlapping images of the photogrammetric block. Hence, space resection and intersection<sup>9</sup> of every tie point is resolved and a sparse point cloud with 3D coordinates in an arbitrary coordinate system is generated.

Georeferencing: Control information is necessary to scale and orientate the resultant sparse point cloud and photogrammetric block, determining the precise 3D shape of a surface. It is usually provided in the form of surveyed GCPs (indirect georeferencing, IG), or obtained from the positions and/or orientations of the camera exposure stations (direct georeferencing, DG). This information is used as weighted observations (i.e. external constraints) in conjunction with the tie points (i.e. internal constraints) in a least squares bundle adjustment, thereby re-estimating the camera's IOPs, EOPs and the 3D coordinates of the sparse point cloud in the desired coordinate system.

Dense point cloud (DPC) reconstruction: Given the already established epipolar geometry of the photogrammetric block from the first phase, disparities are computed at all pixels via area-based image matching approaches. The pixels are back-projected to all images and triangulated (i.e. via spatial intersection) to form a 3D surface without abrupt irregularities through gradient-based and energy minimization algorithms. The SfM-MVS pipeline results in a RGB-colored DPC that constitutes the raw form of a 3D surface representation.

### ***3.2.2 DSM/DEM generation***

A DSM and DEM constitute the common digital mathematical surface representations (2.5D or quasi-3D models) with each grid point comprising one single elevation value, as opposed to true 3D surface with multiple elevations over a particular point (Turner, 1997; Koch and Heipke, 2006; Wolf et al., 2014). A DSM represents the earth's terrain, including manmade features and vegetation, whereas a DEM only includes the bare earth

---

<sup>8</sup> Equivalent to coplanarity condition (see Section 2.2.1).

<sup>9</sup> See Section 2.2.1

(Aguilar et al., 2005). Both models are structured either in the form of a regular grid or a triangulated irregular network (TIN) (Wolf et al., 2014).

In a grid DEM the elevation values are stored in a double array of square pixels with a uniform size (Wolf et al., 2014; de Smith et al., 2015). Additional georeferencing information, such as XY coordinates of the centres of the four corner pixels, are typically embedded into a DEM. A TIN involves the creation of unique triangles from a point cloud representing planar facets with XYZ coordinates at their nodes. The triangles are structured with Delaunay triangulation, which connects the points with each other to form the triangle edges based on a particular assumption. This requires that any circle passing through three vertices of a triangle does not include any vertex from another triangle, resulting in triangles with non-intersecting edges (Wolf et al., 2014; de Smith et al., 2015). Compared to a TIN, a grid DEM is suitable for the generation of orthophotomosaics and surface morphological attributes as it supports algorithmic processing in a computationally efficient way (Wolf et al., 2014). Alternatively, a TIN needs to be converted into a grid DEM with the aid of interpolation (Wolf et al., 2014).

To generate any form of DEM, interpolation is performed from discrete point-based observations, creating a continuous surface without voids. Interpolation techniques are divided into two general categories: a) deterministic and b) probabilistic (Maune et al., 2007; Bater and Coops, 2009; Godone and Garnero, 2013). The deterministic techniques rely on mathematical relationships between neighboring values, whereas the probabilistic techniques, also called geostatistical methods, predict this relationship by investigating the spatial autocorrelation of neighbouring points (Maune et al., 2007; Bater and Coops, 2009; de Smith et al., 2015).

Some common deterministic interpolation techniques applied in landslide monitoring studies are: natural neighbour, Delaunay triangulation, inverse distance weighted (IDW) and spline (Glenn et al., 2006; Kasai et al., 2009; Stumpf et al., 2013; Turner et al., 2015; Al-Rawabdeh et al., 2016b). Natural neighbor is based on Thiessen (or Voronoi) polygons. It assigns an elevation value on each point from those of the nearest Thiessen polygons, which define the region of influence around each point (Sibson, 1981; Guo et al., 2010). Delaunay triangulation is a linear interpolation technique and closely associated with the generation of the Thiessen polygons. These are formed by connecting the centres of the circumcircles of each triangle derived from Delaunay triangulation. IDW is based on the fundamental law of geography (Tobler, 1970), expressing that closest

points are more similar than distant ones (Guo et al., 2010). The weights used in IDW are inversely proportional to a power of the horizontal distance (usually a power of two) between a grid point and the nearest observed point (Chaplot et al., 2006). Splines create a smooth surface by fitting a combination of different linear functions to the observed points within a specified search radius (Guo et al., 2010; Godone and Garnero, 2013; Wolf et al., 2014). Apart from the aforementioned techniques, there are others such as nearest neighbour, bi-linear and bi-cubic interpolation, mostly suitable for image resampling (e.g. a bi-cubic technique was applied in Debella-Gilo and Käab (2011)). For a complete description of available interpolation techniques refer to de Smith et al. (2015).

Regarding geostatistical methods, Kriging is the most popular. Firstly, a semi-variogram is created, which indicates the spatial correlation between the values of observed points and their distances. Then, an empirical mathematical model is fitted to the semi-variogram providing the autocorrelation values used to derive the kriging weights for the observed values of known locations. Based on these weights, kriging can predict the values to all unknown locations and generate the interpolated surface. For instance, in Immerzeel et al. (2014), kriging was applied to manually extracted points from UAV derived orthophotomosaics to compare their displacement against UAV derived DEMs. A detailed explanation of geostatistical methods can be found in Sarma (2009).

In surface change detection studies, with point clouds of high but irregular density (e.g. derived with TLS or UAV), interpolation is sometimes avoided to prevent smoothing effects (Lague et al., 2013; James et al., 2017b). However, as time-series of morphological attributes and orthophotomosaics are utilised (see Chapters 5 and 6), interpolation is essential. The choice of an interpolation technique can affect the quality of a DEM in terms of how closely it models the true surface, regardless of the geomatics method applied to obtain the observations (Bater and Coops, 2009; Fan and Atkinson, 2015).

Numerous studies have investigated the influence of various factors into the resultant interpolated surface, such as sampling point density, spatial resolution and morphology of the terrain (Lloyd and Atkinson, 2002; Aguilar et al., 2005; Chaplot et al., 2006; Bater and Coops, 2009; Aguilar et al., 2010; Guo et al., 2010; Fan and Atkinson, 2015). Aguilar et al. (2005) and Guo et al. (2010) concluded that high sampling point density does not necessarily decrease interpolation errors, as noise from strong surface variations can be added, especially over rough terrain. Conversely, they highlighted that the higher the point density is the higher the DEM quality becomes, but the computational effort

increases. However, oversampling can often decrease the DEM quality as in the case of merging a sparse with a denser point cloud (e.g. Buckley and Mitchell (2004)). Moreover, to reduce points, surface morphology should be taken into account so that a DEM properly reflects important characteristics. Guo et al. (2010) also reported that DEM quality is linearly correlated to the spatial resolution, with worse quality produced by coarser resolutions. Overall, there is no single interpolation technique outperforming others. For instance, in the context of landslides, spline and kriging are not suitable to model convex and concave breaks in slope, as noted by Tarolli et al. (2012). TIN can cope better with surface discontinuities than the other two techniques (Heritage et al., 2009). To improve the quality and faithfulness of a surface representation using TIN the insertion of breaklines of significant discontinuities that have constant slope is a necessity (Wolf et al., 2014). However, this requires additional human intervention and high computational effort when dealing with millions of points for DEM generation.

To overcome the inclusion of breaklines and reduce the additional noise in high-density point clouds, recent studies have implemented moving planes interpolation with ALS and TLS datasets (Hollaus et al., 2010; Milenkovic et al., 2015). Compared to previous techniques, moving planes interpolation takes into consideration the local surface morphology. It fits the best-tilted plane to a specified number of nearest neighbour points, by minimizing the vertical distance in a least squares sense (Lancaster and Salkauskas, 1981; Kraus et al., 2006; Hollaus et al., 2010). Hollaus et al. (2010) demonstrated that this technique can accurately model an inclined surface and Kraus et al. (2006) highlighted that it can handle possible outliers which exist above or below the surface through the least squares adjustment. Such outliers can be found in UAV derived point clouds, which makes the moving planes interpolation suitable for UAV DEM generation, especially over grassy and rough terrain.

### ***3.2.3 Orthophotomosaic generation***

To generate an orthophoto, which represents a continuous image grid with a uniform mapping scale, orthorectification is undertaken (Mikhail et al., 2001; Wolf et al., 2014). This ensures that each object is mapped in its true orthographic positions and relief displacement is removed from the orthophoto. Orthorectification is achieved with the inclusion of a DEM and the systematic use of collinearity condition for all grid points per image (Wolf et al., 2014). The pixels of an image are projected onto the DEM, their coordinates in object space are defined, and then are back-projected onto the image. Possible pixel differences, caused by relief displacement and perspective errors, are

minimised through interpolation to generate the orthoimage (Mikhail et al., 2001). By mosaicking orthoimages together, an orthophotomosaic is created.

### 3.2.4 SfM-MVS software description

Over the last decade a series of low-cost commercial and open-source SfM-MVS software has emerged and been used for UAV image processing (see Table 3.1). Such software are different from the high-end photogrammetric software (e.g. *ImageStation*, *IMAGINE Photogrammetry*, *LPS*, *Inpho* and *SOCET GXP*), as noted by Granshaw (2016b). Pure photogrammetric software was designed for fixed image block geometry, such as 100% nadir imagery, unlike the abrupt variations in flight altitudes and perspective views contained within a UAV image block (Rosnell and Honkavaara, 2012; Nex and Remondino, 2014; Wolf et al., 2014). Hence, traditional photogrammetric software cannot readily cope with the instability of on-board UAV compact cameras (Whitehead and Hugenholtz, 2015).

Table 3.1: List of software produced to-date that adopts (partially or fully) the SfM-MVS pipeline.

Software	Source	Commercial/ Open-source
<i>Autodesk 123D Catch</i>	(Autodesk, 2017)	Open-source
<i>VisualSfm</i>	(Snavely et al., 2008; Wu, 2017)	Open-source
<i>Bundler</i>	(Snavely et al., 2008; Lourakis and Argyros, 2009)	Open-source
<i>Clustering View for Multi-view Stereo (CMVS)</i>	(Furukawa and Ponce, 2010)	Open-source
<i>Patch-based Multi-view Stereo (PMVS2)</i>	(Furukawa and Ponce, 2010)	Open-source
<i>MicMac-Apero</i>	(Pierrot Deseilligny and Clery, 2011)	Open-source
<i>Surface Reconstruction (SURE)</i>	(Haala and Rothermel, 2012)	Commercial
<i>PhotoModeler</i>	(PhotoModeler, 2017)	Commercial
<i>Pix4D</i>	(Pix4D, 2016)	Commercial
<i>Agisoft PhotoScan</i>	(PhotoScan, 2016a)	Commercial

Among the reported software in Table 3.1, only *PhotoScan*, *Pix4d* and *MicMac* follow the full SfM-MVS pipeline as previously described. For example, *CMVS*, *PMVS2* and *SURE* are only designed for the DPC reconstruction and have augmented *VisualSfm*. Table 3.1 includes a list of the most frequently used tools within published studies. An extended list is described in Eltner et al. (2016).

In recent years, *PhotoScan* has gained popularity in the scientific community, as evidenced in Figure 3.2, mostly due to its user-friendly, almost “black-box”, workflow (Eltner et al., 2016; James et al., 2017a). The number of published studies have gradually increased relative to *Pix4D*, whereas there is a steady linear trend for *MicMac* use (Figure 3.2). It should be noted that the results in Figure 3.2 include UAV studies from many

scientific communities, and not only photogrammetry. *PhotoScan*'s simple workflow has appealed to non-photogrammetric experts. Whilst comparison of the various SfM-MVS software is not a core aim of this study, their review has supported the understanding of *PhotoScan*'s routines, since *PhotoScan* was implemented and integrated into the proposed monitoring strategy.

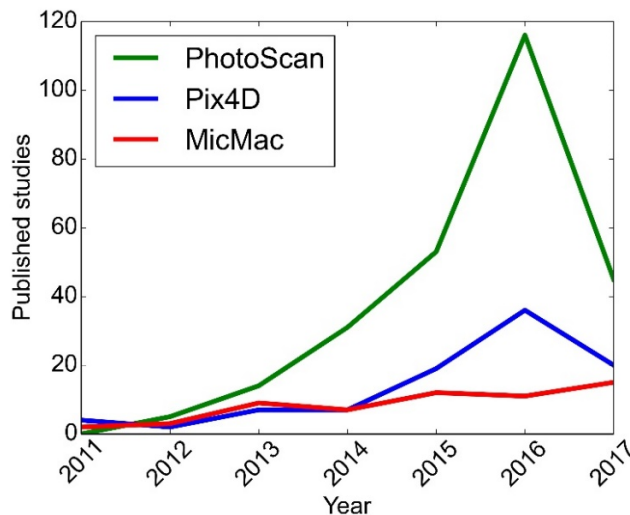


Figure 3.2: Number of published studies processing UAV imagery with *PhotoScan*, *Pix4D* and *MicMac* in the last six years, as extracted from *Scopus*<sup>10</sup>.

According to previous studies (Pierrot Deseilligny and Clery, 2011; Fonstad et al., 2013; Woodget et al., 2015) it is more likely that *PhotoScan* utilises a similar algorithm to SIFT (introduced by Lowe (2004)) in combination with a RANSAC-style algorithm for image alignment and sparse point cloud reconstruction. Compared to classical photogrammetric routines with image cross-correlation functions (Helava, 1978; Ackermann, 1984; Gruen and Baltsavias, 1988), the SIFT operator is not affected by variations in spatial resolution (Fonstad et al., 2013). This is because SIFT processes the images under multiple levels of blur and image resolutions. It detects interest points on the images at the local extremes created by the difference-of-Gaussian smoothing functions (Lowe, 2004). This particular property of SIFT makes feature-detection invariant to image translations, rotations and illumination differences, favorable for aligning UAV imagery (Fonstad et al., 2013; Woodget et al., 2015). This was also demonstrated in Snavely et al. (2008) through aligning internet photos acquired in different seasons, with different sensors and spatial resolutions. A comprehensive description of SIFT implementation can be found in Lowe (2004) and Ives and Delbracio (2014). In addition, Jazayeri and Fraser (2010) identified a collection of various feature detectors/descriptors not yet widely established in close

<sup>10</sup> Three searches performed in *Scopus* on 13<sup>th</sup> June 2017, based on the three software names titles, as follows: [“software name” AND “UAV” OR “RPAS” OR “drones”].

range photogrammetry and demonstrated their performance on image matching. A more recent study (Kehl et al., 2017) investigated the performance of various SIFT-like algorithms under multiple scenarios of different illumination conditions. They reported that few algorithms successfully detected homologous features due to radiance variations observed on the images. Overall, different SIFT implementations can lead to different results depending on their algorithmic settings alongside the environmental conditions at the time of image acquisition.

### ***3.2.5 SfM-MVS pipeline in PhotoScan***

#### ***Sparse point cloud reconstruction***

The numerical implementation of SIFT-RANSAC, and the definition of the arbitrary coordinate system during the sparse point cloud reconstruction phase, is not clearly explained in *PhotoScan*'s documentation. However, based on other studies (Hartley and Zisserman, 2004; Snavely et al., 2008; Barazzetti et al., 2010), the RANSAC outlier detection algorithm appears to rely on the photogrammetric block's relative orientation and epipolar geometry, which are expressed by the fundamental matrix. The fundamental matrix links points in overlapping images along their epipolar lines (Hartley and Zisserman, 2004; Snavely et al., 2008; Barazzetti et al., 2010; Granshaw and Fraser, 2015). Firstly, candidate corresponding points detected by SIFT are stored in a connectivity graph (with nodes and edges), which links the spatial relationship between multiple image pairs. The graph nodes correspond to the images and the graph edges to the image pairs associated with the number of corresponding matches (Snavely et al., 2008; Rupnik et al., 2015). An initial image pair selection establishes a first stereo view. The selection is based on the high number of image correspondences and a wide baseline with large intersection angle, as searched within the connectivity graph (Snavely et al., 2008).

To define the relative orientation of the initial stereo pair and estimate an approximate fundamental matrix, the Nistér (2004) method is typically applied. Five corresponding points are chosen among all SIFT candidate correspondences (Snavely et al., 2008; Barazzetti et al., 2010). RANSAC recomposes the relative orientation by eliminating outliers given an a priori threshold. Then, an initial sparse point cloud of the first stereo pair is reconstructed via space resection and intersection. This point cloud incrementally extends, as points from more image pairs are concatenated (Snavely et al., 2008; Remondino et al., 2014; Rupnik et al., 2015). A self-calibrating bundle adjustment solves for the minimisation of a global reprojection error with the aid of iterative optimisation

methods such as Gauss-Newton, Gauss-Markov and Levenberg-Marquardt (Snaveely et al., 2008; Lourakis and Argyros, 2009; Pierrot Deseilligny and Clery, 2011; Remondino et al., 2012).

This bundle adjustment also estimates the camera's IOP based on specified camera distortion models. For example, *PhotoScan* has adopted the Brown distortion model (Brown, 1971), widely used in photogrammetry, which is expressed as (Zhang, 1996; Wolf et al., 2014; Carbonneau and Dietrich, 2016):

$$\begin{bmatrix} \hat{x} \\ \hat{y} \end{bmatrix} = (1 + K_1 r^2 + K_2 r^4 + K_3 r^6 + K_4 r^8) \begin{bmatrix} x \\ y \end{bmatrix} + \begin{bmatrix} (2P_1 xy + P_2(r^2 + 2x^2))(1 + P_3 r^2 + P_4 r^4) \\ (P_1(r^2 + 2y^2) + 2P_2 xy)(1 + P_3 r^2 + P_4 r^4) \end{bmatrix} \quad (3.1)$$

$$r = \sqrt{(x - x_p)^2 + (y - y_p)^2} \quad (3.2)$$

where  $(x, y)$  are the distorted image coordinates,  $(\hat{x}, \hat{y})$  the undistorted (i.e. distortion-corrected) image coordinates,  $(x_p, y_p)$  the image coordinates of principal point location,  $r$  the radial distance,  $(K_1, K_2, K_3, K_4)$  parameters of symmetrical radial lens distortion and  $(P_1, P_2, P_3, P_4)$  parameters of decentring (asymmetric radial and tangential) distortion (Wolf et al., 2014). Based on the central perspective geometry, the principal point is considered as the origin of the image coordinate system. Typical symmetrical radial distortion patterns are barrel and pincushion, with magnitudes of distortion towards and outwards from the image centre respectively. Decentring distortion is caused by misalignments of the lens system (Wolf et al., 2014).

*PhotoScan* provides the option to select a number of parameters to be re-estimated; otherwise the parameters are regarded as fixed and not included in the bundle adjustment. However, for compact cameras, it is preferable to account for the radial distortion estimation only, as decentring generally does not provide a comparable significant distortion magnitude (Eltner and Schneider, 2015). *MicMac* and *Pix4D* also offer the capability to select other distortion models, such as polynomial models of higher degrees, or to create a theoretical model, or even combine all provided ones together (Pierrot Deseilligny and Clery, 2011; Tournadre et al., 2015). Older SfM-MVS tools with limited functionality (e.g. *VisualSfM*) use only the  $K_1$  symmetrical radial lens distortion parameter. For a detailed comparison of the different SfM-MVS software capabilities the reader can refer to Eltner and Schneider (2015) and Eltner et al. (2016).

In the case of UAV imagery acquired with off-the-shelf compact cameras, the self-calibrating bundle adjustment is generally preferred to fixing the pre-calibration values of distortion parameters. This is because the self-calibrating bundle adjustment can compensate for on-board instability and the imaging network irregularity in an off-the-shelf camera (Luhmann et al., 2016). Carbonneau and Dietrich (2016) noted that estimated values of camera distortion parameters derived from multiple SfM-MVS self-calibration experiments under identical environmental and sensor conditions varied significantly. Harwin et al. (2015) compared the SfM-MVS self-calibrating solution against the SfM-MVS bundle adjustment with fixed pre-calibrated distortion values. They conducted experiments with the same UAV imagery under different scenarios (e.g. with and without the inclusion of oblique imagery and with various numbers of GCPs). They concluded that overall the self-calibrating bundle adjustment provided smaller errors at independently surveyed CPs.

However, recent studies (James and Robson, 2014; Eltner and Schneider, 2015; Carbonneau and Dietrich, 2016; James et al., 2017a; James et al., 2017b) have demonstrated that SfM-MVS self-calibrating bundle adjustment was unable to entirely resolve camera lens distortion. This was found to be particularly relevant in the case of low-cost cameras and in the absence of GCPs. Unresolved distortion formed bowl-shape systematic patterns that were recognisable either in the undistorted images (Eltner and Schneider, 2015) or in the vertical error distributions at independent CPs (James and Robson, 2014; James et al., 2017a).

### ***Georeferencing***

Regarding the georeferencing phase of the SfM-MVS pipeline, *PhotoScan* also supports the inclusion of external constraints (i.e. GCPs or camera exposure stations). Based on previous studies (James and Robson, 2014; Nex and Remondino, 2014; Rupnik et al., 2015; James et al., 2017a) the georeferencing phase has two roles, namely a) to define the datum i.e. absolute orientation of the photogrammetric block; and b) to alleviate the bowl-shape systematic effect. Typically a seven parameter Helmert transformation (three translations, three rotations and a scale) is performed after the self-calibrating bundle adjustment to transform the 3D point cloud from the arbitrary to the desirable coordinate system defined by the GCPs or the camera exposure stations (Eltner et al., 2016). Then, a least squares bundle adjustment is followed using weighted observations and estimating the camera's IOPs and EOPs (James et al., 2017a). This step is optional in *PhotoScan* but

highly recommended (James et al., 2017a), whereas it is not included in *VisualSfM* and *Bundler* (Snavely et al., 2008; Eltner and Schneider, 2015).

The internal and external constraints in *PhotoScan* are weighted according to four parameter settings, as named in *PhotoScan* (Reshetyuk and Mårtensson, 2016; James et al., 2017a):

- a) camera positional accuracy, which corresponds to the measurement precision of the camera exposure stations and orientations, usually associated with the uncertainties of on-board GNSS/INS sensors. Typical values of 10 m for position and 50° for camera angles (i.e. yaw, pitch, roll) are recommended for low-cost UAV platforms (PhotoScan, 2016b; PhotoScan, 2016a; Reshetyuk and Mårtensson, 2016). They were adopted in all experiments of this study;
- b) marker accuracy in meters, referring to the precision of measured GCPs or CPs as derived from field survey or any other adopted method. For mm-level precisions, a marker accuracy value between zero to five mm is recommended (Reshetyuk and Mårtensson, 2016; James et al., 2017a);
- c) marker accuracy in pixels, related to the precision of a marker (GCP or CP) after back-projecting from 3D object to image space. *PhotoScan* recommends a typical value of 0.1 pixels (PhotoScan, 2016a; James et al., 2017a);
- d) tie point accuracy in pixels, which corresponds to the precision of a tie point after back-projection from the 3D object to image space. *PhotoScan* recommends a typical value of four pixels (PhotoScan, 2016a; James et al., 2017a).

It is noteworthy that after importing the 3D coordinates of GCPs into *PhotoScan* the user is required to locate at least three of them in the imagery. Given the already established epipolar geometry, *PhotoScan* allows for locating the remaining GCPs in an automated manner, mapping also the epipolar lines per image pair. The user then visually checks whether the result is correct or not, taking into consideration the estimated reprojection error per point. The user can refine the position of GCPs on images with sub-pixel movements if necessary.

The aforementioned accuracies serve as a priori uncertainties in a weight matrix accompanying the observations in the least squares bundle adjustment (not explicitly described in *PhotoScan*'s documentation). The first three settings (a-c) are related to the weights of external constraints, whereas the fourth (d) is associated with the internal constraints. In an attempt to understand the functionality of the weight matrix, James et

al. (2017a) assessed the relationship between the last three parameters by computing the average 3D RMSEs at 15 GCPs and 15 CPs after repeating the least squares bundle adjustment with different values of the parameters. In their experiments, they used UAV imagery acquired in d'Oleire-Oltmanns et al. (2012). They demonstrated that marker pixel accuracies lying within the range of 0-1 pixel do not have a significant impact on 3D RMSEs variations. They also concluded that higher accuracy values are equivalent to lower weights in the bundle adjustment. Based on *PhotoScan*'s recommended settings of four pixels tie point accuracy and 0.1 pixels marker accuracy, they estimated that the GCPs were over-weighted. A trade-off between the two settings is required to prevent overfitting the observations towards tie point or marker weights (James et al., 2017a). They also recommended that the standard deviation of all image observations residuals after the sparse point cloud reconstruction phase can serve as tie point accuracy.

### ***Dense point cloud (DPC) reconstruction***

Concerning the DPC reconstruction phase, it is most likely that *PhotoScan* utilises an algorithm similar to SGM designed by Hirschmüller (2008) (Remondino et al., 2014; Eltner and Schneider, 2015). This approach is based on the assumption that in a stereo pair, neighboring pixels are expected to have similar disparities. The algorithm searches every single pixel along the epipolar line to find its potential correspondent disparity by assigning costs based on pixel value differences of its nearest neighbors (Dall'Asta and Roncella, 2014; Remondino et al., 2014). The search is performed in multiple directions within a neighborhood and the assigned costs are aggregated and evaluated through penalties. These control the smoothness level of the resultant 3D DPC. For example, neighboring pixels with large disparity variations get higher penalties. Costs and penalties are combined into a global cost function (Equations 13 and 14 in Hirschmüller (2008)). The final disparity per pixel corresponds to the disparity with the minimum cost (Hirschmüller, 2008; Dall'Asta and Roncella, 2014).

Detailed descriptions of various area-based image matching approaches for 3D DPC reconstruction can be found in Remondino et al. (2014) and Dall'Asta and Roncella (2014). After comparing the performance of various approaches, both studies concluded that no overall significant differences of the reconstructed DPCs were observed. They also reported that matching algorithms are mostly sensitive to shadows and local sharp surface discontinuities.

*PhotoScan* offers three different disparity options to control the smoothness level during reconstruction, namely mild, aggressive and moderate. The mild option maintains minor

surface details, the aggressive option filters out these details and the moderate option produces an intermediate smoothing. In combination with the aforementioned options, *PhotoScan* requires the specification of an image pyramid level upon which the reconstruction can be based. Four levels are provided, namely ultra-high, high, medium and low, with the first one maintaining the initial image spatial resolution. Each other level subsequently downscales the spatial resolution by 50%, decreasing proportionally the DPC density, similar to a subsampling filter. An optimal selection of disparity and image pyramid level is a trade-off between desired spatial resolution and computational effort (Remondino et al., 2014).

After the SfM-MVS pipeline, the raw 3D DPC usually has an irregular structure, resulting in heterogeneous point density. At the edges of a study area with lower image overlap, the point density usually decreases (Cook, 2017). Moreover, the presence of high frequency noise may affect the DPC quality. This noise usually occurs when a group of points close to each other represent the same 3D point on a surface (Remondino et al., 2014). To overcome this, a filtering step can be applied to raw point clouds such as resampling and thinning (Dyn et al., 2008; Rychkov et al., 2012; Remondino et al., 2014). It is worth noting that *PhotoScan* provides a filtering step through the aforementioned settings of DPC reconstruction. For instance, Cook (2017) compared the noise on three SfM-MVS point clouds reconstructed with three different image pyramid levels (ultra-high, high, and medium). They concluded that, although the medium level smooths high frequency noise over terrain with complex texture (e.g. sparse vegetation mixed with bare earth), the spatial resolution was degraded to an extent unsuitable for application-volume estimation of individual boulders. They also reported difficulty in the data handling of millions of points generated with the ultra-high level setting. Overall, any filtering method should maintain the informative surface characteristics at the required level based on the morphological application (Remondino et al., 2014).

### ***DEM and orthophoto generation***

After 3D DPC creation, it is recommended to remove very low or high points. This is usually performed manually. Then, a ground classification is performed to remove the “off-ground” features from the DPC. *PhotoScan* has adopted a slope-based routine for classification similar to the algorithm implemented in TerraSolid TerraScan (TerraScan, 2016). Firstly, it creates an initial triangulated surface from points with the lowest elevation within a certain grid size. This grid size is specified by the user and indicates the average size of a region with “off-ground” points, which exists in the study area (e.g.

a building or a densely vegetated sub-region). The user also needs to define two limits for angle and distance which indicates how far a ground point should be from the actual surface. It is recommended to use small angles for flat terrain, and conversely large angles for steep terrain. Then, the algorithm searches for points, located within these limits; it classifies these as ground and adds them into an initial triangulated surface. This surface is iteratively updated until all points from the initial DPC have been checked and classified.

Prior to interpolation *PhotoScan* performs a triangulated mesh computation which blends the previously generated disparities at a pixel level from the filtered DPC, creating planar facets (Verhoeven et al., 2012). Afterwards, the triangulated mesh is rasterised via IDW and then combined with median filtering. *PhotoScan* does not allow the import of an externally generated DEM. In parallel to the creation of the triangulated mesh, a texture map is generated assigning colors to all triangle nodes from the most nadir images (Verhoeven et al., 2012; PhotoScan, 2016a). The images are corrected for distortion, based on the previously estimated distortion parameters (Equations (3.1) and (3.2)). Each image pixel is reprojected onto the terrain mesh creating an ortho-image (Mills and McLeod, 2013) as part of the orthorectification process, described in Section 3.2.3. All ortho-images are then blended together to generate an orthophoto of the study area with the aid of global stitching methods that smooth edge effects, such as the one presented in Mills and McLeod (2013). It is not clear which method is implemented in *PhotoScan*. A list of documentation related to *PhotoScan's* tools can be found in PhotoScan (2016b).

### **3.2.6 Error sources in SfM-MVS derived products**

Numerous recent studies have revealed the presence of systematic errors in the automatic SfM-MVS pipeline which generate deformations in the derived products (James and Robson, 2014; Sieberth et al., 2014; Eltner and Schneider, 2015; Harwin et al., 2015; Carbonneau and Dietrich, 2016; Eltner et al., 2016; James et al., 2017a). Carbonneau and Dietrich (2016) demonstrated that these deformations, if unsolved, propagate into rotational, translational and vertical offsets, creating systematic tilt and/or radial patterns that adversely affect the UAV time-series observations. The systematic errors usually originate from image sensor characteristics, camera distortion models included within the SfM-MVS software, SfM-MVS software settings, imaging network configurations, GCP characteristics, surface texture, lightning and weather conditions, as well as over-parameterisation. Image sensor characteristics were mentioned in Section 2.3.1. The camera distortion models and the various SfM-MVS settings, mostly related to

*PhotoScan*, were discussed in Section 3.2.5. The remaining error sources are described in this section.

### ***Imaging network configurations***

Many published studies (Lucieer et al., 2014; Stöcker et al., 2015; Turner et al., 2015; Woodget et al., 2015) reported pre-planned image overlap percentages for parallel UAV flight lines below 100 m height, exceeding the standard 60% forward with 20% to 30% lateral overlap used in conventional aerial metric film camera surveys (Mikhail et al., 2001; Wolf et al., 2014). High pre-planned overlaps can prevent occlusions caused by UAV instability combined with wind turbulence. In general, low overlap might yield mismatches during the initial image alignment step of the SfM-MVS pipeline and generate discontinuities in the reconstructed sparse point cloud (Harwin et al., 2015; Dietrich, 2016). This, in turn, can destabilise the bundle adjustment solution and errors can propagate into the DEMs (Harwin et al., 2015). The higher the image overlap, the greater the number of optical rays that intersect an object point, thereby attaining increased redundancy in point determination (Haala and Rothmel, 2012). However, with the increase of image overlap, and hence higher number of images, the increase of computational effort is unavoidable; an important parameter to consider for UAV image post processing (James and Robson, 2012; Eltner et al., 2016).

James and Robson (2014) demonstrated that parallel flight lines can cause vertical systematic bowl-shape deformations on the resultant DEM. According to James and Robson (2014) these errors can be significantly reduced either by acquiring convergent images, flight lines in opposing directions or with the inclusion of evenly distributed GCPs into the bundle adjustment. Convergent imagery can be easily configured with rotor platforms, unlike fixed-wing platforms. For that, James and Robson (2014) recommended the inclusion of smooth banked turns to strengthen the imaging network geometry with fixed-wing UAVs. As noted by Eltner et al. (2016), convergent imagery widens the image baselines thereby improving tie point matching performance.

### ***GCP characteristics***

It has already been stated that a good distribution of an adequate number of GCPs incorporated into the SfM-MVS bundle adjustment can mitigate systematic errors. It is also well-known that high GCP coverage offers redundancy in photogrammetry (Wolf et al., 2014). James et al. (2017a) conducted an experiment to define the optimal number via a Monte Carlo process performing many combinations of randomly selected GCPs among 30 surveyed targets, using the remaining as independent CPs. They noted that no

particular GCP distribution can entirely remove systematic errors. They also illustrated that five GCPs, four of them creating an approximate rectangle and one located in the middle, can generate DEM deformations within a  $\pm 3.0$  cm range compared against a DEM derived with all GCPs. Similarly, Reshetyuk and Mårtensson (2016) concluded that five GCPs of the same installation pattern can deliver sub-cm vertical differences when compared against TLS data over a flat terrain. Many studies have highlighted the importance of establishing GCPs around the edges of the study area otherwise deformations in SfM-MVS DEMs outside the GCP coverage can increase (James and Robson, 2012; Immerzeel et al., 2014; Javernick et al., 2014; Eltner et al., 2016; Cook, 2017). This GCP configuration is similar to the “von Gruben points” which are located on the overlapping region of a stereo pair, typically used for the relative orientation establishment in classical photogrammetry (Kraus, 2007).

Further, the measurement precision of the surveyed GCPs, which serve as weights in the self-calibrating bundle adjustment (Section 3.2.5) and are usually inserted as markers' accuracy in *PhotoScan*, can affect the mitigation level of bowl-shape bias (Eltner et al., 2016; James et al., 2017a). Remondino et al. (2014) suggested that when GCPs constitute “ground truth” for the SfM-MVS pipeline, they should be independently surveyed, providing an estimated precision at least three times better than the expected results. James et al. (2017a) conducted simulated tests to evaluate the influence of GCP weights and their correlation with the camera distortion models with respect to the estimated RMSE at CPs after bundle adjustments in *PhotoScan*. They concluded that when four parameters of symmetrical radial lens distortion and four parameters of decentring distortion are chosen ( $K_1$ - $K_4$ ,  $P_1$ - $P_4$  of Equation (3.1)) GCP weights larger than 0.10 m (i.e. high markers' accuracy values) caused systematic vertical bowl-shape deformations. With the exclusion of the  $K_4$ ,  $P_3$  and  $P_4$  distortion parameters, these deformations decreased significantly. Their investigations were undertaken with a Panasonic Lumix GF1 compact camera mounted on a Sirius I fixed-wing UAV (d'Oleire-Oltmanns et al., 2012). Dietrich (2016) surveyed GCPs with a Trimble GeoXH handheld GNSS receiver attached with an additional antenna that allowed for differential corrections. They achieved a 0.20 cm average measurement precision for inclusion into *PhotoScan*'s bundle adjustment. They reported that the low precision caused DEM deformations when SfM-MVS DEM was compared against an ALS DEM. However, they did not describe the distortion camera model used, thus no conclusion for correlation between GCPs weights and distortion parameters can be deducted.

### ***Surface texture, lighting and windy conditions***

The image matching algorithms in the SfM-MVS workflow are affected by illumination differences, poor and homogenous textures and high gusts of wind (Remondino et al., 2014; Eltner et al., 2016). Illumination differences are caused by either wrong exposure camera settings or variations in lighting during a UAV flight. Overexposing bright areas or under exposing dark areas can vary the distinctive properties of surface features, thereby adversely affecting the tie point detection. A similar effect on overlapping images can be caused by successive transition from strong shadow to sun glare that can occur during a long UAV flight (Eltner et al., 2016). To prevent this, James and Robson (2012) recommended acquiring images under cloudy weather with bright lighting conditions (Eltner et al., 2016). Ideally, SfM-MVS should provide consistent results over any type of surface texture, as noted by (Nex and Remondino, 2014). However, intensity-based algorithms are vulnerable to homogenous textures (e.g. sandy texture in Mancini et al. (2013)), thereby degrading the SfM-MVS performance (Remondino et al., 2014; Eltner et al., 2016). Further, windy conditions with strong gusts can create sudden turbulences and can cause instability and forward motion of the UAV, causing blurred images (Sieberth et al., 2014). As Sieberth et al. (2014) noted, image blur affects the image sharpness which might influence the camera calibration results and might also affect the reliable detection and matching of tie points.

### ***Over-parameterisation***

As several parameters are involved at different stages of the SfM-MVS pipeline, errors are propagated through the process (Eltner et al., 2016). Typical quality indicators of a photogrammetric process are provided from the covariance and correlation matrices computed in bundle adjustment (Granshaw, 1980; Luhmann et al., 2016). However, such estimators are absent in most “black-box” SfM-MVS software and hidden errors of the pipeline are not explicitly explained (Fonstad et al., 2013; Luhmann et al., 2016; James et al., 2017a). A large number of observations from hundreds of images and many estimated parameters in the self-calibrating bundle adjustment can impede the matrix inversion, essential for covariance estimation. Thus, another possible cause of the systematic errors is over-parameterisation, which cannot be easily controlled with SfM-MVS software packages. In response, recent studies (Carbonneau and Dietrich, 2016; James et al., 2017b) suggested analytical ways of quantifying the internal precision of the estimated IOPs within SfM processing. These included multiple Monte Carlo tests either to derive optimal combinations of  $K_1$ - $K_2$  camera distortion coefficients (Carbonneau and Dietrich, 2016) or examination of the optimal SfM software parameters (i.e. marker/tie

points accuracies) and camera distortion models together with strengthening of the image observations (James et al., 2017b). Moreover, the correlation between parameters varies with the different bundle adjustment implementations in various SfM-MVS software. Reshetyuk and Mårtensson (2016) found that using the same SfM-MVS parameters and camera model, different systematic errors were derived from different SfM-MVS software. This implies the necessity to tune each software's parameters and to become familiar with the software capabilities (Remondino et al., 2014), as well as to verify the propagated errors at every step of the SfM-MVS pipeline with the aid of benchmark observations if possible.

### 3.3 Surface morphological attributes

Landslide processes erode the earth's surface causing failure and, as a result, discernible geomorphological features (e.g. scarps, ridges, cracks etc.) are formed (McKean and Roering, 2004; Gunn et al., 2013). Due to underlying surface mechanisms, an active landslide area (i.e. failed terrain) has relatively rougher surface topography than a non-failing region (McKean and Roering, 2004; Glenn et al., 2006; Tarolli, 2014). Unstable terrain can be then represented using a rough surface texture, and vice versa (Baek and Kim, 2015). In the context of multiple epoch surface co-registration to detect surface deformations, the identification of stable terrain is required (Wujanz et al., 2016).

Numerous morphological attributes have been proposed to identify stable/unstable terrain and delineate geomorphological features. These attributes can be classified into three categories based on the derivation. The first category consists of those based on statistical analysis of variations in elevation, such as standard deviation, slope and normal vectors (Hobson, 1972; Shepard et al., 2001; McKean and Roering, 2004; Frankel and Dolan, 2007; Berti et al., 2013). The second category includes attributes derived from those of the first category such as *shaded relief*, *curvature*, *openness* and *Eigen value ratio* (Yokoyama et al., 2002; de Smith et al., 2015). The third category consists of attributes calculated with other more complex analysis, such as Fourier/wavelet transformations and semi-variograms (Glenn et al., 2006; Booth et al., 2009; Berti et al., 2013). Apart from the aforementioned, several other attributes have been implemented for landslide and morphological studies (Hobson, 1972; McKean and Roering, 2004; Glenn et al., 2006; Grohmann et al., 2011; Ventura et al., 2011; Favalli and Fornaciai, 2017), such as area ratio, residual topography, vector dispersion, standard deviation of slope, sky view factor, etc. In this study, the attributes of the first two categories are investigated and incorporated into the proposed monitoring strategy. Favalli and Fornaciai (2017) provide

a detailed comparison of the most commonly used attributes in recent morphological studies.

### ***3.3.1 Morphological attributes derived from elevation variations***

To derive characteristic properties of a 3D surface, an analytical form is fitted to elevations  $z$ , at the DEM grid points,  $(x, y)$  namely  $z = f(x, y)$  within a moving kernel (de Smith et al., 2015). The most common analytical form, used in geomorphological studies, is the bivariate quadratic functional model (Evans, 1979; Tarolli et al., 2012; de Smith et al., 2015; Rigol-Sanchez et al., 2015):

$$z = ax^2 + by^2 + cxy + dx + ey + f \quad (3.3)$$

where  $a - f$  are the quadratic coefficients. The partial derivatives of this functional model are expressed as:

$$f_x = \frac{\partial z}{\partial x} \quad (3.4)$$

$$f_y = \frac{\partial z}{\partial y} \quad (3.5)$$

### ***DEM Standard Deviation***

The standard deviation of a DEM is calculated as follows:

$$SD_{el} = \left[ \frac{1}{n-1} \sum_{i=1}^n (z_i - \bar{z})^2 \right]^{1/2} \quad (3.6)$$

where  $n$  is equal to the number of pixels within a moving kernel of a specified size,  $z_i$  refers to elevation value at each DEM grid point and  $\bar{z}$  is the mean elevation of all grid points within the moving kernel. In the case of a DEM derived from a moving least squares interpolation, its corresponding standard deviation expresses the local variance from the fitted plane (Buscombe, 2016).

The expression in Equation (3.6), as introduced by Shepard et al. (2001), has been the most popular morphological attribute due to its computational simplicity (Grohmann et al., 2011; Berti et al., 2013; Favalli and Fornaciai, 2017). Not only has it been used to express surface roughness, but also to evaluate the DEM quality (Grohmann et al., 2011).

For instance, Wheaton et al. (2010) and Brasington et al. (2012) implemented this attribute as an intermediate step in order to estimate the uncertainty of elevation variation between two epochs. They generated each epoch's DEM with thousands of points surveyed over stable terrain. They concluded that the uncertainty of elevation variation is higher over rough and steep terrain compared to the uncertainty over smooth and flat terrain. Additionally, Berti et al. (2013) and Grohmann et al. (2011) reported that this attribute is sensitive to DEM artefacts. Although this is generally a weakness, it can become an advantage when the DEM standard deviation is used as a DEM uncertainty measure, crucial for morphological monitoring applications.

### ***Slope, aspect and normal vectors***

*Slope* constitutes one of the main parameters used in slope stability and landslide susceptibility modelling (Dawson et al., 1999; Van Westen et al., 2003). In landslide mapping and monitoring, *slope* and *aspect* have been used to identify regions prone to instability and potential active landslides over large regions viewed from satellite, airborne imagery or ALS (Lee and Min, 2001; Iwahashi et al., 2003; Kasai et al., 2009). For close range applications, these attributes can provide local information on steep angles and orientation of eroded surface features to support the understanding of landslide mechanisms (Glenn et al., 2006; Kasai et al., 2009). In addition, Al-Rawabdeh et al. (2016b) computed the distribution of *slope* derived from a UAV DEM to detect landslide scarps given by sharp surface discontinuities. They assumed that potential scarps exist over regions with larger than the average slopes for the whole study area. The average slope also coincided with the average angle of friction in the sub-surface. Apart from feature extraction, *slope* has been utilised in combination with image cross correlation functions to quantify the spatio-temporal movement of earthflows (Daehne and Corsini, 2013; Travelletti et al., 2014).

*Slope* and *aspect* are computed as follows (Veitinger et al., 2014; de Smith et al., 2015):

$$slope = \arctan \left[ \sqrt{(f_x)^2 + (f_y)^2} \right] \quad (3.7)$$

$$aspect = \arctan \left( \frac{f_y}{f_x} \right) \quad (3.8)$$

In Equations (3.7) and (3.8) *slope* indicates the steepest angle of a surface and *aspect* depicts the azimuth of the steepest *slope*. Typically, *slope* is expressed in degrees or

percentage and *aspect* in degrees from 0° degrees to 360°, clockwise with North equal to zero / 360 degrees.

Smooth terrain is characterised by constant *slope* and *aspect*, whereas rough terrain by local variations (Hobson, 1972; McKean and Roering, 2004; Favalli and Fornaciai, 2017). These variations can be mathematically expressed with the unit direction vectors, also called normal vectors, and are always perpendicular to a surface plane at a specified point (Gray, 1997; McKean and Roering, 2004). In the case of a TIN representing the surface topography, a local plane is defined by a triangle. Each triangle of the TIN has three properties: a) normal vector, b) *slope* and c) *aspect*. After converting the TIN into a grid DEM, the normal vectors at the edges of each grid are computed as the average of the vectors of their neighboring triangles within a specified kernel size. The result is illustrated in Figure 3.3.

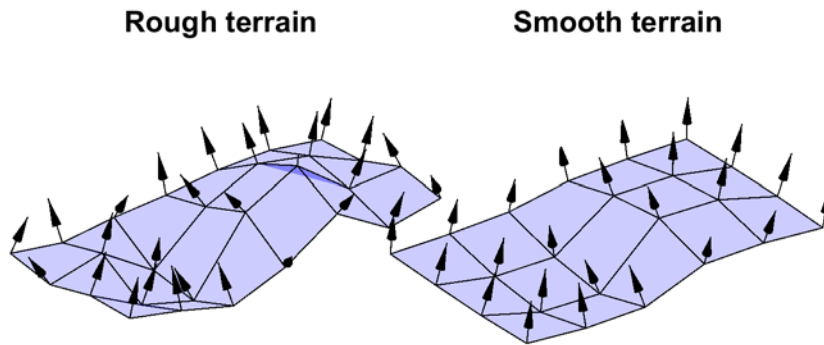


Figure 3.3: Schematic representation of normal vectors mapped in two DEMs visualising a rough and smooth terrain. The variations of vector orientation indicate surface roughness. Reproduced from McKean and Roering (2004) and Hobson (1972).

Normal vectors with coherent orientation imply that local *slope* and *aspect* are similar, as occurs in a smooth terrain. Whereas a random distribution of their orientation indicates a local diversity in slope and aspect. This diversity constitutes a roughness measure of a surface, as evidenced in Figure 3.3.

Based on differential geometry, for a surface represented as in Equation (3.3), the normal vector at a point  $p$  with coordinates  $(x_0, y_0)$  is calculated as (Gray, 1997):

$$N = \begin{vmatrix} f_x(x_0, y_0) \\ f_y(x_0, y_0) \\ -1 \end{vmatrix} \quad (3.9)$$

For example, the surface of a plane in Euclidian space ( $R^3$ ) is defined by:

$$f(x, y, z) = ax + by + cz + d \quad (3.10)$$

with its normal vector, passing through point  $p$ , specified as:

$$N = \begin{bmatrix} a \\ b \\ c \end{bmatrix} \quad (3.11)$$

An alternative expression of normal vectors follows a covariance analysis (Watson, 1966; Woodcock, 1977; McKean and Roering, 2004; Favalli and Fornaciai, 2017). This analysis is commonly implemented with point clouds instead of a DEM or TIN representing a 3D surface (Pauly et al., 2002; Rusu, 2009; Yang and Zang, 2014). A covariance matrix of a point is defined as:

$$C = \frac{1}{n} \sum_{i=1}^n \begin{bmatrix} p_{ix} - \bar{p}_x \\ p_{iy} - \bar{p}_y \\ p_{iz} - \bar{p}_z \end{bmatrix} \cdot \begin{bmatrix} p_{ix} - \bar{p}_x \\ p_{iy} - \bar{p}_y \\ p_{iz} - \bar{p}_z \end{bmatrix}^T \quad (3.12)$$

where  $p_i$  the point  $i$  of a local neighborhood with  $n$  number of points and  $\bar{p}$  the 3D centroid of the neighbourhood. To reconstruct the unit normal vectors, a least squares plane adjustment is applied where the best plane passing through the 3D centroid is fitted to the points in the local neighborhood. Any variation of the points from the best fitted plane are represented with eigenvalues and eigenvectors (Pauly et al., 2002). These are defined by applying the eigenvalue decomposition theorem to the matrix:

$$Cv_l = \lambda_l v_l \quad (3.13)$$

where  $l \in \{1, 2, 3\}$  with  $\lambda_1 > \lambda_2 > \lambda_3 > 0$  the 3 eigenvalues (3x3 diagonal matrix) and  $v_1, v_2, v_3$  their corresponding eigenvectors (3x1 matrix), which always form an orthogonal frame (Watson, 1966). This notation is implemented in point cloud processing software such as Point Cloud Library (PCL)<sup>11</sup> (Rusu, 2009) and Cloud Compare<sup>12</sup> (Lague et al., 2013).

---

<sup>11</sup> [www.pointclouds.org/](http://www.pointclouds.org/)

<sup>12</sup> [www.danielgm.net/cc/](http://www.danielgm.net/cc/)

### 3.3.2 Secondary morphological attributes

#### *Shaded relief*

The *Shaded relief* attribute creates a visually appealing natural representation of the topography through simulated illumination (Horn, 1981; Smith and Clark, 2005; Hiller and Smith, 2008; Liu and Mason, 2016). The illumination is applied to a surface from an artificial light source of a specified elevation angle and azimuth simulating the sun's relative position. Subtle surface characteristics viewed from a certain azimuth can be visually enhanced or suppressed (Hiller and Smith, 2008). This technique is called *relief shading* or *hill shading*, hence its attribute's name (Hiller and Smith, 2008). Together with *contouring* it is one of the oldest and widely implemented techniques for surface visualisation due to its simple interpretation (Smith and Clark, 2005). Another recent use of this technique has been landslide movement detection through image cross correlation functions (Lucieer et al., 2014; Fey et al., 2015; Turner et al., 2015).

All available GIS software packages have adapted the *hill shading* technique considering two criteria: a) a surface should always reflect the incident light uniformly and diffusely from any angle of view (i.e. Lambertian surface); and b) a parallel light from one single source should illuminate a surface at an infinite distance. Then, the *hill shading* estimates the surface brightness proportionally to the cosine of the angle between the normal vector of the surface and the illumination direction (Liu and Mason, 2016; Favalli and Fornaciai, 2017). *Shaded relief (SR)* is calculated within a specified kernel size (Liu and Mason, 2016) as:

$$SR = 255[\cos(za) \cos(slope) + \sin(za) \sin(slope) \cos(az - aspect)] \quad (3.14)$$

with *slope* and *aspect* computed from Equations (3.7) and (3.8),  $za$  the zenith angle (i.e.  $90^\circ$  complement of the elevation angle) and  $az$  the azimuth. Based on Equation (3.14) the values of *shaded relief* attribute varies within 0-255, expressing a relative intensity estimation of an incident light on a slope. For example, a  $45^\circ$  zenith angle and a  $315^\circ$  azimuth (i.e. sun placed in NW) generate a *shaded relief* attribute with low values at the bottom-right of objects highlighting their shadows (Liu and Mason, 2016).

A preferred azimuth mainly affects the visual perception of relief details of a surface producing shadows, which can also lead to misinterpretation of surface roughness (Favalli and Fornaciai, 2017). This is a common limitation of *shaded relief*, called azimuth-biasing (Smith and Clark, 2005). To overcome this angle dependence, a surface can be

visualized: a) with multiple *shaded relief* attributes derived from different azimuths, (Smith and Clark, 2005); b) with one *shaded relief* attribute derived from 90° elevation angle (Favalli and Fornaciai, 2017); c) with a combination of multiple *shaded relief* attributes from different azimuths as a result of mean, minimum or maximum (Zakšek et al., 2011); and d) with a *shaded relief* attribute derived from a homogenous illumination with ambient occlusion technique. The latter applies a diffuse uniform illumination from a non-direct light simulating a cloudy day (Michael and Heinrich, 2000). This smoothens the shadow effect usually produced by lighting from a single direction (Fey et al., 2015; Favalli and Fornaciai, 2017). Michael and Heinrich (2000) showed that depth in a 3D surface can be better perceived and discriminated under diffuse uniform illumination. Among all the aforementioned techniques, the ambient occlusion has been also proved to perform best in quantification of landslide kinematics (Fey et al., 2015).

### ***Curvature***

*Curvature* has been one of the most commonly used morphological attributes for surface feature characterization since 1972 (Evans, 1972; Evans, 1979; Evans, 1980). Evans' method was the first to introduce the derivation of different attributes of *curvature* (e.g. profile, plan, minimum, maximum etc.) via gridded DEMs. Afterwards, a series of alternative expressions have been proposed and implemented in various GIS software packages (Zevenbergen and Thorne, 1987; Shary, 1995; Wood, 1996; Schmidt et al., 2003). A detailed description of several expressions can be found in Rigol-Sanchez et al. (2015) and de Smith et al. (2015).

To determine any expression of *curvature*, two fundamental forms are derived for a 3D surface (Gray, 1997; Pressley, 2010). Based on differential geometry, let  $W$  be a tangent vector at a point  $p$  to surface  $S$  embedded in  $R^3$  Euclidean space. In addition, any set of tangent vectors of  $R^3$  to the surface form a plane-the tangent plane. For  $r$ , a regular parameterisation of surface  $S$ , the tangent plane is considered the image of  $R^2$ . Regular parameterisation means that the  $r_x, r_y$  partial derivatives of  $r$  with respect to  $(x, y)$  variables are linearly independent and a normal vector can be computed as:

$$N = \frac{r_x \times r_y}{|r_x \times r_y|} \quad (3.15)$$

The first fundamental form depicts the arc length of a curve of the  $r(x, y)$  parametric surface, equal to the dot product of the tangent vector, as follows:  $|w|^2 = w \cdot w$ . This can

also be expressed as a linear combination of two vectors with  $(x, y)$  variables (Gray, 1997; Pressley, 2010):

$$I(ar_x + br_y, ar_x + br_y) = Ea^2 + 2Fab + Gb^2 \quad (3.16)$$

The second fundamental form depicts the change of the arc length while the surface  $r(x, y)$  is shifted along its normal vector and is expressed as:

$$II(ar_x + br_y, ar_x + br_y) = ea^2 + 2fab + gb^2 \quad (3.17)$$

Where  $a, b$  are constants,  $E, F, G$  and  $e, f, g$  are the coefficients of the first and second fundamental form, respectively computed as:

$$E = r_x \cdot r_x, \quad F = r_x \cdot r_y, \quad G = r_y \cdot r_y \quad (3.18)$$

$$e = r_{xx} \cdot N, \quad f = r_{xy} \cdot N, \quad g = r_{yy} \cdot N \quad (3.19)$$

with  $r_{xx}, r_{yy}$  and  $r_{xy}$  the second partial derivatives with respect to  $(x, y)$  variables.

The  $(H)$  mean *curvature* is estimated as the average of the  $(k_1)$  minimum and  $(k_2)$  maximum *curvature*, also called principal *curvatures*, both related to the  $(K)$  Gaussian *curvature* (Gray, 1997). Then:

$$K = k_1 k_2 \quad (3.20)$$

$$H = \frac{1}{2}(k_1 + k_2) \quad (3.21)$$

which leads to the solutions of the principal *curvatures* as:

$$k_1 = H + \sqrt{H^2 - K} \quad \text{and} \quad k_2 = H - \sqrt{H^2 - K} \quad (3.22)$$

Based on the coefficients of the two fundamental forms, the mean  $(H)$  and Gaussian  $(K)$  *curvatures* are computed by (Gray, 1997):

$$K = \frac{eg - f^2}{EG - F^2} \quad (3.23)$$

$$H = \frac{eG - 2fF + gE}{2(EG - F^2)} \quad (3.24)$$

### Openness

*Openness* indicates the angle of a cone that can fit to the terrain around a specified spatial extent and is related to the zenith angles (positive *openness*) and the nadir angles (negative *openness*) computed in the terrain's line-of-sight. Figure 3.4 illustrates the two different openness attributes. Positive ( $\varphi_L$ ) and negative ( $\psi_L$ ) *openness* are computed as follows (Yokoyama et al., 2002; Rigol-Sanchez et al., 2015):

$$\varphi_L = \frac{1}{8} \sum_{d \in D} (90 - \beta_{D,L}) \quad (3.25)$$

$$\psi_L = \frac{1}{8} \sum_{d \in D} (90 + \delta_{D,L}) \quad (3.26)$$

$$\vartheta = \arctan \left( \frac{z_{p_c} - z_{p_i}}{r_{p_c p_i}} \right) \quad (3.27)$$

where  $d \in D = (0^\circ, 45^\circ, 90^\circ, 135^\circ, 180^\circ, 225^\circ, 270^\circ, 315^\circ)$  the azimuth angle of 8 compass directions,  $\beta_{D,L}$  the maximum and  $\delta_{D,L}$  the minimum elevation angle ( $\vartheta$ ) along a direction  $D$  within a specified radial distance  $L$ . Given two grid points  $p_c$  and  $p_i$  with horizontal distance  $r_{p_c p_i}$  and elevation values  $z_{p_c}, z_{p_i}$ , respectively, the elevation angle  $\vartheta$  can be computed. The grid point  $p_c$  denotes the centre of a sampling kernel of size  $L$  and the grid point  $p_i$  denotes any point  $i$ , which lies on each direction  $D$  within the spatial limit of  $L$ .

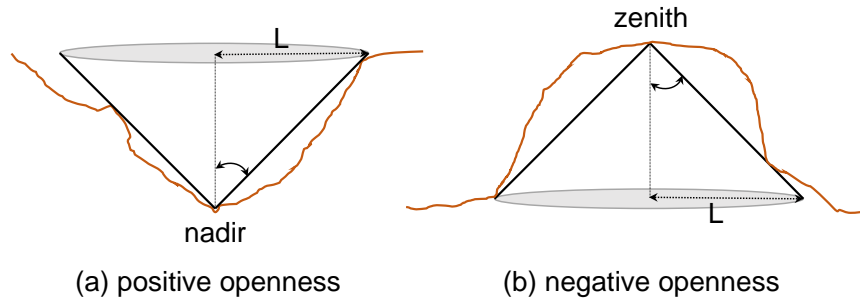


Figure 3.4: Illustration of positive (a) and negative (b) openness at a particular point of a DEM with  $L$  denoting the spatial limit. Extracted and modified from Yokoyama et al. (2002) and Chen et al. (2015).

Positive *openness* expresses the extent of depressions, whereas negative *openness* illustrates the extent of summits of a topographic surface. For a grid point on a summit, the values of positive openness are greater than 90° when looking from above the surface. Conversely the values of negative openness are lower than 90° when looking from below the surface. For a grid point on a relatively flat terrain, both values of positive and negative *openness* vary within the range of 90°-180° (Yokoyama et al., 2002).

Equations (3.25) and (3.26) calculate the mean positive and negative *openness* of the 8 directions respectively, which constitute the original mathematical expression based on (Yokoyama et al., 2002). To highlight characteristic slope breaks on a surface, Equations (3.25) and (3.26) can be transformed to compute the minimum or maximum of corresponding *openness* respectively.

### ***Eigenvalue ratio (EVR)***

An additional morphological attribute derived from *normal vectors* constitute the EVR (McKean and Roering, 2004; Glenn et al., 2006; Berti et al., 2013; Al-Rawabdeh et al., 2016b). EVR is calculated as the natural logarithmic ratio of the normalized eigenvalues (Watson, 1966; Woodcock, 1977; McKean and Roering, 2004; Baek and Kim, 2015):

$$\text{EVR} = \ln\left(\frac{S_1}{S_2}\right) \quad (3.28)$$

$$S_l = \frac{\lambda_l}{n} \text{ with } S_1 + S_2 + S_3 = 1 \quad (3.29)$$

In Equation (3.29) the eigenvalues (see Equation (3.13) for their derivation) are normalized with respect to the number of observations denoted by  $n$ .

EVR indicates the degree of data distribution with respect to the direction of their corresponding eigenvectors (Woodcock, 1977). As Baek and Kim (2015) described, after Watson (1966), when the observations are plotted as points on a unit mass over a spherical surface two basic distributions can be formed; a) a cluster distribution and b) a girdle, as shown in Figure 3.5. In a cluster distribution the data are orientated along one main direction with eigenvalues  $\lambda_1 > \lambda_2, \lambda_3$  whereas in a girdle formation the data are distributed into two directions with eigenvalues  $\lambda_1, \lambda_2 > \lambda_3$  (Figure 3.5). In other words, the dominant orientation of the distribution is based on the magnitude of the eigenvalues and the direction of the eigenvectors. In the case of a uniform distribution the eigenvalues are

equal and the data are plotted in the centre of the spherical surface (McKean and Roering, 2004; Baek and Kim, 2015).

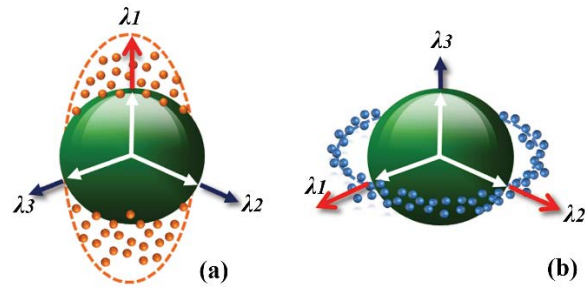


Figure 3.5: Example of two distributions of points projected on a spherical surface; a) cluster distribution where one large eigenvalue ( $\lambda_1$ ) is observed and b) girdle where two comparable eigenvalues ( $\lambda_1, \lambda_2$ ) are dominant. Modified from Baek and Kim (2015).

McKean and Roering (2004) showed that regions over landslides have less clustered surface variations than the adjacent un-failed (i.e. stable) terrain. They also illustrated that in the rough terrain the EVR values create a skewed distribution compared to the normal distribution over a smooth terrain. Baek and Kim (2015) computed the EVR to identify surface irregularities and detect potential hazardous regions. However, both studies used a 1 m spatial resolution DEM derived from ALS. In a more recent study, Al-Rawabdeh et al. (2016b) implemented the EVR and the *slope* to assess how accurate scarp features of a rocky landslide can be automatically delineated. A 0.02 m DEM, obtained with a GoPro Hero 3 camera mounted on the DJI Phantom 2 quadcopter, was used to derive these morphological attributes. They concluded that a 90% accuracy was delivered when compared with ground truth data, as derived from manual digitisation of the scarps using the quadcopter-derived orthophoto. Overall, these studies have proved that the EVR performs well for landslide identification of regions with large extent and without vegetation. No other studies have investigated the sensitivity of EVR over grassy terrain with observations of high spatial resolution, which leaves a question over EVR performance.

### 3.4 Morphology-Based co-Registration (MBR) workflow

Co-registration of 3D surfaces is a fundamental requirement in quantifying deformations in the natural environment. Co-registration refers to the alignment of multi-temporal 3D surfaces with each other. As opposed to georeferencing (Section 3.2.1), co-registration is not related to a reference coordinate system (Wujanz et al., 2016). It matches subsequent 3D surfaces to a reference surface without an input of external information (e.g. GCPs). The reference surface is usually that of the first (oldest) epoch and can be fixed to a

desirable coordinate system either with aid of GCPs (i.e DG) or camera exposure stations (i.e. IG). The proposed MBR workflow has been designed to work in both cases, highlighting the potential for eliminating the requirement for established GCPs within a SfM-MVS monitoring approach.

#### **3.4.1 Related work on co-registration**

Co-registration has been a major area of interest within the field of photogrammetry and computer vision. To handle the co-registration problem two approaches have been extensively used by both communities, namely a) least squares surface matching and b) iterative closest point (ICP) algorithm. A detailed review of these approaches can be found in Gruen and Akca (2005).

An example of a least squares surface matching approach was introduced by Mitchell (1994) and has been further developed at Newcastle University, by Buckley (2003), Mills et al. (2003a); Mills et al. (2005); Miller et al. (2008); and Kunz et al. (2012). The latest version of this approach minimises the Euclidean distance between points of a floating surface to the corresponding plane facets of a reference (fixed) surface by solving a seven-parameter 3D conformal transformation in an iterative least squares sense. This approach has been applied to coastal geohazards (Miller et al., 2008) and glacier monitoring (Kunz et al., 2012) studies. Whilst former variants of the approach (Karras and Petsa, 1993; Zhang and Cen, 2008; Ang and Mitchell, 2010) could align only grid DEMs, the current version of the algorithm can also handle irregular structures of 3D point datasets. In addition, it can cope with observations obtained with different geomatics methods; for example it was implemented with point clouds derived from ALS and airborne photogrammetry in Gneeniss et al. (2015).

Noh and Howat (2014) extended the seven-parameter least squares matching approach by integrating additional similarity constraints to quantify glacier elevation change from satellite imagery. They generated the morphological attributes of *slope*, *aspect* and *standard deviation* (Section 3.3.1) from DEMs at two epochs. They computed a correlation coefficient per attribute to identify stable terrain, based on the assumption that for high similarities the surface is expected to remain unchanged. Further, they applied a seven-parameter least squares matching approach to the detected stable terrain, which served as the control surface for DEM co-registration. However, this approach did not take into account a good distribution of control surfaces across the surveyed extent that would ensure the convergence of least squares.

An alternative co-registration approach constitutes the ICP algorithm, originally proposed by Besl and McKay (1992) and Chen and Medioni (1991). This searches for the closest point correspondences between subsets of 3D point clouds by solving a six-parameter rigid transformation. A comprehensive review of ICP evolution can be found in Pomerleau et al. (2013). Compared to least squares surface matching approaches, ICP variants are more versatile as they allow matching of any type of datasets (e.g. point-to-point technique in Besl and McKay (1992); point-to-tangent plane in Chen and Medioni (1991), etc.).

Teza et al. (2007) applied the original ICP algorithm for monitoring a landslide in the Italian Alps with TLS point clouds. Instead of a global co-registration, they performed the ICP per sub-regions expecting that in adjacent regions the transformation parameters were similar. This approach did not converge at the edges of the study site and over vegetated terrain, delivering erroneous alignments over areas with significant surface change. A recent improvement of ICP proposed by Wujanz et al. (2016) overcame misalignments experienced in the previous study by excluding regions with surface deformations from the resolution of the transformation parameters. Firstly, they applied ICP to point clouds with the aid of an octree<sup>13</sup>. Unstable regions were identified based on the different transformation parameters estimated within each octree level. Finally, they applied global ICP to the corresponding octree stable sub-regions to refine the co-registration. This approach was tested with SfM-MVS point clouds derived from two UAV image acquisitions over an active soil creep site, as described in Al-Rawabdeh et al. (2016a). They reported several centimeters accuracy for the co-registration over the automatically detected stable regions. However, further investigations of the ICP performance over grassy terrain are yet to be carried out.

All aforementioned studies reported that a major limitation of both least squares surface matching and ICP algorithms is the requirement for an adequate approximation of the transformation parameters between control and matching datasets. In the case of DG with consumer-grade UAV of m-level and degree-level precision for position and orientation of camera exposure stations respectively (Chiang et al., 2012; Carbonneau and Dietrich, 2016), an approximate alignment between surfaces may be unachievable. For instance, Miller et al. (2008) extracted GCPs from maps to establish an approximate orientation to

---

<sup>13</sup> Octree and voxel hulls are two 3D space partition structures used in software of point cloud processing. (examples of various structures can be found in Pfeifer et al. (2014)).

archival DEMs. Al-Rawabdeh et al. (2016a) refined the coarse orientation from DG with the inclusion of GCPs into the typical SfM-MVS pipeline prior to ICP application.

An alternative for a coarse alignment is extraction of a few corresponding points between two surfaces, similar to the five-point approach proposed by Nistér (2004) that was adopted in the SfM-MVS software (e.g. *VisualSfm*, Table 3.1, Section 3.2.5). Wujanz et al. (2016) incorporated a similar approach (e.g. four-points-congruent-sets by Aiger et al. (2008)) into their ICP variant to establish an initial alignment. Although this was successfully applied to TLS point clouds on a bare earth quarry face, no investigations have been conducted over terrain with homogenous texture such as grassy terrain or sand dunes (Wujanz et al., 2016). To apply this concept to SfM-MVS outputs, human intervention is required to extract corresponding features over subsequent UAV derived orthophotomosaics. This task can become cumbersome due to illumination variations across epochs, especially over grassy terrain, which constitutes a well-known error source in SfM-MVS products (Section 3.2.6).

Ferraz et al. (2016) proposed extraction of planar patches from ALS point clouds for road detection in a forest environment. This approach could offer an alternative solution for initial transformation through matching corresponding planar patches across point clouds. Liu et al. (2016) demonstrated a co-registration approach with linear features extracted from ALS point clouds, which served as additional constraints into a SfM-MVS UAV imagery processor. Both studies provided co-registration solutions only if a good distribution of planar patches or linear features across the site could be guaranteed. Moreover, it cannot be guaranteed that linear, planar or any other artificial features will be present in a landslide occurring in a natural environment.

To overcome the aforementioned issues in the absence of GCPs over a landslide area, this study formulates co-registration as a morphology-matching, rather than a DEM-matching, problem. The approach assumes that surface morphology over stable terrain remains the same across epochs. Here, the morphological attribute of mean *curvature* was adopted, as described in Section 3.3.2. To co-register multi-epoch *curvature* grids derived from SfM-MVS DEMs coarsely aligned with DG, an algorithm invariant to translations and rotations is required. For that, instead of least squares surface matching or ICP, the SIFT operator was chosen due to its proven robust performance with UAV optical images of different transformations (Fonstad et al., 2013).

The SIFT operator was originally designed for identifying homologous features on optical imagery and has been extensively implemented in SfM-MVS software (Section 3.2.4). Only a few studies have adapted the SIFT operator to images with other than visible electromagnetic wavelength for automatic co-registration purposes. These include intensity images obtained with ALS datasets (Wang et al., 2012), range images generated from TLS observations (Barnea and Filin, 2008), hyperspectral (Sima et al., 2014), and synthetic aperture radar images (Dellinger et al., 2015). In this study, the SIFT implementation identifies homologous key locations of surface structures using mean *curvature* grids of multiple epoch pairs, constituting the essential component of the proposed morphology monitoring strategy. Even though the co-registration problem is firstly treated more as a 2D alignment than 3D matching, the third dimension is later incorporated into a self-calibrating bundle adjustment included in the SfM-MVS pipeline.

### 3.4.2 Implementation and development

The MBR workflow consists of three main stages, as illustrated in Figure 3.6. Stage 1 corresponds to DEM generation of the reference and subsequent epochs, and Stage 2 refers to the creation of pseudo GCPs and co-registration of epoch pairs. Stage 3 is the final error assessment phase that defines the sensitivity level of surface change.

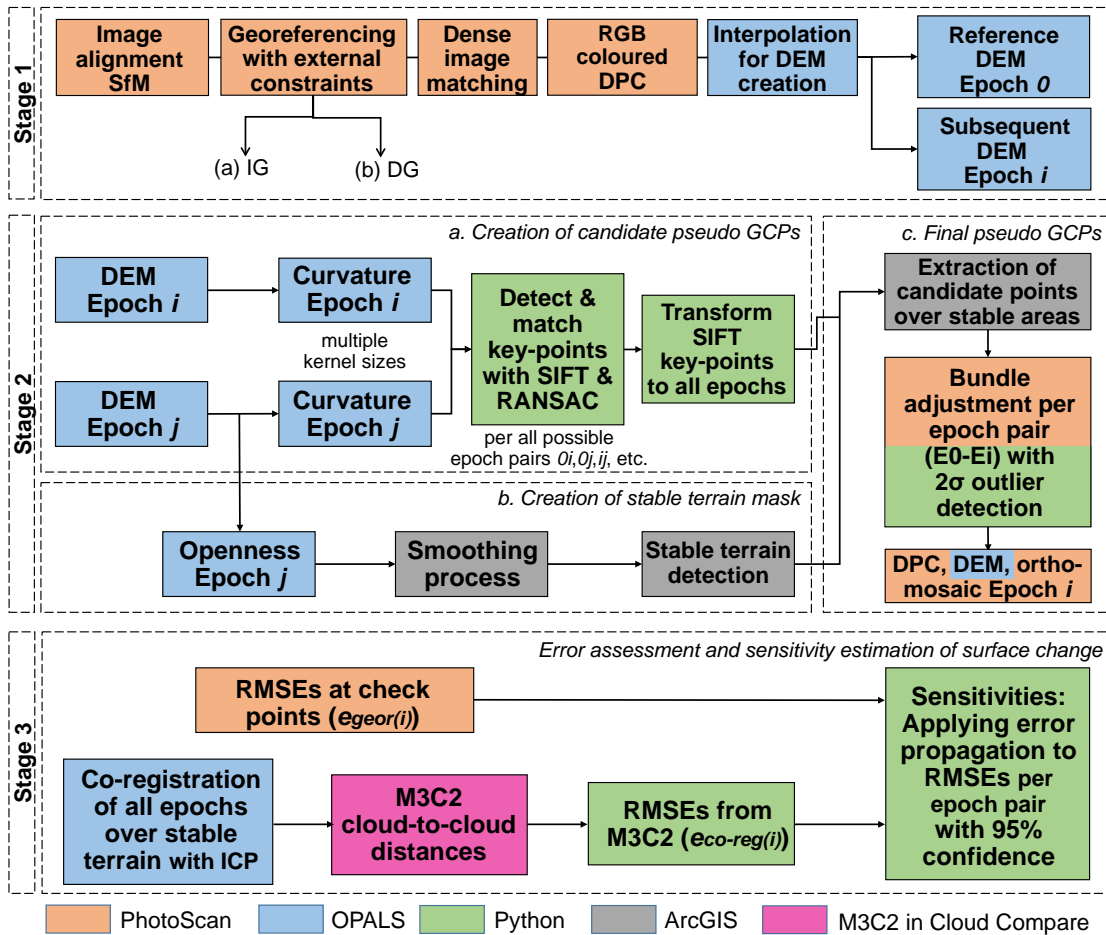


Figure 3.6: Workflow of the MBR approach to generate a UAV-derived DEM time series.

#### Stage 1: DEM generation

In Stage 1 the SfM-MVS pipeline is implemented to create the DEMs at all epochs. Stage 1 follows the typical workflow, as summarised in Section 3.2.1. Two approaches can be used to create the reference E0-DEM that corresponds to the DEM of the first epoch. The first is to use a minimum number of GCPs and the second refers to DG employing the camera exposure stations (steps (a) or (b) in Figure 3.6, respectively). To generate the subsequent DEMs, only step (b) is followed, providing approximate positions for coarse georeferencing.

A python script was developed to automatically extract the approximate 3D camera exposure positions, as this capability is not always provided in commercial UAV systems.

This script reads the EXIF information from all acquired images, calculates the time difference between two subsequent images within one flight and couples them with each image file name. A requirement is that the timestamp, the 3D position and the filename of the first image after launching, are recorded in the UAV autopilot's log file. The script reads these records from the log file and calculates the timestamps of the remaining images per flight based on the previously estimated time differences. Afterwards it searches through the log file to extract the recorded 3D positions that correspond to the calculated timestamp. These extracted camera exposure stations are approximate, as they involve positional errors associated with the consumer-grade UAV capabilities (Section 2.3.1). Nonetheless, at this initial stage of the workflow, these coarse positions are adequate to scale and orient the cloud of tie points at any epoch  $i$ , as  $E_i$  DEMs will be co-registered with respect to  $E_0$  at later stages of the MBR workflow (Figure 3.6). The python script is presented in Appendix A.

The camera exposure stations, as extracted from the aforementioned script, are incorporated into the SfM-MVS pipeline to perform the georeferencing step in *PhotoScan* (Section 3.2.5). Dense image matching, which results in the raw 3D DPCs per epoch, is performed in *PhotoScan*. Additional analysis verifies the optimal *PhotoScan* disparity settings based on the surface characteristics of each study site (see Sections 5.2.1 and 6.1.3).

All DEMs were generated using the Orientation and Processing of Airborne Laser Scanning data (*OPALS*) software (Pfeifer et al., 2014), as it outperforms other point cloud-based and GIS-based software (e.g. *TerraScan*, *ArcGIS*<sup>14</sup>) in the fast processing of millions of points. This task is extremely cumbersome when dealing with time-series of high-density point clouds. *OPALS* transforms the irregular 3D DPC into a grid form and automatically derives statistics (e.g. point density, number of total points etc.), reducing the additional time required with other software. With regard to interpolation, moving planes was adopted in this study, as it best accounts for extreme local surface variations (Section 3.2.2). To find the number of nearest neighbors required for this interpolation, the density of the resultant DPC is taken into consideration in fashion similar to that described by Barbarella et al. (2017). They calculated the number of points that occurred within a desired DEM pixel size via the density tool in *ArcGIS*. More than three neighboring points are required to provide redundancy in the least squares solution

---

<sup>14</sup> GIS software package ([www.arcgis.com/features/index.html](http://www.arcgis.com/features/index.html))

(Milenkovic et al., 2015). Another parameter required for this interpolation is the search radius, which regulates the spatial extent of the interpolation. This parameter should be chosen with care as, for example, a large radius can degrade significant surface variations (Milenkovic et al., 2015).

### ***Stage 2a: Creation of candidate pseudo GCPs***

Stage 2 is divided into three steps (Figure 3.6). In step 1, candidate pseudo GCPs are created by implementing the SIFT operator with multiple pairs of mean *curvature* grids. Mean *curvature* grids were computed in *OPALS*, as the average of principle *curvatures* (Equations (3.22) and (3.23)) after applying partial derivation to a quadratic functional model (Equation (3.3)). SIFT is implemented following a similar process chain to that described in Snavely et al. (2008) and Barazzetti et al. (2014).

A python script was developed to generate the candidate pseudo GCPs and is presented in Appendix A. This script adapts the SIFT operator in the open-source OpenCV python library<sup>15</sup>. The SIFT operator generally consists of two components such as the detector and the descriptor. The former identifies potential key-points on an image by applying the difference-of-Gaussian functions. The latter associates each detected key-point to multiple descriptors, which are invariant to image translation, rotation and scaling (Ives and Delbracio, 2014). The OpenCV library has kept the default values of SIFT parameters, based on its initial implementation, as presented in Lowe (2004) and Ives and Delbracio (2014). Many authors have adopted the same default values for image processing due to the proven robustness of SIFT to image geometrical transformations (Mikolajczyk and Schmid, 2005; Sima et al., 2014). However, Sima and Buckley (2013) and Kehl et al. (2017) have demonstrated the significant improvement of SIFT performance after optimizing its default settings accounting for geometric and radiometric variations.

In the same script, erroneous correspondences are filtered by applying the RANSAC algorithm incorporated into a 2D similarity transformation that comprised two translations, a rotation about Easting and a scale factor (Hartley and Zisserman, 2004). The mathematical expressions are described in Appendix A. RANSAC was chosen as an outlier estimator of the first approximation of candidate key-points due to its simplicity

---

<sup>15</sup> [http://docs.opencv.org/3.1.0/da/df5/tutorial\\_py\\_sift\\_intro.html](http://docs.opencv.org/3.1.0/da/df5/tutorial_py_sift_intro.html)

and high number of breakdown points (Barazzetti et al., 2010). The processing chain of Stage 2, developed in the python script is as follows:

1. Read the input *curvature* grids (geotiff) of a specified kernel size for epoch pair  $ij$ ;
2. Detect key-points for both grids;
3. Compute their descriptors  $D_i$  and  $D_j$  for grid of epoch  $i$  and  $j$  respectively;
4. Match the  $D_i$  and  $D_j$  descriptors between potential key-point pairs and compute the Euclidean distances  $d_{ij}$  per pair;
5. Sort the distances from shortest to longest;
6. Accept detected matches if  $d_{ij}^1/d_{ij}^2 < 0.8$ , where  $d_{ij}^1, d_{ij}^2$  are the first and second-best distance candidates respectively;
7. Store the image coordinates of the matched key-points in pixels;
8. Apply a 2D similarity transformation with RANSAC to the stored key-points for any  $ij$  epoch pair;
9. Accept key-points that provide an average standard error (SE), post transformation  $< 0.9$  pixels;
10. Store the estimated transformation parameters;
11. Store the coordinates in pixel and meters of the final accepted homologous key-points;
12. Store the residuals of each key-point as a quality indicator of the 2D similarity transformation.

In steps 1 to 3, SIFT with *curvature* grids is performed. In steps 4 to 6 a distance ratio test is applied to remove spurious matches, because in most cases a descriptor of image  $i$  can match with more than two descriptors of image  $j$  (Snavely et al., 2008; Barazzetti et al., 2014). Typical ratio values within the range of 0.5 to 0.8 have been adopted from other studies (Snavely et al., 2008; Barazzetti et al., 2010; Barazzetti et al., 2014), allowing a sufficient number of erroneous candidate homologous points to be removed. In steps 7 to 12, RANSAC is recursively performed within a 2D similarity transformation. Step 9 assigns a threshold to support the RANSAC outlier filtering process with sub-pixel accuracy. The average SE (Equation (3.32)) is based on the residuals computed for each set of homologous points after each RANSAC iteration by back-projecting the points of *curvature*  $j$  into *curvature*  $i$ . In step 11, the coordinates of the candidate homologous points (pseudo GCPs) are firstly stored in pixels and afterwards transformed into Easting and Northing based on the spatial reference information embedded into the *curvature* grids (of geotiff format). This information is provided from the coarse alignment in Stage 1 of the MBR workflow. The standard errors for each pseudo GCPs computed after the

final iteration are used as markers' accuracy (Section 3.2.5).and inserted in *PhotoScan* during Stage 2c of the MBR workflow (Figure 3.6).

The described process is repeated for epoch pairs of multiple *curvature* kernel sizes (5x5 to 33x33). For instance, epoch i and j, as shown in Figure 3.6, represent one epoch pair. In the case of n epochs there are  $n(n-1)/2$  epoch pairs. For each epoch pair, SIFT detects numerous different key-points from *curvature* grids of various kernel sizes and this adds redundancy into the process. Identical points are automatically erased in *ArcGIS* when all candidates from all epochs are combined together into one vector file, including their corresponding per epoch 2D coordinates (Easting, Northing). Corresponding elevation values are then interpolated from the points' coordinates on the equivalent DEMs derived in Stage 1.

### ***Stage 2b: Creation of stable/unstable terrain mask***

In step 2, a stable/unstable terrain mask is created based on classification of the area into regions with smooth/rough surface texture using the morphological attribute of *openness*. The computation of an *openness* grid using a DEM is described in Section 3.3.2 and is implemented in *OPALS*. A spatial length is required, which is empirically defined based on a priori knowledge of the extent of surface failures in each study area. Both positive and negative *openness* are computed (Equations (3.25), (3.26) and (3.27)), combined with map-algebra and focal statistics smoothing algorithms in *ArcGIS* to generate the final stable terrain masks for each epoch j. Map-algebra algorithms contain mathematical and logical operators that are applied to raster grids on a cell-by-cell basis. Focal statistics calculate statistics for a grid point based on the neighbouring grid values within a specified kernel size. These algorithms are applied to *openness* raster grids, which are then converted into polygons with vectorisation tools in *ArcGIS*. To remove speckle noise from the stable terrain masks, usually generated from extremely small polygons, additional smoothing is applied by eliminating those with area lower than 10 m<sup>2</sup>. The points that fall outside the stable masks are eliminated from the process.

To verify the stable and unstable detected regions, the EVR grid is computed based on Equations (3.28) and (3.29), implemented in *OPALS*. Histograms of EVR values are generated for sample sub-regions over stable (smooth) and unstable (rough) terrain. According to investigations in McKean and Roering (2004), it is expected that EVR values over smooth terrain follow a normal distribution, as opposed to a skewed distribution over rough terrain. This test constitutes an intermediate independent verification of the stable/unstable mask creation step.

### ***Stage 2c: Final pseudo GCPs***

Up to this point, 3D coordinates of the extracted pseudo GCPs over stable terrain for all epochs (plus the associated standard errors) are included in a single file. This file can be incorporated into the epoch pairwise self-calibrating bundle adjustment, implemented in *PhotoScan*. In particular, given the established coarse alignment from Stage 1 of the workflow (Figure 3.6), the coordinates of pseudo GCPs at epoch  $i$  ( $E_i$ ) can be automatically located on each image of the UAV photogrammetric block. After assigning these as control markers with the aid of the integrated *PhotoScan* python script<sup>16</sup>, the 3D coordinates are then reimported with their values from reference epoch 0 ( $E_0$ ). It is expected that the coordinates at  $E_i$  and  $E_0$  correspond to the same locations. This is checked at step 9 of Stage 2a. The least squares bundle adjustment is expected to re-optimize the solution and co-register the two epochs.

In this study, the bundle adjustment refines, amongst others, the camera's IOPs including focal length, principal point, three radial ( $K_1, K_2, K_3$ ) and two tangential ( $P_1, P_2$ ) distortion parameters. Hence, from Equation (3.1)  $K_4, P_3$  and  $P_4$  are not used in the process. This combination of parameters was chosen as it has been shown to reduce DEM deformations (James et al., 2017a), when tested with a similar compact camera (Section 3.2.6).

After the bundle adjustment in *PhotoScan* statistical measures for each component (Easting, Northing and Elevation) of the pseudo GCPs are computed. The selection of the final pseudo GCPs is performed through an iterative statistical outlier detection test, using the normal distribution with 95% confidence level and 1.96 percentile (Wolf and Ghilani, 2010). A python script was developed for the outlier detection test using input data the statistical measures computed by *PhotoScan*, as presented in Appendix A. Outliers are expected to have Easting, Northing and Elevation outside the range  $\pm 2\sigma$  with  $\sigma$  denoting the standard deviation (Equation (3.33)). The  $\pm 2\sigma$  range is chosen as it is a typical level in error assessment of photogrammetric products (Whitehead and Hugenholtz, 2015). The number of iterations of the statistical test depends on two stopping criteria:

1. The SEs (Equation (3.32)) computed from all inliers in each coordinate component should be lower or equal to the DEM spatial resolution;
2. At least one pseudo GCP should be completely inside each of the five Thiessen polygons the area is divided into.

---

<sup>16</sup> The script can be found in [www.agisoft.com/forum/index.php?topic=4665.0](http://www.agisoft.com/forum/index.php?topic=4665.0)

The first criterion relates the methodology with the achievable spatial resolution of the UAV-derived products. The second criterion ensures that automatically generated pseudo GCPs are well distributed across the study area, as five corresponding Thiessen polygons can define the region of influence around each theoretical GCP. Five theoretical GCPs would provide a convenient establishment of control targets with accuracy level of 1 x GSD as described in Section 5.1. Based on this, five Thiessen polygons can be used to verify a reliable pseudo GCP distribution. Any remaining systematic directional errors are manually checked and removed based on the calculation of their azimuth and creation of polar plots, which support inspection of the dominant direction. The final step of the MBR workflow is to reconstruct the DPC, DEM and orthophoto for each epoch with the exception of E0, through processing performed in *PhotoScan* and *OPALS* (Figure 3.6).

### 3.4.3 Statistical measures

Throughout the process, different outlier tests are performed and a number of statistical measures (Wolf and Ghilani, 2010) are computed to support the analysis of pseudo GCP generation.

A residual is the difference between a single observation and its true, or most probable, value as expressed by:

$$\varepsilon_i = y_i - \mu, u_i = \bar{X} - X_i \quad (3.30)$$

For true known values,  $\varepsilon$  refers to error instead of residual. When the true value is unknown, it is substituted from the value with the highest probability of occurrence. This can be the mean of the observations when many observations are present, given by:

$$\mu = \bar{X} = \frac{1}{n} \sum_{i=1}^n X_i \quad (3.31)$$

where  $n$  is the number of observations. The mean values in Easting, Northing and Elevation of the generated pseudo GCPs are expected to be close to zero. Deviations from zero imply the presence of systematic bias. The standard error expressing the square root of population variance is denoted by:

$$SE = \sqrt{\frac{1}{n} \sum_{i=1}^n u_i^2} \quad (3.32)$$

A unique value of SE is calculated for Easting, Northing and Elevation separately. The standard deviation is an unbiased estimator of the sample variance,  $\sigma^2$ , expressing the precision of the automatically generated pseudo GCPs:

$$\sigma = \sqrt{\frac{1}{n-1} \sum_{i=1}^n u_i^2} \quad (3.33)$$

Compared to the conventional IG with surveyed GCPs, in the MBR workflow the true values of pseudo GCPs are unknown. Hence, the aforementioned statistical measures refer to the mean rather than the true values. It is assumed that after outlier detection tests a relatively high number of pseudo GCPs remain, forming a homogenous distribution with systematic biases removed. These statistical measures are used as indicators of the internal accuracy of the MBR workflow, while the external accuracy is estimated through cross-validation against benchmark observations such as surveyed independent CPs and TLS.

### **3.5 3D sensitivity and estimation of surface change**

#### ***3.5.1 Related work on error assessment***

The primary step of the proposed monitoring strategy, namely the co-registration (Figure 3.1), is completed through the previously described two Stages of the MBR workflow (Figure 3.6). Before quantifying elevation and planimetric surface changes from the co-registered time series, it is important to determine the level of detail that can be achieved with the adopted methodology (Brasington et al., 2003; Lane et al., 2003; Wheaton et al., 2010; Brasington et al., 2012; Smith and Vericat, 2015; Cook, 2017; James et al., 2017b). This process is included into Stage 3 as seen in Figure 3.6.

Whilst many studies (Wheaton et al., 2010; Milan et al., 2011; Brasington et al., 2012; Smith and Vericat, 2015) have compared DEMs, others have compared point clouds (Lague et al., 2013; Cook, 2017; James et al., 2017b) to determine the lowest detectable surface change. The first category proposed the DEM standard deviation (see Equation (3.6)) as a quality indicator to express the spatial distribution of errors. These errors are associated with geomatics and interpolation techniques adopted for DEM generation. The second category proposed statistical measures extracted from point-to-point distance differences. To derive the significant statistical level of change detection (i.e sensitivity), all aforementioned studies have adopted the typical error propagation approach (Wolf and Ghilani, 2010) applied to either point-to-point distances or DEM differences.

Regardless of the approach taken for sensitivity quantification, the most widely established statistical measure for error assessment of 3D point clouds or DEMs is the root mean square error (RMSE). RMSE is usually computed at independent CPs, as suggested by ASPRS guidelines (Abdullah et al., 2015; Whitehead and Hugenholtz, 2015). RMSEs taken at GCPs cannot provide a reliable quality indicator of the final SfM-MVS products as GCPs play a significant role in shaping the resultant 3D surface (James and Robson, 2014; Eltner et al., 2016). Nonetheless, in the absence of ground truth, RMSEs together with mean values reported at GCPs can still quantify unresolved biases after SfM self-calibrating bundle adjustment.

Recent studies (Carbonneau and Dietrich, 2016; James et al., 2017b) showed that the RMSE at CPs provides an overall georeferencing error (related to the defined datum), but fails to identify the spatial distribution of systematic errors, especially for a low number of poorly distributed CPs. Further, when ground truth observations are available (e.g. TLS-based, GNSS/Total station observations), a quality indicator can be retrieved by direct comparison between the SfM-MVS-derived DPC and ground-truth points via point to point or point-to-mesh comparison for flat terrain, or via the multiscale model to model cloud comparison (M3C2) for more complex terrain (Carbonneau and Dietrich, 2016). Mesh-to-mesh comparison is also an alternative but it requires the intermediate step of converting a point cloud to mesh. All algorithms are implemented in *CloudCompare* and described in Lague et al. (2013); the main difference being that M3C2 takes into consideration local surface roughness (Stumpf et al., 2015; Cook, 2017; James et al., 2017b). This makes it superior to all other approaches especially for complex terrain. The point-to-point comparison is more sensitive to different point densities (Eltner et al., 2016). After investigating the performance of point-to-mesh against the M3C2 algorithm with TLS point clouds, Stumpf et al. (2015) concluded that M3C2 provides estimations that are more reliable.

In particular, M3C2 derives distances between two point clouds in two steps: a) firstly it calculates a normal vector at any point of the first cloud and b) projects the calculated normal vector into both clouds. The average position of the two projections along the normal vector constitutes the estimated distance between the two clouds. The M3C2 distance is calculated, either to each point of the first point cloud, or to core points after sub-sampling for faster performance. The normal vector is estimated by fitting a plane to neighbouring points within a radius ( $D/2$ ). The projection is performed at another radius ( $d/2$ ) which defines the size of a cylinder containing subsets of both point clouds. Both

parameters  $D$  and  $d$  define the spatial extent whereby surface variations are considered. For small values of  $D$ , the estimated normal vectors of the first cloud have various orientations which can result in distance overestimation when projected onto the second cloud. A detailed explanation of the M3C2 algorithm can be found in Lague et al. (2013).

Overall, direct comparison of point clouds mitigates against interpolating errors in derivation of the DEMs (Stumpf et al., 2015; Eltner et al., 2016; Cook, 2017). However, it is not always feasible to obtain benchmark point clouds of higher precision than SfM-MVS outputs over large extents. Moreover, M3C2 distances are affected by surface roughness (Lague et al., 2013). For instance, TLS and SfM-MVS point clouds obtained over the same surface at the same epoch represent surface roughness in different levels of detail. TLS allows for a fine representation of surface characteristics as opposed to the smoother result of the SfM-MVS point cloud derived from UAV imagery (also illustrated in Cook (2017)). Hence, when these are compared through the M3C2 algorithm, appropriate selection of parameters (i.e. sub-sampling distance,  $D$  and  $d$  distances) is essential to reduce the effect caused by roughness variations between the clouds (Stumpf et al., 2015). Values lying within the range of 0.3-2.0 m for the  $d$  parameter have been recommended by Barnhart and Crosby (2013) and Lague et al. (2013) when the M3C2 algorithm was tested with TLS point clouds.

James and Robson (2012) and Micheletti et al. (2015) demonstrated that error assessment should be performed after applying a global co-registration to SfM-MVS outputs, even if the inclusion of GCPs was considered. That way the derived quality indicator can also reflect misalignment errors usually present in time-series SfM-MVS outputs. They adapted a six-parameter rigid transformation ICP algorithm (neglecting the scale) when a SfM-MVS point cloud was assessed against a TLS point cloud. The authors confirmed that distance discrepancies were caused by the different technique applied and not attributed to co-registration errors.

Overall, error assessment in photogrammetry involves the quantification of precision and accuracy (Wolf et al., 2014). Precision is related to the repeatability of an output whereas accuracy refers to the closeness to a ground-truth (Wolf et al., 2014; Eltner et al., 2016; Granshaw, 2016a). In the present study, statistical measures, described in Section 3.4.3, deal with precision throughout the monitoring strategy. The sensitivity level described in Section 3.5.3 is indicative of accuracy but also expresses a level of precision, as it includes

errors produced over stable regions from repeated UAV surveys. This step constitutes the final Stage 3 of the MBR workflow, as shown in Figure 3.6.

### ***3.5.2 Related work on surface change estimation***

The last part of the morphology-based monitoring strategy is quantification of elevation change and planimetric surface movement. This is conducted with the aid of DEM differencing and image cross correlation functions combined with surface morphological attributes.

Differencing of successive co-registered DEMs constitutes a standard approach to estimate ground accumulation and depletion in monitoring applications (Daehne and Corsini, 2013; Travelletti et al., 2014). DEM subtraction on a pixel-by pixel basis results in estimation of elevation changes, which in turn leads to volumetric changes. However, the estimated changes can be mixed with unresolved misalignment errors, other systematic errors mostly propagated through the SfM-MVS pipeline, and random noise caused by vegetation. The first two biases have been discussed in Section 3.2.6.

In an attempt to assess the first two biases, Turner et al. (2015) computed the RMSEs of subsequent elevation differences over stable terrain. After a trial and error procedure, a constant shift was applied to DEMs of particular epoch pairs until the RMSEs were minimised. This process generally disregards rotational errors and should be treated with care (Turner et al., 2015). The M3C2 and ICP algorithms, as discussed in Section 3.4.1, account for both planimetric and rotational errors.

It is well-known that vegetation creates high surface roughness, affecting the photogrammetric outcome (Lane et al., 2000). Vegetation is strongly related to surface texture (Section 3.2.6) as it creates surface variations when captured from different angles, hampering tie point matching in the SfM-MVS pipeline (Eltner and Schneider, 2015). Tonkin et al. (2014) reported that the elevation differences between observations obtained with UAV and a total station were higher in areas vegetated with heather than in short grassland. Javernick et al. (2014) identified regions with vegetation height higher than 0.40 m in a SfM-MVS derived DEM. They firstly generated a 0.50 m DEM resolution by calculating the minimum elevation of each pixel. Then, the original spatial resolution of the DPC was degraded to create different DEMs of coarser resolution which were subtracted from the initial DEM. In this way, they mapped the regions of vegetation noise. However, this approach is likely to also smooth regions of local surface variations, and therefore is not suitable for landslide monitoring. Cook (2017) compared ALS with

SfM-MVS point clouds and concluded that the latter does not represent vegetation in a consistent manner since it is influenced by vegetation density. Dense bushes and grass cause surface variability in SfM-MVS point clouds, resulting in a unfavourable bare ground representation which can affect change detection estimation (Cook, 2017). Here, vegetation is initially filtered with *PhotoScan's* ground classification routine (Section 3.2.5) and the DEM standard deviation (Equation (3.6)) is then considered for removing any unfiltered noise prior to pairwise DEM subtraction. Further, to extract real elevation change, deformations within the estimated sensitivity level are excluded from the DEM differences.

With respect to surface planimetric movement estimation, image cross-correlation functions have been implemented in the context of earthquakes (Dominguez et al., 2003; Leprince et al., 2007a; Leprince et al., 2007b; Ayoub et al., 2009a), landslides (Travelletti et al., 2012; Daehne and Corsini, 2013; Lucieer et al., 2014; Fey et al., 2015; Turner et al., 2015; Stumpf et al., 2017) and glaciers (Kääb and Vollmer, 2000; Debella-Gilo and Kääb, 2011; Heid and Kääb, 2012; Messerli and Grinsted, 2015). Compared to the intensive task of manual feature tracking, image cross-correlation functions provide a continuous grid of surface displacements in an automatic fashion. Numerous studies have applied image cross-correlation functions to optical imagery (Kääb and Vollmer, 2000; Dominguez et al., 2003; Leprince et al., 2007a; Leprince et al., 2007b; Ayoub et al., 2009a; Heid and Kääb, 2012; Messerli and Grinsted, 2015; Rosu et al., 2015; Stumpf et al., 2017). Nevertheless, the application of image cross-correlation functions to UAV-derived orthophotomosaics can increase noise due to variations in illumination conditions (Lucieer et al., 2014). Recent studies have demonstrated that the implementation of image cross-correlation functions with DEM morphological derivatives can automatically determine the movement of surface features that preserve their structural patterns over time (Daehne and Corsini, 2013; Lucieer et al., 2014; Travelletti et al., 2014; Fey et al., 2015). Among these, Lucieer et al. (2014) and Turner et al. (2015) found that the UAV-derived morphological attribute of *shaded relief*, implemented with image cross-correlation functions, provided better surface displacement estimation of a landslide than single bands from the corresponding orthophoto. This study evaluates image cross-correlation functions with various UAV-derived morphological attributes (Section 3.3) for 3D landslide deformation monitoring. According to Hiller and Smith (2008), and also highlighted by Favalli and Fornaciai (2017), each morphological attribute can offer a unique representation of geomorphological features. Hence, a comprehensive

investigation of the image cross correlation functions' performance related to various morphological attributes becomes a necessity.

Numerous image cross correlation functions have been proposed, such as those performed in the spatial domain (Lewis, 1995; Käab and Vollmer, 2000; Debella-Gilo and Käab, 2011; Messerli and Grinsted, 2015) and those performed in the frequency domain (Scambos et al., 1992; Leprince et al., 2007b; Rosu et al., 2015; Stumpf et al., 2017). A description of various functions can be found in Heid and Käab (2012). Here, the normalised cross correlation (NCC) function performed in the spatial domain was utilised. This is one of the most popular and mathematically simple functions for Earth mass movement (Debella-Gilo and Käab, 2011; Heid and Käab, 2012).

In a broader context, the NCC function is an area-based matching algorithm (Section 2.3.2), which compares the similarity between intensity values of two grids, corresponding to the covariance between them (Favalli and Fornaciai, 2017). The normalisation refers to the division of the covariance by the standard deviation of a grid (Equation (3.6)), resulting in the correlation coefficient. To derive surface movements between two grids, the NCC function searches for the maximum absolute value of the correlation coefficient by sliding a rectangular patch systematically from a pre-event image (first grid) within a search window in a post-event image (second grid), as expressed by Equation (3.39).

A major limitation of the NCC function is its sensitivity to the large variations of intensity values (Debella-Gilo and Käab, 2011; Heid and Käab, 2012; Travelletti et al., 2014). Such variations are usually caused by different illumination conditions, shadows, dense vegetation, mixed terrain texture (e.g white snow with black rocks as noted in Heid and Käab (2012)) and surface features with various specular reflectance, aspect variability and rotational failures (Debella-Gilo and Käab, 2011; Heid and Käab, 2012; Stumpf et al., 2017). These changes in intensity can result in decorrelation, producing noise within the surface movement estimations. In addition, erroneous estimations can be generated by the presence of co-registration errors in an image pair (Debella-Gilo and Käab, 2011; Stumpf et al., 2017). In particular, the rotational misalignments between two images can strongly affect the computed correlation, as noted by Debella-Gilo and Käab (2011) and Travelletti et al. (2014). Debella-Gilo and Käab (2011) also highlighted that the NCC function does not allow for movement detection magnitude lower than the co-registration

error, implying the necessity of a sensitivity level determination prior to NCC implementation.

To overcome the aforementioned errors, many studies (Kääb and Vollmer, 2000; Milledge et al., 2009; Debella-Gilo and Kääb, 2011; Travelletti et al., 2014) applied filter methods to the estimations. Filters included averaging within a specified window and eliminating movements over regions with correlation lower than a specified threshold and upslope direction. Stumpf et al. (2017) recently proposed a multiple pairwise image correlation algorithm which takes into account the coherence of surface movement over time. For instance, they reduced noise by averaging the magnitude and direction of movement among all epoch pair combinations. The authors also investigated the variations of movement from the theoretical zero over stable terrain and accommodated relevant thresholds into their algorithm to optimise the estimations over unstable terrain. However, regardless of the filtering method adopted, a priori knowledge of the surface kinematics is required. Here, such knowledge is extracted from visual inspection of the co-registered UAV-derived orthophotomosaics, as also recommended by Lucieer et al. (2014).

### 3.5.3 Computational aspects

#### *Error assessment*

The error assessment step is part of Stage 3 of the MBR workflow (Figure 3.6). RMSE at GCPs or CPs in the x-direction are calculated as described in Equation (3.34). The same equation is applied for y and z directions.

$$RMSE_x = \sqrt{\frac{1}{n} \sum_{i=1}^n (x_{obs} - x_{ref})^2} \quad (3.34)$$

$$RMSE_{plan} = \sqrt{RMSE_x^2 + RMSE_y^2} \quad (3.35)$$

$$RMSE_{3D} = \sqrt{RMSE_x^2 + RMSE_y^2 + RMSE_z^2} \quad (3.36)$$

In Equation (3.34)  $(x_{obs} - x_{ref})$  refers to the differences between the SfM-MVS estimated and surveyed point positions. Equations (3.35) and (3.36) are applied to derive planimetric and 3D errors respectively. In the case of pseudo GCPs, Equation (3.32) is used instead of Equation (3.34) for each component, which corresponds to SEs, as

ground-truth of pseudo GCPs is unknown. Hence, reference positions are extracted from the reference epoch. The 3D sensitivity level is derived by applying a classical error propagation approach to the estimated quality indicators of the MBR-based DEMs/point clouds between reference E0 and any other epoch  $i$ , for a 95% confidence level, using:

$$s_1 = t \sqrt{e_{geor(0)}^2 + e_{geor(i)}^2} \quad (3.37)$$

$$s_2 = t \sqrt{e_{geor(0)}^2 + e_{co-reg(i)}^2} \quad (3.38)$$

In Equations (3.37) and (3.38)  $t = 1.96$  is the critical value for 95% confidence,  $e_{geor}$  indicates the RMSE at CPs, with  $e_{co-geor}$  denoting the RMSE calculated from the cloud to cloud M3C2 distances. Together with the mean, standard deviation and RMSE values (Equations (3.31), (3.33) and (3.36) respectively) are also calculated from the M3C2 distances. All statistical measures are computed after applying co-registration of all epochs over stable terrain.

The co-registration algorithm adopted here is the six-parameter rigid transformation (3 translations and 3 rotations)<sup>17</sup>, as implemented in the ICP variant in *OPALS* (Glira et al., 2015). Amongst others, this ICP variant can handle multiple point clouds of subsequent epochs simultaneously without the necessity of a complete overlap, as it uses voxel hulls<sup>13</sup> partitioning. The ICP minimises the sum of squared point-to-plane distances in an iterative least squares adjustment (Milenković et al., 2016). Unlike pairwise ICP variants, this globally optimizes the transformations from all epoch combinations of point clouds with respect to a reference epoch.

Equation (3.37) follows the standard definition of the lowest threshold of change detection between DEM differences of consecutive epochs, while Equation (3.38) uses the co-registration error. The maximum value of  $s_1$  and  $s_2$  characterise the lowest detectable surface change. The spatial distribution of the co-registration error is analysed from the precision map provided in the M3C2 comparison result (Lague et al., 2013). DEM subtraction and volume differences are performed with the aid of the Geomorphic Change Detection toolbox (Wheaton et al., 2010) operated in *ArcGIS*<sup>18</sup>.

<sup>17</sup> [www.geo.tuwien.ac.at/opals/html/ModuleICP.html](http://www.geo.tuwien.ac.at/opals/html/ModuleICP.html)

<sup>18</sup> [www.gcd.joewheaton.org/](http://www.gcd.joewheaton.org/)

### ***The Normalised Cross Correlation (NCC) function***

In this study, the statistical NCC function was firstly implemented in the Co-registration of Optically Sensed Images and Correlation (COSI-Corr) software (Leprince et al., 2007b; Ayoub et al., 2009b) and afterwards in the Correlation Image Analysis (CIAS) package (CIAS, 2012; Heid and Käab, 2012). Unlike COSI-Corr, which generates a continuous grid of surface movement estimations, CIAS allows for individual feature tracking. COSI-Corr requires the input of three rectangular window sizes, namely a) a correlation window whereby the correlation is performed; b) a search patch in which the displacements are estimated and c) a step size used for sliding the patch within the correlation window defining the spatial resolution of the resultant displacement grid. The first two parameters are only necessary for the CIAS package.

Let  $I_1(i, j)$  be the grid value at the  $i^{\text{th}}$  and  $j^{\text{th}}$  grid cell within a correlation window  $W_c$  of a pre-event image  $I_1$ . For a specified step size ( $s$ ) and a post-event image  $I_2$ , the NCC function is expressed as (Käab and Vollmer, 2000; Debella-Gilo and Käab, 2011; Aryal et al., 2012; Heid and Käab, 2012; Travelletti et al., 2014):

$$NCC(i_s, j_s) = \frac{\sum_{i=0}^{W_c} \sum_{j=0}^{W_c} (I_1(i, j) - \mu_{I_1}) \cdot (I_2(i+i_s, j+j_s) - \mu_{I_2})}{\sqrt{\sigma_{I_1}} \cdot \sqrt{\sigma_{I_2}}} \quad (3.39)$$

where  $(i_s, j_s)$  are the grid cell coordinates shifted by ( $s$ ) in both directions,  $\mu$  and  $\sigma$  are the mean and standard deviation of the grid values within the correlation window in the two images denoted with the corresponding subscripts  $I_1$  and  $I_2$ . The computed displacements in Easting and Northing are determined by the matched correlation peak between the two grids (Debella-Gilo and Käab, 2011; Heid and Käab, 2012; Messerli and Grinsted, 2015).

To tune the settings and evaluate the performance of the NCC function shown in Equation (3.39), as applied to various morphological attributes, experiments in this study were conducted with synthetic epoch pairs (Section 6.4.1). Apart from the displacements in Easting and Northing, the COSI-Corr function also calculates a signal-to-noise ratio (SNR), indicative of the correlation quality. SNR values closer to unity are indicative of more reliable results, as high correlation is established.

Favalli and Fornaciai (2017) investigated the level of correlation between many morphological attributes and concluded that some are strongly correlated with each other (e.g. *slope* with *shaded relief* of 90° elevation angle). Here, to assess possible correlations, a comparative analysis of the estimated displacements and derived SNRs, obtained with the synthetic datasets is conducted. This comparison also examines uncertainty in noise and displacements provided from different morphological attributes. These attributes are generally scale variant as they provide different surface representations when DEM spatial resolution and moving kernel size vary (Grohmann et al., 2011). To account for this, the comparative analysis investigates the different estimations and noise levels with the change of spatial extent.

The morphological attributes with the lowest noise levels and more precise displacement estimations are chosen for the NCC implementation within COSI-Corr for an active landslide. Having generated a time-series of 3D surface deformation across the site, an additional investigation over sub-regions with the largest deformations is then performed with the aid of CIAS package. The outcomes are cross-validated with the surface displacements calculated from sample points, manually measured across the SfM-MVS derived orthophotomosaics and independently surveyed with GNSS.

### **3.6 Summary**

Chapter 3 has established the workflow of the morphology-based monitoring strategy that will be applied to the study sites in Chapters 5 and 6. The relative theoretical and computational aspects required for the development and implementation of the proposed monitoring strategy are explained in this Chapter. The monitoring strategy combines the SfM-MVS pipeline to post-process multi-temporal UAV imagery with surface morphology and image-cross correlation functions. The main feature of the monitoring strategy is the co-registration of subsequent SfM-MVS products without the requirement to physically establish GCPs, rendering the approach suitable for inaccessible landslide areas.

## Chapter 4.

# Study sites, ground-based data acquisition and equipment

---

Chapter 3 established the monitoring strategy that is tested and implemented in Chapters 5 and 6. This chapter describes three different sites whereby UAV imagery was collected to support development of the strategy. A farm close to Newcastle University, an experimental site with artificial surface change, and an active landslide constitute the three sites. These sites aided familiarisation with the SfM-MVS pipeline and software described in the previous chapter. This chapter thus introduces the study sites, presenting relevant information such as location, geomorphology, geology, landslide kinematics etc. and describes the ground-based control observations acquired at each site. These observations serve as benchmark datasets for cross-validation at different stages of the monitoring strategy. Finally, this chapter describes the UAV platform with the on-board sensors used for image acquisition.

### 4.1 Cockle Park test site

#### *4.1.1 Site overview and ground-based control data*

Cockle Park farm is located near the town of Morpeth ( $55^{\circ}13'07.44''\text{N}$ ,  $1^{\circ}41'34.07''\text{W}$ ), 27 km north of Newcastle upon Tyne, UK (Figure 4.1). The farm, owned by Newcastle University, provided an opportunity for UAV flight training and collection of experimental datasets to investigate the on-board sensor performance. Cockle Park farm mainly consists of pastureland used for grazing. The ground is relatively flat with short grass suitable for fast post processing of SfM-MVS point clouds without the requirement for additional cleaning.

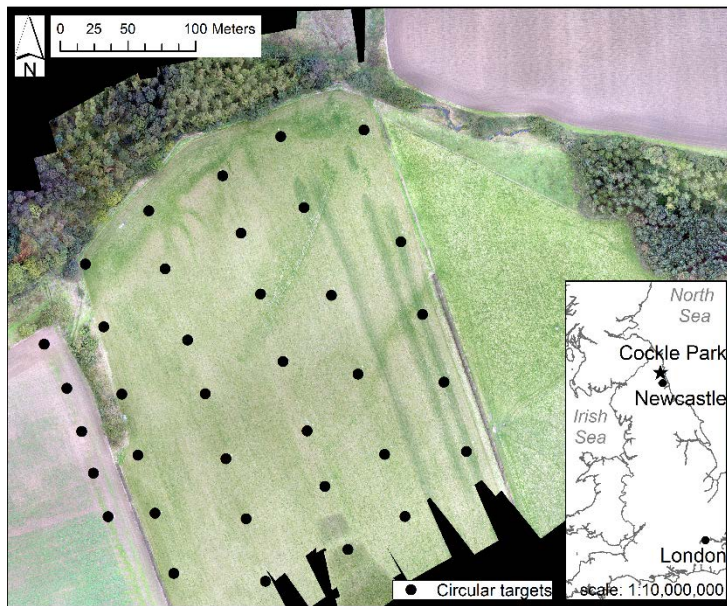


Figure 4.1: Overview of the Cockle Park farm. Inset map locates the site within the UK.

A field campaign was carried out on 8<sup>th</sup> October 2014. 36 black/white circular targets were established and surveyed using RTK-GNSS using Leica GS10 receivers, with a distribution shown in Figure 4.1. The real-time GNSS correction services (SmartNet, provided by Leica Geosystems<sup>19</sup>) worked efficiently at the farm even close to trees. This delivered a 0.01 m planimetric and a 0.02 m vertical absolute accuracy in the Ordnance Survey Great Britain 1936 (OSGB36) coordinate system.

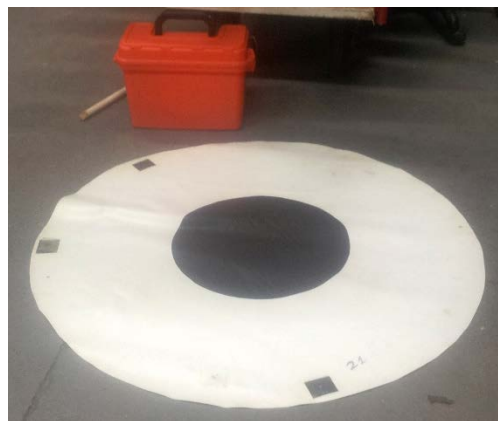


Figure 4.2: A black and white circular target.

The targets were made of sticky-backed plastic with an internal black circle of 0.40 m diameter (Figure 4.2). This diameter is equal to approximately 8-10 pixels on imagery acquired from a flying height of 120 m (i.e. 400 ft), which is the maximum UAV flying height allowed in UK. The targets were anchored to the ground with tent pegs inserted

<sup>19</sup> [www.uk.smartnet-eu.com/](http://www.uk.smartnet-eu.com/)

into four locations at the edges of the white circle (Figure 4.2). A GNSS pole was set up on a bipod and was positioned over a white dot, which marked the centre of the targets.

## **4.2 Sandford Industrial Park test site**

### ***4.2.1 Site overview***

Sandford Industrial Park is located at Prees ( $52^{\circ}54'26.52''\text{N}$ ,  $2^{\circ}37'55.30''\text{W}$ ), 8 km south of Whitchurch, UK (Figure 4.3). The site is mainly utilised for controlled earthworks by the “Safety and training” department of the Hawk Group<sup>20</sup> (a group of companies providing construction solutions) and for UAV flight training undertaken by Leica Geosystems<sup>21</sup>. Data collection was performed on 30<sup>th</sup> November 2016 at a dedicated site, as depicted in Figure 4.3.

The site is an embankment of approximately  $20^{\circ}$  slope and a relatively flat field of mostly bare soil with sparsely distributed low grass of approximately 0.1 m height. To synthetically create surface change, ground material were excavated from the embankment, and placed at the foot of the slope, as seen in Figure 4.4a. The slope change introduced covered an approximate area of  $100\text{ m}^2$  and was generated over two epochs. The change extended 3.50 m along and 6.50 m across the slope with an approximate depth of 0.25 m in epoch E1, and an approximate length, width and depth of  $6.50 \times 9.50 \times 0.50$  m in epoch E2 (Figure 4.4b). The surroundings of the synthetically generated change were stable throughout, apart from the hatched region in Figure 4.3 where access was allowed to excavators and hence, no ground-based observations were performed.

---

<sup>20</sup> [www.hawk-group.co.uk](http://www.hawk-group.co.uk)

<sup>21</sup> [www.leica-geosystems.com](http://www.leica-geosystems.com), [www.aibotix.com](http://www.aibotix.com)

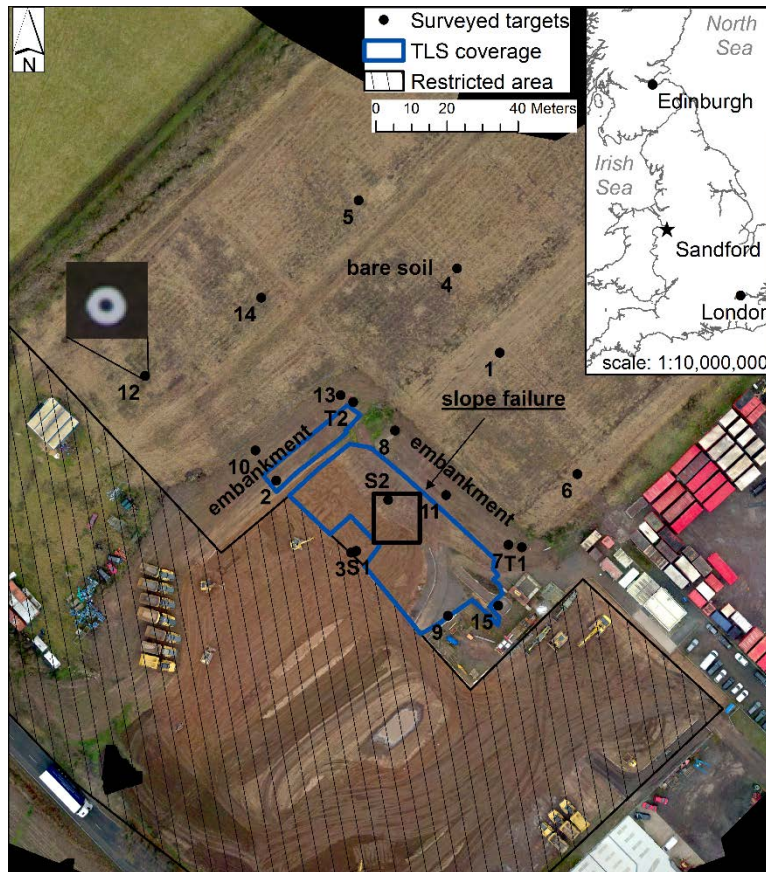


Figure 4.3: Overview of the experimental site at Sandford. Inset map locates the site within the UK. The UAV derived orthophotomosaic at epoch E0 (prior to excavations) is displayed in the background.



Figure 4.4: (a) Excavation of ground material for slope failure performed by the Hawk Group. (b) Overview of the epoch E2 excavations with the GNSS receiver at station S2 in the background.

#### ***4.2.2 Ground-based control data***

At Sandford, ground-based observations were obtained with both GNSS and TLS. The GNSS observations were used for establishing two base and scan stations on stable terrain and for GCPs. Two GNSS base stations (T1 and T2 in Figure 4.3) were established on the top of the embankment and observed in GNSS static mode with Leica GS10 receivers for 1.5 hours. These GNSS observations were combined with RINEX data from five Ordnance Survey Net stations located within a 60 km radial distance<sup>22</sup> and post-processed in Leica Geo Office software (LGO version 8.3). The post-processing delivered a 0.020 m 3D absolute accuracy in OSGB36. 15 circular targets (the same used at Cockle Park farm) were established within the region of interest. An enlarged view part of a typical UAV image capturing a circular target of point 12 is shown in Figure 4.3. These targets were each observed in GNSS rapid static mode for at least four minutes and delivered mm-level 3D accuracy relative to base station T1, as processed in LGO.

TLS observations were collected from two scan positions, S1 and S2 as mapped in Figure 4.3, using a Leica Scanstation P40. The two scan positions were surveyed in GNSS static mode for 10 minutes, delivering mm-level 3D accuracy relative to base station T1. Station T2 was used as an additional constraint to register the scans from S1 and S2, achieving a 0.002 m 3D mean registration error, performed in Cyclone (Leica Geosystems Ltd). The scan position S1 was chosen because it provided a direct incident angle to the slope failure. TLS observations were collected in between excavations for each of the three epochs (Figure 4.5). Due to time limitations, the slope failure was scanned only from S1 for epoch E1. However, to prevent more occlusions the slope was scanned from both S1 and S2 stations in epoch E2, enabling an approximate point cloud density equal to 2000 points/m<sup>2</sup>.

---

<sup>22</sup> [www.ordnancesurvey.co.uk/gps/os-net-rinex-data/](http://www.ordnancesurvey.co.uk/gps/os-net-rinex-data/)

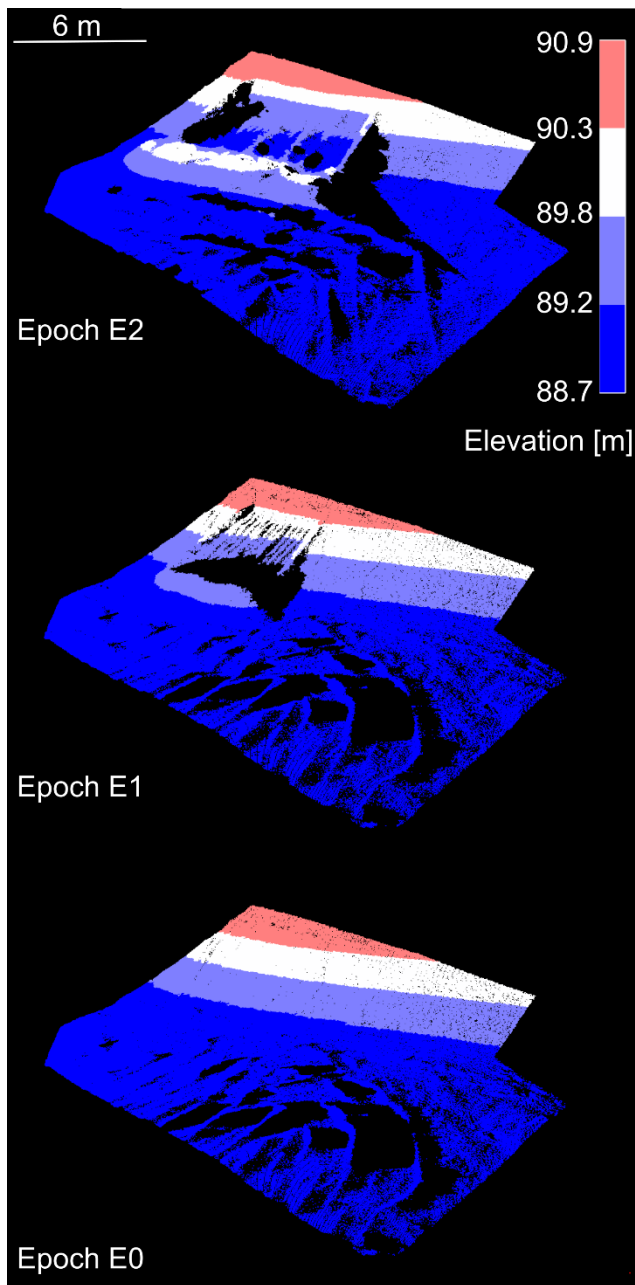


Figure 4.5: Perspective view of TLS point clouds at the three observed epochs over slope failure.

Figure 4.5 illustrates a perspective view of the slope failure at the three epochs. The higher density of the E2 point cloud compared to other point clouds can be observed. However, few occluded regions at the edges of the slope failure were still apparent in epoch E2. To use TLS point clouds as benchmark datasets very low/high points, as well as “off-ground” features (e.g. people, tripods and fences), were manually filtered out. The scanned area was suitable for cross-validation because vegetation was absent, which is also evidenced in Figure 4.4a and b.

## 4.3 Hollin Hill landslide

### 4.3.1 Geological and geomorphological overview

The landslide study area is located at Hollin Hill ( $54^{\circ} 6' 38.90''$  N,  $0^{\circ} 57' 36.84''$  W), 11 km west of Malton, North Yorkshire, UK as shown in Figure 4.6. The site is covered by short grass, with occasional shrubs and trees surrounded by hedgerows. Even though the land is mostly used for grazing, the grass height is uneven across the site, resulting in high surface roughness, especially during spring through autumn. The study area extends approximately 290 m E-W and 230 m N-S. The site is a south-facing linear hillslope of average  $12^{\circ}$  slope, with a 50 m elevation difference in N-S direction (Figure 4.6).

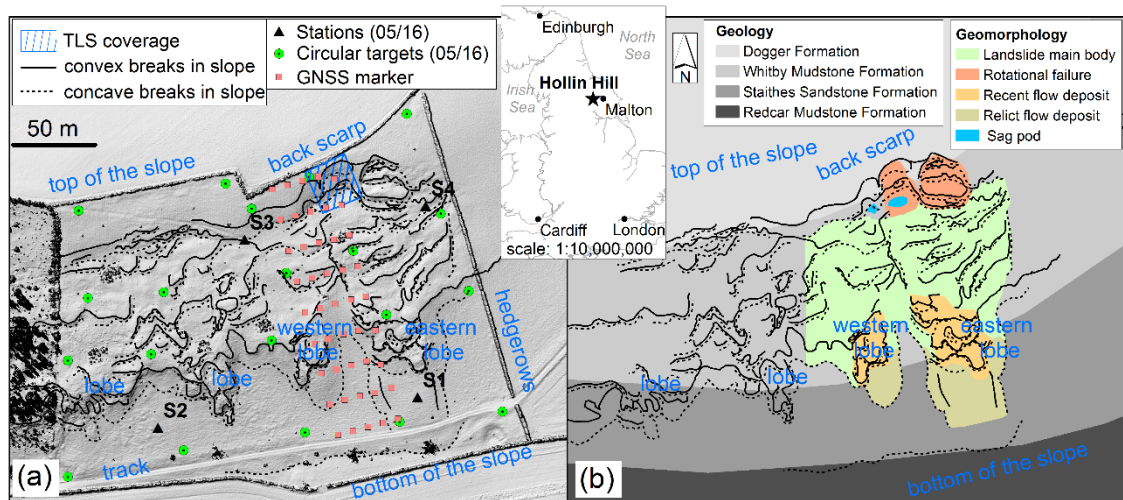


Figure 4.6: (a) Breaks in slope superimposed over *Shaded relief* grid derived from 2011 ALS with (b) geomorphological and geological properties of Hollin Hill landslide. Inset map locates the site within the UK. Modified from Merritt et al. (2014) and Uhlemann et al. (2017).

The Hollin Hill landslide has been a BGS observatory site since 2005<sup>23</sup>. It constitutes typical inland shallow slope failures of Lower and Middle Jurassic formations near Sheriff Hutton Carr (Merritt et al., 2014; Uhlemann et al., 2017). During the ice age this area was an icy lake (Lake Mowthorpe), part of the glacier ice sheet, which covered northern Britain (Merritt et al., 2014). Due to hydrogeological actions, depositions of lake-sediments occurred during and after the ice melt and many sites became prone to failure (Merritt et al., 2014). Chambers et al. (2011) characterised the Hollin Hill landslide as a very slow moving multiple earth slide-earth flow, based on the Cruden and Varnes (1996) classification scheme. The authors reported an average of 2 m/yr movement rate. Uhlemann et al. (2016) observed episodic movements that reached 3.5 m/yr. Earth slide/flow has been mostly triggered by intensive rainfall in combination with responses

<sup>23</sup> [www.bgs.ac.uk/landslides/hollinHill.html](http://www.bgs.ac.uk/landslides/hollinHill.html)

to pore-water pressure of the four geological formations, upon which the landslide sits (Uhlemann et al., 2016). These are the Dogger, the Whitby Mudstone, the Staithes Sandstone and the Redcar formation, mapped in Figure 4.6b, as extracted from Edina Digimap<sup>24</sup>. A description of materials transition from one formation to the other and their properties (e.g. lithological characteristics, depth etc.) can be found in Uhlemann et al. (2016) and Uhlemann et al. (2017).

Long-term investigations by the BGS (Chambers et al., 2011; Gunn et al., 2013; Merritt et al., 2014; Uhlemann et al., 2016; Uhlemann et al., 2017) have identified shallow rotational slumps of weak materials at the upper parts of the slope and translational movements at the lower parts of the slope. Rotational failures have caused ground subsidence, creating a back scarp (Figure 4.6b, Figure 4.7a and Figure 4.7b), which reverts towards the north. These slumps sit on the Whitby Mudstone formation, which has been characterised by Gunn et al. (2013) as the failing material. In addition, Chambers et al. (2011) and Uhlemann et al. (2017) identified the failure as low permeable material sliding over the well-drained Staithes Sandstone formation. The extent of the curved breaks of the slump blocks at the upper parts of the slope is viewed in Figure 4.7a and Figure 4.7b. Many secondary scarps, linear and parallel (Merritt et al., 2014), have emerged across the main landslide body and are depicted in Figure 4.7a and Figure 4.7b as breaks in slope. These were delineated by Merritt et al. (2014) from an ALS DEM acquired in 2011 with the aid of the 3D stereographic software, GeoVisionary.

Figure 4.7a illustrates that the surface gradient is not continuous. A flat plateau in the middle divides the site into top and bottom parts, where the slope becomes steeper. Thus, the top of the slope is not always visible when viewing from the bottom of the site, evidenced in Figure 4.7d.

---

<sup>24</sup> [www.digimap.edina.ac.uk](http://www.digimap.edina.ac.uk)

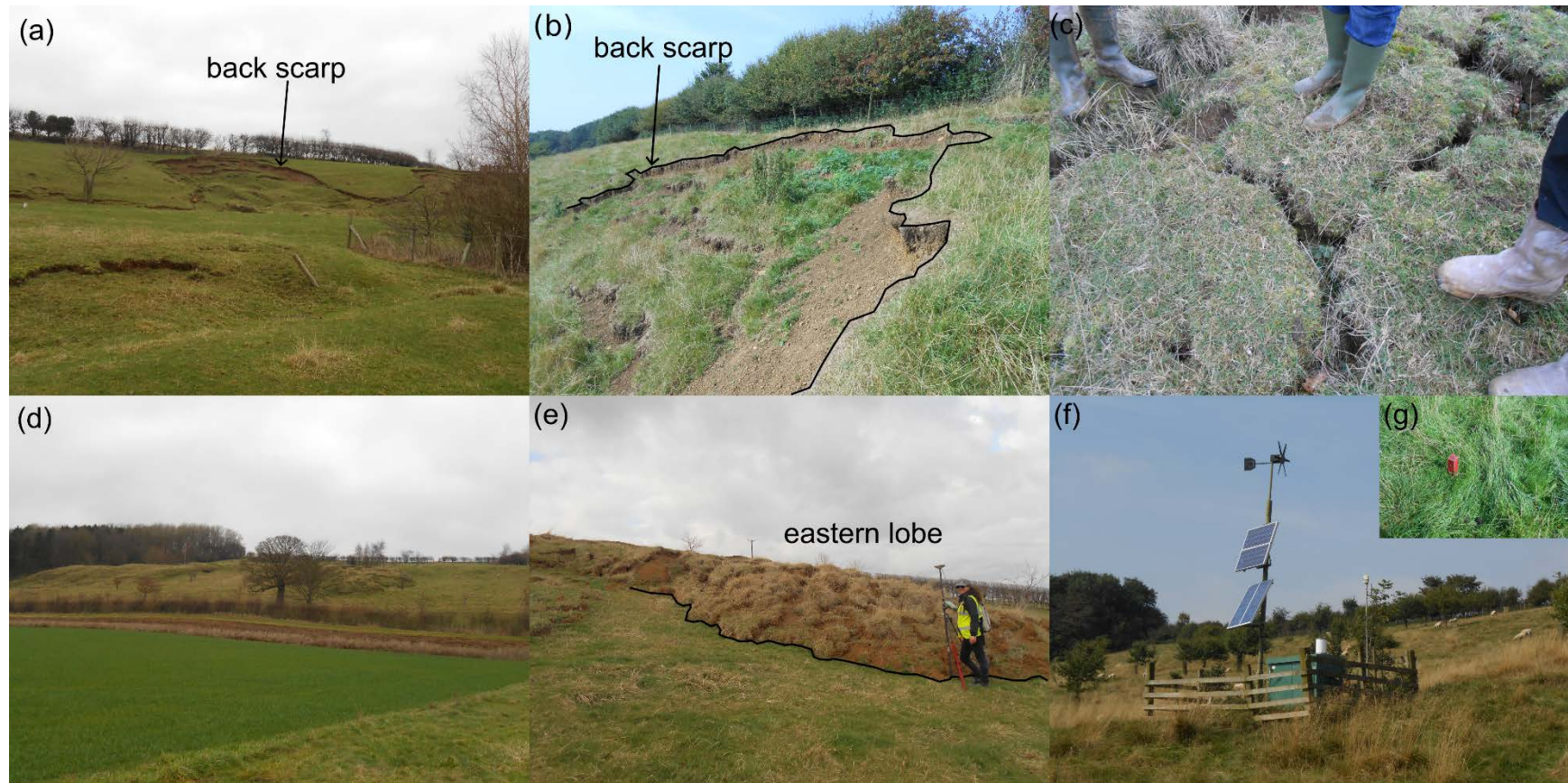


Figure 4.7: (a) Overview of the back scarp at the top of the slope captured on 01/14 during reconnaissance with (b) a closer view taken on 09/15. (c) Surface cracks observed across the site. (d) Formed lobes at the west part of the site, as seen from the foot of the slope (taken on 01/14). (e) A closer view of the eastern lobe captured on 03/15. (f) A weather station installed in the centre of the site together with other sensors and pegs shown in (g).

The flat plateau sits on the failing formation, which has translated downwards. The translation has compressed the surface and created undulations. This has weakened the ground support at the top of the slope while the water forms ponds at the surface (Figure 4.6b) after intensive rainfall. Due to translational movements, the ground has accumulated with a flow-like behaviour. As a result, lobes have formed which have continuously surged towards the toe of the slope. Many curved fissures have been observed over the prograding lobes compared to the parallel linear fissures at the middle part of the landslide body. The aforementioned description of the landslide behaviour is based on the BGS investigations (Merritt et al., 2014; Uhlemann et al., 2016; Uhlemann et al., 2017). Figure 4.6b depicts these characteristics mainly for the eastern part of the site that has been mostly monitored by the BGS.

During the spring-autumn period some breaks in slope are usually covered by bushes and grass (Figure 4.7b). Due to vegetation, the surface texture in Figure 4.7b is rougher than that of Figure 4.7a. In addition, the surface roughness varies over different parts of the landslide. For example, the advancing eastern lobe (formed by fractured ground material creating ridges) (Figure 4.7e) has a rougher texture than the adjacent continuous grassy terrain over deposits (Figure 4.6b). The concave feature, delineated in black in Figure 4.7e, separates this distinctive change of surface *curvature* and roughness. Apart from the continuous breaks in slope, there are also many individual narrow tension cracks across the main landslide body (Figure 4.7c), which tend to widen due to surface translational movements.

The geology, geomorphology and kinematics of the Hollin Hill landslide have been monitored by the BGS with multiple environmental, geotechnical, geophysical, aerial and ground-based observations, using numerous sensors installed across the site. For example, a weather station (Figure 4.7f) was installed in 2008. Geotechnical sensors, namely inclinometers, tiltmeters, acoustic emission monitoring etc., have been established over the most active western and eastern lobes. Moreover, geophysical observations have been collected with electrical resistivity and self-potential tomography from profile arrays of electrodes installed in the subsurface (Section 2.1.1). Refer to Uhlemann et al. (2016) and Uhlemann et al. (2017) for more information about the various observations. These long time series, together with borehole logs, ALS-derived DEM obtained in 2011 and RTK-GNSS surveying (Section 4.3.2) have supported BGS investigations in characterising and interpreting the complex landslide behaviour. UAV derived observations further enhances the ongoing BGS research by providing a higher

spatial and temporal resolution. Overall, the complexity and variability of the landslide dynamics have made this site a challenging scenario to test the morphology-based monitoring approach.

#### ***4.3.2 GNSS and total station observations***

As previously mentioned, BGS fieldwork involved RTK-GNSS measurements on a monthly-basis at permanently installed wooden pegs. An array of pegs has been established between the western and eastern lobes, shown in Figure 4.6a. Each peg is a square of approximately 0.10 m x 0.10 m size, too small to be identified in the UAV-derived orthophotomosaics. The height of the pegs above the ground vary from tens of centimetres (Figure 4.7f) to approximately 0.50 m. The GNSS pole on a tripod was positioned behind each peg to collect the measurements.

During the fieldwork of this study, the following tasks were performed:

- (1) A GNSS base station was established on stable terrain in an adjacent field and observed in GNSS static mode for between three and eight hours;
- (2) The same circular targets described in Section 4.1.1 were evenly distributed over the landslide and surveyed in GNSS rapid static mode (three-minute observations);
- (3) Additional stations for topographic surveying and laser scanning observations were established and observed in GNSS static mode for at least twenty minutes;
- (4) Spot heights of characteristic concave/convex surface features and other features on grassy terrain were topographically surveyed using total station and/or rapid static GNSS (three-minute observations) for validation purposes (Figure 4.8).

Table 4.1: Data processing details of surveyed base stations, circular targets and spot heights.

Campaign (day/month /year)	Easting [m]	Northing [m]	Elevation [m]	Ordnance Survey's Net stations	Planimetric standard deviation as exported from LGO [m]	Vertical standard deviation as exported from LGO [m]	Duration	Number of circular targets	Number of spot heights	Geomatics technique applied for surveying spot heights
15/05/14	468486.494	468792.437	54.129	LOFT, YEAS, SWAN, SCAO, LEED	0.005	0.017	7h 38'	17	-	-
15/12/14	468260.482	468814.849	65.979	LOFT, YEAS, SWAN, SCAO	0.003	0.013	4h 56'	10	48	GNSS rapid static
19/03/15	468105.219	468650.441	44.603	LOFT, YEAS, SWAN, SCAO	0.005	0.021	3h 40'	11	52	GNSS rapid static
10/06/15	468105.246	468650.443	44.629	LOFT, YEAS, SWAN LEED	0.004	0.013	7h 28'	18	98	Total station
27/09/15	468103.917	468632.373	43.080	LOFT, YEAS, SWAN LEED	0.003	0.010	5h 40'	20	-	-
12/02/16	468105.224	468650.442	44.602	LOFT, YEAS, SWAN, SCAO, LEED	0.003	0.013	6h 44'	20	65	Total station
27/05/16	468105.221	468650.435	44.590	LOFT, YEAS, SWAN SCAO ,LEED	0.004	0.014	6h 12'	20	559	Total station

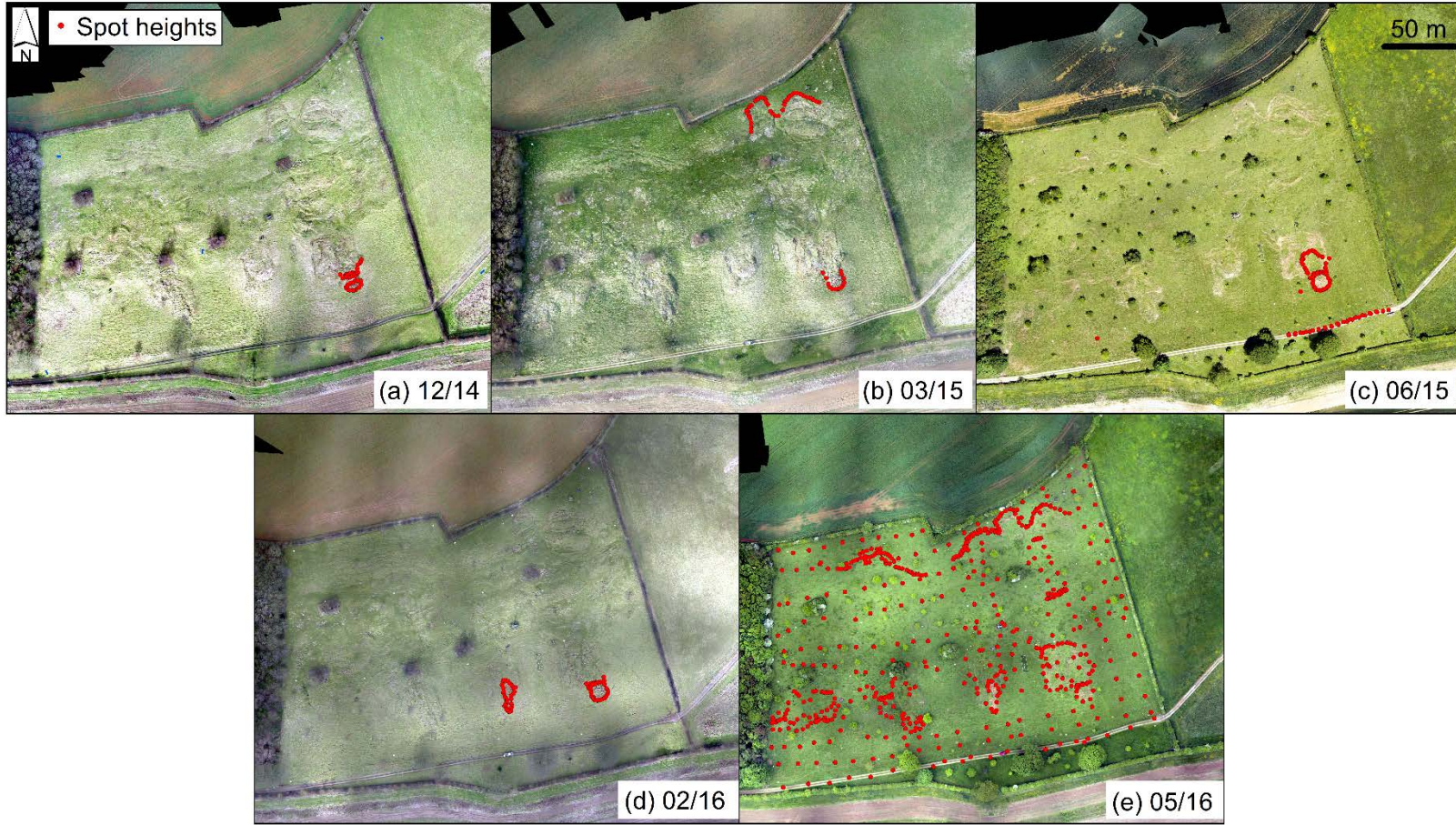


Figure 4.8: Location of surveyed spot heights per campaign.

The equipment used was a Leica GPS 1200 and a Leica Viva GS10 for GNSS observations and a Leica TCR805 for total station measurements. To derive the coordinates of the base stations, RINEX observations from at least four Ordnance Survey Net stations<sup>22</sup> were used and post processed in LGO. The OS Net stations, together with the estimated coordinates and standard deviations of the base stations after network adjustments, are reported in Table 4.1. Among all OS Net stations, YEAS is closest to the study area (11 km distance) while the others are 40-50 km from the site. As listed in Table 4.1, the maximum standard deviation was estimated as 0.005 m in plan and 0.020 m in elevation.

Due to tractor movements and farming activities, the base station was set up at different locations for three of the campaigns. However, for four campaigns 03/15, 06/15, 02/16, 05/16 (Table 4.1) it was possible to establish the base over the same peg, 90 m south of hedgerows at the bottom of the slope (Figure 4.6a). A view of the west part of the landslide from this location can be seen in Figure 4.7d. 0.014 m planimetric and 0.016 m vertical standard deviations were estimated from the positions of the four campaigns. This verified that the base station was on stable terrain. Given the long baselines between the peg and the OS Net stations, any uncertainty can be attributed to the GNSS related errors and not to surface movement.

Due to logistics, the number of circular targets and spot heights varied for each campaign (Table 4.1). Figure 4.6a shows the distribution of the circular targets and the locations of the stations for 05/17. The locations of all spot heights per campaign are shown in Figure 4.8. The most complete survey was conducted in the last campaign. After post processing the GNSS and total station observations, a 3D accuracy at the mm-level relative to the GNSS base stations was delivered for all campaigns.

#### ***4.3.3 Terrestrial laser scanning observations***

TLS observations were undertaken with a Leica Scanstation P40 during the last two campaigns (Table 4.1) with the support of a related project (Chidburee et al., 2016). The observations covered a sub-region of the rotational failure at the upper part of the slope of area 722 m<sup>2</sup> (Figure 4.6a and Figure 4.6b). Four stations were established around the failure to tackle occlusions and surveyed in GNSS rapid static mode, as mentioned in the previous section. The four scans were registered with scan-to-scan registration and georeferenced from the coordinates of the four stations in OSGB36 using Cyclone. An RMSE of 0.005 m for the registration was estimated for both campaigns. An automatic

ground classification was not efficient due to the high density of the point clouds and computer memory issues. For that, “off-ground” features, mostly bushes, were manually removed from the point clouds by Chidburee et al. (2016) in TerraSolid TerraScan (TerraScan, 2016). This resulted in two TLS point clouds with density of an average 10,000 points/m<sup>2</sup> over the rotational failure that were used to cross-validate the SfM-MVS derived point clouds. (Section 6.2.2). Figure 4.9 illustrates the TLS point clouds of the last two campaigns after filtering. The point clouds were colored using the images captured with the scanner. Even though four scan stations were used, there are still occluded areas due to the complex surface irregularities, as shown in black in Figure 4.9. Two of the scan positions were established in front of the slope face with a direct incident angle to the cracks. Thus, the back scarp can be depicted in detail, as evidenced in Figure 4.7a and Figure 4.7b when compared to Figure 4.9.

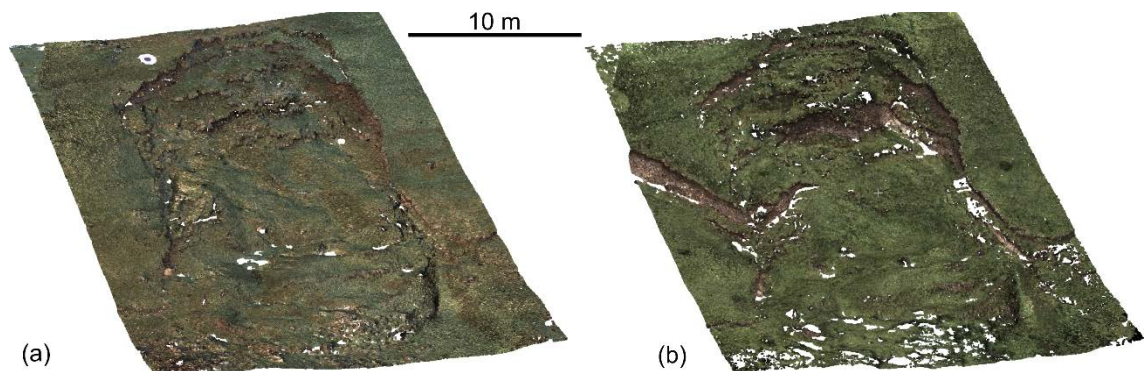


Figure 4.9: Rotational failure at the top of the slope, as observed with TLS (a) in 02/16 and (b) in 05/16.

## 4.4 UAV system

### 4.4.1 Platform overview

A fixed-wing Quest-300 UAV manufactured by QuestUAV Ltd, UK, was used for all experiments reported in this study. This UAV is made of hard compressed foam, has a maximum payload of 5 kg and a flight duration of approximately 15 minutes utilising a Lithium polymer battery (Figure 4.10a). The UAV platform is equipped with one or two compact digital cameras (detailed below), an on-board single-frequency GNSS receiver (Fastrax IT500, SkyCircuits Ltd<sup>25</sup>) and a consumer-grade MEMS-IMU (SkyCircuits Ltd<sup>25</sup>). The latter comprises a 3-axis accelerometer, 3-axis gyroscope and 3-axis magnetometer. It also contains a micro-processor with autopilot software (SkyCircuits Ltd<sup>25</sup>) that interprets predefined flight mission parameters (a series of 3D way-points that describe the flight path and the camera exposure time), enabling the UAV to fly

<sup>25</sup> [www.skycircuits.com/](http://www.skycircuits.com/)

autonomously. The autopilot system allows for assisted piloting through the aerial link to the transmitter (Figure 4.10b), handling abrupt movements with respect to roll/pitch axes usually generated by an inexperienced pilot. The assisted mode supports a secure landing that can be controlled by the pilot.

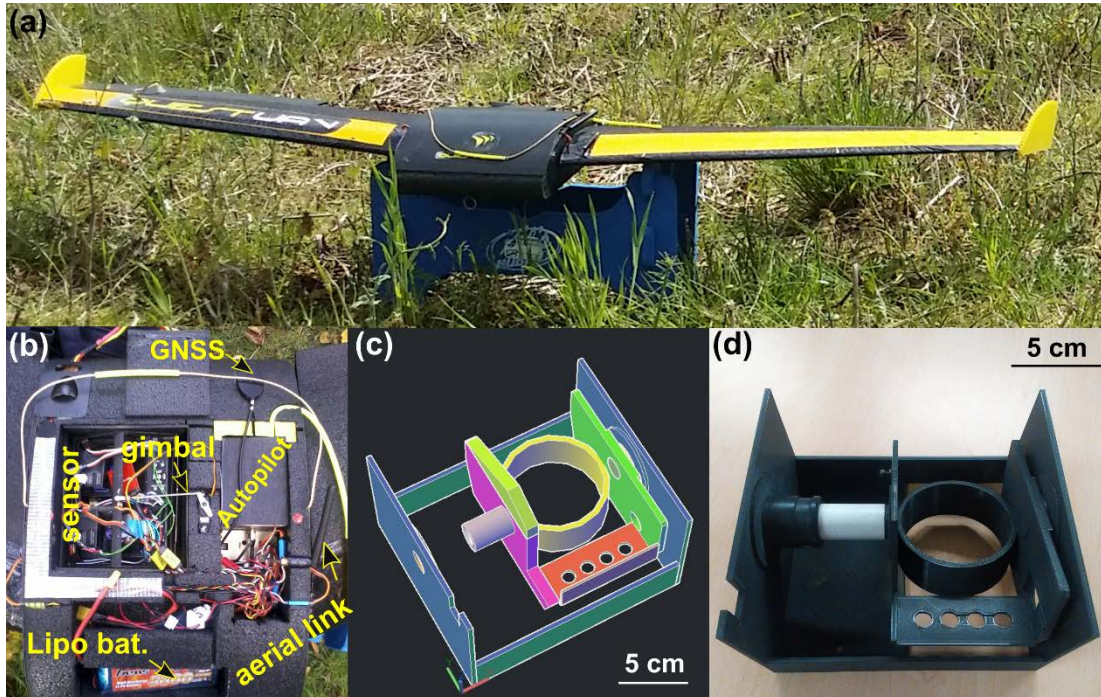


Figure 4.10: (a) Overview of Quest-300 UAV. (b) Payload setup inside the main UAV body. (c) AutoCAD 3D model and (d) 3D printed version of a camera case to hold the Sony A6000 camera.

The micro-processor stores a log file which describes the flight trajectory information, including the time-tagged 3D UAV position at 10 Hz. This position is recorded in World Geodetic System 1984 (WGS84) coordinates (longitude, latitude and altitude), as estimated after the integration of GNSS with MEMS-IMU observations through an extended Kalman filter. This is implemented in real-time within the micro-processor (SkyCircuits Ltd<sup>25</sup>). The UAV log file also stamps the time and 3D position of the first image only as captured after the aircraft's launch and triggered by the autopilot. This configuration is typical of most consumer-grade UAV systems used for photogrammetric capture (Section 2.3.1).

#### 4.4.2 On-board sensors

The utilized Quest-300 UAV was initially fitted with two compact digital cameras (Panasonic Lumix DMC-LX5) for RGB and near infra-red image acquisition. RGB imagery was used in this study (Chapters 5 and 6). Both cameras are fixed in a wooden case which is mounted on gel, for vibration damping, and fitted in the main UAV body (Figure 4.10b). A simple gimbal, attached to the UAV body (Figure 4.10b), compensates

for the aircraft's movements along the roll axis, thereby enabling the camera to capture close to nadir images.

An additional compact digital camera, a Sony A6000, for visible imagery was purchased in 2015 during the course of the study. To mount this camera in the Quest-300 UAV a new case was designed and modelled by the author at Newcastle University using AutoCAD 3D<sup>26</sup> (Figure 4.10c). This was then 3D printed using BGS facilities (Figure 4.10d). The fit of the new case to the UAV body frame was also implemented by the author. After mounting the new camera, it was vital to ensure that the UAV's centre of gravity was unaltered. Due to different materials and weights of the two camera cases, an extra weight was added close to the nose of the UAV to maintain the same weight balance. To confirm that the UAV flying performance was effectively the same using either camera, trial flights were conducted at Cockle Park farm.

Regarding the sensor's characteristics, the Panasonic DMC-LX5 has a 5.1 mm nominal focal length Leica lens, an 8.07 x 5.56 mm CCD sensor with 2 x 2  $\mu\text{m}$  nominal pixel size creating an image of 3648 x 2736 pixels. The Sony A6000 carries a Sony E 16 mm F2.8 pancake interchangeable lens with a 16.0 mm nominal focal length. It has a 24 megapixel (6000 x 4000 pixels) APS-C CMOS sensor of 23.5 x 15.6 mm size with a 3.9 x 3.9  $\mu\text{m}$  nominal pixel size.

Prior to UAV flights, the Panasonic DMC-LX5 and Sony A6000 were calibrated in *PhotoModeler* and *PhotoScan* respectively. A calibration grid board with coded targets that can be automatically identified by *PhotoModeler* was used for Panasonic DMC-LX5 calibration on 02/07/2012 (Figure 4.11a). On 26/09/2015, a separate indoor calibration test field was established using targets at several depths over a 6 m range, as seen in Figure 4.11b. The positions of the targets were precisely surveyed using a total station. For both tests, 12 convergent images at 0° and  $\pm 90^\circ$  roll angles were captured from four different positions. Even though the same camera model (Equations 3.1 and 3.2) is adopted in both *PhotoModeler* and *PhotoScan*, the bundle adjustments in the two software packages involve different type of observations, which consequently yield different IOP estimations. For example, as compared to *PhotoScan*, *PhotoModeler* does not implement the SfM workflow in its calibration toolbox and only observations at the locations of the coded targets are used for spatial resection and intersection (Section 2.2.1). For comparative purposes between the two software packages, the damped bundle

---

<sup>26</sup> [www.autodesk.co.uk](http://www.autodesk.co.uk)

adjustment toolbox (DBAT) implemented in Matlab and created by Börlin and Grussenmeyer (2016) was utilised.

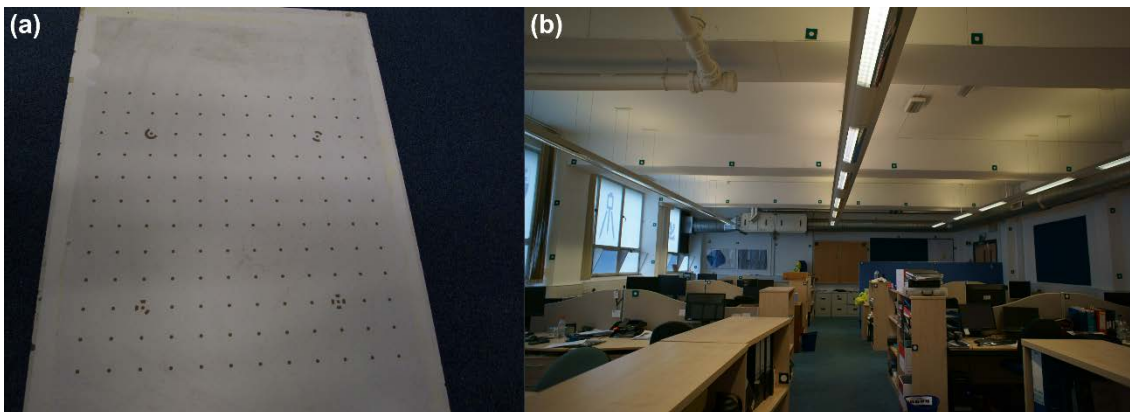


Figure 4.11: Illustration of (a) the calibration board used in *PhotoModeler* and (b) the calibration test field used in *PhotoScan*.

DBAT runs a self-calibrating bundle adjustment (Börlin and Grussenmeyer, 2013; Börlin and Grussenmeyer, 2016). DBAT uses as image observations the image coordinates of coded targets and tie points as derived from the two software. In addition, it uses approximate camera IOPs and EOPs determined from the two software and then it re-estimates them through bundle adjustment. The DBAT tool was more advantageous for calibration than *PhotoScan* as high correlations between parameters could be identified and quality indicators derived, which are not available in *PhotoScan*. The results derived from *PhotoModeler*, *PhotoScan* and DBAT for both cameras are reported in Table 4.2. DBAT re-estimated all distortion parameters listed in Table 4.2 apart from the format width and height.

Table 4.2: Calibration results prior to UAV flights for Panasonic DMC-LX5 and Sony A6000, as derived from *PhotoModeler*, *PhotoScan* and DBAT.

Panasonic DMC-LX5-Calibration 02/07/2012				
Determined parameters	<i>PhotoModeler</i>		DBAT	
	Value	$\sigma$	Value	$\sigma$
f-focal length [mm]	5.129	$5.30 \times 10^{-04}$	5.128	$5.43 \times 10^{-04}$
$x_p$ -principal point [mm]	3.565	$3.70 \times 10^{-04}$	3.565	$3.68 \times 10^{-04}$
$y_p$ -principal point [mm]	2.718	$4.00 \times 10^{-04}$	2.718	$3.82 \times 10^{-04}$
$F_w$ -format width [mm]	7.225	$1.20 \times 10^{-04}$	7.225	-
$F_h$ -format height [mm]	5.419	-	5.419	-
$K_1$ -radial distortion 1	$2.72 \times 10^{-04}$	$8.50 \times 10^{-06}$	$2.64 \times 10^{-3}$	$1.40 \times 10^{-05}$
$K_2$ - radial distortion 2	$-1.03 \times 10^{-04}$	$4.00 \times 10^{-07}$	$-9.04 \times 10^{-5}$	$2.06 \times 10^{-06}$
$K_3$ - radial distortion 3	$3.91 \times 10^{-06}$	-	$3.32 \times 10^{-6}$	$9.53 \times 10^{-08}$
$P_1$ - decentering distortion 1	$3.83 \times 10^{-04}$	$4.00 \times 10^{-06}$	$3.84 \times 10^{-4}$	$3.99 \times 10^{-06}$
$P_2$ - decentering distortion 2	$-9.36 \times 10^{-05}$	$4.30 \times 10^{-06}$	$-9.08 \times 10^{-5}$	$4.12 \times 10^{-06}$
Sony A6000-Calibration 26/09/2015				
	<i>PhotoScan</i>		DBAT	
	Value	$\sigma$	Value	$\sigma$
f-focal length [mm]	16.204	-	16.200	$1.02 \times 10^{-03}$
$x_p$ -principal point [mm]	11.992	-	11.994	$7.42 \times 10^{-04}$
$y_p$ -principal point [mm]	7.857	-	7.858	$6.08 \times 10^{-04}$
$F_w$ -format width [mm]	23.997	-	24.000	-
$F_h$ -format height [mm]	16.000	-	16.000	-
$K_1$ -radial distortion 1	$3.07 \times 10^{-04}$	-	$2.90 \times 10^{-04}$	$1.02 \times 10^{-06}$
$K_2$ - radial distortion 2	$-1.76 \times 10^{-06}$	-	$-1.53 \times 10^{-06}$	$1.46 \times 10^{-08}$
$K_3$ - radial distortion 3	$1.14 \times 10^{-09}$	-	$2.17 \times 10^{-10}$	$6.04 \times 10^{-11}$
$P_1$ - decentering distortion 1	$3.47 \times 10^{-05}$	-	$3.74 \times 10^{-05}$	$1.12 \times 10^{-06}$
$P_2$ - decentering distortion 2	$-2.76 \times 10^{-05}$	-	$2.90 \times 10^{-05}$	$9.15 \times 10^{-07}$

For the Panasonic DMC-LX5, the differences of the estimated values and standard deviations from *PhotoModeler* and DBAT were insignificant, giving confidence to the DBAT solution. Both calibrations resulted in an overall RMSE of 0.20 pixel as calculated from the residuals of the point observations, i.e. 4 control and 141 additional points detected on the grid board (Figure 4.11a). For the Sony A6000, *PhotoScan* used 43 calibration targets (as GCPs) which were located in the imagery (Figure 4.11b). 25185 tie points across 10 images were automatically identified. This configuration delivered an RMSE of 0.30 pixel at GCPs and 0.80 pixel at all observations including tie points, after the DBAT solution. The higher RMSE compared to the *PhotoModeler* value is possibly attributed to the fact that the average optical ray-angle generated from the tie points was  $4^\circ$ , whereas the average optical ray-angle from GCPs was  $44^\circ$ . The latter was close to the  $50^\circ$  average optical-ray angle computed from the grid board configuration. The  $4^\circ$  angle implies that the majority of tie points were detected in the centre of the test field, and sub-optimal for calibration purposes. This was also checked during the calibration experiment. As noted by (Kraus, 2007), the various optical ray-angles can influence the

bundle adjustment solutions. Acquired images with a wider baseline and a better convergent angle closer to  $44^\circ$  would improve the overall RMSE as more tie points at the corners of each image could be identified. However, the size of the room restricted the space available and for that reason the grid calibration board was used later for additional calibration tests (Section 6.5.3).

For both cameras, DBAT showed that  $K_2$  and  $K_3$  were 98% correlated, implying that  $K_3$  can be excluded from the self-calibrating bundle adjustment. However, these tests were performed indoors under ideal conditions with cameras mounted on tripods and triggered with an external trigger device (Panasonic DNC-LX5) or an infra-red LED connection (Sony A6000) to minimise shaking and blurring (Sieberth et al., 2014). Assuming that during a UAV flight these ideal conditions are violated, the self-calibrating bundle adjustment would produce different calibration solutions. The results in Table 4.2 were only used as reference to compare against other indoor calibration tests, which were performed under the same configurations during and after the end of the monitoring period (Section 6.5.3) to examine each camera's stability.

## Chapter 5.

# Control testing of morphology-based strategy

---

Chapter 4 presented three study areas and described the ground-based observations undertaken in each area. It described the Quest-300 UAV platform with the on-board image sensors used for experiments. This chapter presents four experiments carried out at the Cockle Park and Sandford study areas. The experiments examine the performance of the SfM-MVS pipeline under the selection of different number of GCP. The MBR workflow is tested and evaluated under various scenarios. For cross-validation benchmark datasets obtained with TLS are utilised. Analysis of the MBR-based results shows the potential of the co-registration solution without the requirement of GCPs.

### 5.1 Experiment description

The four experiments are as follows:

- 1) The first experiment carried out at the Cockle Park study area to define a minimum number of GCPs which can deliver georeferencing accuracy equal to the GSD;
- 2) The second experiment, named GCP-based experiment, carried out at the Sandford study area with the inclusion of the optimally-defined number of GCPs;
- 3) The third experiment, named MBR-GCP experiment, adopted the MBR approach (Section 3.4.2) with a reference epoch generated from the GCP-based SfM-MVS process.
- 4) The fourth experiment is the MBR-UAV experiment, which implemented the MBR approach excluding the GCPs in the reference epoch. This scenario resembles a realistic case of monitoring an inaccessible hazardous environment with a consumer-grade UAV platform.

The third and fourth experiments were undertaken at Sandford. The last three experiments involved identical *PhotoScan* parameters, these being camera position accuracy equal to 10 m, marker accuracy for CPs equal to 0.050 m, tie point accuracy equal to 1.0 pixel, projection accuracy equal to 0.1 pixels, “ultra-high” quality and aggressive disparity mode. The imaging network (i.e. number of images and characteristic flight lines) was

also identical for the three experiments. For all experiments described in this chapter, a Panasonic DMC-LX5 camera was utilised for image capture.

### 5.1.1 UAV image acquisition and processing

Three UAV flights were carried out on 8<sup>th</sup> October 2014 at Cockle Park (Section 4.1.1) at flying heights (above ground level) of 250 ft, 300 ft and 350 ft, which correspond to 76 m, 91 m and 107 m respectively. The Panasonic DMC-LX5 camera was set in shutter priority mode with a shutter speed of 1/800 s, at ISO 400 and varying aperture. The focal distance was set to infinity to ensure that surface objects captured at different heights were within the camera's depth of field. A 2.5 s exposure interval, with a UAV speed of 18 m/s was selected to produce a 60 % forward and a 60 % lateral overlap.

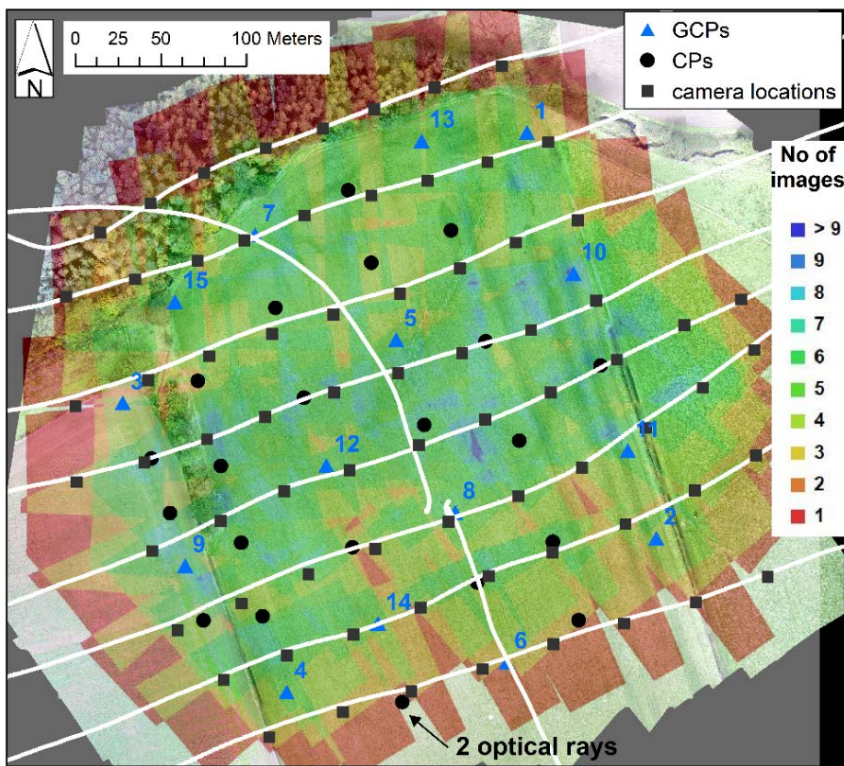


Figure 5.1: The 250 ft post-flight trajectory (in white), with the number of overlapping images (in colour), the camera exposure positions after post-processing together with the distribution of targets.

The distance between two neighbouring flight lines was computed equal to 54 m, taking into consideration the lowest flying height (i.e. 250 ft). In addition, the image ground footprint was estimated to be 109 x 82 m. Cross-wind parallel flight lines were configured for all three surveys. The post-flight trajectory of the 250 ft height can be seen in Figure 5.1. Given the flight specifications, an adequate image overlap was achieved with most GCPs and CPs appearing in at least three images. As an example, the flight configuration, highlighting image overlap for the 250 ft flight after post-processing in *PhotoScan*, is

depicted in Figure 5.1. Increased image overlaps were achieved for the 300 ft and 350 ft UAV flights.

Four *PhotoScan* projects for the different scenarios were created as listed in Table 5.1. The first three projects included imagery from the three different flying heights and a fourth project combined images from all flights. The estimated average height, calculated in *PhotoScan*, mismatched the predefined height which is also reported in Table 5.1 This is possibly because of wind turbulence and errors associated with the consumer-grade on-board sensors, such as the GNSS and MEMS-IMU (Section 4.4.1).

Table 5.1: Processing details of four UAV projects used in the Cockle Park experiment.

Configuration	Predefined flying height [ft (m)]	No of images over the region of interest	Estimated GSD [m]	Estimated average flying height [m]	Optical rays per tie point
1	250 (76)	72	0.029	85.934	2.7
2	300 (91)	76	0.036	104.362	3.1
3	350 (107)	84	0.041	119.863	3.1
4	combined	232	0.039	100.000	4.0

Each project was post-processed using the SfM-MVS pipeline (sparse point cloud reconstruction and georeferencing phases) with default settings in *PhotoScan* (Section 3.2.5). After removing images and points with  $> 1$  pixel reprojection error (Section 3.2.1), an average of 0.5 pixels global reprojection error was estimated in all projects. The SfM-MVS pipeline was repeated 14 times per project; in the first run, no GCPs were included, only the camera exposure stations derived from autopilot (Stage 1 in Figure 3.6); and for the remaining 13 runs, three to 15 GCPs were successively incorporated. The GCP distribution is shown in Figure 5.1. The numbers indicate which GCP was used for each run. For instance, three GCPs generated a triangle with indices 1, 2 and 3; four GCPs generated a rectangle with indices 1-4, etc. (Figure 5.1). A set of 21 independent CPs was used for accuracy assessment, which is discussed in the following section.

### ***5.1.2 Experimental results and analysis***

For the different numbers of GCPs the SfM-MVS bundle adjustment provided solutions with various RMSEs at each CP, as computed from Equations (3.34), (3.35) and (3.36). The average RMSE in plan, elevation and in full 3D magnitude at 21 CPs are plotted with respect to the number of GCPs per project in Figure 5.2. Figure 5.2a shows that the 3D RMSEs derived from the three GCP-based bundle adjustment significantly varies within a range of 0.20 m with respect to the three flying heights. The three GCP-based bundle adjustment of the combined project provided a 3D RMSE less than 0.10 m. However, when no GCPs were incorporated into the SfM-MVS bundle adjustment m-level RMSEs were estimated regardless of the different flying height scenarios (Table A.1 in Appendix A). These m-level values were associated with the low precision of the consumer-grade UAV GNSS-INS sensors, as also observed in previous studies (Chiang et al., 2012; Shahbazi et al., 2015; Carbonneau and Dietrich, 2016).

In the case of the five GCP solution, planimetric RMSEs (Figure 5.2c) decreased with respect to a higher number of GCPs. The highest RMSEs were provided from the 350 ft flying height. This was expected, as the estimated GSD was also higher at 350 ft than for the flights with lower flying heights (Table 5.1). For five GCPs, the RMSEs in plan lie within a maximum 0.022 m difference between the 350 ft and the combined height scenario. Regarding RMSEs in elevation, the range difference between the 350 ft and the combined height scenarios is equal to 0.052 m for five GCPs, higher than the range difference in plan (Figure 5.2d and Table A.1 in Appendix A). Among all scenarios with five GCPs, the combined scenario delivered a planimetric RMSE closer to 1 x GSD and a 3D RMSE approximately 1.5 x GSD (Table 5.1 and Table A.1 in Appendix A). These findings indicate that a minimum number of GCPs can deliver SfM-MVS outputs with accuracy level of 1 x GSD, eliminating the need for establishing and surveying numerous GCPs.

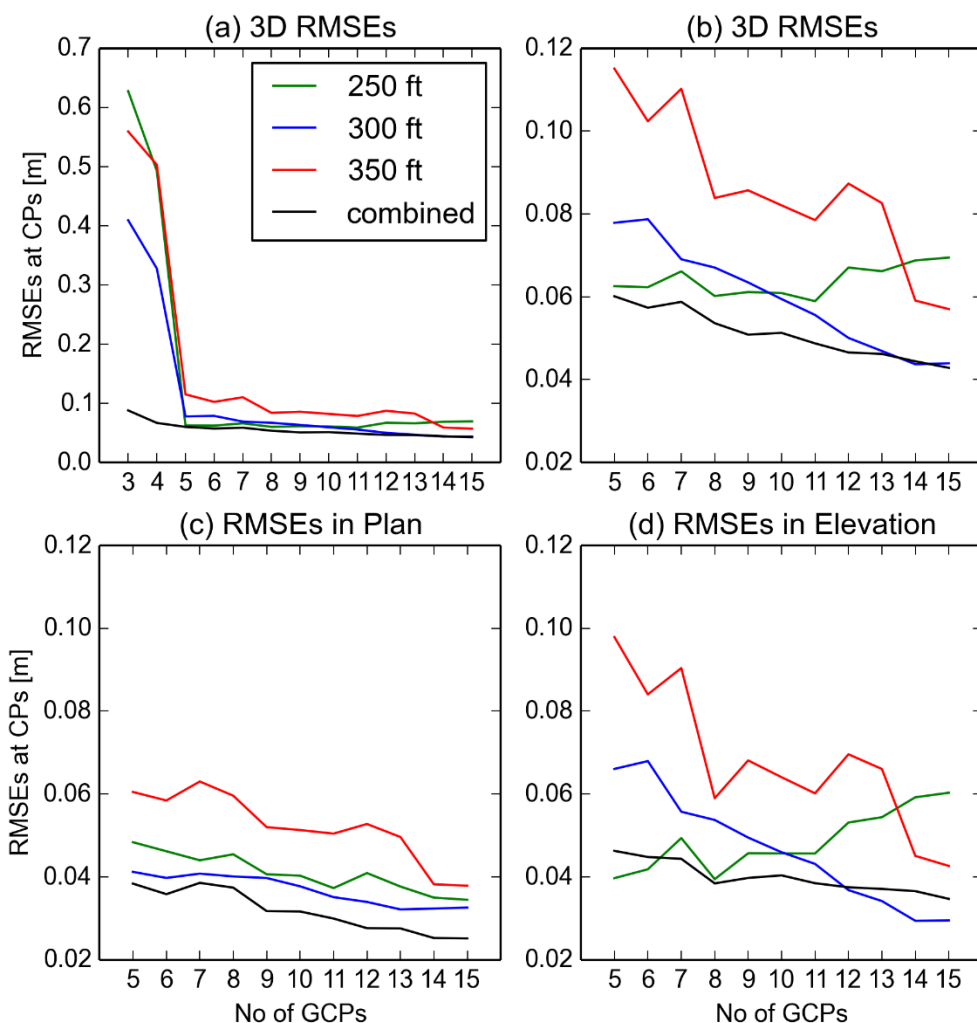


Figure 5.2: Average RMSEs at 21 CPs under different scenarios of flying height and number of GCPs.

The 250 ft height RMSEs in elevation showed an upward trend with respect to the higher number of GCPs, unlike the downward trends of the other three height scenarios (Figure 5.2d). This is possibly due to the overall lower image overlap of the 250 ft mission (Figure 5.1). For instance, the analysis showed that a CP at the south of the site with two optical rays (in other words projections i.e. number of images that a point can be back-projected) at 250 ft provided a 0.086 m elevation error, indicated in Figure 5.1. Whereas, a -0.047 m (half of the 250 ft elevation error) was calculated at the same CP for 350 ft, which allowed for five optimal rays. Table 5.1 reports the number of optical rays. This is computed as a ratio of the total number of optical rays over the total number of tie points detected, indicating the effective image overlap. The highest number of optical rays per tie point was estimated from the combined height scenario. As a result, CPs viewed by fewer images adversely affected the average RMSE in elevation.

Apart from the error magnitude, error distribution also varied relative to the number of GCPs included into the SfM-MVS georeferencing. Figure 5.3a and b show two examples

of planimetric and vertical errors for the combined height scenario estimated from five GCPs and 15 GCPs respectively. When only five GCPs were utilised, the majority of planimetric vectors at CPs are oriented towards the south (Figure 5.3a). Whereas with the inclusion of extra GCPs the distribution of error vectors became more random (Figure 5.3b). The error in elevation, interpolated with the natural neighbour interpolation technique (Section 3.2.2), formed bowl-shape patterns in both scenarios. Figure 5.3a shows a dishing pattern with negative values at the SE and a doming pattern with positive values at the NE of the study area. The input of more GCPs significantly reduced the SE dishing effect, while it slightly increased the spread of the NE doming effect (Figure 5.3a and b). According to Carbonneau and Dietrich (2016) these complex distortion patterns (a combination of dishing and doming shapes) are mostly apparent in compact digital cameras. The causes of these errors were already described in Section 3.2.6. The present analysis has found that the higher number of GCPs did not entirely reduce the bowl-shape systematic biases in the case of parallel flight lines. James and Robson (2014) and James et al. (2017a) reported similar findings and suggested that the inclusion of convergent imagery and flight lines of opposing direction could mitigate these effects (Section 3.2.6.).

Repeating the SfM-MVS pipeline under various GCP configurations resulted in variations in the estimated camera IOPs. Figure 5.4 plots the estimated values of focal length and the  $K_1$  lens distortion parameter. The latter was chosen because it is considered the most critical among all lens distortion parameters, especially in the case of compact digital cameras (James and Robson, 2014; Carbonneau and Dietrich, 2016). Maximum variations in focal length and  $K_1$  estimations were observed in the 250ft and 300 ft height scenarios. Such variations imply that SfM-MVS self-calibrating bundle adjustment is sensitive to both the number of GCPs and imaging network configurations. Remondino et al. (2012) demonstrated that the SfM-MVS pipeline also estimated numerically inconsistent camera IOPs with other SfM software - i.e. this is not restricted to *PhotoScan*. This numerical instability of the SfM-MVS solution was also presented by Shahbazi et al. (2015). The authors noted high correlations between focal length and the camera's EOPs (mostly in elevation) when images were acquired from a constant flying height. Figure 5.4 shows that minimum variations were observed in the combined height scenario, which provides a more consistent focal length and  $K_1$  value.

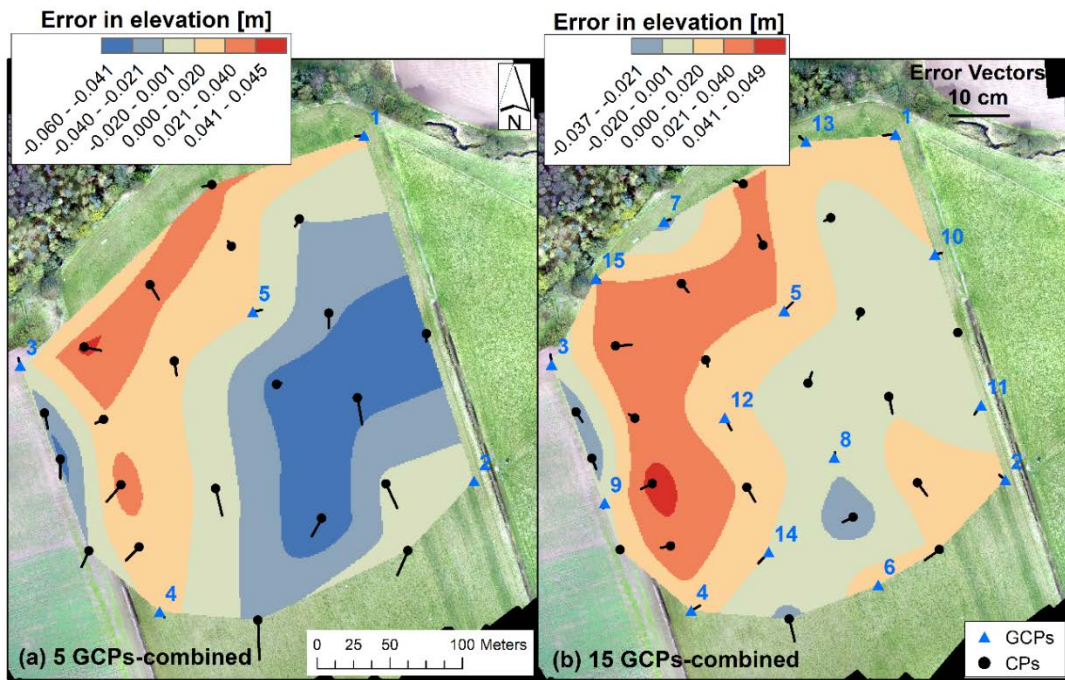


Figure 5.3: Planimetric error vectors and errors in elevation after interpolation at GCPs and CPs.

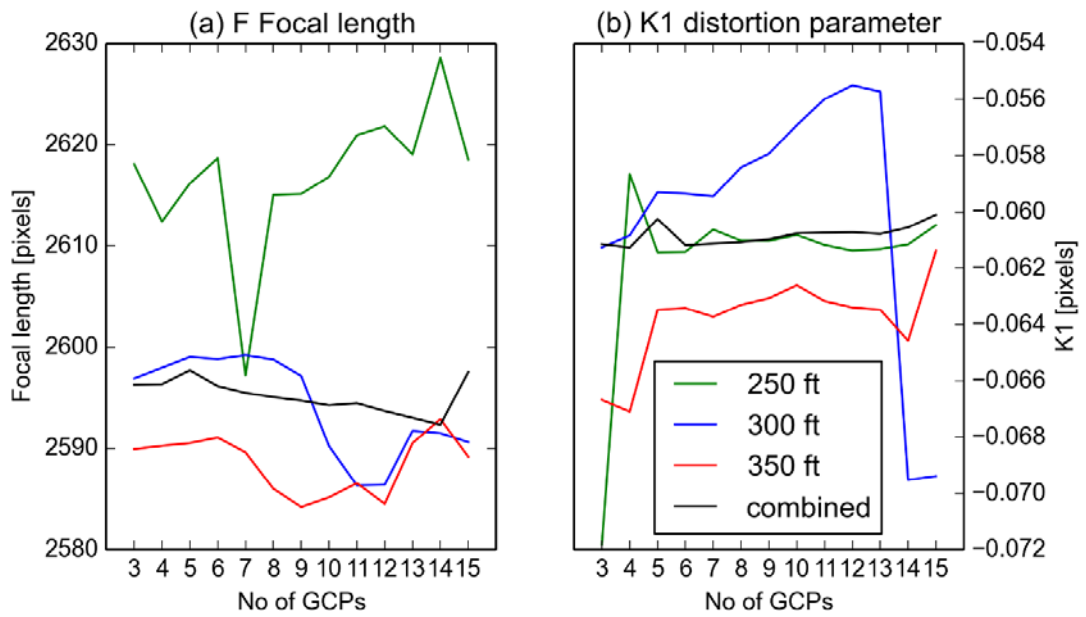


Figure 5.4: Values of (a) camera's focal length and (b)  $K_1$  lens distortion parameter estimated after the SfM-MVS self-calibrating bundle adjustment.

## 5.2 Morphology-based co-registration experiments at Sandford Industrial Park

### 5.2.1 UAV image acquisition and DPC pre-processing

Three UAV flights were performed on 30<sup>th</sup> November 2016 before and after artificial surface changes, as described in Section 4.2.1, with the following camera and flight plan settings:

A fixed shutter speed of 1/800; fixed aperture of f/2; ISO 100; 2 s exposure interval; 90 % forward and lateral overlap with 5 parallel flight lines of NW to SE direction; one additional NS crossing with two smooth turns; and a 120 m predefined flying height. The flight plan was designed taking into account the dominant west wind direction. The flight line separation was defined as 25 m. The flying height was set up to the maximum allowed flying height (400 ft) due to health and safety requirements.

Information about the number of images acquired and used, estimated GSD with average flying height and optical rays per tie point are listed in Table 5.2. Compared to the Cockle Park experiment (Table 5.1), the flight plan and camera settings ensured a higher image overlap, thereby providing higher redundancy with more optical rays per tie point. The pre-processing details, reported in Table 5.2, were derived after the sparse point reconstruction phase of the SfM-MVS pipeline (Section 3.2.5).

Table 5.2: UAV image acquisition over Sandford Industrial Park.

Epoch	No of Images	Estimated GSD[m]	Estimated average flying height [m]	Optical rays per tie point
E0	33	0.043	123	4.2
E1	39	0.043	124	5.2
E2	33	0.044	127	4.3

Prior to MBR implementation, an investigation was conducted to derive optimal disparity settings (page 47 in Section 3.2.5). This involved the DPCs reconstruction under mild, aggressive and moderate disparity over a relatively smooth terrain of a 4 m x 9 m extent, as depicted in red in Figure 5.5. This test used the “ultra-high” quality parameter to maintain the original image resolution during processing. Then, the three UAV DPCs were compared against TLS DPC of epoch E2. Observations from this epoch were chosen primarily because the E2 TLS data provided a denser point cloud expressing detailed surface characteristic unlike the other two epochs (Section 4.2.2 and Figure 4.5). To

achieve the comparison and reduce possible misalignments between UAV and TLS, five GCPs were incorporated into the georeferencing step, as indicated in Figure 5.6c.

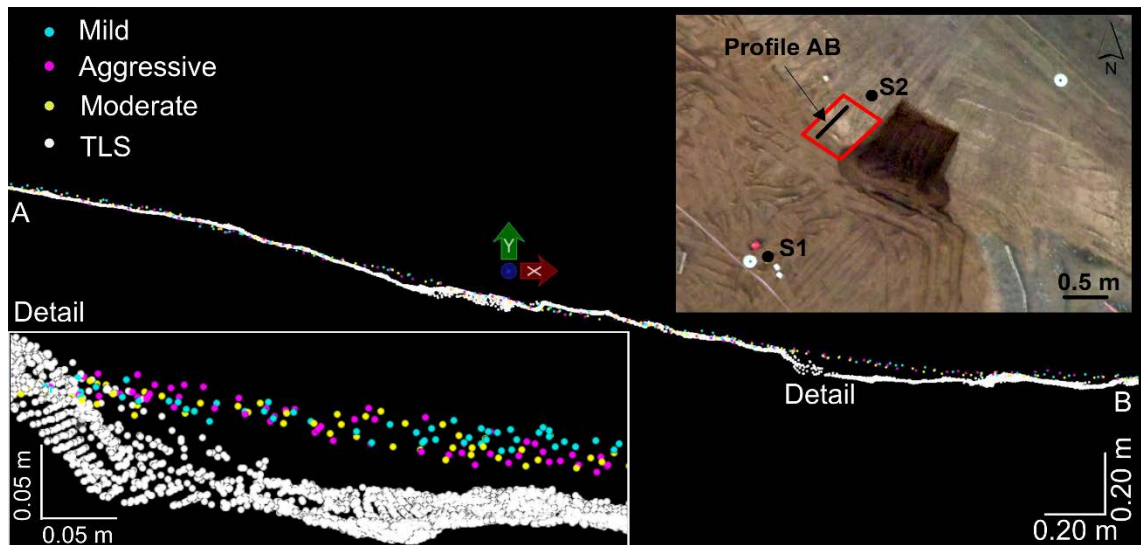


Figure 5.5: Profile of UAV and TLS-derived DPCs. Inset map locates profile AB within the study area.

Figure 5.5 clearly shows that UAV imagery could not capture high frequency surface irregularities regardless of the disparity settings used. As depicted in the detailed perspective view of a sub-region, the UAV DPCs smoothed the vertical depth of a maximum 0.05 m along an approximately 0.65 m length. This is an example along the profile AB, however these vertical irregularities, generated by the excavators, were close to the estimated 0.044 m GSD, as reported in Table 5.2. Because of the flattened result derived from UAV DPCs, this terrain can be considered relatively smooth compared to the failed surface right next to it. After conducting a similar comparison, Cook (2017) highlighted that UAV point clouds usually round off sharp surface edges. Possibly a better level of detail would have been achieved with lower flying height and a sensor with a larger number of pixels than those of the presented study.

Statistical results of the comparison performed with the M3C2 algorithm (Section 3.5.1) over the red rectangle area in Figure 5.5 are listed in Table 5.3. To examine the effect of the surface roughness in the M3C2 computation, two different scale settings were considered ( $D$  and  $d$  parameters, as described in Section 3.5.1). In the first case, both parameters were equal to  $3 \times \text{GSD}$  (i.e. 0.132 m) and in the second case both parameters were equal to 1.00 m (a value that lies within a recommended range, as per Section 3.5.1).

Table 5.3: Statistics of M3C2 comparison between UAV and TLS DPCs.

Disparity settings	M3C2 scale: 0.132 m					M3C2 scale: 1.000 m				
	$\mu$	$\sigma$	RMSE	Min.	Max.	$\mu$	$\sigma$	RMSE	Min.	Max.
Mild	0.017	0.026	0.031	-0.227	0.215	0.017	0.011	0.021	-0.009	0.056
Moderate	0.015	0.027	0.030	-0.224	0.273	0.016	0.013	0.020	-0.010	0.064
Aggressive	0.013	0.024	0.028	-0.123	0.128	0.011	0.009	0.014	-0.027	0.042

As seen in Table 5.3 for a smaller M3C2 scale, standard deviations and RMSEs are one larger than those computed with a 1.000 m scale. This is possibly because in the latter case more neighbouring points are considered into the distance computation and a lower weighting for high surface roughness is taken into account. However, insignificant discrepancies between different disparity settings were found as the mean distance values were similar at both M3C2 scales. In this analysis, the boxplots of the M3C2 comparison (Figure A.1 in Appendix A) showed that the aggressive mode provided outliers with the smallest M3C2 distances. This is also evidenced in Table 5.3 as the smallest standard deviations and RMSEs are obtained from the aggressive mode. For this reason, the aggressive mode was chosen during the DPC reconstruction in all following experiments described in this chapter and Chapter 6. Further investigations for the characteristics of SfM-MVS derived DPCs would be vital for a study with mm-level surface modelling (e.g. soil roughness in Milenković et al. (2016)), but this is outside of the scope of this study.

### 5.2.2 MBR-based implementation and analysis

For the GCP-based experiment, three DEMs of epochs E0, E1 and E2, were generated, utilising five GCPs (with indices 5, 6, 8, 9 and 12 in Figure 5.6c). These GCPs were deployed very close to the five theoretical GCPs, depicted in Figure 5.6c, creating an ideal rectangle. These theoretical GCPs were used to generate the five Thiessen polygons which supported the examination of pseudo GCP distribution throughout the MBR workflow. The E0 DEM was used as a reference for the MBR-GCP experiment with DEMs of epochs E1 and E2 being constructed with the aid of pseudo GCPs (Section 3.4.2). For the MBR-UAV experiment, no GCP-based reference DEM was utilised and the E1 DEM was co-registered relative to the E0 DEM derived from UAV coarse alignment (Figure 3.6 in Section 3.4.2). In all experiments, DPCs and DEMs with 0.044 m spatial resolution were constructed. The DPCs delivered an approximate point density of 600 points/m<sup>2</sup>, sufficient for the moving planes interpolation to create a continuous DEM, without pixel voids, using 15 nearest neighbouring points (Section 3.2.2 and 3.4.2).

“Off-ground” feature filtering was considered unnecessary as the vegetation was sparse and low, and the openness grid allowed for masking all manmade features (Figure 5.6d).

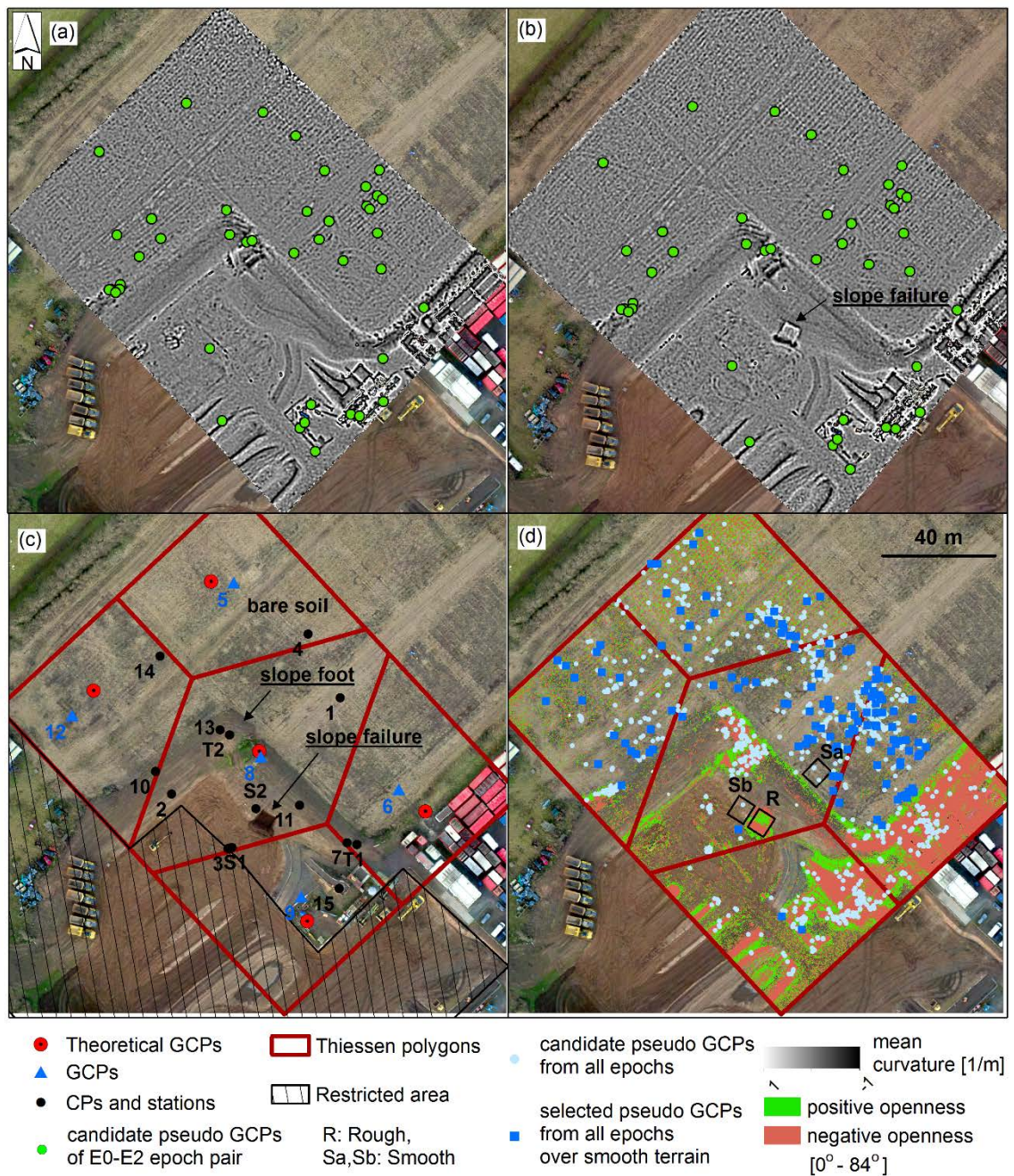


Figure 5.6: Mean *curvature* grids of (a) E0 and (b) E2 epochs with their corresponding candidate pseudo GCPs. (c) Distribution of GCPs and CPs, used for the GCP-based experiment. (d) Overview of *openness* grids together with the detected pseudo GCPs.

### ***Analysis of the MBR-GCP experiment***

In the MBR-GCP experiment (Stage 2 in Section 3.4.2), 1565 candidate pseudo GCPs (light blue circles in Figure 5.6d) were detected at locations of slope variations at the foot of the embankment, at the edges of storage units, roofs, fences, machines and over bare earth where the excavator's movement formed structures. For example, Figure 5.6a and b show the 51 candidate pseudo GCPs detected from the SIFT algorithm implemented with the mean *curvature* grids with kernel size 21 x 21 pixels for E0 and E2 epochs. The SIFT algorithm did not extract points over the slope failure, (Figure 5.6a, b and c) which was advantageous for automatic co-registration. It can be noted in Figure 5.6d that a considerable number of candidate pseudo GCPs were detected N-E of the site where the sparse short grass structured characteristic *curvature* variations. South of the site over the bare soil the SIFT algorithm did not detect many interest points, possibly due to the homogenous surface texture, a well-known error source in the SfM-MVS process (Section 3.2.4).

Positive and negative *openness* grids (Equations 3.25, 3.26 and 3.27) were computed from the E2 DEM within a 75 x 75 pixel radial distance, equivalent to 3.3 m for 0.044 m pixel resolution, adequate to capture the extent of the artificial failure. A threshold of 84°, which is the average *openness* value for this area, was selected to differentiate the smooth texture for relatively flat terrain from rougher texture over the steeper terrain. Regions with *openness* angles exceeding 84° were classified as smooth-stable terrain, otherwise regions were classified as rough-unstable terrain, as displayed in green and orange for positive and negative respectively in Figure 5.6d (see also Figure 5.9b). These were combined to create a single grid that represents the rough-unstable terrain mask. A simple smoothing process was performed to filter speckle noise from the mask, as described in Stage 2b in Section 3.4.2. It is noteworthy that the foot of the embankment, indicated in Figure 5.6c, was detected as unstable terrain because of the narrow positive *openness* angle (Figure 5.6d). An example of *openness* grid over the slope failure is shown in Figure 5.9a and b.

At this site, the slope foot was stable, however in reality, the steepest point of the slope could be prone to failure in a landslide environment. It is well-known that a variety of triggering factors can cause landsliding (Section 1.1.1, Lee (2004)). Under certain circumstances (e.g. intense rainfall event (Lee, 2004)) the strength of loose materials cannot resist the shear stress leading to slope failure. Typically, materials from the top of the slope are pushed down to the foot deforming the surface. Steep and low points of a slope as well as concave and convex features can change during a landslide event. In this

context, the *openness* grid could identify regions of potential hazard and aid in landslide mapping.

To verify the smooth and rough terrain extraction with *openness*, the EVR grid (Section 3.3.2 and 3.4.2) was computed from the E2 DEM. According to Favalli and Fornaciai (2017), the EVR grid is not correlated to *openness* grids, hence it can be used for an independent comparison. The histograms of EVR values over a smooth and a rough region are plotted in Figure 5.7. The two sample regions are selected based on the *openness* mask outcome with *Sa* indicating the smooth and *R* the rough region, as shown in Figure 5.6d. The histograms and the reported statistics in Figure 5.7 clearly illustrate the wider spread of EVR distribution over rough terrain compared to the distribution over smooth terrain. This provides confidence in the *openness* mask extraction based on McKean and Roering (2004) (Section 3.3.1).

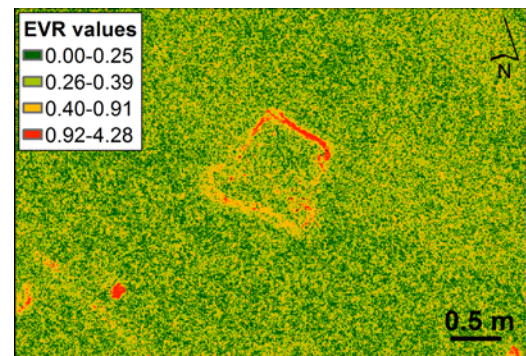
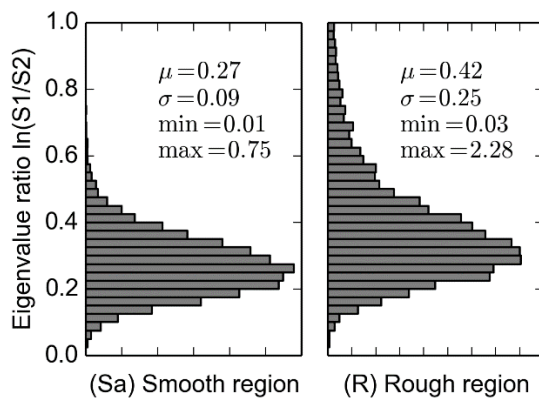


Figure 5.7: Histograms of EVR values for epoch E2. Figure 5.8: Example of EVR grid for epoch E2.

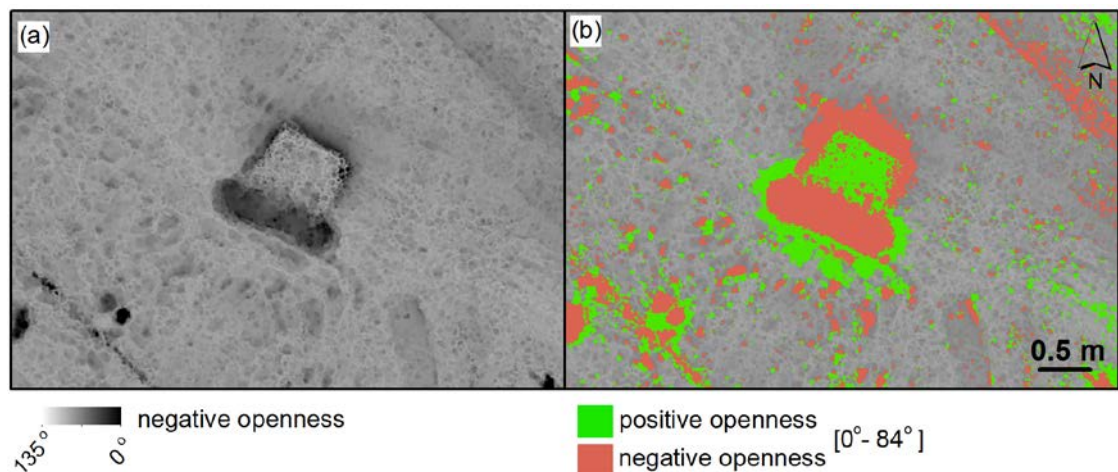


Figure 5.9: E2 *Openness* (a) before and (b) after applying a threshold of 84° over slope failure.

However, it was expected that the mean  $\mu$  value would be closer to 0 over the *Sa* region, indicating the flatness of the terrain. This shift from 0 is possibly caused by the fact that the short grass affected the surface roughness. The EVR values were also calculated for the *Sb* smooth region of bare soil (Figure 5.6d) and the histogram gave results similar to the *Sa* region. Figure 5.8 illustrates an example of EVR where high values depicted the sharp edges of the artificial slope failure. The noisy data in the surroundings of the failure can explain the sensitivity of EVR to surface irregularities due to grass height variations or the excavator's movements. In contrast to the smooth-rough mask derived from *openness* (Figure 5.9a and b), the EVR grid could only capture the boundaries of unstable terrain.

After stable-unstable terrain extraction, the step of pseudo GCP generation was finalised. From the 1565 candidates only 168 pseudo GCPs were extracted over smooth terrain (depicted as blue rectangles in Figure 5.6d), most generated from *curvature* grids of kernel sizes 9 x 9 to 23 x 23 pixels (Figure 5.10a). The use of many kernel sizes allowed the identification of numerous interest points with different *curvature* characteristics across the site. It is well-established in digital photogrammetry that for an automated image block triangulation, more than a handful of tie points (typically detected by an operator) can aid in the camera's EOP estimation (Schenk, 1997). In this context, the MBR workflow identifies candidate control points from a multi-scale *curvature* implementation offering higher redundancy.

Figure 5.10b presents the estimated errors of the 2D transformation for the selected pseudo GCPs within the MBR workflow (Equation 3.32). This indicates sub-pixel accuracy of the SIFT implementation when the RANSAC threshold was 0.9 pixels, resulting in a 0.021 m average error. Tests showed that choosing a lower RANSAC threshold, with the aim to reduce the average error, resulted in a considerably lower number of pseudo GCPs with a sparse distribution, particularly in the south of the area. For that reason, a RANSAC threshold of 0.9 pixels was considered adequate for the proposed MBR workflow.

As Figure 5.6d shows, sufficient pseudo GCPs were distributed within the Thiessen polygons from N-W to N-E, but only two were located at the south as many candidate points on the manmade features and surface variations were masked out. These variations over the restricted area (Figure 5.6c) were not deliberately imposed but created by the excavators and were classified as rough terrain within the generated *openness* mask.

The 3D coordinates of the 168 pseudo GCPs were imported into the *PhotoScan* project corresponding to the E1 DEM. Given the established coarse alignment from Stage 1 of the MBR workflow (Figure 3.6), the points were automatically located on each image of the UAV photogrammetric block. After assigning the errors shown in Figure 5.10b to control markers, the points were then reimported with their 3D coordinates from reference E0. By performing the bundle adjustment, the residuals of the pseudo GCPs were estimated and imported into the statistical test (Section 3.4.2). The same process was followed for epoch E2. The statistical test was iterated until the SEs (Equation 3.32) in Easting, Northing and Elevation were lower than 0.044 m, which corresponds to the estimated maximum GSD (Table 5.2).

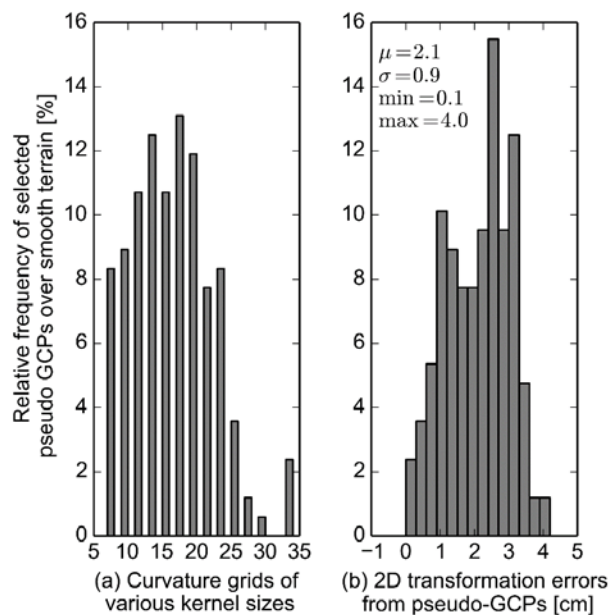


Figure 5.10: Histograms of pseudo GCPs with respect to (a) different *curvature* kernel sizes and (b) errors derived from the MBR workflow.

Vectors of the estimated errors were plotted to check for apparent systematic patterns. Their azimuths were also computed alongside the polar plots (Figure A.3 in Appendix A). In both epochs the error vectors were distributed within a narrow band of the azimuth spectrum before removal. This band defined the dominant orientation. For example, in epoch 1 the error vectors had a NE to SE orientation falling within the  $[30^\circ-60^\circ]$  and  $[210^\circ-240^\circ]$  band respectively. Thus, points with this dominant orientation and remaining error magnitude greater than 0.044 m were removed. The polar plots after removal show a better distributed spread across all orientations (Appendix A). Finally, the bundle adjustment was repeated using the selected pseudo GCPs after removal. The statistical values are summarised in Table 5.4.

The fact that the  $\mu$  values were not close to zero was indicative of systematic error. After the removal procedure, especially in E1, the  $\mu$  values were decreased by a factor of 0.5 and  $\sigma$  and RMSEs by a factor of 0.6 in plan. The statistical errors in elevation did not change significantly, indicating that the systematic errors were only present in the horizontal plane. After bias removal in both epochs, a normal distribution can be fitted to the histograms of the pseudo GCPs residuals, as expected (Figure A.2 in Appendix A). However, a systematic error was still observed, after removal for E2 (Figure 5.13), since the  $\mu$  value in Northing increased from 0.020 m to 0.070 m (Table 5.3). This is because of a low number of pseudo GCPs with relatively high error magnitudes, combined with a dominant systematic pattern, which could not be removed, as the second criterion to keep at least one point within each Thiessen polygon would not be fulfilled (Section 3.4.2). For example one pseudo GCP at the south, shown in Figure 5.13b and d, was not removed even though its error was relatively higher than the other pseudo GCPs and its orientation fell within the dominant NE direction.

Table 5.4: Statistics of the pseudo GCPs before and after the removal of points with error vectors showing systematic pattern (MBR-GCP experiment).

Epoch	Pseudo GCPs	Easting [m]			Northing [m]			Plan [m]			Elevation [m]		
Before removal													
		$\mu$	$\sigma$	SE	$\mu$	$\sigma$	SE	$\sigma$	SE	$\mu$	$\sigma$	SE	
E1	144	0.013	0.028	0.031	0.070	0.032	0.033	0.043	0.045	-0.000	0.029	0.027	
E2	152	0.009	0.034	0.035	0.020	0.043	0.044	0.055	0.056	-0.001	0.020	0.020	
After removal													
		$\mu$	$\sigma$	SE	$\mu$	$\sigma$	SE	$\sigma$	SE	$\mu$	$\sigma$	SE	
E1	94	0.006	0.019	0.020	0.000	0.021	0.021	0.028	0.029	0.002	0.030	0.030	
E2	102	0.050	0.021	0.022	0.070	0.020	0.028	0.035	0.036	-0.050	0.020	0.020	

### Analysis of the MBR-UAV experiment

The MBR workflow was repeated for all epochs in the MBR-UAV experiment and an example of the detected candidate pseudo GCPs with kernel size equal to 21 is shown in Figure 5.11. The black dots correspond to the points of reference E0 and the red dots to the corresponding points of subsequent epochs. The white lines connecting the corresponding points indicate the 2D translation and rotation of the reference epoch with respect to the subsequent epochs. For instance, Figure 5.11a shows that there is a NE to SW shift between E0 and E1 whereas Figure 5.11b illustrates a rotation between E0 and E2 (equal to  $4.5^\circ$  about Easting). The 2D translational, rotational and scale differences between the subsequent epochs are attributed to the coarse coordinate systems established by the UAV camera exposure stations. The SIFT implemented with multiple *curvature* kernel sizes allowed for the recovery of these differences and extracted 199 final pseudo GCPs over stable terrain for all epoch pairs combined with a 0.021 m average error.

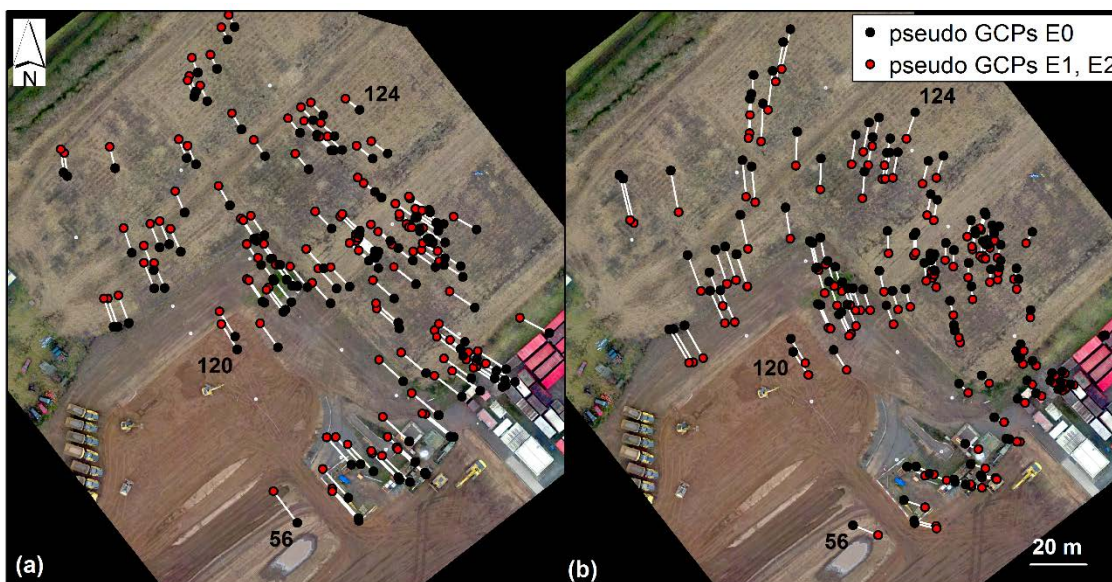


Figure 5.11: Candidate pseudo GCPs detected on (a) epoch E1 and (b) epoch E2.

The MBR workflow was successfully completed for epoch E1 and only three iterations of the statistical test (Section 3.4.2) were required so that the SEs in Easting, Northing and Elevation were lower than the GSD. However, for epoch E2 when the E0 coordinates of pseudo GCPs were reimported in *PhotoScan*, the bundle adjustment failed to transform the sparse point cloud from E2 relative to E0, delivering errors of m-level at pseudo GCPs. The E2 sparse point cloud had a completely different shape from the reference sparse point cloud due to the large rotational variations between the two epochs. This resulted in *PhotoScan*'s bundle adjustment converging to the wrong solution. Thus, only the MBR-UAV of E1 is assessed in this section.

The SEs of the 149 final pseudo GCPs in E1 are listed in Table 5.5. The SEs in Plan and Elevation (Table 5.5) were in the same order with the corresponding SEs in the MBR-GCP experiment of epoch E1, reported in Table 5.4. This gives confidence to the MBR-UAV results. Figure 5.12a depicts the planimetric error vectors and Figure 5.12b shows their directional distribution on a polar plot. This shows that no dominant systematic error was observed, as the direction of vectors spanned the whole polar spectrum, therefore no pseudo GCPs were removed.

Table 5.5: Statistics of the final pseudo GCPs for E1 (MBR-UAV experiment).

Epoch	Pseudo GCPs	Easting [m]			Northing [m]			Plan [m]			Elevation [m]		
		$\mu$	$\sigma$	SE	$\mu$	$\sigma$	SE	$\sigma$	SE	$\mu$	$\sigma$	SE	
E1	149	-0.050	0.037	0.037	-0.090	0.028	0.029	0.047	0.048	-0.030	0.031	0.031	

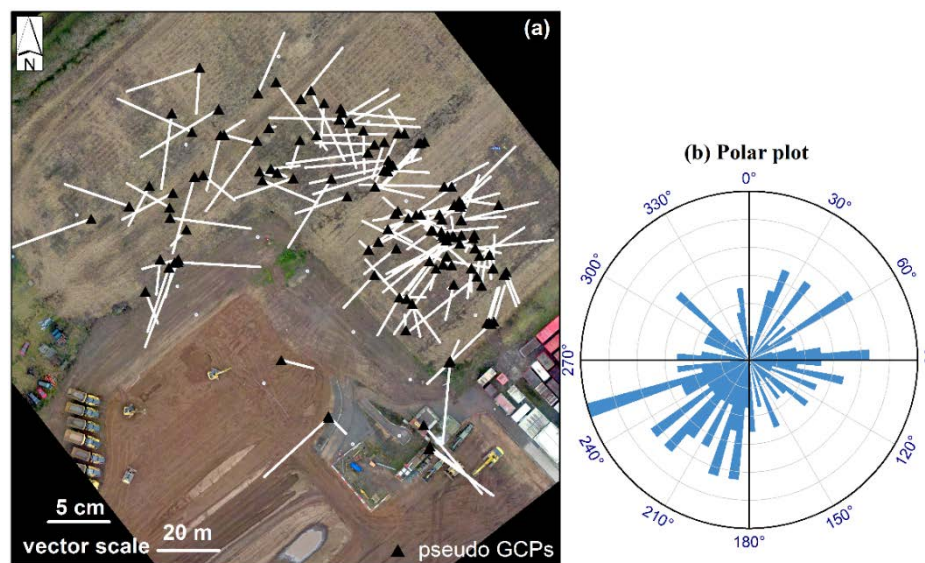


Figure 5.12: (a) Planimetric error vectors at pseudo GCPs of the MBR-UAV experiment with (b) their directional distribution

### 5.2.3 Assessment of co-registration solutions

#### *Solution of the MBR-GCP experiment*

To evaluate the MBR-GCP experiment, the results were compared against the GCP-based results as these provided solutions after the input of a minimum number of five GCPs. Figure 5.13 depicts the elevation differences,  $DEM_{\text{MBR}} - DEM_{\text{GCP}}$ , plotted at the level of  $1\sigma = 0.030$  m, the maximum  $\sigma$  in elevation of the pseudo GCP residuals (Table 5.4). The highest elevation differences, larger than  $-2\sigma$ , were observed around the manmade objects in both epochs. This shows that control points should only be extracted over bare ground features and not over hard edges. Firstly, hard edges in a landslide environment can represent regions prone to instability, as explained previously. Secondly, SfM-MVS derived DEMs smooth the sharp surface discontinuities (as mentioned in Section 5.2.1, Cook (2017)). Hence, the *openness* measure worked efficiently, as it masked out the points over regions with strong *curvature* variations.

For E1 the elevation differences showed a general linear slope where the MBR overestimated the elevations in NW and underestimated in SE (Figure 5.13a), compared to GCP-based outputs. This tilt remained after removal of the pseudo GCPs with systematic patterns, but with a slight change in direction (Figure 5.13c). In E2 the elevation differences were within  $\pm 2\sigma$ , lower than those of E1, creating a radial pattern with lower differences in the centre of the study area and higher towards its corners (Figure 5.13c). After removal of pseudo GCPs there was no significant change in the elevation differences of E2 (Figure 5.13d).

The planimetric residuals and error vectors at CPs are included in Figure 5.13. Figure 5.13a and b clearly show error vectors of pseudo GCPs with a systematic pattern in the NE direction and a relatively higher magnitude than the remainder. After their removal, the magnitude and direction of the vectors at CPs did not significantly change and a systematic pattern still remained, especially for E2 in Figure 5.13d. This is because a single pseudo GCP with the highest error in the south was not removed (Figure 5.13d), as this weakened the geometric pseudo GCPs configuration. Analysis after removing this only pseudo GCP showed that additional rotational errors were introduced in the north, thereby further increasing the vertical offsets observed in the elevation differences between GCP-based and MBR-GCP DEMs, at the periphery of the site. The error magnitudes at CPs after the removal of the dominant biases are described in Table 5.6 and compared against values from GCP-based results. The MBR workflow delivered an

average  $e_{geor}$  in plan (Table 5.6) for both epochs lower than the DEM spatial resolution (0.044 m).

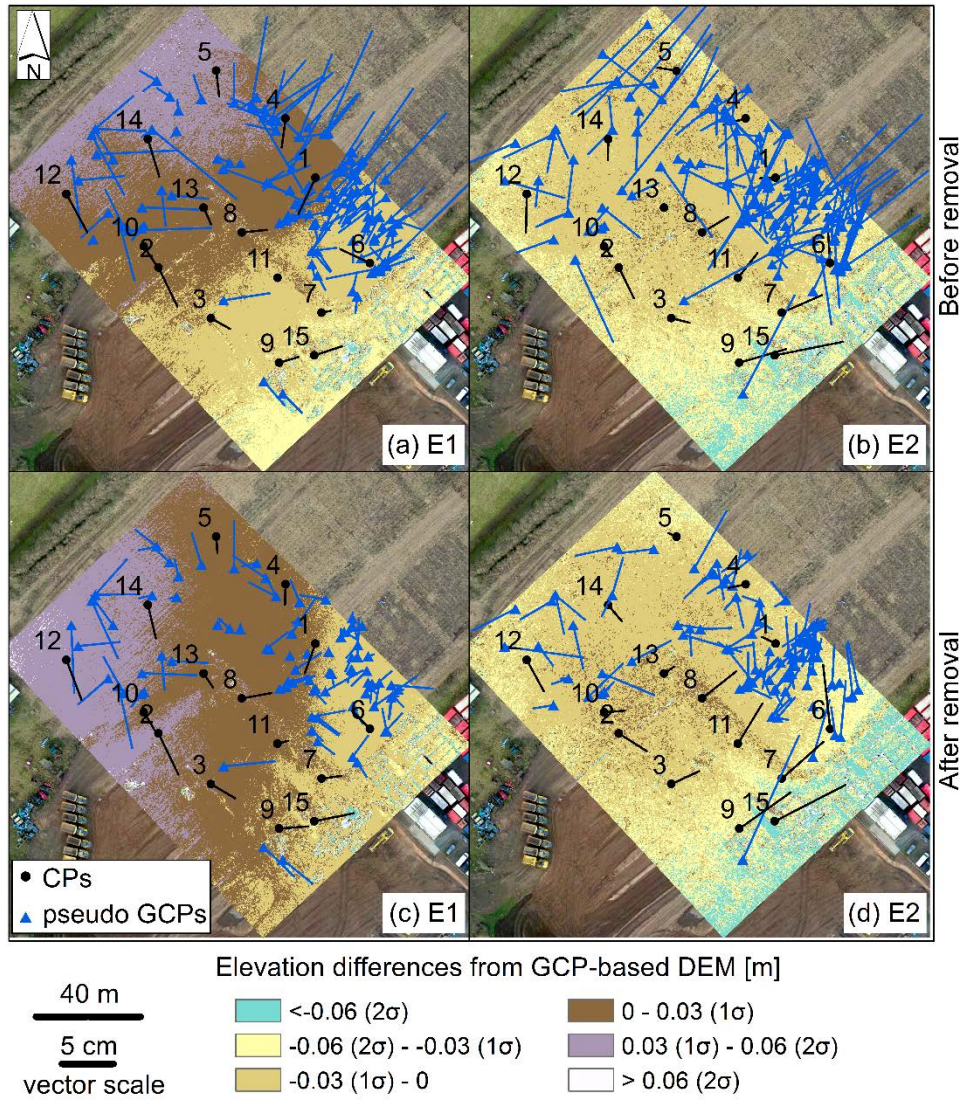


Figure 5.13: Elevation differences between GCP-based and MBR-GCP DEMs, before (a, b) and after (c, d) removal of pseudo points with systematic error.

Table 5.6: Statistics at CPs derived from the MBR-GCP and GCP-based experiment.

Epoch	$\sigma$ [m]		RMSEs [m]		
MBR-GCP based experiment (15 CPs)					
	Plan	Elevation	Plan	Elevation	3D Full magnitude ( $e_{geor}$ )
E1	0.024	0.019	0.029	0.019	0.035
E2	0.031	0.019	0.042	0.028	0.050
mean	0.030	0.019	0.036	0.024	0.043
GCP-based experiment (10 CPs)					
	Plan	Elevation	Plan	Elevation	3D Full magnitude ( $e_{geor}$ )
E0	0.013	0.023	0.018	0.024	0.030
E1	0.013	0.021	0.017	0.024	0.029
E2	0.017	0.013	0.020	0.012	0.024
mean	0.014	0.019	0.018	0.020	0.028

Table 5.7 summarises the M3C2 comparison between GCP-based and MBR-GCP derived DPCs against TLS. Also presented are the statistics of the co-registrations over stable terrain within the TLS coverage (Figure 4.3), undertaken with the global ICP algorithm. For the M3C2 comparison, the  $d$  and  $D$  scale parameters were equal to 1.000 m to give less weight to high surface roughness, as described in Section 5.2.1. In Table 5.7 the negative  $\mu$  values show that the DPCs were always below the “ground-truth” data (TLS or reference E0). The differences between the estimated RMSEs over all epochs were statistically insignificant given the DEM spatial resolution. The RMSEs of the MBR-GCP experiment were within the range of the 3D RMSEs, based on the CPs uncertainties of Table 5.6, which was not the case for the GCP-based results. For example, the mean RMSE after applying the ICP algorithm, as reported in Table 5.7, was approximately double the mean 3D RMSE of Table 5.6 (i.e.  $0.046 = 1.66 \times 0.028$  m). This is possibly attributed to the relatively small number and sub-optimal distribution of the ten CPs.

Table 5.7: Statistics of M3C2 comparison against TLS and after ICP per experiment.

Epoch	GCP-based experiment [m]			MBR-GCP based experiment [m]		
Similar epoch to epoch comparison against TLS DPC						
	$\mu$	$\sigma$	RMSE ( $e_{co-reg}$ )	$\mu$	$\sigma$	RMSE ( $e_{co-reg}$ )
E1	-0.023	0.039	0.045	-0.027	0.042	0.049
E2	0.002	0.043	0.043	-0.021	0.040	0.045
mean	-0.011	0.041	0.044	-0.024	0.041	0.047
After ICP over stable terrain						
	$\mu$	$\sigma$	RMSE ( $e_{co-reg}$ )	$\mu$	$\sigma$	RMSE ( $e_{co-reg}$ )
E1	-0.010	0.049	0.050	-0.024	0.039	0.046
E2	0.011	0.041	0.042	-0.027	0.030	0.040
mean	0.001	0.045	0.046	-0.026	0.035	0.043

### ***Solution of the MBR-UAV experiment***

In the MBR-UAV experiment, the E0 DEM was georeferenced to the UAV’s arbitrary coordinate system with a DG approach (Figure 3.6). Thus, error differences from “ground-truth” observations (i.e. CPs and TLS) were not evaluated. The co-registration error (i.e.  $e_{co-reg}$ ) was computed from M3C2 comparison after ICP over stable terrain. For M3C2 comparison, the  $D$  and  $d$  scale parameters were set equal to 1.000 m identical to the MBR-GCP experiment.

Table 5.8: Statistics of M3C2 comparison after ICP of the MBR-UAV experiment.

Epoch	$\mu$	$\sigma$	RMSE ( $e_{co-reg}$ )	min	max
E1	-0.032	0.048	0.058	-0.179	0.204

In this evaluation, the stable terrain consisted of the whole site (the outer red rectangle shown in Figure 5.6c and d) apart from the south section where slope failure was generated and excavators were moving. Vegetation and storage units were also masked out. Extreme values after M3C2 comparison were observed at the edges of the study area. It is noteworthy that discrepancies of the statistical values between MBR-GCP (Table 5.7) and MBR-UAV (Table 5.8) experiments were not statistically significant given the GSD.

### 5.3 Assessment of surface change estimations at Sandford Industrial Park

#### 5.3.1 3D sensitivity estimations

The two sensitivities  $s_1$  and  $s_2$  (Equations 3.37 and 3.38), utilising the  $e_{geor}$  (RMSEs at CPs in Table 5.6) and the  $e_{co-reg}$  (RMSEs of M3C2 comparison in Table 5.7) respectively, are listed in Table 5.9. For the MBR-UAV experiment, georeferencing error ( $e_{geor}$ ) was not included because errors at CPs were not computed. Thus,  $s_2$  indicates a relative sensitivity without the absolute uncertainty. For the other two experiments, the uncertainty of E0 was 0.030 m ( $e_{geor}$  in Table 5.6). All estimated sensitivities are comparable in magnitude, which is mostly for the MBR-UAV experiment. The maximum difference of GCP-based and MBR-GCP estimations was 0.040 m in E2 for  $s_1$ . This difference is lower than the 0.044 m DEM spatial resolution, therefore it is considered insignificant. The maximum value, rounded to 0.12 m, quantifies the lowest detectable 3D surface change in absolute units for the GCP-based and MBR-GCP solutions. The value of 0.12 m indicates the relative lowest detectable 3D surface change for the MBR-UAV solution.

Table 5.9: 3D Sensitivity estimations per experiment.

Epoch	GCP-based experiment [m]		MBR-GCP experiment [m]		MBR-UAV experiment [m]
	$s_1$	$s_2$	$s_1$	$s_2$	$s_2$
E1	0.082	0.114	0.090	0.107	0.113
E2	0.075	0.099	0.115	0.098	-

#### 5.3.2 Elevation and volume differences

To compare the three experiments and extract a relative change, elevation differences of epoch pair E1-E0 over the same region of interest were computed. As explained in the previous section, the MBR-UAV solution provided different absolute scale due to the different reference coordinate systems compared to the other two solutions. Hence, to

generate the region of interest a polygon was manually delineated by the centres of four targets with indices 5, 6, 9 and 12 (Figure 5.6c).

The centres were identified on the orthophotomosaics per each epoch of the MBR-UAV experiment. Statistical values after DEM differencing, with values exceeding the  $\pm 0.12$  m sensitivity level filtered out, are listed in Table 5.10.

Table 5.10: Statistics following DEM subtraction of the epoch pair E1-E0 per experiment.

Experiment	GCP-based	MBR-GCP	MBR-UAV
Total area of detectable change [m <sup>2</sup> ]	46.89	41.10	76.58
Percentage of total area with change [%]	0.70	0.61	0.91
Total volume of difference [m <sup>3</sup> ]	11.21 $\pm$ 5.63	10.26 $\pm$ 4.93	17.95 $\pm$ 9.19
Mean of elevation differences $\mu$ [m]	-0.04	0.01	-0.01
Standard deviation of elevation differences $\sigma$ [m]	0.27	0.28	0.27
RMSE of elevation differences [m]	0.27	0.28	0.27
Minimum of elevation differences [m]	-0.83	-0.74	-0.91
Maximum of elevation differences [m]	0.65	0.67	0.73

The discrepancies of estimated total areas and volumes with detectable change between the MBR-UAV solution and the other two solutions were caused by the different scale, as expected. The variations of the estimated percentage of the area of change with respect to the total region of interest did not exceed 0.3% between the experiments. In addition, the standard deviations and RMSEs of elevation differences fell within the same order of magnitude in all experiments. The maximum absolute difference of the estimated mean elevation differences was 0.03 m, which is lower than the DEM spatial resolution (i.e. 0.044 m in Table 5.2). These findings show that the SfM-MVS outputs were relatively consistent under the two co-registration scenarios, i.e. GCP-based and MBR-based.

To evaluate the absolute change, DEM differences of epoch pair E2-E0 were computed over the region of slope failure and cross-validated with respect to TLS derived differences. This epoch-pair was chosen because E0 TLS included a coverage of the slope failure with no voids and E2 TLS provided fine details of the surface edges scanned from two positions (Figure 4.5). To perform a valid comparison between TLS and UAV products, the occluded areas generated from E2 TLS observations needed to be excluded from the computations. To achieve this, a density raster was calculated from the E2 TLS point cloud with pixel size equal to UAV derived DEM spatial resolution. The sub-regions with less than three points in each pixel were extracted from the density raster

representing the occluded areas. For the elevation change computations in all experiments, the sensitivity level was also excluded.

Table 5.11: Statistics of elevation differences of epoch pair E2-E0 over area of slope failure.

Experiment	$\mu$ [m]	$\sigma$ [m]	RMSE [m]	Minimum [m]	Maximum [m]
TLS	0.10	0.58	0.58	-0.77	1.17
GCP-based	0.12	0.52	0.53	-0.74	1.02
MBR-GCP	0.09	0.52	0.53	-0.76	0.99

As evidenced in Table 5.11, the statistical values of elevation differences showed consistency, regardless of the absence/presence of GCPs in the derivation of subsequent DEMs. The MBR-GCP results varied within 1.4 x GSD (i.e. 0.062 m) with the exception of a relatively high difference observed at the maximum values (i.e. 0.180 m) when compared to TLS results.

Table 5.12: Area and volume of detected changes of epoch pair E2-E0.

Experiment	Area of change [m <sup>2</sup> ]		Volume change [m <sup>3</sup> ]		
	Cut	Fill	Cut	Fill	Net
TLS	21.82	27.35	-10.14 ± 2.62	15.26 ± 3.28	5.12 ± 4.20
GCP-based	19.98	27.48	-8.63 ± 2.40	14.20 ± 3.30	5.57 ± 4.08
MBR-GCP	21.22	26.09	-9.27 ± 2.55	13.52 ± 3.28	4.25 ± 4.04

Table 5.12 lists the changes in area and volume per experiment. Given the fact that TLS datasets constitute the “ground-truth”, the total area of detected change was estimated as 49 m<sup>2</sup>. SfM-MVS results from GCP-based and MBR-GCP experiments slightly underestimated the excavated area. TLS observations captured the subtle surface structures formed by the digging bucket, as shown in Figure 4.4b. These detailed surface characteristics cannot be modelled with the acquired UAV imagery after SfM-MVS processing, as illustrated in Figure 5.5. TLS estimated a cut of 39.92 % and a fill of 60.08 % of the total volume. SfM-MVS estimations of volume change fell within the range of ± 2 % in relation to TLS results.

Up to this point, analysis has compared the results from the three experiments over particular sub-regions. Figure 5.14a displays the DEM differences of the epoch-pair E2-E0 generated from the GCP-based and the MBR-GCP solutions over the whole region of interest. Positive and negative values indicate regions of fill and cut respectively. The lowest bound of the elevation differences are equal to the ± 0.12 m sensitivity level. Erroneous values were observed at the north corner of the region (indicated with (i)) and

over the manmade structures for both workflows. These errors were mostly at the edges of the region over stable terrain with a few exceptions over vegetation close to the middle of the region as indicated with (ii). It is not surprising that SfM-MVS outputs generated errors over sharp edges and vertical walls. Firstly, because no convergent imagery was included to capture the façades of the storage units. Secondly, it is known that SfM-MVS processing tends to smooth corners (Cook, 2017), as described in Section 3.2.4. Additional false elevation differences in the SE which belong to the band [-0.30:-0.12 m] (shown with (iii) in yellow in Figure 5.14b) were observed in the MBR-GCP results. These are possibly due to rotational errors, not entirely resolved by the SfM-MVS pipeline and propagated as deformations into the DEM, as described in Carbonneau and Dietrich (2016). Real change was observed in the SW, indicated with (iv) as part of the company's training. Excavators' movements were also captured in (v) which did not reflect real surface change.

In an attempt to understand the cause of the erroneous results generated by the MBR-GCP experiment, a similar test to James et al. (2017a) was conducted for E2 of the MBR-GCP experiment. Here, the self-calibrating bundle adjustment was repeated 13 times (using the same camera model with  $K_1$ - $K_3$ ,  $P_1$ - $P_2$  of Equations 3.1 and 3.2), using the 102 final pseudo GCPs of E2 (Table 5.4), and varying the marker accuracies within the range 0.01-0.06 m on each iteration. The 3D RMSEs at pseudo GCPs and 15 CPs were calculated separately with the corresponding boxplots depicted in Figure 5.15a and b. The median is displayed in red, the blue boxes indicate the 25<sup>th</sup> -75<sup>th</sup> percentiles, the whiskers locate the minimum and maximum after exclusion of outliers, with these outliers denoted by crosses.

The box plots for both pseudo GCPs and CPs show a generally consistent pattern without significant discrepancies. However, especially at the CPs in Figure 5.15b, the variation is skewed and significantly increases for marker accuracies in the range of 0.1-1.5 cm. Values of marker accuracy greater than 1.5 cm causes the 3D RMSEs to plateau. The test analysis also showed that the increase is most apparent in elevation. Compared to the distribution of 3D RMSEs at GCPs (Figure 5.15a) the distribution at CPs is wider (Figure 5.15b). In the GCP-based and MBR-GCP experiments the estimated SEs did not exceed the 0.044 m GSD (Figure 5.10b). Similarly, the median values of the boxplots in Figure 5.15b were lower than the GSD. James et al. (2017a) observed similar variations at vertical RMSEs at CPs, especially for marker accuracies within 0.01-0.10 m. These variations were considered as systematic errors of the vertical component that the SfM-

MVS pipeline could not resolve. As a result of the observed fluctuations, it is speculated that assigned uncertainties of the pseudo GCPs of values mixed within the 0.1-1.5 cm range possibly caused DEM deformations (indicated with (iii) in Figure 5.14b).

In SfM-MVS processing it is not expected to use GCPs with uncertainties higher than the estimated GSD. However, that could represent an extreme scenario; for example obtaining GCPs with a handheld GNSS receiver (Shahbazi et al., 2015). Under such a scenario the low uncertainties should not be incorporated as weights into the process and the GCPs should be utilised only to orientate and scale the SfM-MVS point clouds, as recommended by James et al. (2017a). However, in the presented experiments the uncertainties, being lower than the GSD, were incorporated into the SfM-MVS bundle adjustment as part of an automated workflow. In an attempt to entirely remove possible systematic errors, future recommendations of additional intensive post-processing checks within the workflow should be taken into consideration (Section 7.1.1).

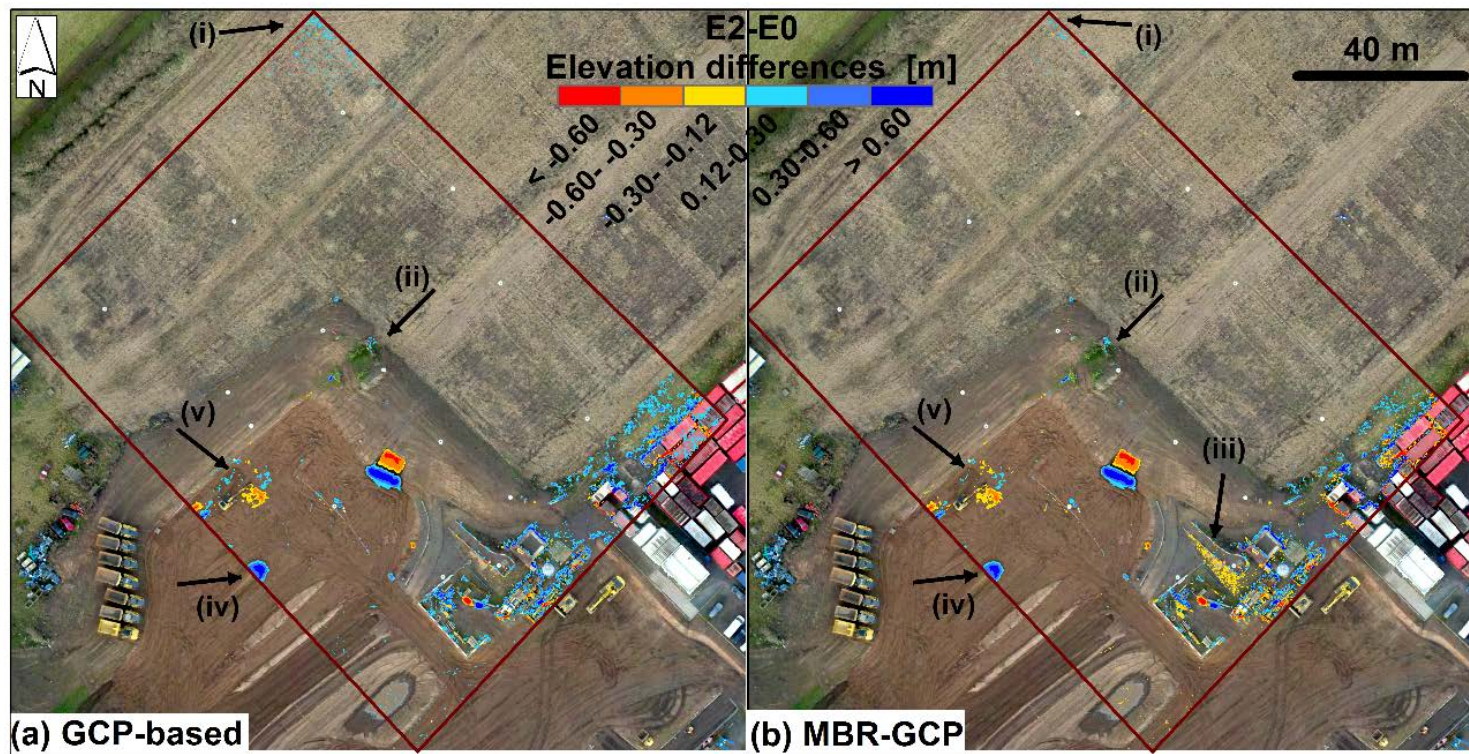


Figure 5.14: Elevation differences of E2-E0 epoch pair derived from (a) the GCP-based and (b) the MBR-GCP experiments.

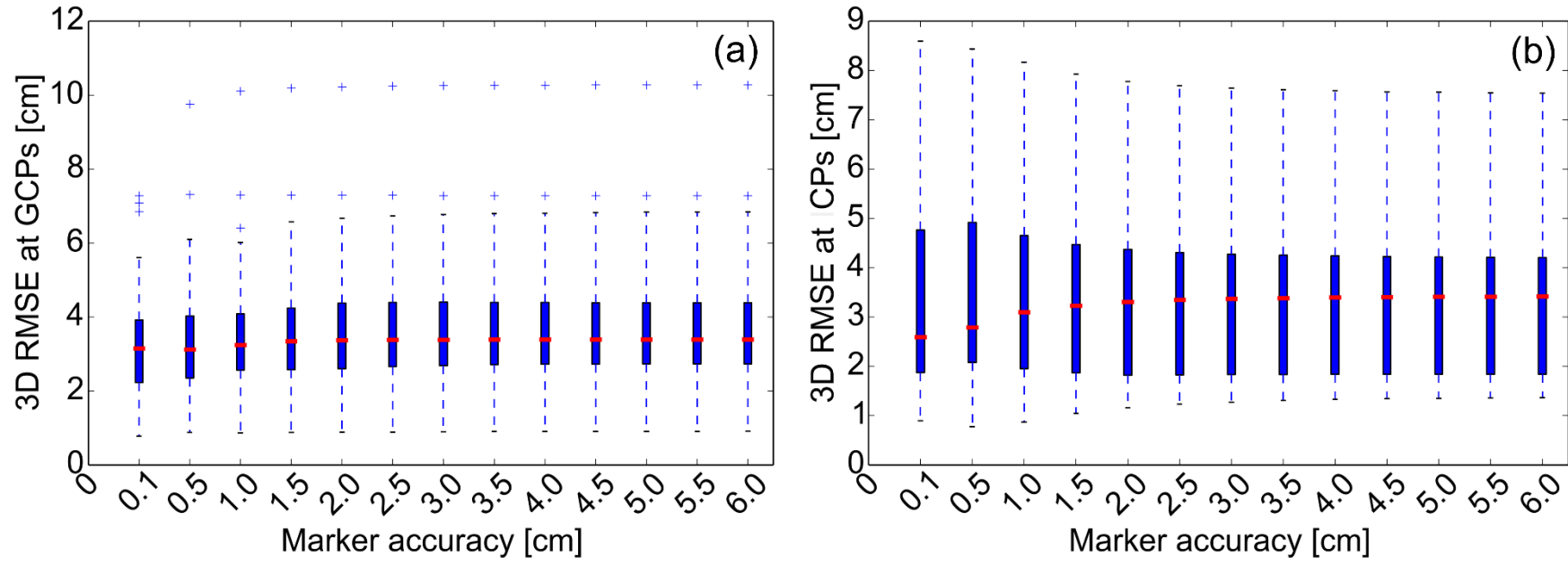


Figure 5.15: 3D RMSEs at (a) 102 pseudo GCPs and (b) 15 ICPs for E2 of MBR-GCP experiment.

## 5.4 Summary

The GCP-based experiment at Cockle Park firstly examined the capabilities of a Quest-300 fixed-wing UAV fitted with a Panasonic DMC-LX5 camera. This UAV system was capable of generating DPCs at approximately 0.04 m GSD. This experiment has also demonstrated the overall improvement of the SfM-MVS output georeferencing accuracy when images from various flying heights are included. With this imaging network configuration, a 3D RMSE at CPs of 2 x GSD was delivered, when three GCPs were incorporated into the SfM-MVS pipeline. Moreover, this analysis has shown that the presence of five GCPs can further improve the vertical accuracy to approximately 1 x GSD. In the context of landslide monitoring, five GCPs with a distribution depicted in Figure 5.3a, can provide a convenient establishment of control targets. Four GCPs can be set up at the outer extent of the area and a fifth in the middle close to the landslide. A similar GCP configuration was also suggested in Reshetyuk and Mårtensson (2016). This establishment could be considered as a trade-off between fieldwork time and optimal accuracy. The higher number of GCPs could increase the accuracy but could also increase the operational costs that constitute a critical aspect of periodical UAV surveys. This configuration is adopted in all GCP-based experiments included in this study (Chapters 5 and 6) providing the benchmark SfM-MVS results.

The experiment at Cockle Park also evaluated the performance of the SfM-MVS pipeline. Even with the incorporation of 15 GCPs into the SfM-MVS pipeline, bowl-shape deformations cannot be entirely removed. Sources of these deformations were discussed in Section 3.2.6. Further, inconsistent camera IOP solutions from SfM-MVS self-calibrating bundle adjustments have been demonstrated. This inconsistency can be minimised with the inclusion of images acquired from different UAV flying heights.

The experiments conducted at Sandford supported the development of the MBR workflow, which constitutes the first aspect of the morphology-based monitoring strategy (Section 3.1). The experiments also compared the estimated 3D sensitivities and elevation changes in the absence and presence of GCPs under a controlled environment. This involved an artificial slope failure surrounded by known stable areas. The experiments did not deal with planimetric movement estimations as only excavations were carried out. In such cases, the NCC function can be applied, as demonstrated in Chapter 6.

The analysis has demonstrated that the performance of the MBR workflow is relatively consistent in terms of the estimated 3D georeferencing accuracy and sensitivity when

compared to benchmark SfM-MVS approach including five GCPs. The two MBR experiments, a) with and b) without the presence of GCPs in the reference epoch yielded results of the same order of magnitude. Both experiments estimated a minimum detectable 3D surface change of  $2.7 \times \text{GSD}$ . The GSD in these experiments corresponded to the DEM spatial resolution. It was possible to quantify the volume of change with  $\pm 2\%$  difference from TLS-derived solutions. Given that TLS outperforms UAV measurements obtained from high flying heights, this comparison provided confidence in the MBR-derived outcome. The errors of the SfM-MVS pipeline were also addressed through the experimental analysis. Regardless of GCPs inclusion, false DEM differences were observed at the edges of the area, over vegetation and manmade objects. However, the MBR results indicated that unresolved rotations from the SfM-MVS pipeline were propagated into DEM differences, generating additional false DEM offsets. This error was possibly caused by the uncertainties of pseudo GCPs introduced into the SfM-MVS pipeline. The MBR workflow showed a sensitivity to high rotations between subsequent DEMs, in the absence of GCPs from the reference epoch. However, in conclusion, it can be summarised that the MBR workflow, with inclusion of a minimum number of five GCPs in the reference epoch, provides stable performance. The MBR-workflow can therefore potentially constitute a practical, low-cost means of repeat monitoring of hazardous terrain.

## Chapter 6.

### Real world assessment at Hollin Hill landslide

---

Chapter 5 demonstrated the capabilities of the Quest-300 UAV fitted with a Panasonic DMC-LX5, evaluated the SfM-MVS pipeline performance at Cockle Park and tested the MBR workflow (described in Section 3.4.2) at Sandford. This chapter implements the morphology-based monitoring strategy at Hollin Hill landslide examining all three aspects of the strategy (Section 3.1). Firstly, it describes the UAV imagery acquisitions across multiple epochs obtained with the Panasonic DMC-LX5 and the Sony A6000. Next, it presents the data preparation required for the MBR workflow. Co-registration solutions from both cameras are evaluated by means of comparison against GCP-based benchmark solutions that were derived from SfM-MVS processing with five GCPs (five was investigated in Chapter 5 to be the optimal low number of GCPs). After assessment of the co-registrations, the 3D sensitivity levels, constituting the second aspect of the morphology-based monitoring strategy (Section 3.1), are estimated from the various solutions. Inter-epoch elevation differences together with volume changes are computed indicating significant landslide deformations. 2D surface displacements are estimated with the implementation of the NCC function, as described in Section 3.5.3. The 3D surface change, as output of the morphology-based monitoring strategy, is cross-validated with benchmark observations obtained with GNSS, total station and TLS at each stage of the process. A discussion about the 3D landslide motion in relation to previous knowledge is also presented. Throughout this chapter, various tests are conducted to tune settings of the different software used and to examine possible error sources associated with the monitoring strategy. Part of the work presented in this chapter was demonstrated in Peppas et al. (2016) and Peppas et al. (2017).

## **6.1 Description of experiments, data acquisition and data cleaning**

### ***6.1.1 Experiment description***

Five experiments are analysed with different co-registration characteristics, as follows:

- 1) GCP-based Panasonic experiment: six DEMs from Panasonic imagery were co-registered utilising the SfM-MVS pipeline with the inclusion of five GCPs. Part of this experiment was presented in Peppas et al. (2016);
- 2) MBR-GCP based Panasonic experiment: six DEMs from Panasonic imagery were co-registered after applying the MBR workflow incorporating five GCPs only in the reference epoch;
- 3) GCP-based Sony experiment: two DEMs from Sony imagery were co-registered utilising the SfM-MVS pipeline with the inclusion of five GCPs;
- 4) MBR-GCP based Sony experiment: two DEMs from Sony imagery were co-registered after applying the MBR workflow incorporating five GCPs only in the reference epoch; and
- 5) MBR-UAV based Sony experiment: two DEMs from Sony imagery were co-registered after applying the MBR workflow without any ground control information.

### ***6.1.2 UAV imaging network configurations***

Seven field campaigns were carried out spanning a two-year period, as listed in Table 5.1. For the first three campaigns (05/14, 12/14 and 03/15), the Panasonic camera was set in shutter priority mode with a shutter speed of 1/800 s, at ISO 400 and varying aperture. An exposure interval of 2.5 seconds enabled image capture with a standard 60% forward and 40% lateral overlap. After gaining a better understanding of the UAV's operational capabilities under different wind conditions, the settings for the last four campaigns (16/15, 09/15, 02/16 and 05/16) were changed. In particular, the exposure interval was set to 2 seconds and the lateral overlap increased to 70% to enable better overlapping coverage. The Panasonic camera was set up with a fixed shutter speed of 1/800 s to decrease image blurring, ISO 100 to ensure that images were captured with low noise (Sieberth et al., 2014) and a fixed aperture of f/2 to ensure that sufficient light reached the sensor.

For the last two campaigns (02/16 and 05/16) additional flights were carried out using the Sony A6000 fitted in the new 3D printed case designed by the author (Section 4.4.1). The

Sony A6000 was set up with fixed aperture of f/4, fixed shutter speed of 1/1600, ISO 250 and 2 s exposure interval. Due to infra-red LED trigger connection (Section 4.4.2) a time delay was unavoidable. Thus, images acquired from three consecutive flights per campaign were processed to ensure a sufficient image overlap.

Table 6.1: Details of SfM-MVS processing of UAV imagery.

Campaign (day/month /year)	No of Images	No GCPs	No CPs	Estimated GSD[m]	Estimated average flying height [m]	Optical rays per tie point	Mean reprojection error [pixels]	Average point cloud density [points/m <sup>2</sup> ]
Panasonic DMC-LX5								
15/05/14	56	15	2	0.038	109	2.6	0.5	177
15/12/14	67	5	5	0.034	108	3.4	0.7	214
19/03/15	200	5	6	0.030	87	5.0	0.7	271
10/06/15	257	5	13	0.031	87	5.4	0.4	265
27/09/15	197	5	15	0.028	83	3.7	0.4	314
12/02/16	195	5	15	0.028	90	3.7	0.7	309
27/05/16	189	5	15	0.029	84	3.4	0.8	292
Sony A6000								
12/02/16	144	5	15	0.018	79	3.7	0.8	761
27/05/16	221	5	15	0.019	82	3.5	0.9	717

Because of the 50 m elevation difference the NS direction at Hollin Hill, the distance of the camera to the ground could not be kept fixed. In an attempt to compensate for this elevation change, the UAV’s flight plan was designed to gradually increase the UAV’s height as it climbed towards the top of the slope. This was planned for the first three campaigns. However, the fixed wing platform did not follow this flight plan as firstly it reached the desired height and then headed towards the predefined direction. That plan would work with a rotary platform, which allows for a steady climb. Therefore, for the remaining four campaigns the plan was configured differently. In particular, parallel flight lines of EW direction and cross lines of NS were designed with an approximately 60 m line separation and flying heights of 300 ft to 350 ft. Combined flying heights were chosen as they improved the SfM-MVS georeferencing accuracy in the Cockle Park experiment (Section 5.2.2). Further, flight lines in opposing directions were added, according to the recommendations of James and Robson (2014), in order to achieve a better flight configuration and to minimise systematic errors (Section 3.2.6). These plans were adopted for both cameras.

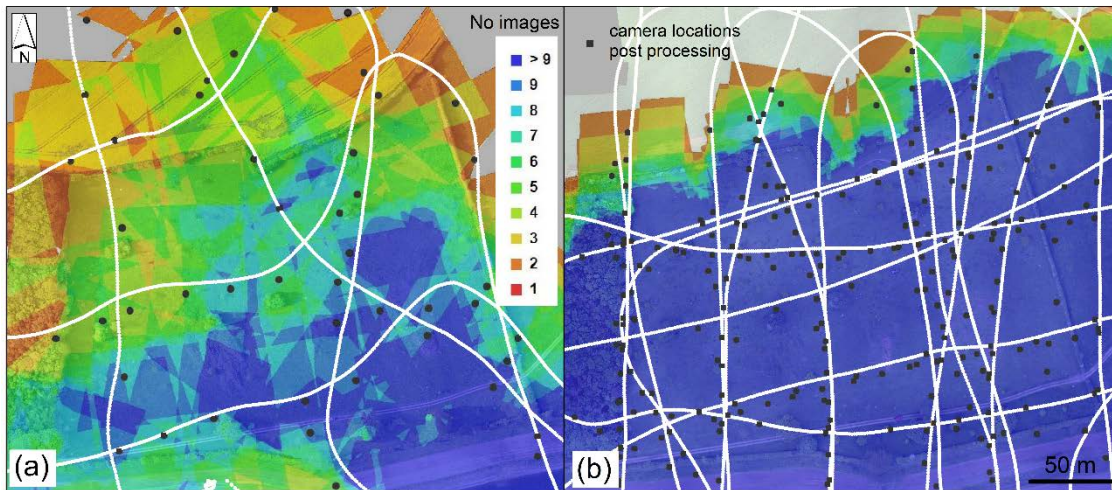


Figure 6.1: Image overlap and post flight trajectories for (a) 05/14 and (b) 05/16 campaigns.

Figure 6.1a and b illustrate the imaging network configuration of the first and last campaigns respectively. Less than four images covered the upper part of the slope in Figure 6.1a, resulting in a significantly lower number of optical rays per tie point compared to all other campaigns (Table 5.1). The lower point density for the first two campaigns (05/14 and 12/14) are also noticeable in Table 5.1. As is shown in Figure 6.1b, alterations in the flight settings strengthened the imaging network, increasing the number of images considerably. However, it should be noted that on 03/15 a relatively high number of optical rays per point was computed because of the inclusion of some oblique images. In particular, 57 out of 200 images exceeded the  $\pm 10^\circ$  roll angle. A test investigated the inclusion or exclusion of these images and showed that, after excluding those, the average SE (Equation 3.32) in elevation at GCPs was 10 times higher than the SE computed after including those images. The exclusion of these images decreased the redundancy in point determination and adversely affected the SEs. Thus, the images were included in all following experiments.

It should be noted that UAV imagery is stored in RAW format which does not apply any enhancement to the digital numbers (Verhoeven, 2010). However, *PhotoScan*, as well as other SfM-MVS software, are not able to read RAW format. For that reason, the original images were converted into tiff by applying an RGB transformation in the Panasonic and Sony dedicated software. This transformation did not include additional image enhancement processing. As a result, no brightness or contrast transformation was applied to underexposed and overexposed images (e.g. Figure B.4 in Appendix B).

### 6.1.3 DPC pre-processing and vegetation filtering

#### DPC pre-processing

An investigation to define the optimal disparity settings for DPC reconstruction was undertaken at Sandford (Section 5.2.1). This showed that the aggressive mode delivered the best results. However, this test was undertaken over bare soil. Therefore, it was repeated at Hollin Hill to investigate the choice of disparity settings over vegetated terrain. Thus, post processing in *PhotoScan* for three different disparity settings (mild, moderate and aggressive, Section 3.2.5) was carried out over a subarea, as seen in Figure 6.2 with images acquired on 09/15. A section through a reconstructed DPC located across a shrub with height lower than 0.50 m is illustrated in Figure 6.2. The aggressive option was finally adopted because it was seen to remove points from such low vegetated areas (Peppia et al., 2016).

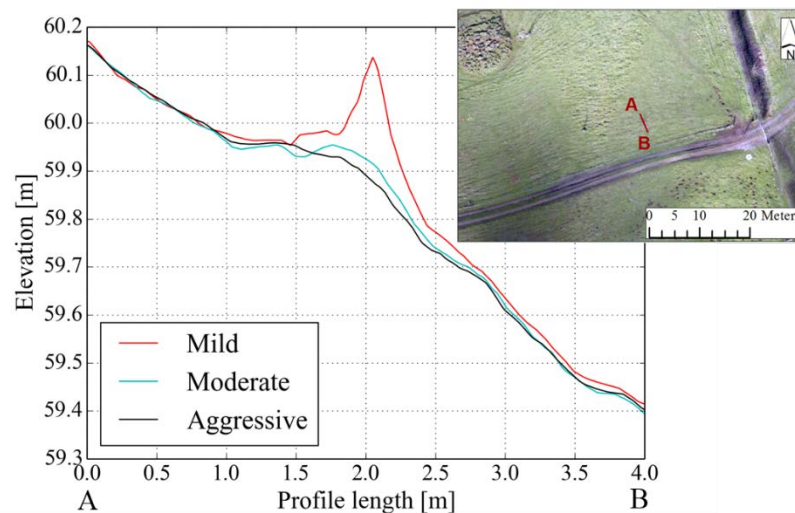


Figure 6.2: Profile of a DPC reconstructed with three disparity options (Peppia et al., 2016).

An additional test was carried out to investigate the optimal choice of image pyramid level (Section 3.2.5). In this test 33 images of 12/14 campaign over a 0.061 km<sup>2</sup> subarea, were processed with aggressive filtering and three image pyramid level options, namely a) “Ultra-high”, b) “High” and c) “Medium”. Option (a) produced a 0.03 m DEM spatial resolution, equal to the achievable GSD (Table 5.1) and density of 1010 points/m<sup>2</sup>, with 7.3 hrs of computation time. After 1 hr, option (b) reduced the spatial resolution 0.06 m with density of 253 point/m<sup>2</sup>. Option (c) further decreased the original resolution by 4 resulting in 63.3 points/m<sup>2</sup> density after 7 min of processing. Hence, aggressive with “High” image pyramid level were selected for all campaigns and experiments as a trade-off between computational time and spatial resolution.

Other *PhotoScan* parameters were set as follows: camera position's accuracy=10 m, 3D marker accuracy for GCPs and CPs=0.010 m, tie point accuracy=1.0 pixel and projection accuracy=0.1 pixels. The estimated post processing values for GSD and point densities are listed in Table 6.1. For the GCP-based and MBR-based Panasonic experiments, seven DEMs with 0.06 m spatial resolution were generated. For the GCP-based and MBR-based Sony experiments, two DEMs with 0.04 m spatial resolution were generated. In all experiments, the DEM spatial resolution was double the average GSD. Due to larger sensor size, Sony imagery delivered higher spatial resolution as expected (Section 4.4.2).

### ***Vegetation filtering***

Vegetation filtering was conducted in *PhotoScan* as described in Section 3.2.5. Together with DEMs, DEM standard deviation grids (Equation 3.6) were constructed for all campaigns in *OPALS*<sup>27</sup>. Even after *PhotoScan*'s vegetation filtering, "off-ground" points remained, mainly around the densely vegetated regions. Thus, a test was undertaken to derive which values of the DEM standard deviation grid represent those regions. The test showed that DEM standard deviation values greater than 0.01 m mostly indicated the remaining vegetation, as evidenced in Figure 6.3. Applying this threshold, the DEM standard deviation grids were classified into two categories representing regions with standard deviation a) from 0 m to 0.01 m and b) greater than 0.01 m. The regions of (b) category were converted into polygons and used to remove the erroneously classified features from the DEM.

Figure 6.3a shows an example of vegetated areas, detected at the upper part of the site for 05/16 datasets. Points in red (Figure 6.3b) were erroneously classified as bare ground in *PhotoScan* and then masked out with the DEM standard deviation threshold higher than 0.01 m. Figure 6.3a also maps other objects detected such as fences, photovoltaic panels and sheep. Even though the DEM standard deviation aided in cleaning spurious classification results from *PhotoScan*, it created few errors over the landslide scarp west of the site (Figure 6.3a). These subareas were identified with the aid of the orthophotomosaic and excluded from cleaning. The pre-processing filtering step was repeated for all campaigns and experiments.

---

<sup>27</sup> [www.geo.tuwien.ac.at/opals/html/index.html](http://www.geo.tuwien.ac.at/opals/html/index.html)

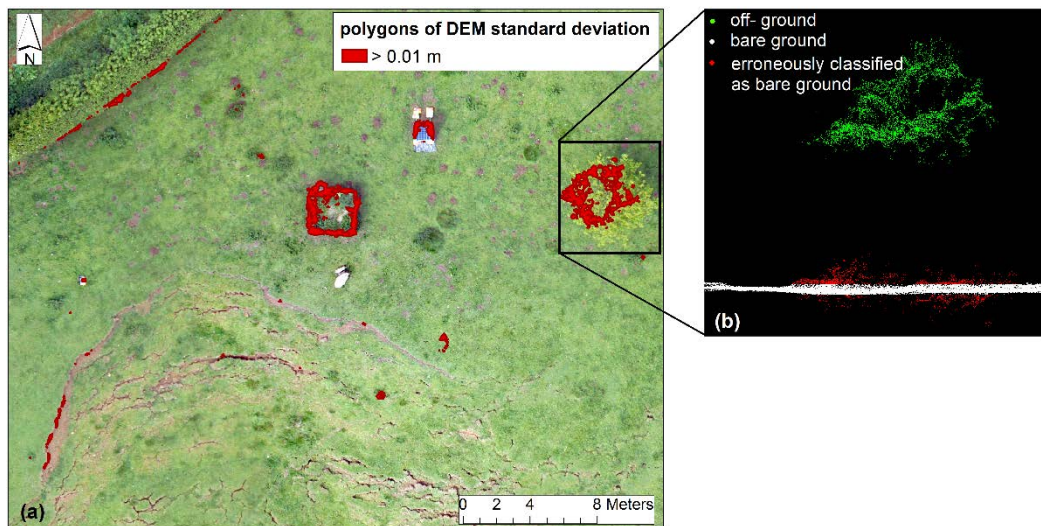


Figure 6.3: (a) Polygons of DEM standard deviation for masking out (b) erroneously classified vegetated regions.

Apart from cleaning, the DEM standard deviation grid also indicated DEM quality. For example, it revealed linear artefacts in the 05/14 dataset. These artefacts originated from sharp discontinuities that occurred in the point cloud due to mismatches caused by low image overlap (Figure 6.1a), as discussed in Section 3.2.6. Harwin et al. (2015) explained that it is difficult to remove such discontinuities especially in a grassy terrain, such as Hollin Hill. This is because a photogrammetric approach records the vegetation surface and is unable to capture the underlying terrain, compared to ALS for example. DEM standard deviation grids for 05/14, 12/14, 02/16 and 05/16 datasets are shown in Figure B.1 in Appendix B. It is noteworthy that the linear artefacts in the DEM standard deviation grid for 05/14 were correlated with the linear edges of overlapping images depicted in Figure 6.1a. It can be deduced that all imaging network configurations, with the exception of the first campaign, generated standard deviations with low noise and without linear artefacts. Due to artefacts, the 05/14 dataset was excluded from the experiments in the following sections.

## 6.2 Co-registration solutions

### 6.2.1 MBR-based implementation and analysis

According to the MBR workflow described in Section 3.4.2, pseudo GCPs were firstly generated with combined SIFT and mean *curvature* grids. The mean *curvature* for each epoch was computed within the range of 5x5 to 35x35. For low kernel sizes the *curvature* grid illustrates fine surface details, whereas, as the kernel increases, the *curvature* becomes smoother. For epoch pairs with 5x5 kernel size SIFT detected only 4 points corresponding to an unreliable solution. This is attributed to the fact that the high

frequency of the *curvature* variations within a 0.30 m spatial extent (kernel size x spatial resolution) did not allow for extraction of characteristic features. For that reason, *curvature* grids of 5x5 kernel size were eliminated from the MBR workflow.

In a similar manner to the experiments in Sandford (Section 5.2) a RANSAC threshold of 0.9 pixels was used, corresponding to the average standard error post transformation (step 9 of Stage 2 in Section 3.4.2). For a RANSAC threshold of 0.5 pixels a considerably lower number of candidate points were identified. For example, in the epoch pair E04 (12/14-02/16) of the Panasonic experiment, almost 50% fewer points were detected with 0.5 RANSAC compared to the number of points detected with 0.9 RANSAC. It was expected that within an eighteen-month duration (15/12/14-27/05/16) surface *curvature* would change due to landslide activity, hence with a strict 0.5 pixels threshold fewer points were identified. Therefore, RANSAC equal to 0.9 pixels was adopted, as it generates a sufficient number of candidate pseudo GCPs even within a long period which can aid in eliminating possible systematic errors in the later stages of the MBR workflow.

For all experiments described in this chapter, processing was performed only over the region surrounded by hedgerows, as adjacent fields were subjected to environmental change (e.g. crop growth) that would adversely affect identification of stable/unstable terrain. Figure 6.4a displays an example of negative *openness* generated from the GCP-based Panasonic experiment derived from the E2 and E4 DEMs within a spatial extent of 4.5 m. This extent allowed for capturing landslide fissures and surface openings. The smooth texture of the “stable” terrain around the landslide fissures was represented by wide *openness* angles, whereas the rough texture of landslide patterns corresponded to narrower *openness* angles. Positive *openness* for the E2 and E4 epochs are depicted in Figure 6.4c and Figure 6.4d respectively. As described in Section 3.3.2, positive and negative *openness* illustrate complementary surface characteristics. By combining these together, as in case of the Sandford experiments (Section 5.2), both concave and convex features that were present within the landslide bodies were captured. The focal statistics tool (Stage 2b in Section 3.4.2) was applied until small polygons were removed from the main landslide bodies and the final mask was smooth and continuous, as shown in red and blue polygons in Figure 6.4a. Because of this smoothing, the track in the south of the site (Figure 4.6a), with a 3.7 m width lower than the 4.5 m *openness* spatial extent, was excluded from the smooth terrain (Figure 6.4).

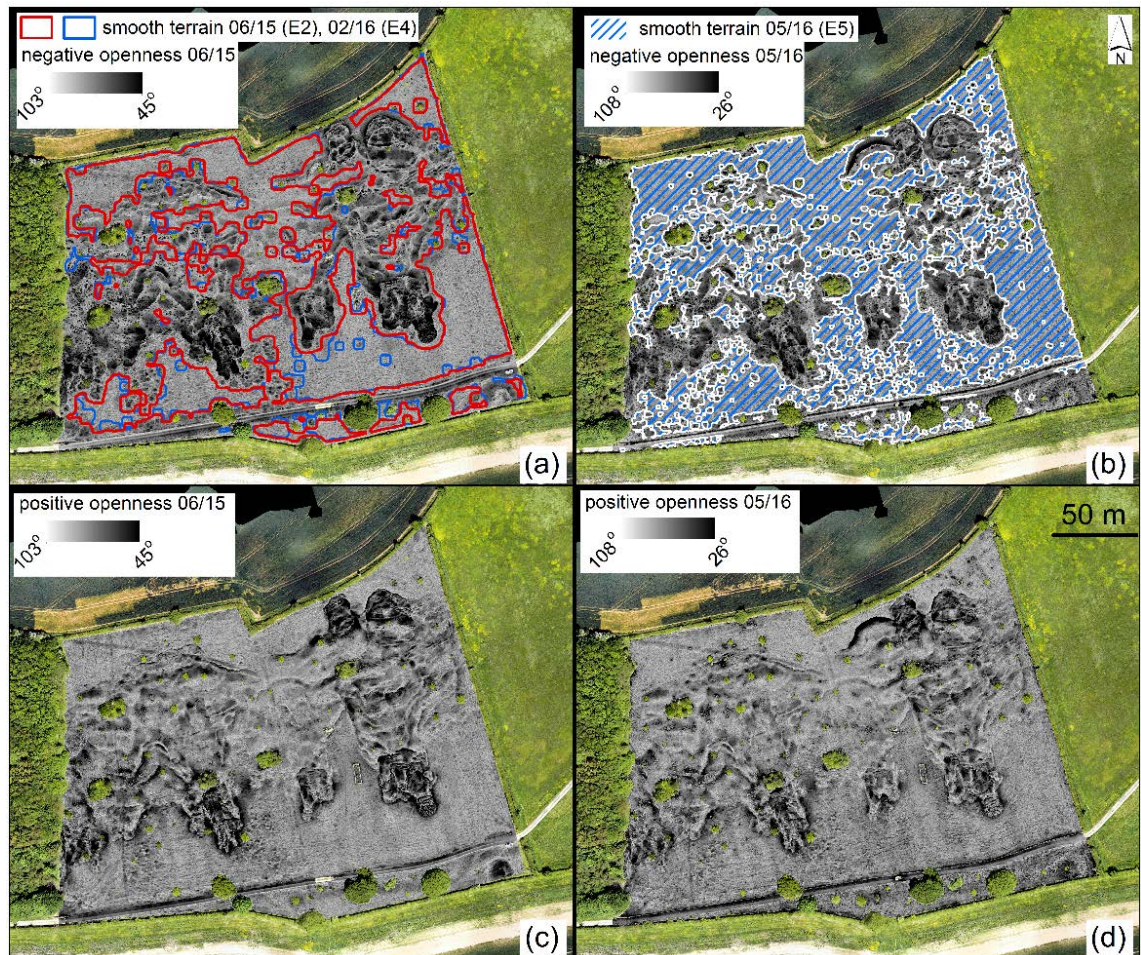


Figure 6.4: *Openness* grids for stable terrain extraction from the GCP-based Panasonic experiment.

Moreover, it is evidenced in Figure 6.4a and b that parts of the flat plateau in the middle of the site (Section 4.3.1) were characterised as stable terrain due to the wide *openness* angles derived over that region (Figure 6.4a and b). For E3 and E5, the presence of longer grass, caused high surface roughness around the lobes at the foot of the slope and affected the smoothness of the mask (E5 in Figure 6.4b).

The *openness* grids generated from the DEMs of the MBR-based experiments were identical to those of the GCP-based experiments, extracting the same stable terrain. However, these grids were shifted and orientated with respect to the coordinate system of the coarse alignment defined in each epoch (Stage 1 of the MBR workflow in Section 3.4.2). This was not an issue because the coordinates of the candidate pseudo GCPs were shifted and orientated accordingly, as derived from the 2D transformation implemented within SIFT.

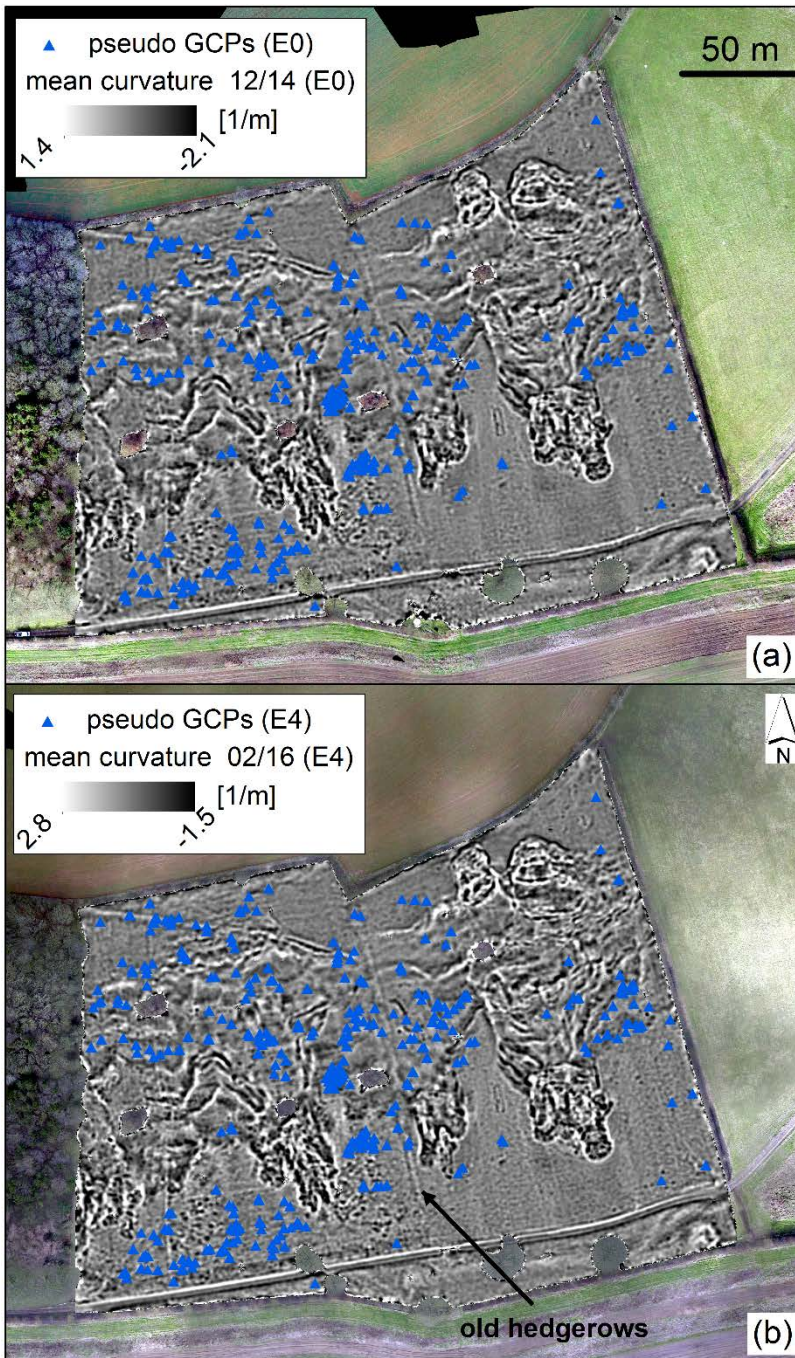


Figure 6.5: Mean *curvature* grids of (a) E0 and (b) E4 epochs with their corresponding pseudo GCPs over stable terrain.

Figure 6.5a and b present two examples of mean *curvature* grids derived with kernel size of 25x25 for epoch E0 and E4 respectively. Within this period, different maximum and minimum *curvature* values were observed over failing parts of the landslide. These extreme values of the *curvature* indicate features with steep slopes unsuitable for pseudo GCPs. Over the smooth terrain, extracted by *openness*, the mean *curvature* was unchanged. The final pseudo GCPs selected for epoch pair E0-E4 generated from the MBR workflow are superimposed over the grids corresponding to each epoch (Figure 6.5a and b). The locations of these points represent features outside of the main landslide

bodies, but with distinctive surface characteristics over the smooth terrain. For example, ridges on the surface in the NS direction were structured from old hedgerows that were removed before the UAV acquisitions by the land owner (Figure 6.5). Many pseudo GCPs were generated over these structures, providing a valid solution as the structures were considered stable and not caused by landslide deformation.



Figure 6.6: Key-points as derived from the SIFT implementation with (a) E0 and (b) E4 orthophotomosaics using exactly the same settings described in Section 3.4.2.

To demonstrate the superiority of using *curvature* grids with the SIFT algorithm instead of optical images, an additional test was conducted for the E0-E4 epoch pair with results shown in Figure 6.6. The RGB E0 and E4 orthophotomosaics, as generated from the GCP-

based Panasonic experiment, were firstly converted into grayscale and then implemented with the SIFT algorithm using identical settings to the MBR workflow (Stage 2a in Section 3.4.2). As evidenced in Figure 6.6 this implementation failed to detect correct key-points with the exception of one and only key-point 2. This result contrasts with the numerous key-features detected with the MBR workflow of the same epoch pair, as shown in Figure 6.5. The poor result derived from the SIFT implementation with the orthophotomosaics was caused by illumination and vegetation variations (Kehl et al., 2017), well-known error sources that adversely affect the quality of image matching algorithms (Section 3.2.6). Overall, this test justifies the use of morphological surface attributes (e.g. *curvature*) for the detection of candidate pseudo GCPs with the SIFT algorithm, as implemented in the OpenCV python library (python script in Appendix A).

Following the analysis of the SIFT implementation with *curvature* grids, it is noteworthy that *curvature* kernel sizes lower than 11x11 did not contribute to the MBR solution as no points from any epoch pair of that kernel size, were finally selected over stable terrain. This contrasts with the Sandford experiments (Figure 5.9). For example, in epoch E3 approximately 60% of the pseudo GCPs were generated from *curvature* kernel sizes of 33, 29, 19, 13, 11 and 35. In epoch E5 the smallest kernel size of 11x11 contributed only 3% of the pseudo GCP generation. Hence, the use of multiple kernel sizes provided additional redundancy increasing the number of pseudo GCPs. An average 0.03 m SE (Equation 3.32) was computed from all pseudo GCPs. A normal distribution could be fit to the histogram of the pseudo GCP residuals.

Prior to the final selection of pseudo GCPs, manual inspection of systematic patterns was performed for all epochs and experiments. An example of using polar plots for 09/15 campaign is illustrated in Figure B.2 in Appendix B. The selected pseudo GCPs, showed an error in the NW direction with azimuth ranging between 280°-315°. The majority of the pseudo GCPs were gathered within this narrow band. Points with error magnitudes greater than the DEM spatial resolution (i.e. 0.06 m) were identified and removed in ArcGIS, according to the first stopping criterion in Stage 2C (described in Section 3.4.2). Whilst the directional error was not entirely removed, as evidenced in Figure B.2 in Appendix B, it was slightly better distributed across the quarters of the polar spectrum. The pseudo GCPs for all other epochs showed a good directional distribution; therefore no removal was required. As numerous points were detected, there was an absence of dominant systematic directional pattern within any particular quarter of the polar plot (polar plots of E5 results are shown in Figure B.3 in Appendix B). For the MBR-based

Sony experiments, even though comparably fewer points were extracted over stable terrain for E5 (Table 6.3) than for the corresponding Panasonic experiment (Table 6.2), all quarters of the polar plot were filled (Figure B.3 in Appendix B).

Statistical analysis of the final pseudo GCPs of the MBR-GCP based Panasonic experiment are presented in Table 6.2. The vertical SEs were lower than the planimetric, with a maximum value of 0.03 m similar to Sandford experiments (Table 5.4). The highest error, equal to 0.05 m in Easting and Northing, were observed at E5, still lower than the 0.06 m DEM spatial resolution (Table 5.1). The mean values in Easting and Northing were lower than 0.01 m in all epochs with the exception of E3, which included the least number of pseudo GCPs. In both Easting and Northing, the E3 statistical values had approximately the same order of magnitude per epoch; hence no systematic bias towards one particular direction was observed.

Table 6.3 presents the statistical results of the MBR-based Sony experiments. Interestingly, a 0.03 m vertical SE was achieved in the MBR-GCP based experiment, lower than the 0.04 DEM spatial resolution. A 0.053 m planimetric error just above the DEM spatial resolution was delivered. A significant part of the errors come from the Northing component, as the mean value was higher in the Northing than the Easting (Table 6.3). This planimetric error was still lower than the error achieved with the Panasonic experiment in E5 (see Table 6.2 for comparison). Comparing the two Sony experiments in Table 6.3 there is no substantial difference in the estimated SEs. However, the mean values in all coordinate components of the MBR-UAV based experiment were greater than 0.02 m, which is equal to the GSD (Table 5.1). This is possibly attributed to the low number of pseudo GCPs detected between the epochs E4 and E5, compared to the Panasonic experiments.

Further analysis of the Panasonic experiment showed that approximately 50% of the pseudo GCPs detected in E2, E3 and E4 separately, were identical to the points used in E5. For instance, 333 points out of the total 743 points of E2 were transferred to E5 (Table 6.2). Even 40% of the E1 detected points were maintained in E5. This indicated that there were surface features with invariant through time *curvature*, which could be shared across epochs.

Table 6.2: Statistics of the coordinate residuals of the MBR-derived pseudo GCPs from Panasonic experiment.

Epoch	Pseudo GCPs	Easting [m]			Northing [m]			Plan [m]		Elevation [m]		
		$\mu$	$\sigma$	SE	$\mu$	$\sigma$	SE	$\sigma$	SE	$\mu$	$\sigma$	SE
E1	1096	0.002	0.023	0.023	0.001	0.019	0.019	0.030	0.030	0.001	0.028	0.028
E2	743	0.006	0.029	0.029	-0.003	0.035	0.035	0.045	0.045	-0.004	0.018	0.018
E3	541	-0.019	0.034	0.039	0.018	0.034	0.038	0.048	0.054	-0.002	0.020	0.021
E4	654	0.001	0.021	0.021	0.000	0.027	0.027	0.034	0.034	0.000	0.016	0.016
E5	1298	-0.004	0.050	0.050	0.008	0.050	0.050	0.071	0.071	0.002	0.029	0.029

Table 6.3: Statistics of the coordinate residuals of the MBR-derived pseudo GCPs from Sony experiments.

Epoch	Pseudo GCPs	Easting [m]			Northing [m]			Plan [m]		Elevation [m]		
		$\mu$	$\sigma$	SE	$\mu$	$\sigma$	SE	$\sigma$	SE	$\mu$	$\sigma$	SE
MBR-GCP based Sony experiment												
E5	37	0.004	0.035	0.035	-0.012	0.038	0.039	0.052	0.053	-0.005	0.030	0.030
MBR-UAV based Sony experiment												
E5	28	-0.023	0.035	0.041	0.025	0.035	0.043	0.050	0.059	-0.031	0.034	0.045

## 6.2.2 Assessment of co-registration solutions

### *Evaluation of GCP-based Panasonic and Sony results at check points*

For GCP-based experiments, processing was performed with the GCPs included as reported in Table 5.1. After processing with *PhotoScan*, an assessment of georeferencing accuracy was performed. Statistical values at CPs computed by Equations 3.34, 3.35 and 3.36 are listed in Table 6.4. An average of 0.031 m 3D RMSE was derived for all epochs, approximately equal to the GSD. The differences of less than 0.01 m between the standard deviation values and RMSEs imply that there are no systematic biases. Planimetric error vectors at CPs are also included in Figure 6.7. As illustrated, no general systematic directional pattern was observed at CPs. This indicates that a reliable solution was achieved in the horizontal plane for all epochs.

Table 6.4: Statistics at CPs from the GCP-based Panasonic experiment.

Campaign (month/year)	Epoch	No of CPs	$\sigma$ [m]		RMSEs [m]		
			Plan	Elevation	Plan	Elevation	3D ( $e_{geor}$ )
12/14	E0*	10	0.014	0.016	0.020	0.026	0.033
03/15	E1*	11	0.013	0.016	0.014	0.019	0.024
06/15	E2	13	0.020	0.030	0.019	0.031	0.036
09/15	E3	15	0.035	0.018	0.038	0.024	0.045
02/16	E4	15	0.011	0.019	0.012	0.019	0.022
05/16	E5	15	0.021	0.015	0.024	0.015	0.029
average			0.019	0.019	0.021	0.022	0.031

\* Errors of GCP-based results were calculated from both GCPs and CPs due to limited number of available CPs.

There are, however, a few planimetric vectors of comparatively higher magnitude, for example a 0.088 m planimetric error on 09/15 at point GP15 (Figure 6.7d). This error might originate from a few overexposed images acquired over that region generating glared surfaces (Section 3.2.6). The sun glare reflected on the dark part of the target hampered the centre detection of the target and reduced its black/white contrast. This is illustrated in Figure B.4 of GP15 target (Appendix B). The high planimetric error at this point resulted in 3D RMSE in epoch E3 exceeding the 0.03 m average GSD (Table 6.4).

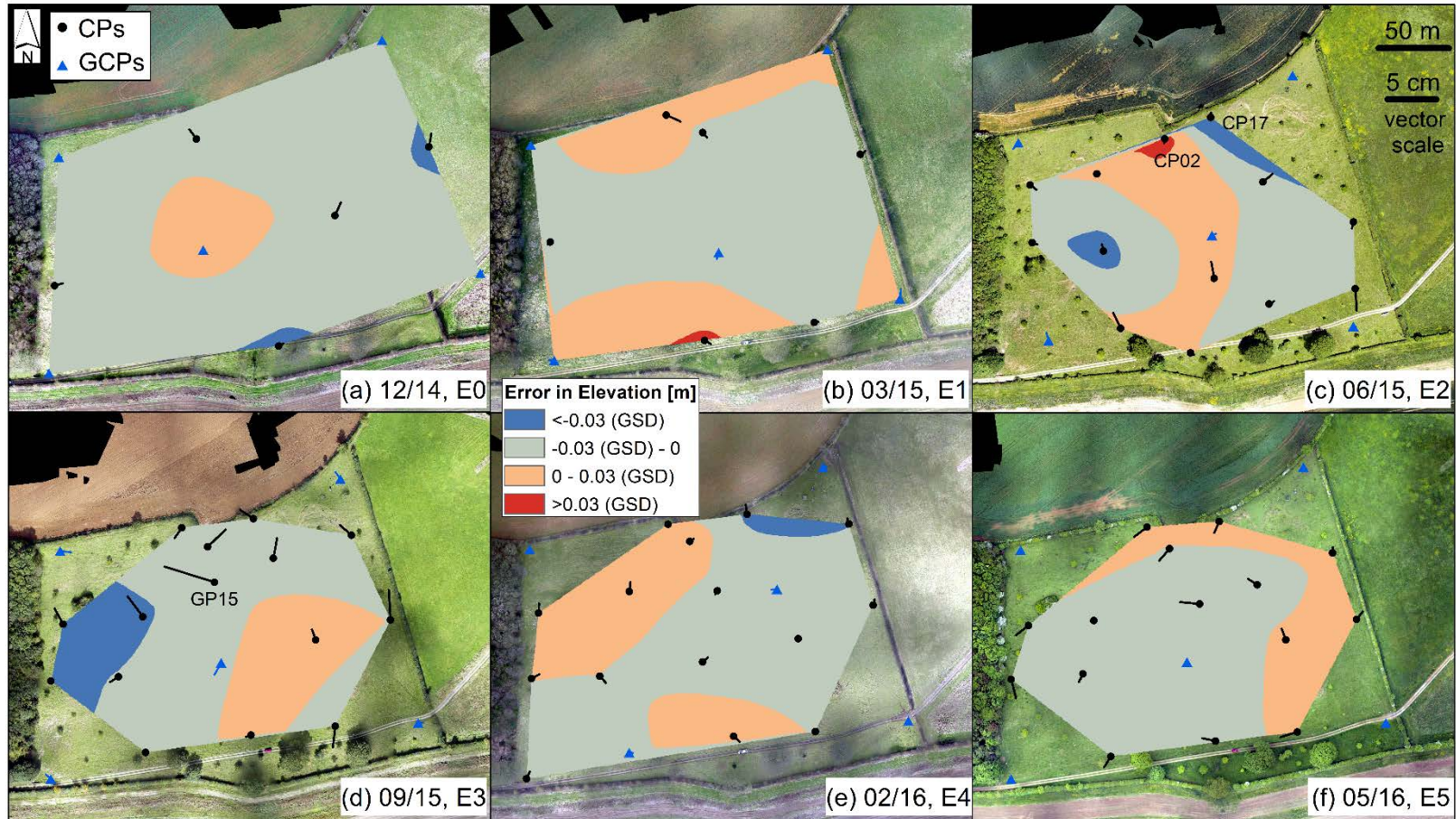


Figure 6.7: Planimetric error vectors and errors in elevation after interpolation at CPs in the GCP-based Panasonic experiment. For (a) and (b) interpolation performed at both GCPs and CPs due to a limited number of CPs (Table 6.4).

Figure 6.7 depicts the vertical error distribution as interpolated with the natural neighbour technique (Section 3.2.2) to form a continuous error surface. The magnitude of the vertical error was relatively small within  $\pm 0.03$  m for all epochs. However, E2 displayed high errors across the north of the site (Figure 6.7c). For example a  $-0.078$  m vertical error at the CP17 point and a  $0.045$  m vertical error at CP02 point were observed in E2 (Figure 6.7c). The former is caused by the low number of four images viewing this target point compared to the number of optical rays corresponding to all other targets. This resulted in a high error due to low image overlap which led to low redundancy in elevation derivation (Section 3.2.6). The vertical error at CP02 is likely to have originated from strong gusts of wind, which destabilised the UAV while turning from east to south. This created blurred images over that region, degrading the image resolution (Sieberth et al., 2014) and yielding vertical deformations (Section 3.2.6). An example of a blurred image over the CP02 target is shown in Figure B.5 in Appendix B, illustrating that the target's original circular shape was altered due to UAV instability. Even though the extreme blurred images were excluded at the beginning of the pre-processing step (Section 6.1.2), a few remained as they could not be removed as this would have resulted in insufficient overlapping images.

It is noteworthy that during processing, tests were carried out to investigate the optimal combination of five GCPs with the distribution recommended in Section 5.1. The tests involved which five GCPs delivered the lowest average RMSE. Thus, the corner targets were not always chosen as GCPs, an example is shown in E4 (Figure 6.7e). Moreover, additional tests were undertaken to investigate the presence of bowl-shape deformations (Section 3.2.6). DEMs derived from the GCP-based Panasonic experiment were subtracted from the DEMs generated from all available GCPs. Based on this DEM differencing, (see Figure B.6 in Appendix B), an unresolved deformation was observed in epoch E5 with values ranging within  $[-0.06-0.03]$  m. Although deformations of lower magnitude were found in epoch E1. These deformations were also observed in the Cockle Park experiment and discussed in Section 5.2.2.

Statistical results of the GCP-based Sony experiment computed at CPs after *PhotoScan* processing are summarised in Table 6.5 and mapped in Figure 6.8. Both  $\sigma$  and RMSEs have comparable order of magnitude per epoch indicating an absence of systematic errors. However, statistics in elevation of E4 epoch were higher than the statistical results of E5 epoch. As shown in Figure 6.8a, error deformations in excess of  $0.02$  m were observed over the upper part of the slope. Note the different classification scheme adopted in Figure

6.8 compared to Figure 6.7, This is because the GSD achieved with the Sony imagery was different from the GSD derived from Panasonic imagery (Table 5.1). A 0.056 m vertical error at PCT10 point and a 0.066 m vertical error at PCT14 point were observed in E4. It is likely that the error was caused by a few underexposed dark images acquired over that region. A general issue with this dataset was the acquisition of relative dark images which might have degraded the vertical accuracy (Section 3.2.6). Further investigations on image enhancement prior to *PhotoScan* were not applied as they are outside the scope of this study. Overall, an average 0.032 m 3D RMSE was achieved with Sony imagery, which is close to the average 3D RMSE from Panasonic imagery.

Table 6.5: Statistics at CPs from the GCP-based Sony experiment.

Campaign (month/year)	Epoch	No of CPs	$\sigma$ [m]		RMSEs [m]		
			Plan	Elevation	Plan	Elevation	3D ( $e_{geor}$ )
02/16	E4	15	0.021	0.030	0.022	0.030	0.037
05/16	E5	15	0.017	0.011	0.021	0.018	0.028
		average	0.019	0.021	0.021	0.024	0.032

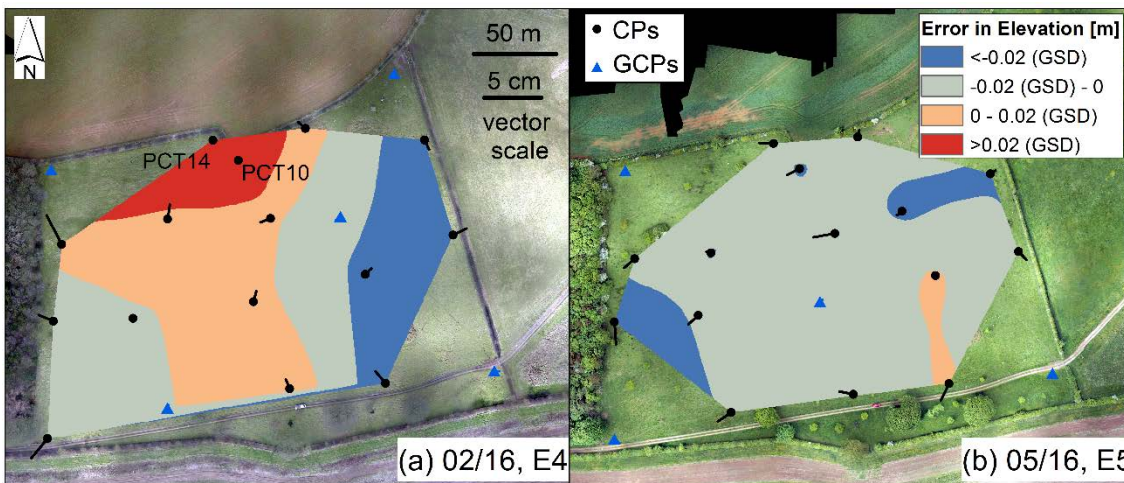


Figure 6.8: Planimetric error vectors and errors in elevation at CPs of the GCP-based Sony experiment.

Elevation values from the derived DEMs were cross-validated against elevations at spot heights independently surveyed with GNSS and a total station (Figure 4.8 in Section 4.3.2). The cross-validation of GCP-based Panasonic result is summarised in Table 6.6. Vertical RMSEs of 0.043 m difference across epochs were achieved. However, a high mean value was observed at epoch E1. This is possible because almost all spot heights were located at the edges of the landslide scarp and convex breaks, as seen in Figure 4.8. The most rigorous statistical result was epoch E5 with close to zero mean value from spot heights well distributed across the site. Hence, E5 observations, being the most reliable, are used for cross-validation in the experiments described in the following Sections.

Table 6.6: Statistics of elevation differences derived from the comparison of the GCP-based Panasonic outputs against independently observed elevations at sample points.

Campaign (month/year)	Epoch	No of points	$\mu$ [m]	$\sigma$ [m]	RMSE [m]
12/14	E0	48	0.047	0.100	0.110
03/15	E1	52	-0.110	0.079	0.131
06/15	E2	98	-0.050	0.090	0.102
02/16	E4	65	0.058	0.087	0.104
05/16	E5	559	0.003	0.088	0.088

Elevation cross-validation of the GCP-based Sony outputs in E5 delivered a 0.004 m mean value and standard deviation and RMSE equal to 0.081 m. From both Panasonic and Sony experiments a normal distribution can be fit to the histograms of elevation differences at spot heights in E5.

### ***Evaluation of MBR-based Panasonic and Sony results at check points***

Table 6.7 summarises the statistical values derived at CPs from the MBR-GCP Panasonic experiment. The MBR workflow delivered better and more consistent RMSEs in elevation than in plan across all epochs of less than 0.06 m. The discrepancies between  $\sigma$  and RMSEs imply the presence of non-zero mean values between the surveyed and estimated CP coordinates. Interestingly, an average 0.04 m vertical RMSE was achieved, lower than the 0.06 m DEM spatial resolution.

Table 6.7: Statistics at CPs from the MBR-GCP based Panasonic experiment.

Campaign (month/year)	Epoch	No of CPs	$\sigma$ [m]		RMSEs [m]		
			Plan	Elevation	Plan	Elevation	3D ( $e_{geor}$ )
03/15	E1	11	0.043	0.044	0.056	0.044	0.071
06/15	E2	18	0.042	0.027	0.070	0.027	0.075
09/15	E3	20	0.054	0.022	0.057	0.037	0.067
02/16	E4	20	0.022	0.024	0.070	0.050	0.086
05/16	E5	20	0.032	0.040	0.099	0.042	0.108
average			0.039	0.032	0.070	0.040	0.082

Comparing the statistics from GCP-based and MBR-GCP Panasonic experiments (Table 6.4 with Table 6.7 respectively), a difference was observed in planimetric RMSEs. The coordinates in elevation at 559 spot heights in E5, surveyed with a total station, were compared against the MBR-derived elevations. A mean value of -0.014 m, standard deviation of 0.103 cm and RMSE of 0.104 m verified the 3D error magnitude estimated at CPs (0.108 m in Table 6.7). This RMSE value was only 0.02 m different from the corresponding RMSE derived from the GCP-based cross-validation in E5, as seen in Table 6.6.

Figure 6.9 depicts the planimetric error vectors of pseudo GCPs and CPs, as calculated by the MBR workflow. The vectors are plotted over elevation differences, which were obtained by subtracting the MBR-GCP DEM from the GCP-based DEM at each epoch. The classification scheme of the elevation differences adopted is identical to that shown in Figure 5.12 for the Sandford experiment (Section 5.3.3). Various deformation patterns were observed in Figure 6.9, illustrating random behaviour across all epochs. For example a radial pattern is shown in E1 and E2 (Figure 6.9a and b) while a tilt is apparent in E5 (Figure 6.9e). Both radial patterns in E1 and E2 show a dishing distortion (Carbonneau and Dietrich, 2016) with larger deformations at the edges of the site. Comparing these two, the error magnitude in E2 is  $1\sigma$  smaller. The deformation patterns in E3 and E4 (Figure 6.9c and d) also seem radial but with a rather wide spread with the centre of distortion not coinciding with the centre of the site as in E1. Figure 6.9e shows a clear tilt with lower deformations in the north and higher in the south. The error vectors at CPs (in Figure 6.9e) show a generally dominant N-S direction, similar to the direction of the landslide movement previously estimated by BGS (Uhlemann et al., 2016). Nevertheless, as is already described in Section 6.2.1, the error vectors of pseudo GCPs provide a random error distribution without showing dominance towards a particular direction. Further investigation with other benchmark datasets, described in Section 6.5.2, explained how the landslide motion negatively affected the MBR-GCP outcome. Overall, among all epochs, E3 (Figure 6.9c) shows the smallest vertical deformation magnitude across the site with a relatively random planimetric directional distribution at CPs.

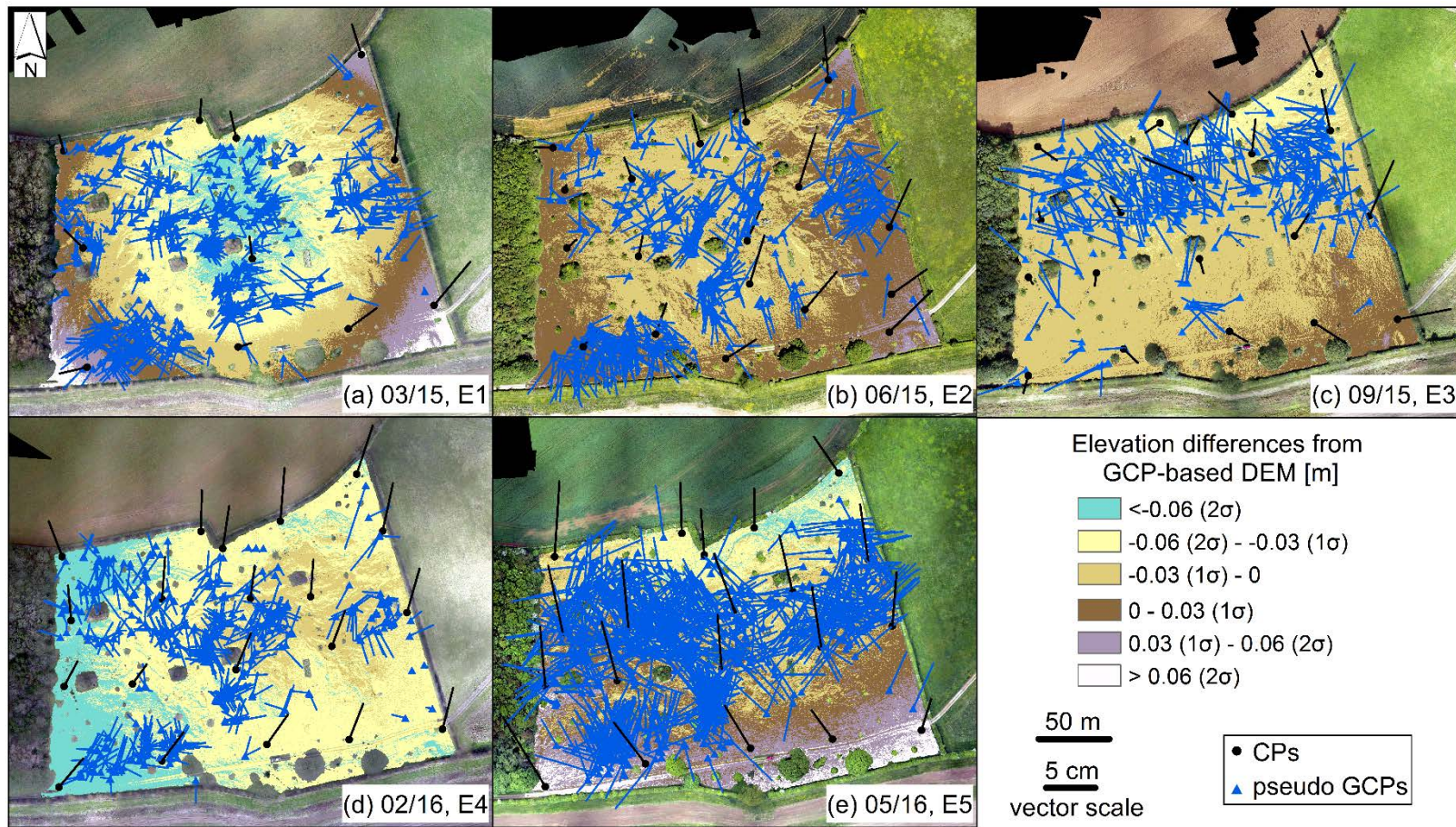


Figure 6.9: Planimetric error vectors of pseudo GCPs and CPs with elevation differences between GCP-based and MBR-GCP based Panasonic experiments.

Table 6.8 reports the statistics at CPs of the MBR-GCP Sony results. Interestingly, a 0.039 m RMSE in elevation was achieved, very close to the RMSE in E5 of the corresponding Panasonic experiment seen in Table 6.7. However, the Sony experiment delivered a much lower RMSE value in plan than the Panasonic experiment (Table 6.7 versus Table 6.8).

Table 6.8: Statistics at CPs from the MBR-GCP Sony experiment.

Campaign (month/year)	Epoch	No of CPs	$\sigma$ [m]		RMSEs [m]		
			Plan	Elevation	Plan	Elevation	3D ( $e_{geor}$ )
05/16	E5	20	0.029	0.034	0.053	0.039	0.066

In the Panasonic experiment numerous pseudo GCPs were detected from all possible epoch pairs, transformed into E5, and not extracted only from the epoch pair E4-E5 as in the Sony experiment. Even though the numerous pseudo GCPs aided in generating a good distribution of control points across site, an error might have been introduced because of epoch-to-epoch transformation. This could possibly explain the discrepancy of the error magnitude in plan between the two experiments. On the other hand, when few pseudo GCPs were detected, as in the Sony experiment, a relatively poor distribution of control points was generated with no points at the upper parts of the slope (Figure 6.10a).

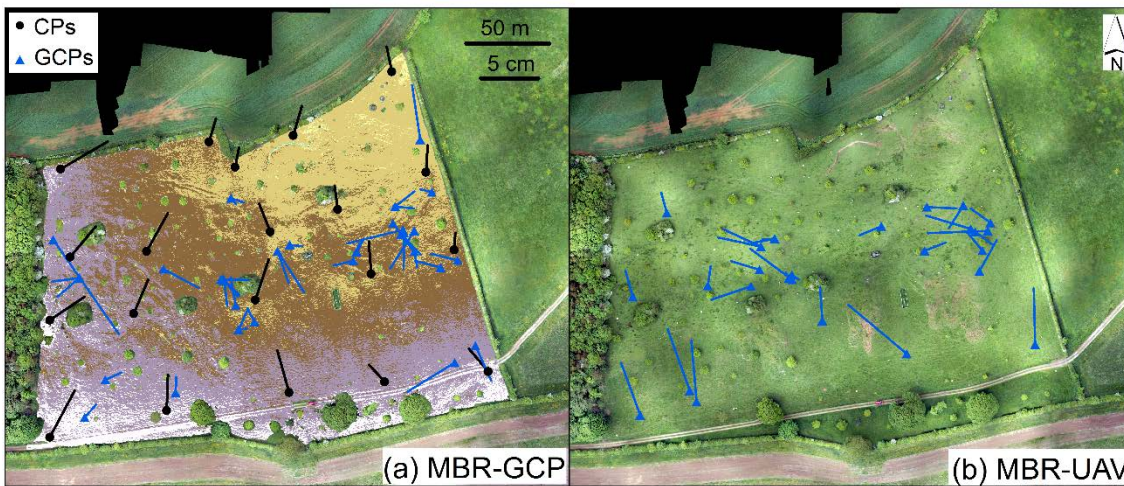


Figure 6.10: (a) Elevation differences between GCP-based and MBR-GCP Sony experiment with planimetric error vectors in E5. (b) Planimetric error vectors at pseudo GCPs of the MBR-UAV Sony result.

Although the planimetric error magnitude in Table 6.8 was better than the error in Table 6.7, there was an apparent N-S directional error at CPs and an unresolved radial deformation (Figure 6.10a). Note that the elevation differences in Figure 6.10a are plotted with the same color scheme seen in Figure 6.9.

MBR-GCP Sony outputs were cross-validated against the 559 spot heights surveyed in E5. Interestingly, the cross-validation delivered a 0.01 m mean value and standard deviation and RMSE equal to 0.089 m, close to the GCP-based results of both Panasonic (Table 6.6) and Sony datasets. This verified a good overall co-registration solution in elevation.

Figure 6.10b presents the planimetric error vectors of pseudo GCPs derived from the MBR-UAV Sony experiment. As no OSGB36 georeferencing was involved in this experiment, errors at CPs and/or spot heights could not be assessed. Comparing Figure 6.10a and b, it can be seen that different pseudo GCPs were identified despite the fact that imagery of an identical camera and epoch pair were processed. The only difference between the two experiments is the way the reference DEM was derived. In particular, in the MBR-GCP experiment, E4 DEM was derived with the inclusion of five GCPs whereas, in the MBR-UAV experiment E4 DEM was generated after a coarse alignment from the UAV camera exposure stations (Figure 3.6). Due to the absence of GCPs, the E3 3D surface had a relatively different shape from the “ground-truth” (i.e. 3D surface derived with five GCPs) which in turn generated a different *curvature* grid. This, combined with the coarse horizontal coordinates, resulted in a *curvature* epoch pair with other characteristics than the epoch pair of the MBR-GCP experiment. As result, SIFT detected points at different locations.

As also investigated in the Sandford experiments (Section 5.4.2), further tests were carried out to analyse possible sources of distortion as seen in Figure 6.9 and Figure 6.10a. The test involved investigating whether the distortion was attributed to the pseudo GCPs uncertainties. These are the computed SEs that served as markers’ accuracies in the SfM-MVS pipeline (Section 3.4.2). In a manner similar to Sandford (Section 5.3.2). 13 self-calibrating bundle adjustments were conducted with respect to different markers’ accuracies within the range of 0.1-6.0 cm, for the Panasonic MBR-GCP experiment. Figure 6.11 displays the resulting boxplots of the first and last epoch. The boxplots in Figure 6.11a and b show an expanding spread as the marker accuracy increases, whereas in Figure 6.11c and d show a relatively more consistent spread. The boxplots at CPs, in Figure 6.11b, also illustrate a skewed RMSE distribution compared to the boxplots of pseudo GCPs, in Figure 6.11a. The distortions, depicted in Figure 6.9a, can possibly be correlated with the patterns of the boxplot spreads. The same test was performed with the datasets from the GCP-based datasets for E1, with similar results to those in Figure 6.11a

and b. Thus, DEM errors in E1 probably resulted from the imaging network itself, and not the actual MBR workflow.

Regarding E5, the tilt in Figure 6.9e, is unlikely to be entirely attributable to the various marker accuracies, since the boxplots in Figure 6.11c and d do not reveal any dramatic variations. Moreover, the average magnitude of the 3D RMSEs of the last epoch (Table 6.7, Figure 6.9e and Figure 6.11d), was relatively greater than the previous epochs. This implies that the landslide movement within the monitoring period was possibly propagated through processing and integrated into the results.

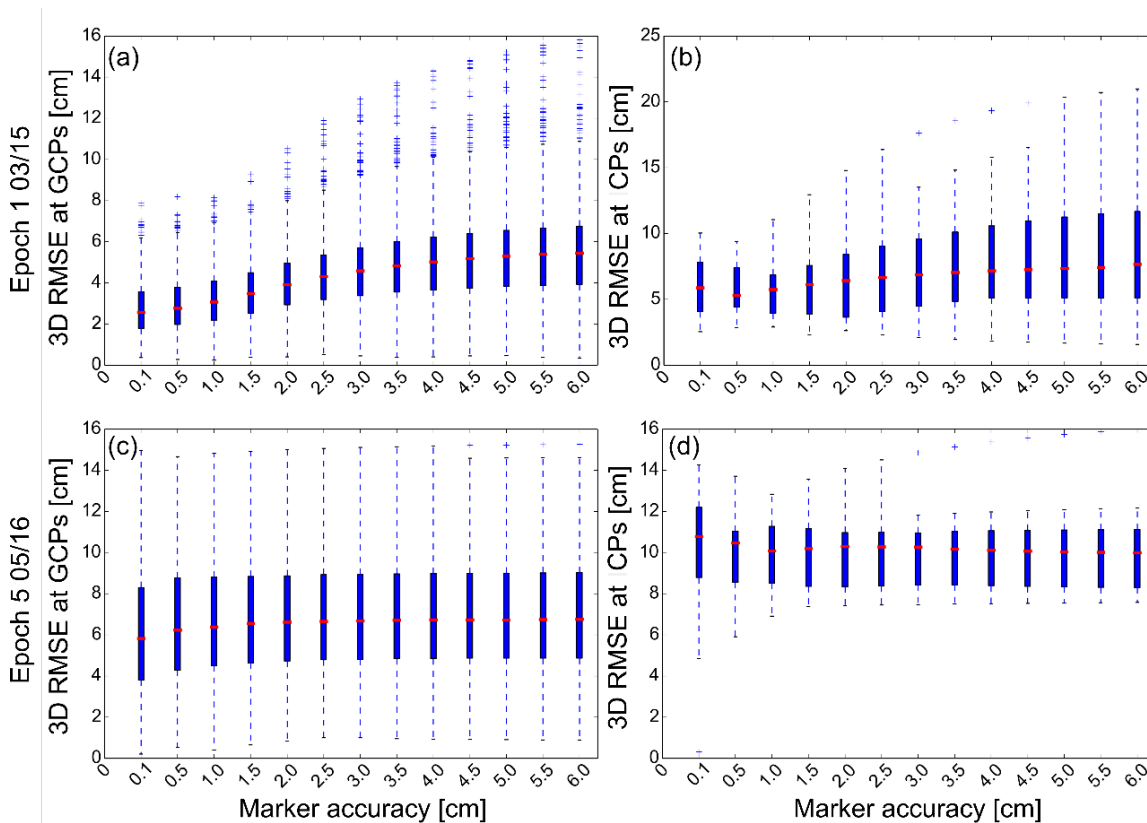


Figure 6.11: 3D RMSEs of MBR-GCP processing at (a) 1096 pseudo GCPs, (b) 11 CPs of E1, also at (c) 1298 pseudo GCPs and (d) 20 CPs of E4.

After applying the ICP algorithm for the sensitivity computation (Section 3.5.3), E5 DEM was reconstructed by applying the transformation parameters estimated from the algorithm, and compared against the GCP-based derived DEM. The comparison showed that the tilt in E5 remained and its direction was reversed with negative error in the south and positive in the north, as opposed to Figure 6.9e. This is possibly because the E4 DEM had significant differences from E0 DEM caused by landslide movement and seasonal changes. As also stated in Eltner et al. (2016), ICP cannot recover errors when it is applied to surfaces with substantial changes.

### Comparison with TLS datasets

In Section 5.3.1, a test was conducted comparing SfM-MVS outputs with TLS datasets to define the optimal M3C2 settings (D and d scale parameters, Section 3.5.1). As that test was applied to a flat region at Sandford, it was repeated for the back scarp of TLS coverage at Hollin Hill (Figure 4.6). The M3C2 algorithm was implemented with the the MBR-GCP based and TLS datasets of E5 for a range of 0.1-2.0 m for D and d parameters. A uniform scale was used for both parameters to simplify the computations as recommended by Lague et al. (2013). The results of the test are presented in Figure 6.12.

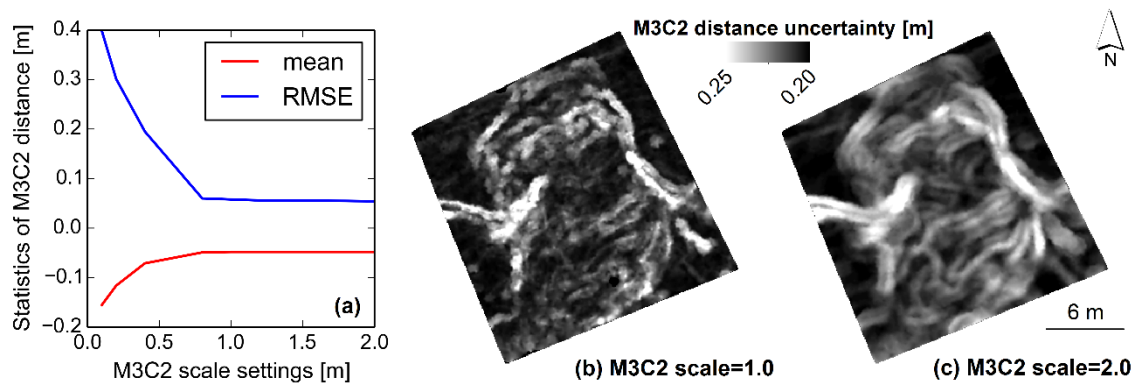


Figure 6.12: Implementation of the M3C2 algorithm for various scale settings.

Figure 6.12a shows the mean value and RMSE of the M3C2 distance computed between the MBR-GCP and TLS point clouds for different scale parameters. The mean and RMSE of the M3C2 distance reached a plateau for scale greater than 0.8 m. For small scale the magnitude of the M3C2 distance was overestimated due to possibly improper estimation of the normal vectors over regions with strong *curvature* variations (Section 3.5.1). Lague et al. (2013) noted that for small spatial extents mostly over cliffs, the orientation of the normal vectors becomes parallel to the local orientation of the overhanging parts of the surface yielding to distance overestimation. To overcome these errors, Lague et al. (2013) recommended higher scale values within the range of 0.5- 2.0 m.

However, the test showed that for a large scale of 2.0 m, the M3C2 algorithm over smoothed the surface roughness. The M3C2 algorithm also delivered an uncertainty map of the estimated distance between the two point clouds. This was computed based on the error propagation applied to estimated standard deviations of each point cloud (see Lague et al. (2013) for further description). For example, the distance uncertainty maps derived from scales set to 1.0 m and 2.0 m are shown in Figure 6.12b and c respectively. As expected the distance uncertainty was higher over surfaces scars, because subtle surface details can be better modeled with TLS than UAV imagery. However, Figure 6.12c shows

that for 2.0 m scale, the M3C2 algorithm smoothed the local surface variations creating a smooth uncertainty map. Hence, to consider the local surface roughness without miscalculating the point cloud distances, M3C2 scales  $D$  and  $d$  were set equal to 1 m in all computations presented in this Section.

Using the above M3C2 settings, statistics of the epoch to epoch direct comparison with TLS observations for both cameras and experiments are presented in Table 6.9.

Table 6.9: Statistics of M3C2 after epoch to epoch comparison with TLS datasets.

Panasonic						
Epoch	GCP-based experiment [m]			MBR-GCP based experiment [m]		
	$\mu$	$\sigma$	RMSE	$\mu$	$\sigma$	RMSE
E4	0.014	0.014	0.020	-0.028	0.020	0.035
E5	0.001	0.028	0.028	-0.048	0.031	0.058
average	0.007	0.021	0.024	-0.038	0.025	0.046
Sony						
Epoch	GCP-based experiment [m]			MBR-GCP based experiment [m]		
	$\mu$	$\sigma$	RMSE	$\mu$	$\sigma$	RMSE
E4	0.055	0.017	0.057			
E5	-0.025	0.026	0.036	-0.044	0.027	0.051
average	0.015	0.021	0.046	-0.044	0.027	0.051

The statistics of the Panasonic datasets show that for both epochs the MBR-GCP derived data are below the TLS data. The RMSE magnitude in E5 is higher than the magnitude in E4 for both GCP-based and MBR-GCP workflows. This is possibly due to significant changes at the back scarp between 02/16 and 05/16. For the Sony GCP-based experiment, a relatively high value of mean and RMSE were observed in E4. This coincides with the vertical errors depicted at CPs over the upper part of the site over the TLS coverage (Figure 6.8a). A possible reason would be the inferior UAV imagery acquired at that epoch, as mentioned in Section 6.2.2. Interestingly, for the two MBR-GCP based results, mean and RMSE values were in the same order of magnitude in E5. The 0.051 m RMSE in E5 derived from the Sony MBR-GCP result was close to the 0.066 m 3D RMSE at CPs (Table 6.8). Overall, these results provide confidence in the MBR workflow. However, it should be noted that TLS observations only covered a sub region at the top of the slope. SfM-MVS outputs typically show usually higher errors at the edges of a site (Section 3.2.6). Hence, the estimated RMSEs in Table 6.9 indicate the extremes of the achieved georeferencing accuracy for all experiments.

## 6.3 3D sensitivity and estimation of elevation change

### 6.3.1 3D sensitivity estimations

Up to this point, the georeferencing accuracy is estimated from GCP-based, and MBR-GCP Panasonic and Sony experiments. To derive 3D sensitivities, co-registration errors were computed by the M3C2 comparison after applying the ICP algorithm over stable terrain (Section 3.5.3). The stable regions were generated based on Stage 2b of the MBR workflow (Section 3.4.2) per epoch. For each experiment in the ICP computation, point clouds of the reference epoch served as datasets with a fixed coordinated system. The M3C2 comparison post ICP implementation indicated an overall 3D error that could not be entirely removed from the workflows.

Table 6.10 reports the Panasonic statistics. With respect to the Panasonic GCP-based outputs in Table 6.10, the calculated RMSEs across all epochs lie within the range of the 3D RMSEs reported in Table 6.4. The ICP minimised possible misalignments and decreased the mean value close to zero, as expected, with the exception of E1 and E5 for the MBR-GCP Panasonic results (Table 6.10). The higher RMSEs of E1 and E5, reflect deformation patterns attributed to a combination of possible errors, such as inferior imaging configuration together with landslide movement and errors introduced by the MBR workflow. Figure 6.11 also reveals errors caused partly by the marker's accuracy incorporated in the SfM-MVS pipeline (Section 6.2.2). In both experiments, the comparably higher RMSE of E5 could also be caused by the vegetation change. This is also seen through the *openness* mask creation which showed rough texture mostly around the lobes (Figure 6.4b). On the other hand, the E2 and E4 *openness* masks (Figure 6.4a) do not show high surface roughness outside the main landslide bodies. The RMSEs of E2, E3 and E4 in the MBR-GCP results of Table 6.10, have similar magnitude and lower than the 0.06 m DEM spatial resolution (Table 5.1), showing consistency in the co-registration accuracy. At these epochs, the 3D RMSEs at CPs (Table 6.4) and the RMSEs of the M3C2 comparison (Table 6.10) do not differ by more than 0.03 m, equal to the achieved GSD. It seems that the MBR workflow did not introduce additional errors and the MBR outcome was not affected by high roughness as opposed to E1 and E5 datasets.

Table 6.10: Statistics of M3C2 comparison after ICP implemented with respect to E0 over stable terrain, for Panasonic datasets.

Panasonic						
Epoch	GCP-based experiment [m]			MBR-GCP based experiment [m]		
	$\mu$	$\sigma$	RMSE ( $e_{co-reg}$ )	$\mu$	$\sigma$	RMSE ( $e_{co-reg}$ )
E1	0.000	0.018	0.018	0.026	0.108	0.108
E2	0.000	0.019	0.019	0.000	0.031	0.031
E3	0.001	0.027	0.027	0.000	0.055	0.055
E4	0.000	0.017	0.017	0.000	0.041	0.041
E5	-0.002	0.030	0.030	0.023	0.087	0.087
average	0.000	0.022	0.022	0.010	0.064	0.064

With respect to processing of the Sony imagery, the M3C2 results after the ICP implementation per experiment are listed in Table 6.11.

Table 6.11: Statistics of M3C2 comparison after ICP implemented with respect to E4 over stable terrain, for Sony datasets.

Sony				
Epoch	$\mu$ [m]	$\sigma$ [m]	RMSE ( $e_{co-reg}$ ) [m]	Experiments
E5	0.012	0.057	0.057	GCP-based
E5	0.003	0.090	0.090	MBR-GCP
E5	-0.013	0.077	0.078	MBR-UAV

For Sony datasets E4 was used as a reference fixed surface for ICP. Hence, the statistics cannot be directly comparable with the results from Panasonic datasets. Perhaps the most interesting finding in Table 6.11 is that the statistical values of MBR-UAV results have magnitude similar to the magnitude of MBR-GCP statistical values. Both experiments provided  $e_{co-reg}$  (Table 6.11) and  $e_{geor}$  accuracies (Table 6.8) which do not differ by more than 0.04 m, equal to the DEM spatial resolution derived from Sony datasets.

Having computed the georeferencing and co-registration uncertainties, sensitivities  $s_1$  and  $s_2$ , derived from Equations 3.37 and 3.38, are reported in Table 6.12 and Table 6.13 for Panasonic and Sony datasets respectively. For the GCP-based results in Table 6.12, the two sensitivities match across all epochs. In the MBR-GCP results, E1 and E5  $s_2$  sensitivities are the largest, indicating unresolved errors, as explained previously. Conversely, E2 and E4  $s_2$  sensitivities are similar to the corresponding sensitivities of GCP-based results. It is noteworthy that the average sensitivities across epochs of MBR-GCP Panasonic results were approximately double the sensitivities derived from the GCP-based experiments (Table 6.12).

Table 6.12: Sensitivities estimated for Panasonic experiments.

Epoch	GCP-based [m]		MBR-GCP [m]	
	$s_1$	$s_2$	$s_1$	$s_2$
E1	0.079	0.073	0.153	0.221
E2	0.096	0.074	0.161	0.088
E3	0.109	0.083	0.147	0.126
E4	0.078	0.072	0.180	0.103
E5	0.085	0.087	0.221	0.182
average	0.089	0.078	0.172	0.144

Comparing the sensitivities from the two cameras (Table 6.12 and Table 6.13),  $s_1$  and  $s_2$  derived from Sony GCP-based and Sony MBR-GCP respectively are similar to the equivalent values of Panasonic experiments. Moreover,  $s_2$  sensitivity of the Sony MBR-UAV results, which does not include the absolute uncertainty, still lies within the bounds of  $s_1$  and  $s_2$  of the Sony MBR-GCP experiment (Table 6.13).

Table 6.13: Sensitivities estimated for Sony experiments.

Epoch	GCP-based [m]		MBR-GCP [m]		MBR-UAV [m]
	$s_1$	$s_2$	$s_1$	$s_2$	$s_2$
E5	0.091	0.133	0.148	0.191	0.153

Overall, these 3D sensitivity estimations coming from different experiments suggest that the MBR workflow detected a lowest surface change that lies within the range of 0.088-0.22 m. The 0.088m threshold is the minimum value and the 0.22 m is the maximum value between the two sensitivities across all epochs (Table 6.12). The minimum sensitivity, which is very close to the sensitivities of the GCP-based results, represents the optimal outcome when no biases are involved. The maximum sensitivity, which is double the maximum sensitivity estimated from GCP-based experiment (i.e. 0.109 m), represents the threshold of surface change that can be identified from SfM-MVS outputs that involve biases. The two maximum sensitivities 0.109 m and 0.221 m from the GCP-based and MBR-GCP experiments respectively were used to mask out the elevation differences from Panasonic results. Whereas from the Sony results the two maximum sensitivities 0.133 m and 0.191 m represent the lowest detectable 3D change derived from the GCP-based and MBR-GCP experiments respectively.

### 6.3.2 Estimation of elevation and volume change

Figure 6.13 plots the elevation differences between E0-E1, E1-E4 and E4-E5 derived from the GCP-based (Figure 6.13a, b, and c) and MBR-GCP Panasonic experiments (Figure 6.13d, e and f). E2 and E3 observations were excluded from Figure 6.13 due to small differences and additional noise caused by vegetation change. An example of this noise is seen in E0-E3 elevation differences, which are depicted in Figure B.7 in Appendix B. The  $\pm 0.109$  m sensitivity level was excluded from Figure 6.13a, b and c, while Figure 6.13e, f and d did not include the  $\pm 0.221$  m sensitivity level. Shades of blue and red indicate the ground accumulation and depletion respectively.

As seen in Figure 6.13, the Hollin Hill landslide showed a non-systematic and a non-continuous vertical deformation. The eastern and western lobe, as well as the back scarp, constitute the most active parts of the landslide. However, over these parts the magnitude of change varied spatially and temporally. For instance, elevation changes of the front part of the eastern lobe occurred between E0-E1 (Figure 6.13a) and E4-E5 (Figure 6.13c), whereas this part was inactive during E1-E4 (Figure 6.13b). This mixed behaviour of activation/inactivation was corroborated by BGS ground-based investigations (Uhlemann et al., 2016). Moreover, elevation changes occurred predominantly along the convex and concave geomorphological features that can be highlighted with the *shaded relief* in Figure 6.13. These observations were also confirmed by BGS research (Merritt et al., 2014). Ground accumulation ( $[-0.11:-0.22]$  m change in yellow) usually followed ground subsidence ( $[0.11:0.22]$  m change in cyan) forming surface undulations, as clearly seen at the back scarp in Figure 6.13b and Figure 6.14c (see Section 4.3.1).

Part of the western lobe collapsed ( $25.14 \text{ m}^2$  in extent), sliding downwards, and created a dramatic change of  $-0.70$  m maximum ground loss and a  $+0.50$  m maximum ground accumulation within eleven months (Figure 6.13b). The failure appeared to have occurred between the 09/15 and 02/16 campaigns. However, part of the western lobe was eroding after 03/15. As far as the eastern lobe is concerned, ground material had continuously accumulated at the toe of the eastern lobe, which appears to have surged forward post-05/14. Even though the 05/14 DEM was not included in the experiments, DEM subtraction from 05/16 DEM illustrated a total deposition (equal to  $59.74 \text{ m}^3$ ) of the front part of the most active lobe observed within two years (Figure B.8 in Appendix B). At the upper part of the slope, the surface was ruptured generating new curvilinear features near the back scarp (Figure 6.13c, Figure 6.14c). These features could also be identified on the *openness* grids as seen in Figure 6.4b and d as well as on the slope map as illustrated

in Figure 6.14d. The surface failure appeared to have occurred after 02/16 yielding a maximum ground subsidence of approximately - 1.70 m, whereas material sliding down-slope created a maximum elevation increase of approximately + 1.05 m between E4-E5 epochs (Figure 6.13c).

Among all pairs, E1-E4 (Figure 6.13b) produced the clearest picture of landslide elevation differences due to minimal seasonal variations during winter. Even though a filtering process for removing vegetation was implemented (Section 6.1.3), elevation differences were apparent around the trees, hedgerows and fences. An example of this is seen at the top of the slope in Figure 6.13a, where grass growth was observed as positive change near hedgerows. Grass growth was also observed in Figure 6.13c at the bottom of the slope. As mentioned in Section 4.3.1, Hollin Hill is used for grazing. The farmer occasionally kept sheep within the upper area, north of the track. Because of that, the grass grew up to 0.30 m at the foot of the slope between E4-E5 epochs (Figure 6.13c). Given the background knowledge from BGS investigations (Section 4.3.1), no landslide movement was observed at the toe of the site; hence this elevation change was certainly caused by grass growth. However, negative elevation differences were apparent west of the site in Figure 6.13c. It is possible that vegetation changes were mixed with actual erosion, which was observed as elongated geomorphological features over the lobes. Although no significant deformation was captured from UAV observations over the lobes west of the site, this part appeared active during the 2011-2014 period before the UAV flights. This is seen from elevation changes between DEM derived from ALS 2011 and the UAV reference DEM (Figure B.9 in Appendix B). Thus, negative elevation changes seen in Figure 6.13c may indicate a landslide reactivation over the western part.

Figure 6.14a and c illustrate a perspective 3D view of the surface model over the back scarp for E0 and E5 epochs respectively. The surface models (i.e. 3D meshes) were produced and textured in PhotoScan for visualisation purposes. Figure 6.14b and d display the surface slope as generated in the Visualisation and Interpretation Software – LIME (LIME, 2018). Various geomorphological features such as ridges, undulations and cracks can be clearly identified in both epochs. The dramatic elevation change (Figure 6.13c), was the result of a surface rupture occurred between E4-E5 epochs, as illustrated in Figure 6.14b and d. Also, the 3D views help in identifying small bushes appeared on the surface cracks due to seasonal changes across epochs, thereby allowing visual interpretation of surface deformation.

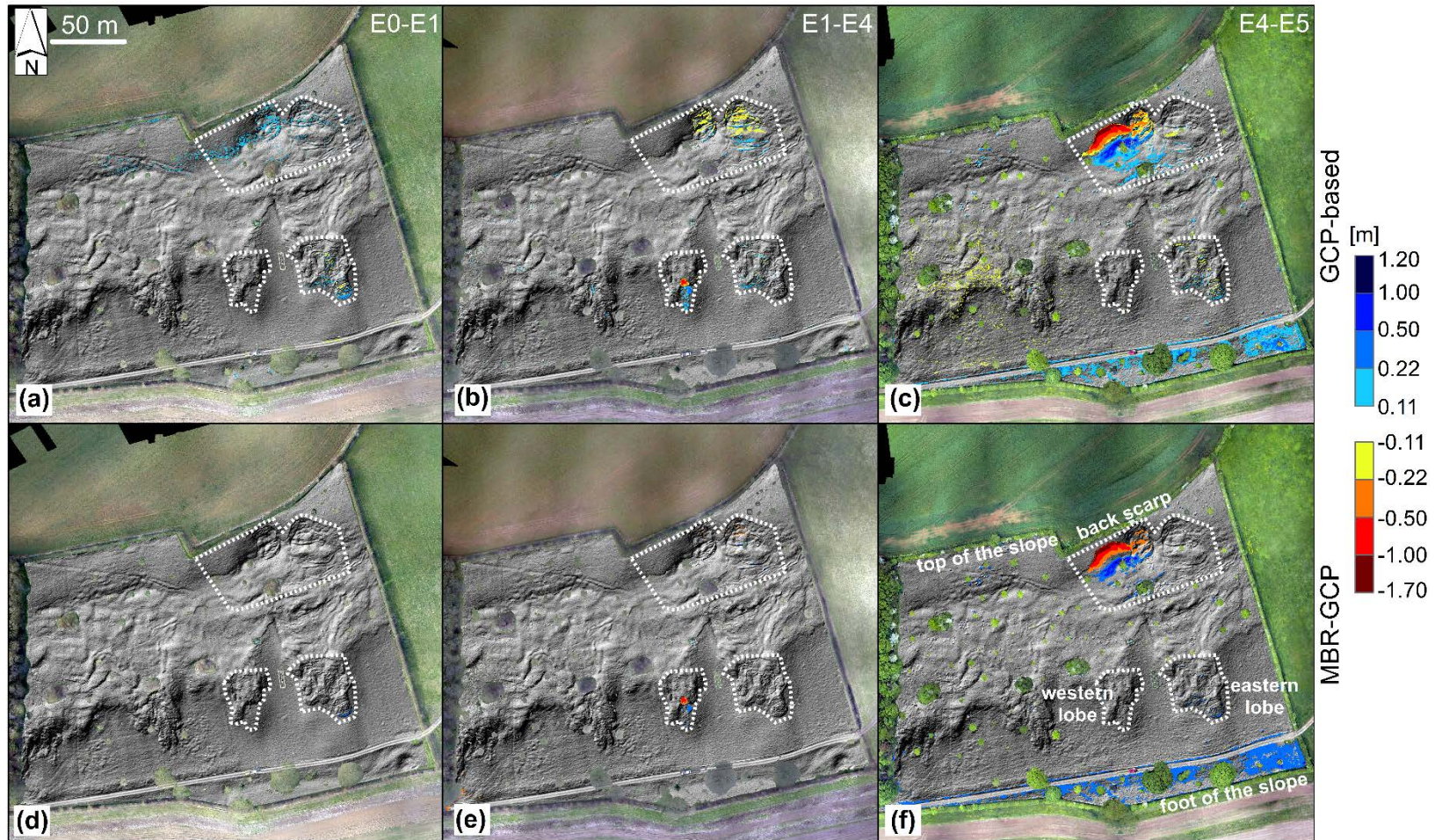


Figure 6.13: Elevation differences of three successive epoch pairs derived from GCP-based and MBR-based experiments

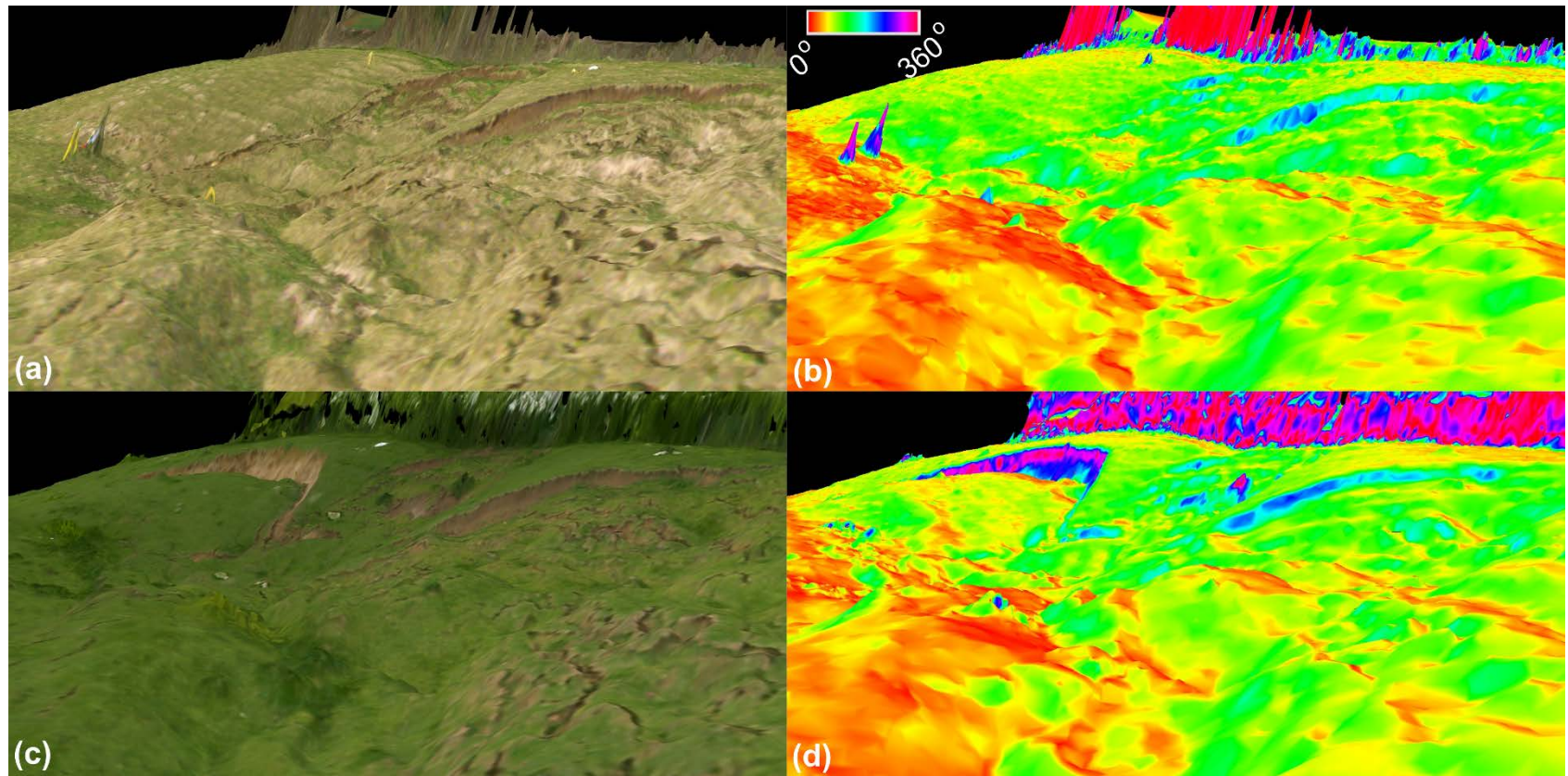


Figure 6.14: Perspective 3D views of (a) E0 and (c) E5 textured surface models with their corresponding (b) E0 and (d) E5 slope maps over back scarp derived from GCP-based experiment.

To this point, the aforementioned analysis involved only elevation differences estimated with the GCP-based processing. Comparing the GCP-based (Figure 6.13a, b and d) with the MBR-GCP results (Figure 6.13e, f and g), it can be noted that the MBR-GCP outcome missed small landslide deformations, given the  $\pm 0.22$  m sensitivity threshold. Apart from that, it also overestimated grass growth at the foot of the slope (see Figure 6.13f, possibly because of the additional systematic errors observed at that epoch (see Figure 6.9e). The analysis showed better results and lowest sensitivities for E2, E3 and E4 epochs (Table 6.12).

Volume changes were estimated between the two workflows over the most active parts for various epoch pairs (Section 3.5.3). In particular, volume changes were computed over the back scarp and eastern lobe for the E0-E1, E1-E4 and E4-E5 epoch pairs, as well as over the western lobe for E1-E4 and E3-E4 epoch pairs. These regions are delineated in Figure 6.13. The aforementioned epoch pairs were selected as they show the indicative landslide deformation. Volume change was computed for both GCP-based and MBR-GCP workflows based on the elevation differences plotted in Figure 6.13. The volume change for the back scarp and eastern lobe together with the computed standard errors are presented in Figure 6.15.

The volume change over the back scarp is significantly larger than over the eastern lobe throughout the monitoring period. The volume change over western lobe was comparably smaller, and, for that reason, it is not presented in Figure 6.15. Among all epoch pairs, the highest difference in volume change computation between GCP-based and MBR-GCP results, was observed in E4-E5 with fill volume equal to  $50 \text{ m}^3$  at the back scarp. This was expected because of the observed tilt in E5 MBR-GCP derived DEM (Figure 6.9e). The smallest difference in volume change was derived in E3-E4 over the western lobe. This outcome was also expected as DEMs of E3 and E4 epochs had small systematic errors especially in the middle of the site over the western lobe (Figure 6.9c and d).

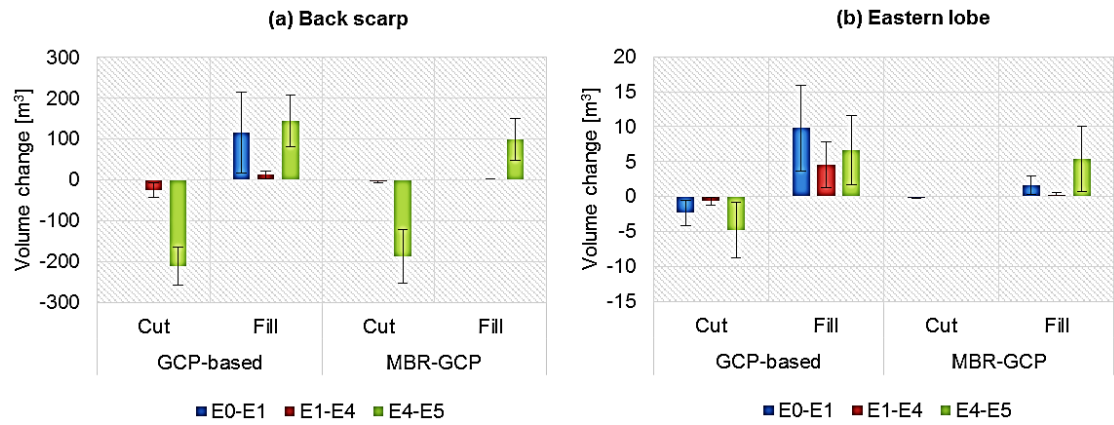


Figure 6.15: Volume change over (a) back scarp and (b) eastern lobe for three successive epoch pairs computed by GCP-based and MBR-GCP elevation differences.

A total volume cut of  $-262.28 \text{ m}^3$  across the selected epoch pairs was calculated from GCP-based results. Out of this total, an average  $-6.95 \text{ m}^3$  difference in volume change between the two workflows was estimated. This corresponds to approximately 3% in volume change computation. Similarly, for a  $312.48 \text{ m}^3$  total fill volume, an average  $24.72 \text{ m}^3$  difference was computed which is equivalent to 8%. In the same manner, volume changes were computed between E4-E5 over the back scarp with the GCP-based and MBR-GCP Sony outputs. Overall, a 8.5% difference in volume change between the two workflows was estimated. Considering that the GCP-based results are closer to the “ground truth”, this percentage indicate the relative lowest detectable volume change that can be derived with the MBR-GCP workflow.

## 6.4 Evaluation of the NCC function

### 6.4.1 NCC implementation with synthetic datasets

Prior to NCC implementation with morphological attributes derived from GCP-based and MBR-GCP products, an experiment was conducted with synthetic epoch pairs to evaluate the performance of the NCC function. To generate the synthetic displacement, translations of:

- 0.050 m in Easting and -0.100 m in Northing (i.e. 0.112 m total magnitude) were applied to Region A (Figure 6.16), approximating to the  $\pm 0.109 \text{ m}$  sensitivity level;
- shifts of 0.455 m in Easting and -0.544 m in Northing (0.709 m total magnitude) applied to Region B (Figure 6.16) in the E0 Panasonic GCP-based DEM, simulating typical inter-epoch movement of the real landslide.

Among all morphological attributes described in Section 3.3, four (*shaded relief*, *slope*, positive *openness* and *curvature*) were used in this experiment. *Shaded relief* was created

with the aid of the ambient occlusion tool in the SAGA GIS package<sup>28</sup>. This applies homogenous illumination to the DEM, providing the best results for quantification of landslide planimetric displacement as evidenced in Fey et al. (2015) and described in Section 3.3.2. The remaining three morphological attributes were all generated using OPALS. In this experiment: a) *slope* indicates the steepest slope angle of the surface (Section 3.3.1); b) positive *openness* represents the minimum angle of a cone fitted in the DEM, as viewed from above the surface (Section 3.3.2, Figure 3.4a); c) *curvature* constitutes the average of minimum and maximum *curvature*, representing concave and convex surface features respectively (Section 3.3.2). Of these, only *shaded relief* and *slope* have been tested with the NCC function in previous studies (Daehne and Corsini, 2013; Lucieer et al., 2014; Travelletti et al., 2014; Fey et al., 2015; Turner et al., 2015).

It should be noted that positive *openness* used in this experiment is not the same as positive *openness* used for stable terrain extraction in the MBR workflow (Section 3.4.2). That *openness* was computed based on the mean value, whereas the positive *openness* used in this experiment was computed based on the minimum value between the 8 directions expressed in Equations 3.25 and 3.26. This was chosen as it more clearly identifies concave breaks in slope. With respect to *curvature*, this is exactly the same morphological attribute used with SIFT for the generation of pseudo GCPs (Section 6.2.1 and Figure 6.5). Overall, these four morphological attributes were chosen, as they were proved to be uncorrelated in Favalli and Fornaciai (2017).

Morphological attributes of *slope*, positive *openness* and *curvature* were computed using a 3x3 pixel radial distance, equivalent to 0.18 m at 0.06 m pixel resolution. Four pairs of morphological attributes were then derived from both the original E0 DEM and the synthetically shifted DEM. Each pair, comprising the pre- and post-event images, was imported into the COSI-Corr function. An explanation of the NCC function is described in Section 3.5.3. After a trial and error procedure, a correlation window size of 64x64 pixels (3.84 m) with a step of 16x16 pixels (0.96 m) and a search patch of 20x20 pixels (1.20 m) were chosen for this experiment. The 16x16 pixels step parameter dictated the spatial resolution of the estimated horizontal displacements. The trial and error procedure showed a spatial resolution less than 0.96 m (by using a lower than 16x16 step value) generated more noise and required more computational time. A trade-off between spatial resolution and computational effort has also been taken into consideration in Daehne and

---

<sup>28</sup> [www.saga-gis.org/en/index.html](http://www.saga-gis.org/en/index.html)

Corsini (2013). The chosen settings ensured that the maximum imposed shift over Region B could be detected and was therefore chosen in line with a priori knowledge of the Hollin Hill landslide movement rates (Uhlemann et al., 2017).

The COSI-Corr function calculates the displacements in Easting and Northing and a signal-to-noise ratio (SNR), indicative of the correlation quality. SNR values closer to unity are indicative of more reliable results. A comparative analysis of the estimated displacements and derived SNRs, obtained with the four morphological attributes, was then performed to determine which of the morphological attributes produced the optimal results. All four morphological attributes underestimated the assigned displacement of Region A, delivering an average displacement  $0.030 \text{ m} \pm 0.027 \text{ m}$  in Easting and  $0.054 \text{ m} \pm 0.030 \text{ m}$  in Northing. For Region B, the closest result to the truth in Easting was delivered by positive *openness*, with an average value of  $0.435 \text{ m} \pm 0.145 \text{ m}$ , whereas *shaded relief* detected the best average displacement in Northing of  $-0.528 \text{ m} \pm 0.131 \text{ m}$ . Statistics of SNR values derived from all attributes are reported in Table B.1 in Appendix B.

Figure 6.16a and b depict the SNR results, derived from positive *openness* and *shaded relief* respectively, over stable terrain outside Regions A and B. Figure 6.17 presents the boxplots of the comparative SNR analysis. SNR values close to zero (Figure 6.16b) indicated decorrelation, which is also illustrated as outliers in the boxplot of *shaded relief* over stable terrain, whereas the other three morphological attributes were less noisy (Figure 6.17). For Regions A and B all morphological attributes with the exception of *curvature* produced similar boxplots. The boxplots reveal greater variation in SNR in Region B than in Region A (Figure 6.17) possibly due to the noise caused by the extreme local surface variations around Region B. Overall, *slope* and positive *openness* provided comparable displacements and noise levels. Thus, both attributes were chosen for the estimation of Hollin Hill landslide motion.

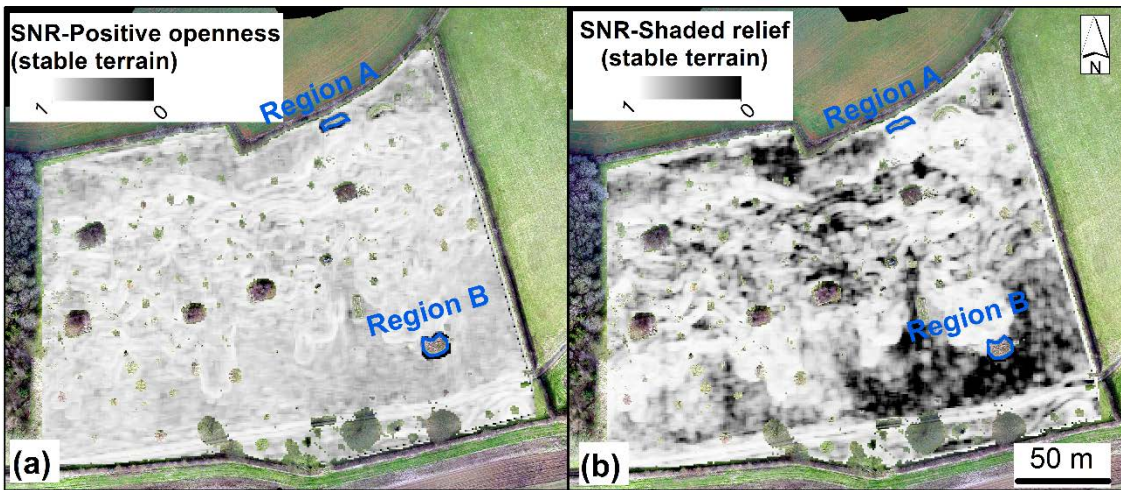


Figure 6.16: SNR maps derived from Cosi-Corr with (a) positive openness and (b) shaded relief generated from synthetic datasets of E0 Panasonic GCP-based DEM (Peppia et al., 2017).

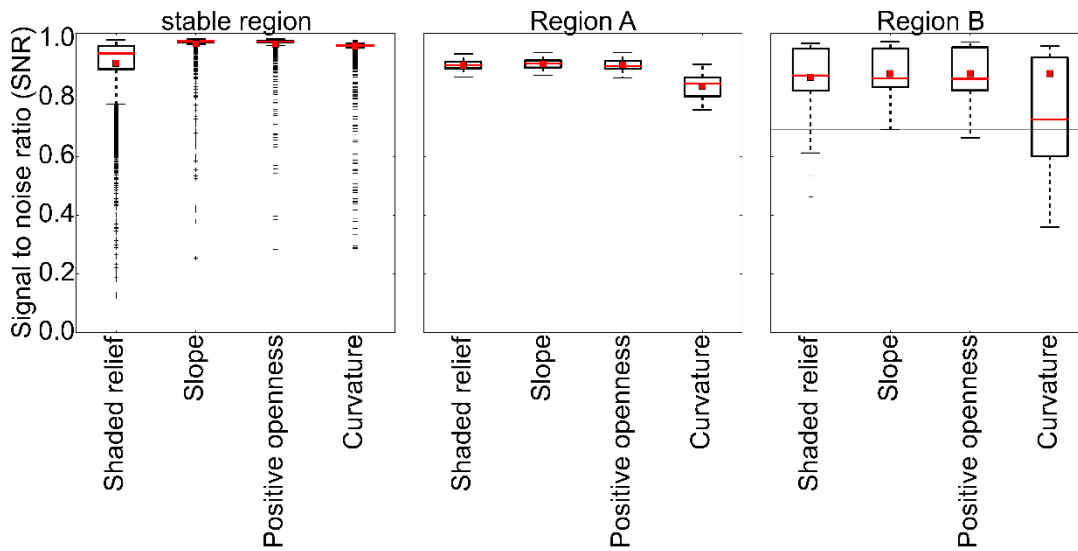


Figure 6.17: Box plots for stable terrain, Regions A and B, as derived from the implementation of COSI-Corr with *shaded relief*, *slope*, *positive openness* and *curvature* applied to synthetic datasets. The median is displayed as a red line, the mean as a red rectangle, the whiskers as black horizontal lines and the outliers as black crosses (Peppia et al., 2017).

#### 6.4.2 Sensitivity analysis of the NCC function with real datasets

*Slope* and positive *openness* together with the COSI-Corr function, was applied to successive epoch pairs of the Hollin Hill landslide. A series of experiments were carried out to compare the COSI-Corr estimations produced with these two morphological attributes, and examine the selection of COSI-Corr settings with respect to the real motion. For this analysis, datasets of the GCP-based Panasonic experiment were utilised.

In the first experiment, the settings in COSI-Corr were the same used with the synthetic datasets (i.e. correlation window: 64x64, step size: 16x16 and search patch: 20x20, see Section 3.5.3 for description). The COSI-Corr result was cross-validated with the surface displacements calculated from 27 sample points, manually located on the multi-temporal derived orthophotomosaics (Figure 6.21). These points were identified on characteristic surface breaks evenly distributed across the site with displacement magnitude spanning cm to m-level. For instance, a 0.065 m and a 1.128 m maximum displacement was observed in E2-E3 and E4-E5 respectively. This independent validation indicated the sensitivity of the NCC function to different displacement magnitudes.

The scatterplots in Figure 6.18 show a general systematic overestimation of the displacement magnitude derived from COSI-Corr. Some scattered points fell within the  $\pm 0.109$  m 3D sensitivity level (i.e. maximum sensitivity in Table 6.12 for GCP-based experiment) shown in grey, especially for E1-E2 and E2-E3 epoch pairs. Significant movement was observed mostly between E0-E1, E3-E4 and E4-E5 epoch pairs, which is also evidenced from the elevation differences in Figure 6.13a, b and c.

The NCC function with positive *openness* (Figure 6.18a) delivered results in good agreement with the manual measurements (closer to the straight line) for small displacements. However, it miscalculated the surface movement of the last epoch pair, when compared to the NCC estimations derived from *slope* (Figure 6.18b). There are a few outliers within the grey zone possibly caused by the vegetation change in both scatterplots (Figure 6.18a and b). Due to insignificant landslide motion in E1-E2, E2-E3 and E3-E4 epoch pairs and additional noise generated from grass growth, the comparison was also repeated for the E1-E4 pair.

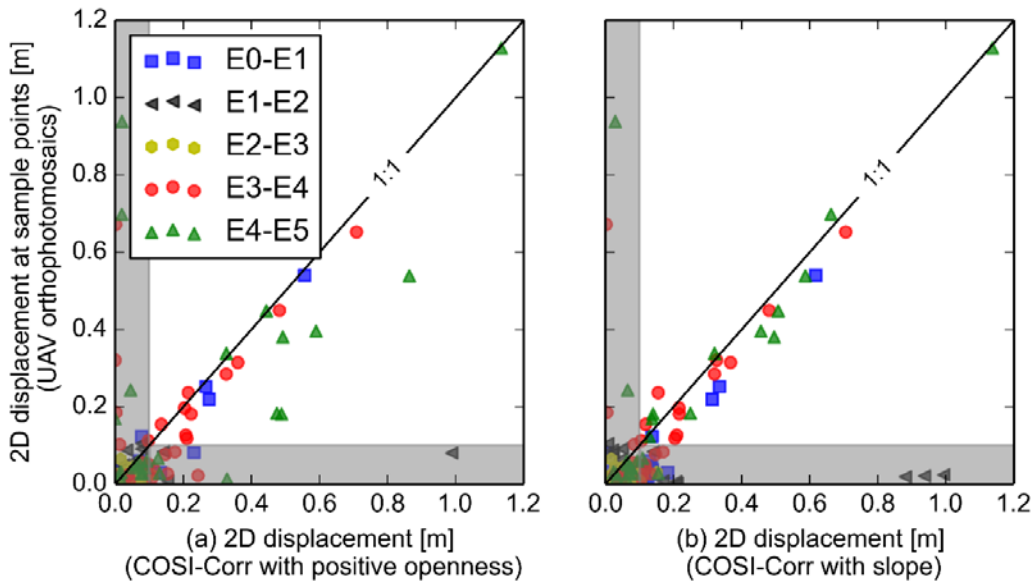


Figure 6.18: Scatterplots of estimated surface displacements determined by COSI-Corr with (a) positive *openness* and (b) *slope* plotted against manual observation per epoch pair (Peppia et al., 2017).

The RMSEs, computed from the manual observations and the NCC estimations, were lower in E0-E1 and E1-E4 epoch pairs when implemented with positive *openness* than *slope* (see Table B.2 in Appendix B). For the E4-E5 epoch pair the converse was true (see RMSEs in Table B.2, Appendix B).

This first comparison showed that COSI-Corr performs differently with respect to the displacement magnitude and the morphological attribute used. For instance, *slope* does not illustrate the distinctive surface characteristics to such a degree as positive *openness*. As a result, after significant surface change, pre and post *slope* maps show a better correlation aiding the NCC performance in delivering less noisy estimations. The NCC surface displacements estimated with positive *openness* and *slope* over the eastern lobe for E4-E5 epoch pair are depicted in Figure 6.19a and b respectively. The voids observed in Figure 6.19a indicate the decorrelation produced by positive *openness* mostly over surface breaks, around vegetated areas and monitoring sensors. The NCC implemented with *slope* resulted in a smoother surface displacement map without many voids over stable terrain around eastern lobe (Figure 6.19b).

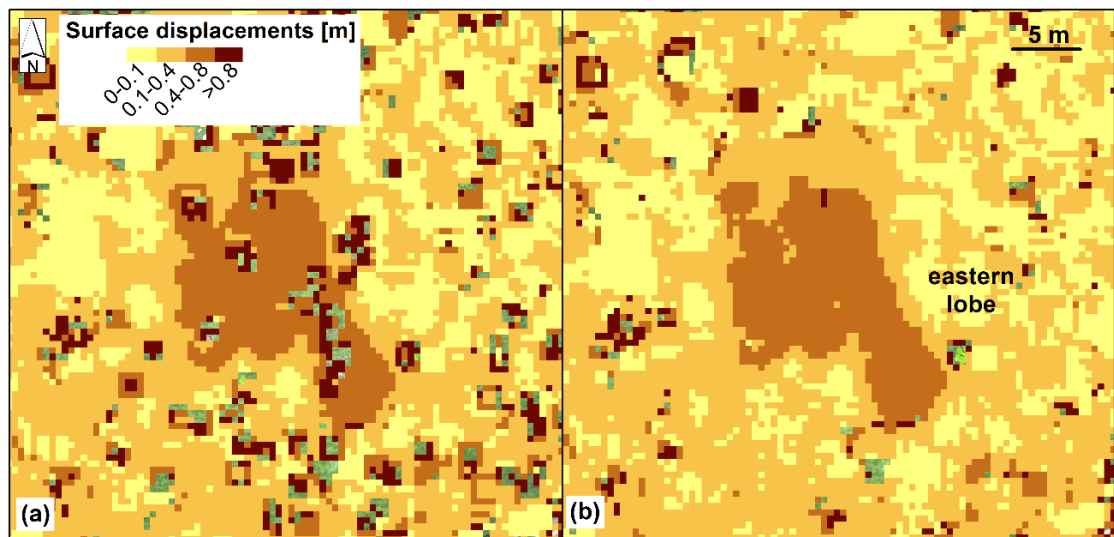


Figure 6.19: COSI-Corr results over eastern lobe for E4-E5 epoch pair derived with morphological attributes of (a) positive *openness* and (b) *slope*.

To further investigate the NCC sensitivity, additional analysis using the morphological attribute of *slope* for the E4-E5 epoch pair was carried out. This compared results from three correlation windows, specifically 128x128, 64x64 and 16x16, without altering the other COSI-Corr settings, against the manual observations (see Figure B.10 in Appendix B). Of all, the small window produced the highest noise, as erroneous correlation was resolved. This incorrect correlation was possibly produced from the same features that could be identified within the vicinity of the small window size (Travelletti et al., 2014; Fey et al., 2015). This was also called a “self-similarity” problem in Fey et al. (2015). On the other hand, the 128x128 pixel correlation window delivered a 0.323 m RMSE higher than the 0.185 m RMSE computed with the 64x64 pixel window, when compared against manual observations. Moreover, the NCC function with the largest correlation window increased the spatial voids around vegetated regions, reducing the overall coverage of the surface displacement map.

In a similar manner, a test was conducted to verify the choice of the optimal search patch. Utilising a 64x64 pixels correlation window with a 16 pixels step parameter, COSI-Corr was repeated for three different search patches of 10x10, 20x20 and 30x30 pixels. In the E4-E5 epoch pair, the smallest search patch could not generate a displacement higher than 0.8 m. The largest search patch overestimated the movement producing a 2.9 m maximum displacement. COSI-Corr results under various window sizes and search patches are mapped in Figure B.11 in Appendix B.

A final experiment examined the impact of the moving kernel size, which is required for the generation of *slope* and positive *openness*, with respect to the NCC performance. This test compared the displacements derived from manual observations against the displacements of the COSI-Corr outcome from kernel sizes within the range of 3x3-21x21 pixels. The computed RMSEs of this comparison are presented in Figure 6.20 as derived from the GCP-based Panasonic E4-E5 datasets. The analysis showed that the largest kernel size did not suppress the noise level produced by grass growth in the E4-E5 epoch pair for both morphological attributes. In addition, no significant variation in RMSE values was observed for the result of positive *openness*. Conversely, the NCC outputs computed with *slope* and large kernel sizes overestimated the real displacements, and produced higher RMSE values, approximately three times the  $\pm 0.109$  sensitivity level.

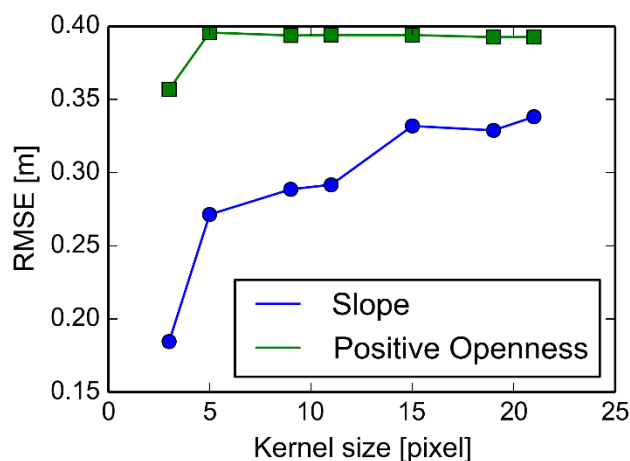


Figure 6.20: RMSEs computed from the differences between manually observed displacements and COSI-Corr displacements derived with various kernel sizes for morphological attributes of E4-E5 epoch pair.

Overall, the sensitivity and comparable analysis implemented with COSI-Corr indicated that the 3x3 pixels kernel size produced the closest to the actual horizontal displacement. Through the analysis the derived optimal COSI-Corr settings included a 64x64 pixels correlation window, a 20x20 pixels search patch and a 16 pixels step parameter. Among all morphological attributes examined, positive *openness* provided NCC outcome with the lowest noise levels over stable terrain for small displacements (E0-E1 and E1-E4 epoch pairs). For large displacements in the E4-E5 epoch pair *slope* generated the lowest noise and estimated closer to the real displacements.

## 6.5 2D landslide motion and validation

### 6.5.1 GCP-based and MBR-GCP estimations of 2D displacements

#### *NCC implementation in COSI-Corr*

The NCC function in COSI-Corr was applied to both GCP-based and MBR-GCP derived morphological attributes of positive *openness* and *slope* with the settings described in the previous Section. Positive *openness* was used for E0-E1 and E1-E4 epoch pairs, while *slope* was used for the last epoch pair. The 2D displacement maps are presented in Figure 6.21. Blue hatched polygons represent areas with reliably estimated surface displacements, of SNR greater than 0.7. This value is equivalent to the lowest whisker of the *slope* boxplot (horizontal line in Region B in Figure 6.17), representing the outlier threshold as:

$$w = Q_1 - 1.5(Q_3 - Q_1) \quad (6.1)$$

where  $Q_1$  and  $Q_3$  the 25% and 75% percentiles of the data respectively. The lowest whisker of the *slope* was equal to 0.69 and the lowest whisker of the *openness* box plot was calculated equal to 0.66. Because these values generated similar SNR polygons, the final outlier threshold was rounded to 0.7. There are a few erroneous displacements, mostly at the edges of the study site, around vegetated areas and outside the blue hatched polygons for both experiments. Moreover, SNR values lower than 0.7 outside of landslide deformation in the E4-E5 epoch pair indicated that the grass growth affected the NCC function's reliability. As already discussed, voids on the maps were caused by decorrelation mostly over extreme surface deformation (e.g. back scarp in Figure 6.21c and f).

With regard to the MBR-GCP displacements, the best outcome was delivered from the E1-E4 epoch pair (Figure 6.21e). The good agreement between E1-E4 GCP-based and MBR-GCP displacement estimations is illustrated in Figure 6.22b. The scatterplots in Figure 6.22 correlate the displacements that fell within the blue hatched polygons excluding those that were lower than the 0.221 m MBR-GCP sensitivity level (Table 6.12).

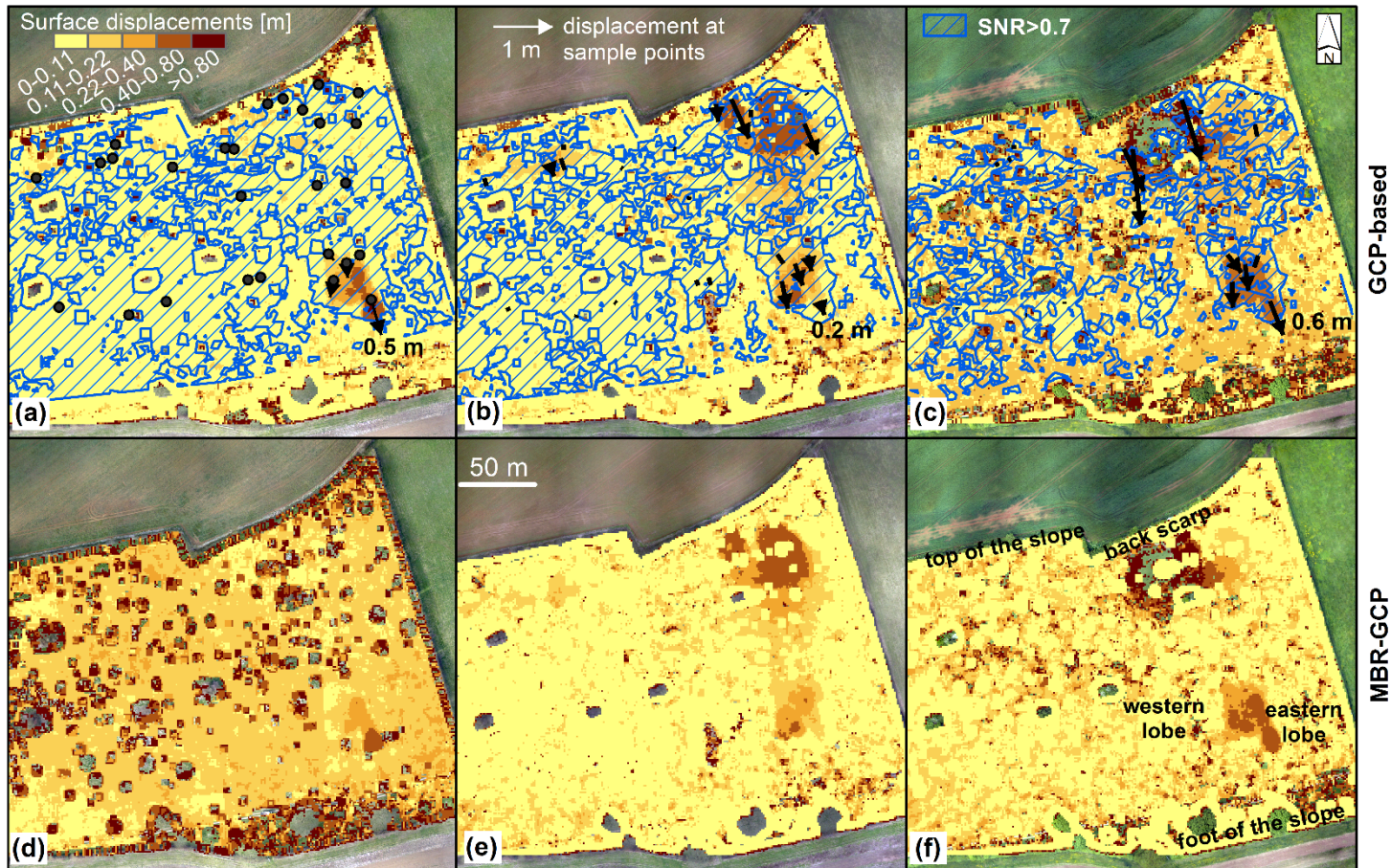


Figure 6.21: Maps of surface displacements of (a and d) E0-E1, (b and e) E1-E4 and (c and f) E4-E5 epoch pairs from GCP-based and MBR-GCP datasets. Manually derived planimetric vectors at sample points are also superimposed.

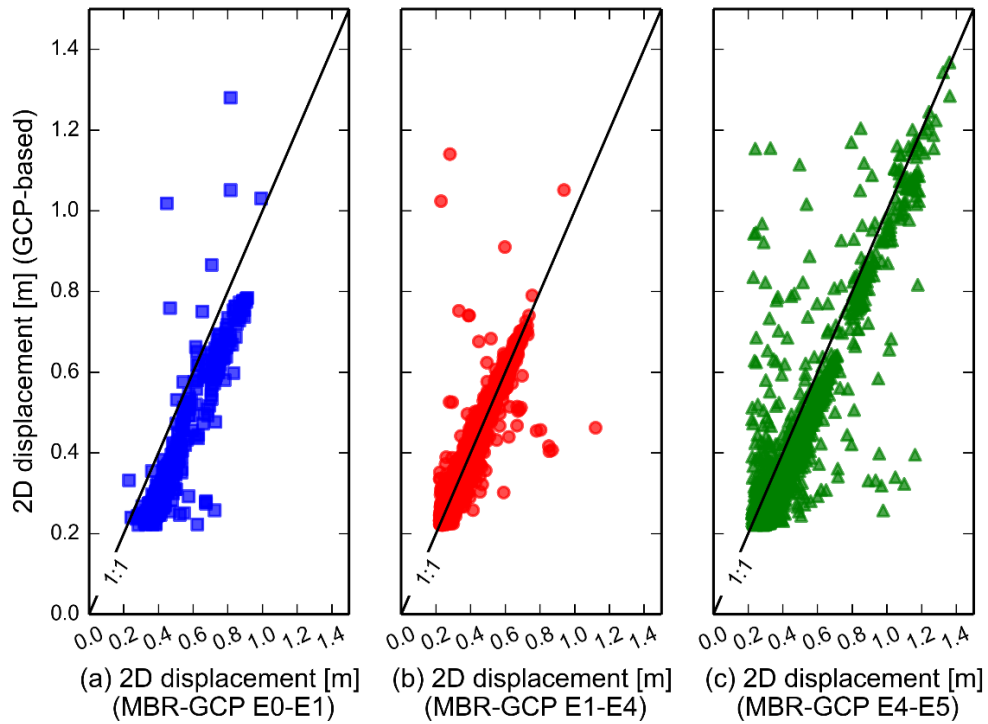


Figure 6.22: Scatterplots of 2D displacements between GCP-based and MBR-GCP results for three consecutive epoch pairs.

However, for the E0-E1 and E4-E5 epoch pairs a general systematic overestimation was observed. An overestimation especially over stable terrain is seen in Figure 6.21d, compared to Figure 6.21a. Conversely, according to the scatterplots in Figure 6.22a and c, MBR-GCP results underestimated the large displacements, especially over the eastern lobe (Figure 6.21d and f). This mixed outcome could possibly be attributed to systematic biases observed in E1 and E4 DEMs and discussed in Section 6.2.2).

COSI-Corr allows for the derivation of a vector field map from the 2D surface displacements by averaging them within a specified window size. The vector field maps corresponding to the 2D displacements of Figure 6.21 are displayed on Figure B.12 in Appendix B. The vectors were averaged within a window size of 11x11 pixels after a trial and error procedure. Even though, this window size removed spurious vectors, many remained at the edges of the site and around vegetated areas. As expected, erroneous vectors were observed in E0-E1 epoch pair of the MBR-GCP experiments (Figure B.12d in Appendix B) for the reasons explained previously. The vector field map provides additional directional information to the landslide kinematics across the whole site compared to the motion at discrete locations (e.g. GNSS pegs in Figure 6.24).

### *NCC implementation in CIAS*

To further investigate significant landslide deformations, the GCP-based E5 positive *openness* was superimposed over the corresponding map from E0 and is presented in Figure 6.23a and b. Figure 6.23c illustrates that narrow angles of *openness* can distinguish surface undulations sliding down-slope. For instance, point 1 moved 1.10 m along the profile AB towards the south. To visualise these structures a threshold of  $63^\circ$  was applied to the *openness* maps (Figure 6.23a and b). Different thresholds can visualise different morphological features. The threshold of  $63^\circ$  was derived with the aid of visual inspection along profiles at multiple locations over active parts of the landslide. Positive *openness* also captured the surface rupture that occurred at the top of the slope between E4 and E5 epochs (Figure 6.13c and Figure 6.21c).

Coordinates of distinctive features were identified in E0 positive *openness* and used as input data to the NCC function implemented in CIAS (Section 3.5.3, CIAS (2012)), together with the E0 and E5 positive *openness* maps (Section 3.5.3). The sizes of correlation window and search patch set in COSI-Corr were also used in CIAS. Unlike COSI-Corr, CIAS allows individual feature tracking without generating a continuous displacement map. The planimetric vectors of the distinctive features are plotted in Figure 6.23a and b, as automatically determined with CIAS. Manual cleaning to remove spurious vectors was also necessary. This process was semi-automated by application of threshold parameters. For example, vectors with length lower than  $\pm 0.109$  sensitivity level were removed. In addition, vectors with azimuth within the range of  $[270^\circ-90^\circ]$  were excluded from Figure 6.23. This was based on previous knowledge about the landslide motion (Uhlemann et al., 2017). Spurious vectors were observed at the edges of the back scarp, possibly generated by rotational failures as investigated by BGS (Uhlemann et al., 2016). Perhaps the erroneous vectors, previously discussed in Section 6.4.2, were also caused by the “self-similarity” issue between the two *openness* maps. These errors are not attributable to misalignment biases as the Panasonic GCP-based datasets delivered an approximate 0.02 m co-registration accuracy (i.e.  $e_{\text{co-reg}}$  Table 6.10).

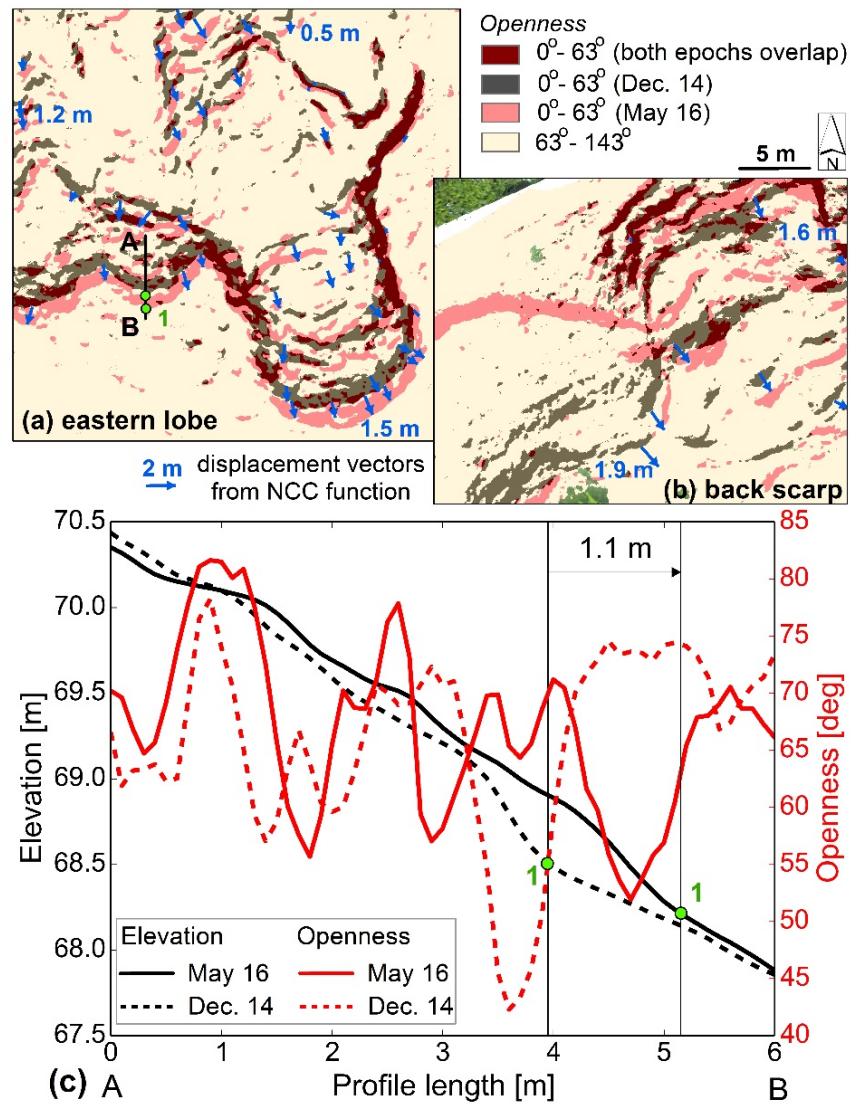


Figure 6.23: Detailed view of E0 and E4 positive *openness* maps over (a) eastern lobe and (b) back scarp with elevation and *openness* plotted along (c) Profile AB from Panasonic GCP-based datasets (Peppia et al., 2017).

### 6.5.2 Comparison with GNSS and rainfall observations

The 27 features, manually detected and used in Section 6.4.2 to cross-validate the NCC function, were also used to derive the landslide movement rate from GCP-based and MBR-GCP datasets and compared to movement estimated from GNSS permanent pegs (Section 4.3.2). The planimetric vectors (Figure 6.24) indicate 2D incremental displacement between E0-E4 (Figure 6.24a and b) and between E0-E5 (Figure 6.24c and d) epoch pairs. The start positions are coordinates of the reference E0 for both the 27 sample points and the GNSS pegs. Figure 6.24a and c illustrate the movement rate as computed from GCP-based Panasonic datasets whereas Figure 6.24b and d present the MBR-GCP results. The UAV and GNSS field campaigns did not coincide with the exception of the reference E0 (15/12/2014, Table 5.1). Because there were no GNSS observations for E4, the displacements were derived by interpolating the corresponding observations from the GNSS campaigns from the 15/12/2015

and 20/03/2016. Similarly, E5 GNSS displacements were calculated by means of interpolation from the 21/04/2016 and 30/06/2016 GNSS observations.

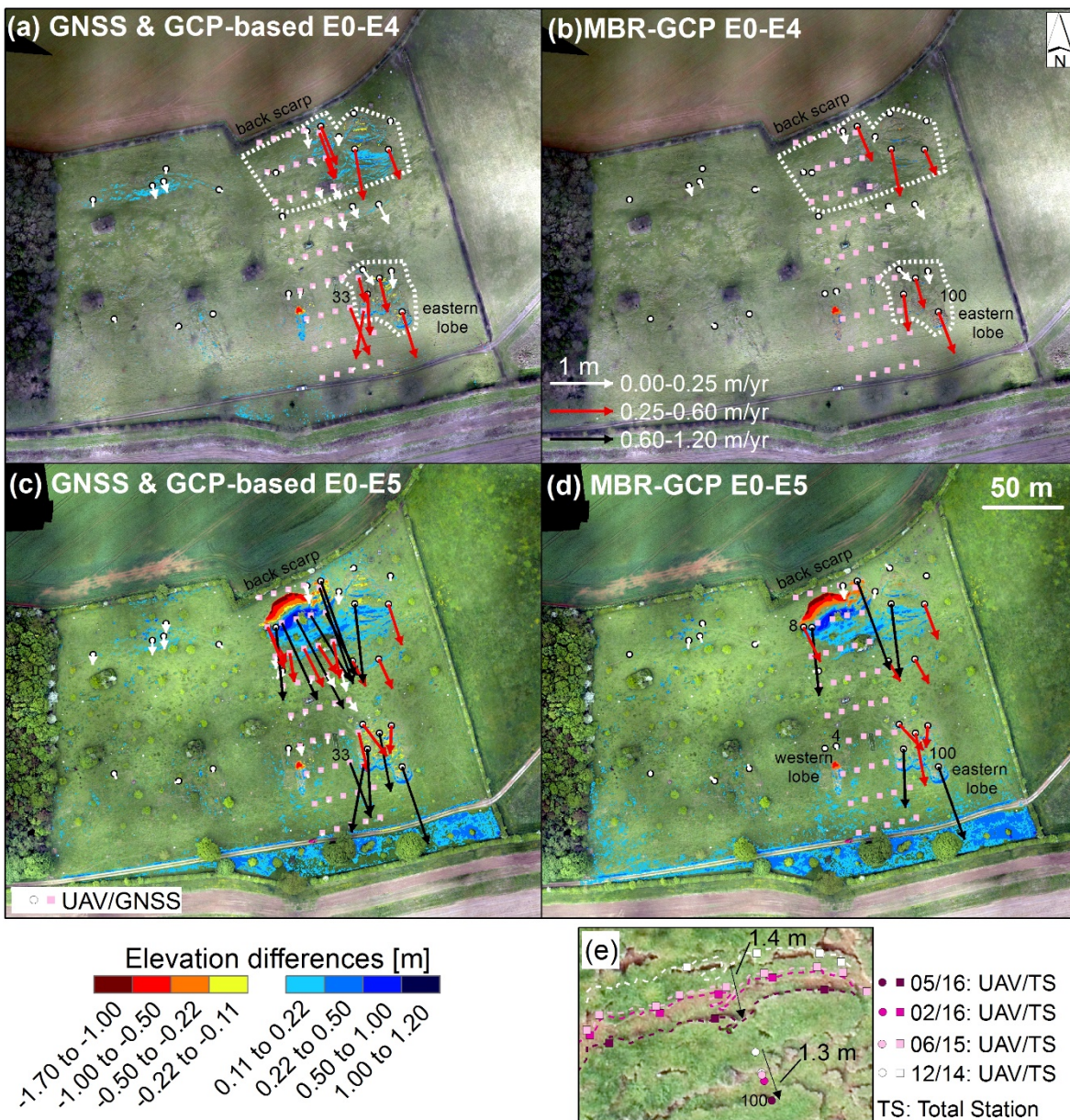


Figure 6.24: Elevation differences and planimetric vectors indicating the horizontal 2D incremental displacement rate of E0-E4 and E0-E5 epoch pairs derived from GNSS, total station, GCP-based and MBR-GCP observations.

Utilising 27 sample points, the E0-E5 displacement rates between the GCP-based and MBR-GCP workflows gave a mean difference of  $-0.05 \text{ m} \pm 0.03 \text{ m}$ . The E0-E4 displacement rates delivered a mean difference of  $-0.03 \text{ m} \pm 0.02 \text{ m}$  between the two workflows. The smaller difference in E4 was expected, as the E4 MBR-GCP products had small average errors compared to other epochs (e.g. lower sensitivity of E4 compared with E5 in Table 6.12). The MBR-GCP workflow slightly underestimated the movement rate for typically small magnitudes (e.g. the motion at the upper part west of the site shown in Figure 6.24b and d versus Figure 6.24a and c respectively).

With respect to the motion, the two workflows provided good agreement in directions. Satisfactory results were also achieved compared to the directions derived from GNSS observations (Figure 6.24a and c versus Figure 6.24b and d). Further, Figure 6.24e verifies the direction of both workflows, by depicting the movement of a crack close to point 100. This movement was delineated with multi-epoch total station observations, in combination with the GCP-based orthophotomosaics. The displacement in Figure 6.24e can also be cross-correlated with the movement illustrated in Figure 6.23a, as derived from the CIAS implementation. This verified the direction and magnitude of landslide motion over the eastern lobe as estimated with different approaches.

One difficulty with the Panasonic imagery was that GNSS permanent pegs could not easily be identified on the orthophotomosaics. The detection was not feasible because of the pegs' small size (Section 4.3.2) related to the estimated GSD (i.e. approximately 0.03 m across all epochs in Table 5.1). Only two GNSS pegs could be detected, peg 8 and peg 4, shown in Figure 6.24d. For these two, the incremental displacement and elevation differences from E0 were calculated from GNSS, GCP-based and MBR-GCP observations.

Figure 6.25 displays the time-series for peg 8 only as peg 4 moved less than the  $\pm 0.109$  m sensitivity level; hence it was excluded from the graph. The x-axis shows the exact dates of UAV acquisitions (Table 5.1) which are different from the GNSS surveys. As the GNSS observations constitute the "ground truth" datasets, a piecewise linear and a polynomial of degree 3 were fitted to the horizontal and the elevation differences respectively (blue curves in Figure 6.24). In the horizontal displacements, R-squared was equal to 0.39 for the first part and 0.89 for the last part of the linear curve. A value 0.89 of R-squared elevation differences was estimated. Due to limited GNSS observations, R-squared was not always close to unity. However, the modelled curves were used to compare the two approaches. The comparison against GNSS curves showed good agreement of the 3D surface changes with an estimated 0.081 m 3D RMSE for the differences between both GCP-based and MBR-GCP approaches for peg 8. This is lower than the  $\pm 0.109$  m sensitivity.

With respect to the Sony imagery, a GSD of approximately 0.02 m (Table 5.1) allowed for identification of 20 out of the total 45 permanent GNSS pegs on the E5 orthophotomosaic. However, due to darker E4 Sony imagery, only 10 common GNSS pegs were detected on both E4 and E5 orthophotomosaics. Comparison of the 3D movement from the three types of observations was performed. To achieve this, the 3D coordinates of GNSS pegs were interpolated for the exact dates of E4 and E5 UAV campaigns. A 0.11 m 2D RMSE and a

0.06 m 3D RMSE were computed from the differences of the 2D motion and elevation respectively between GNSS and GCP-based datasets. Moreover, RMSEs derived from the comparison of GNSS against MBR-GCP observations (0.09 m 2D RMSE, 0.05 m 3D RMSE) delivered similar agreement. This independent validation showed RMSEs lower than the sensitivity levels reported in Table 6.11, providing confidence to the MBR-GCP workflow.

Figure 6.25 displays the daily effective rainfall during the eighteen-month monitoring duration, as observed from the weather station at Hollin Hill (Figure 4.7f) and calculated by BGS (Uhlemann et al., 2016; Uhlemann et al., 2017). The effective rainfall represents the remaining water level that is derived by subtracting potential evapotranspiration from the absolute rainfall (Shaw, 1999). Evapotranspiration indicates water loss due to evaporation to the atmosphere and transpiration from vegetation (Shaw, 1999). Figure 6.25 also presents the 3D movement of peg 8, located at the back scarp, and point 100 at the eastern lobe. Figure 6.25 shows how the top and bottom parts of the landslide responded differently in relation to the rainfall variations. In particular, after a relatively dry winter in 2015, with lower than  $\pm 10$  mm/day effective rainfall, peg 8 was displaced less than the  $\pm 0.109$  m sensitivity level until the start of the winter 2016. This indicated the relatively stable upper part of the site. In contrast, point 100 over the eastern lobe moved approximately 0.16 m in 3D, showing a steadily linear motion, but with no significant horizontal displacement.

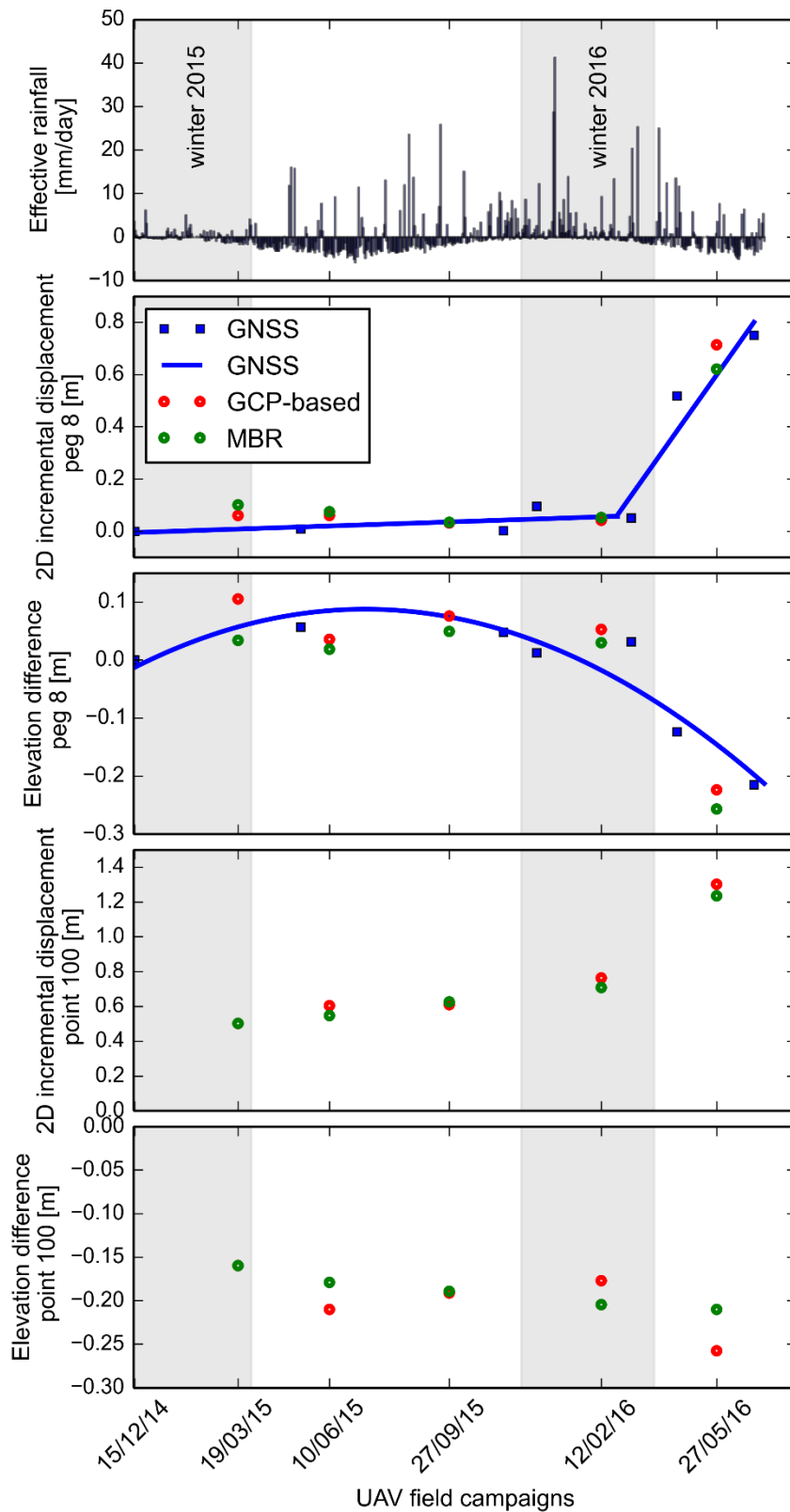


Figure 6.25: 2D incremental displacements and elevation differences from GNSS, GCP-based and MBR-GCP datasets over peg 8 and point 100. Effective rainfall is superimposed.

However, after the comparably wet spring and summer period of 2015 together with the intensive rain during winter 2016, the landslide was dramatically activated. For instance, point 100 was displaced almost 0.5 m from 02/16 to 05/16 (Figure 6.23, Figure 6.24 and Figure 6.25). Peg 8 was pushed downwards 0.6 m by the failing material from the top of the slope within the same period (Figure 6.24 and Figure 6.25). This activation/reactivation period of the landslide was previously investigated by BGS with multiple ground-based observations acquired since 2009 (Uhlemann et al., 2016; Uhlemann et al., 2017). As mentioned in Uhlemann et al. (2016) the Hollin Hill landslide reactivation has been triggered by a combination of factors. In particular, intensive rainfall over long durations increased soil moisture causing high stress to the geological materials. This stress weakened the material leading to failure. Rotational failures at the top forced the material to prograde downwards adding extra pressure. This can possibly explain why the displacement over the lobes were relatively greater than the movement at the top of the slope, even during non-active periods before the 2016 winter. This phenomenon occurred in previous years as explained in Uhlemann et al. (2016). The rainfall fluctuations also affected the pore water pressure levels in the subsurface causing acceleration/deceleration of the landslide (Uhlemann et al., 2016). For example, higher movement rates were observed over the eastern lobe after 02/2016, as shown in Figure 6.24. This acceleration was possibly triggered by the significant rainfall event at the beginning of winter 2016 (Figure 6.25).

It is noteworthy that motion was also observed at GNSS pegs located between the two lobes (e.g. peg 33 in Figure 6.24). This region was characterised as stable/smooth terrain when generated from the openness mask with the MBR workflow (Figure 6.4a). No surface fissures were apparent on the orthophotomosaics, thus the smooth characterisation was valid. However, the instability of the subsurface, caused by the factors discussed previously, most probably resulted in peg's 33 motion. This peg is located in close vicinity to the active eastern lobe (Figure 6.24); hence, it was more affected than other pegs located within the smooth terrain. It is possible that, while generating pseudo GCPs based on the MBR approach (Section 6.2.1), the subsurface movement was propagated into the process. As a result, a systematic pattern was observed at the CPs in Figure 6.9 with a N-S direction similar to the motion's direction (Figure 6.24). Moreover, due to landslide acceleration after intensive rainfall in winter 2016, the directional bias was even more pronounced in Figure 6.24d and e giving a higher georeferencing 3D RMSE in E5 (Table 6.7).

### 6.5.3 Camera stability checks

The unstable SfM-MVS solutions with respect to different markers accuracies is previously discussed in Section 6.2.2 and Figure 6.11, with or without the inclusion of GCPs. That test showed the variation of 3D RMSEs computed at CPs. Here, an additional test describes the variation of focal length as estimated from the three experiments, a) GCP-based, b) MBR-GCP and c) MBR-UAV in *PhotoScan*. The focal length values are displayed in Figure 6.26 with a continuous line for the GCP-based and a dashed line for the MBR-based workflows.

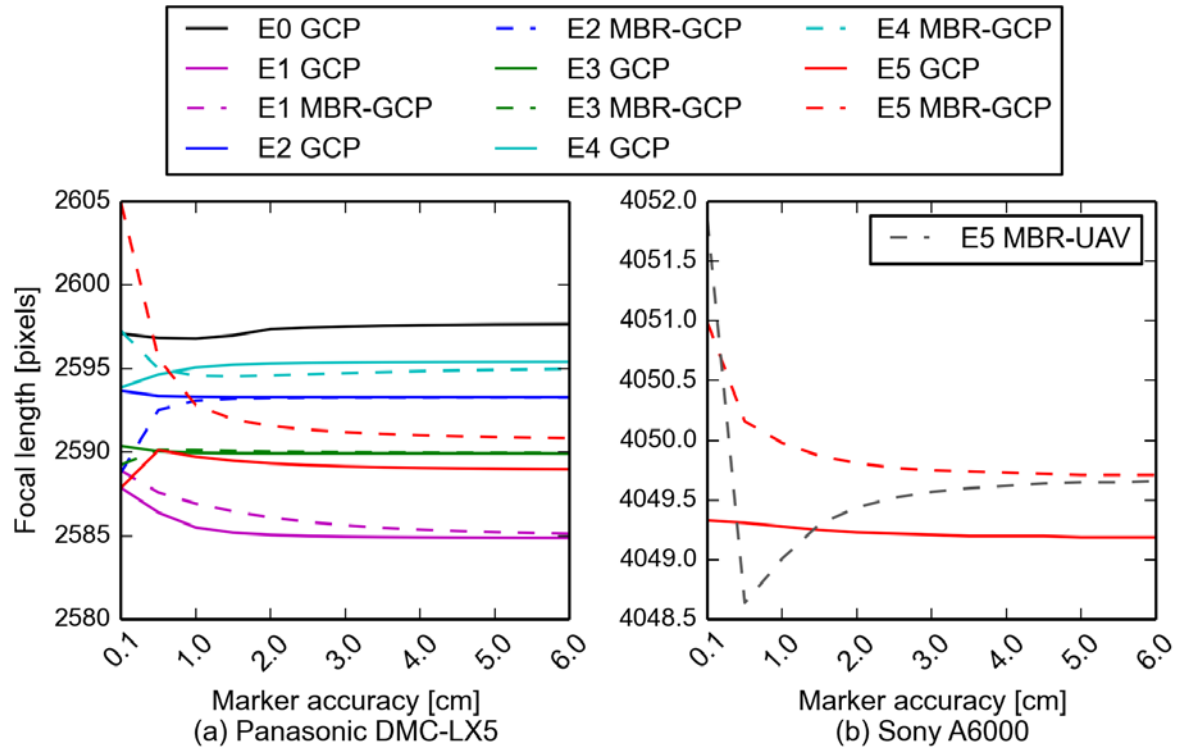


Figure 6.26: Focal lengths estimated by different workflows across all epochs for (a) the Panasonic DMC-LX5 and (b) the Sony A6000.

With respect to the Panasonic GCP-based results, a maximum of 12 pixels was observed between E0 and E1 epochs (Figure 6.26a). This, multiplied by the 0.03 m GSD (Table 5.1), corresponds to 0.36 m ground distance. The second largest difference was observed between E0 and E5 epochs equal to eight pixels, equivalent to 0.24 m ground distance. Two possible reasons might have caused these large discrepancies. Firstly, Panasonic DMC-LX5 was extensively used for UAV imagery acquisitions after 2012, with the most frequent usage during 2014 and 2015. Hence, the numerous landings might have caused the internal units of the camera to suffer sudden shocks. This could have altered the camera's IOPs. Secondly, inconsistent camera IOP solutions from SfM-MVS self-calibrating bundle adjustments may have contributed to the discrepancies in focal length across epochs. This inconsistency is a known issue as discussed and investigated in Section 3.2.6 and Section 5.2.2 respectively.

Regarding the variations of the focal length values derived from the GCP-based and MBR-GCP workflows, it can be noted that E1 and E5 provided the highest discrepancies (Figure 6.26a). DEMs from these two epochs showed high errors in Figure 6.9a and Figure 6.9e. In addition, high  $s_2$  sensitivities were also estimated in E1 and E5 (Figure 6.13). Thus, it is possible that E1 and E5 MBR-GCP datasets suffer from biases either because of inferior imaging network configurations or the fact that landslide motion has been integrated into the observations (also mentioned in Section 6.2.2). The latter is also seen through GNSS observations in Section 6.5.2.

Figure 6.26a shows variations of the focal length values in relation to the marker accuracy for each epoch. This shows the sensitivity of the SfM-MVS self-calibrating bundle adjustment to marker accuracy. A similar sensitivity is presented in Section 6.2.2. In Figure 6.26a, the highest variations are observed for marker accuracy within the range of 0.001 m to 0.020 m. For instance, the E5 curve displays an exponential decrease in Figure 6.26a, indicating instability of the SfM-MVS solution, which also corresponds with the estimated high errors (Section 6.2.2 and 6.3.1). Interestingly, similar exponential curves are observed in Figure 6.26b for E5 MBR-GCP and MBR-UAV experiments conducted with the Sony A6000. However, for the Sony experiments, focal length values vary within a 3.5 pixels range that correspond to 0.07 m ground distance for a 0.02 GSD (Table 5.1). This shows the sensitivity of the SfM-MVS self-calibrating bundle adjustments in relation to different cameras.

To independently validate the camera's internal stability across the monitoring period, indoor calibration tests were carried out before, during and after the UAV field surveys. The results of the first indoor calibration experiment conducted, before the UAV imagery acquisitions, are presented in Section 4.4.2. For the Panasonic DMC-LX5 two additional calibration tests were carried out during the monitoring period of 26/02/15 and 26/09/15. One extra test was conducted post UAV fieldwork on 22/07/17. For Sony A6000 two calibration tests were conducted one before (26/09/15) and one after the UAV fieldwork (22/07/17). The estimated parameters of 22/07/17 calibration for both cameras are reported in Table B.3 in Appendix B. All calibrations were processed in *PhotoModeler* using the calibration shown in Figure 4.11a with the exception of the 26/09/15 test which was processed in *PhotoScan* which used the test field shown in Figure 4.11b. To bring all solutions under the same bundle adjustment, the DBAT software was adopted to reestimate the IOPs, as explained in Section 4.4.2. Both cameras radial distortion curves are displayed in Figure 6.27.

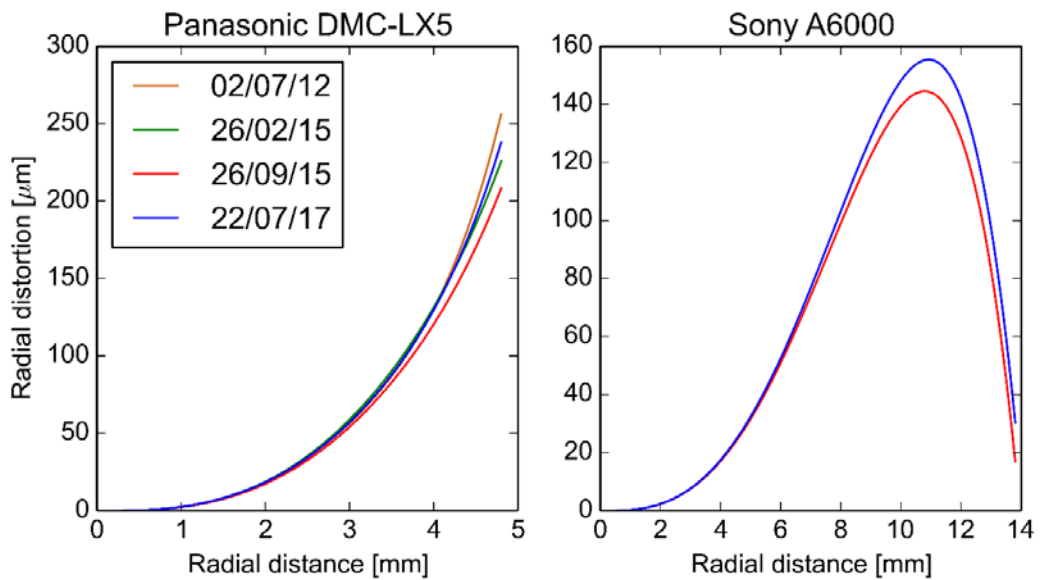


Figure 6.27: Radial distortion curves of the on-board Quest-300 UAV used cameras.

Considering Panasonic DMC-LX5 results, the highest difference (approximately  $47\mu\text{m}$ ) was observed between 02/07/12 and 26/09/15 at the outer corners of the Panasonic image (Figure 6.27). This is equivalent to 23.5 pixels (1 pixel equals to  $2\mu\text{m}$ ) corresponding to 0.705 m ground distance for a 0.03. m GSD. Such large deviation possibly stemmed from the extensive use of the camera during the monitoring period. In contrast, at two thirds of the radial distance, the distortion only varies  $6\mu\text{m}$  which is equal to 0.09 m ground distance. For the Sony A6000, the highest deviation was observed closer to two thirds of the radial distance, equal to  $11\mu\text{m}$ , which gives 0.06 m (1 pixel corresponds to  $3.9\mu\text{m}$ ). It should be noted that the Sony A6000 was used less extensively than the Panasonic DMC-LX5.

## 6.6 Summary

Chapter 6 has demonstrated the performance of a morphology-based monitoring strategy with imagery collected over an active landslide at the Hollin Hill observatory site. Images were acquired with a Panasonic DMC-LX5 and a Sony A6000 fitted on a Quest-300 UAV. The chapter described data acquisition and all necessary tasks for tuning *PhotoScan's* settings and generating free from vegetation multi-epoch DEMs. Co-registration, 3D error boundaries and 3D surface change were investigated for various scenarios.

Results of the MBR workflow with the inclusion of five GCPs at the reference epoch were compared against benchmark GCP-based SfM-MVS co-registration outputs. This comparison showed that a  $\pm 0.221$  m minimum 3D change could be detected with the MBR workflow, which is double the sensitivity levels of the benchmark GCP-based results. Below these limits, systematic biases were observed. These included misalignment errors that deformed the DEMs and caused underestimation of the real 3D surface change (e.g. E1 and E5 datasets). It is possible that errors were introduced as a combination of numerous factors, namely the automatic generation of pseudo GCPs with various uncertainties, inferior imaging network configurations, change in vegetation, the landslide motion itself and the instability of the SfM-MVS self-calibrating bundle adjustment solutions. However, there were cases (e.g. E2, E3 and E4 datasets) where the MBR-based solutions provided comparable results with the benchmark GCP-based solutions. This verifies the presence of low biases and the reliability of the MBR workflow. In addition, the MBR-based solutions provided consistent 3D RMSEs with both cameras, when compared against independently surveyed CPs and TLS observations, in all but the E1 and E5 datasets.

After co-registration and 3D sensitivity assessment, inter-epoch elevation differences and volume changes are estimated. Given the estimated sensitivity levels and DEM deformations, the MBR workflow masked small elevation differences and overestimated grass growth. The MBR results from both cameras underestimated the volume change by about 8.5% over the active parts of the landslide when compared to the GCP-based results.

In addition, this chapter demonstrated implementation of the NCC function, as adopted in COSI-Corr and CIAS software, with four surface morphological attributes of *shaded relief*, *slope*, positive *openness* and *curvature*. Tests are described that evaluated the NCC function with synthetic datasets and aided in tuning the software's optimal settings. Among all morphological attributes, positive *openness* and *slope* provided the lowest noise. Inter-epoch 2D displacements were estimated and compared with benchmark GNSS and compared with

rainfall observations. The analysis has presented the potential of the NCC function to provide a continuous multi-epoch displacement map over the whole site and to track the motion of distinctive surface features over the most active parts. Unreliable NCC estimations over vegetated regions and over regions with rotational failures are highlighted, as they caused map voids and spurious vectors.

This chapter presented a time-series of the 3D Hollin Hill landslide motion within an eighteen-month period, as provided by the morphology-based monitoring strategy. It should be noted that the 3D deformation is delivered through subsequent planimetric displacement maps and motion vectors as well as elevation differences. This is because the monitoring strategy involves analysis of raster datasets (e.g. DEM, *openness*, *curvature* etc.). The true 3D motion could be derived if the 3D point clouds were analysed instead of raster datasets. However, the strategy also delivered any type of co-registered SfM-MVS products including DEMs, morphological attributes, 3D point clouds and orthophotomosaics. This offers the potential to derive metric information, for example how the dimensions of slope failure change across epochs. Future improvements are presented in Chapter 7. The results of Chapter 5 and 6 are the basis for a discussion about the limitations, merits and opportunities the morphology-based monitoring strategy has to offer.



# Chapter 7. Discussion and Conclusions

---

Chapter 7 discusses the overall performance of the proposed monitoring strategy, separately examining the challenges and opportunities that each step of the strategy provides. The discussion links all results presented in Chapters 5 and 6 and includes a comparison with previous studies to show the potential of the proposed strategy in the absence of GCPs. Challenges that hampered landslide monitoring are also presented. Through the discussion, the research outcomes are presented and the research objectives are revisited. Finally, the research contribution and its outlook for natural hazard investigations are demonstrated.

## **7.1 Discussion of research outcomes**

### ***7.1.1 Performance of the MBR workflow***

#### ***With respect to flying height***

To bring together the results from Chapter 5 and 6 and compare them with other morphological studies (previously described in Chapter 2), relative error ratios are calculated, based on Equation 2.2, for each experiment performed in this research as listed in Table 7.1. The 3D errors correspond to the 3D RMSEs computed at independent CPs and were exported from a) Table B.1 for Cockle Park; b) Table 5.6, 5.7 and Table 5.8 for Sandford; and c) Table 6.4, 6.5, 6.7, 6.8 and 6.11 for Hollin Hill. Table 7.1 reports the highest estimated errors from the Sandford experiments and both highest and lowest errors from the Hollin Hill experiments. The relative error ratios indicate the magnitude of error in relation to the flying altitude (James and Robson, 2012; Woodget et al., 2015; Eltner et al., 2016).

Table 7.1: Relative error ratios per experiment.

Experiment	3D error [m]	Average flying height [m]	Relative error ratio	Highest/lowest error
GCP-based at Cockle Park (5 GCPs, Panasonic)	0.060	107	1:1783	
GCP-based at Cockle Park (15 GCPs, Panasonic)	0.043	107	1:2488	
GCP-based at Sandford (5 GCPs, Panasonic-E1)	0.050	124	1:2480	
MBR-GCP at Sandford (5 GCPs in E0, Panasonic-E2)	0.050	127	1:2540	
MBR-UAV at Sandford (without GCPs, Panasonic-E1)	0.058	124	1:2138	
GCP-based at Hollin Hill (5 GCPs, Panasonic-E4)	0.022	90	1:4091	Lowest
MBR-GCP at Hollin Hill (5 GCPs in E0, Panasonic-E3)	0.067	83	1:1239	Lowest
GCP-based at Hollin Hill (5 GCPs with Panasonic-E3)	0.045	83	1:1844	Highest
MBR-GCP at Hollin Hill (5 GCPs in E0, Panasonic-E5)	0.108	84	1:778	Highest
GCP-based at Hollin Hill (5 GCPs, Sony-E4)	0.037	79	1:2135	Highest
MBR-GCP at Hollin Hill (5 GCPs in E4, Sony-E5)	0.066	79	1:1197	
MBR-UAV at Hollin Hill (without GCPs, Sony-E5)	0.078	79	1:1013	

Table 7.1 reports relative error ratios in the range 1:800-4000, with the lowest ratio attributable to biases in the E5 MBR solution (see Sections 6.2.2 and 6.3.2) and the highest ratio achieved with the GCP-based E4 solution. Apart from the extremes, a general consistency in the error ratios at various study sites was observed. Further, the error ratios are comparable to the error ratios computed for previous studies as described in Table 2.2. In particular, in the absence of GCPs the MBR workflow delivered relative error ratios (1:800-2000) in good agreement to the ratios 1:1600-1900 of two studies (Gerke and Przybilla (2016) and Dall'Asta et al. (2017)) that evaluated an RTK-GNSS integrated UAV (see Table 2.2). To date there have been few studies (Gerke and Przybilla, 2016; Benassi et al., 2017; Dall'Asta et al., 2017) investigating the accuracies of such UAVs. Moreover, the suitability of RTK-GNSS UAVs for monitoring without GCPs has not yet been comprehensively examined. Erroneous ambiguity resolution will possibly yield co-registration errors in subsequent UAV-derived products (Section 2.3.1). According to Benassi et al. (2017), in order to derive cm-level accuracies with RTK-UAVs, the establishment of at least one GCP is still a necessity. Moreover, the high-end UAVs augmented with RTK-GNSS and/or PPP solutions (Section 2.3.1) are at least an order of magnitude more expensive than consumer-grade UAVs (Carbonneau and Dietrich, 2016). In response to these, the presented research has demonstrated the potential of the MBR workflow as a low-cost, co-registration solution providing accuracies commensurate to that of RTK UAV solutions.

In addition, all relative error ratios listed in Table 7.1 reveal accuracies of acceptable level regardless of GCP inclusion, achieved with SfM-MVS processing coupled with off-the-shelf UAV mounted cameras. The levels can be considered acceptable as the ratios in Table 7.1 are in good agreement with the ratios 1:1080-9400 which were estimated from the use of DSLR

cameras and conventional photogrammetric procedures by James and Robson (2012). The use of off-the-shelf compact cameras, with their portability and low cost compared to DSLR cameras, is favourable for repeat surveys with fixed-wing UAVs. The engineering task to manufacture a camera case for a compact camera is also now a simple task, as demonstrated in Section 4.4.1, reducing the costs for logistics, which is a critical factor in a monitoring strategy.

#### ***With respect to spatial resolution***

RMSE magnitudes at CPs resulting from the GCP-based and MBR Sandford experiments showed a general consistency. The planimetric and vertical RMSEs were estimated at approximately 1 x GSD. The highest error was delivered from the MBR-UAV experiment (i.e. 0.058 m in Table 7.1), corresponding to 1.3 x GSD. For these particular experiments, the GSD (0.044 m, see Table 5.2) was equal to the DEM spatial resolution. For the Hollin Hill experiments, the MBR workflow estimated planimetric and vertical RMSEs in the region of 1.9-3.3 x GSD and 1-1.6 x GSD respectively, for both the Panasonic DMC-LX5 and the Sony A6000 cameras (Table 6.7 and 6.8). It should be noted that GSD values of 0.03 m and 0.02 m were derived from Panasonic and Sony images respectively, and the corresponding DEMs had spatial resolution of 2 x GSD. The analysis presented in Sections 5.2.3 and 6.2.2 cross-validated the aforementioned uncertainties with benchmark TLS and total station observations. The MBR workflow provided better co-registration accuracies in elevation than in plan due to misalignment biases that are discussed in the following section.

These uncertainties are comparable to uncertainties reported in previous studies (see Section 2.3.3) with RTK-UAVs in the absence of GCPs (Woodget et al., 2015; Gerke and Przybilla, 2016; Dall'Asta et al., 2017). For example, vertical errors of 1.4 x GSD and 2.4 x GSD were derived in Dall'Asta et al. (2017) and Gerke and Przybilla (2016) respectively. Moreover, errors higher than 5 x GSD, caused mostly by vegetation, were reported in Woodget et al. (2015). Overall, this discussion showed the potential of the MBR workflow to achieve adequate accuracy levels of 1 x GSD and provide cost-effective co-registration for the morphological monitoring of inaccessible areas.

#### ***With respect to biases***

Perhaps the most significant weakness of the MBR workflow, compared to the benchmark SfM-MVS pipeline with five GCPs, is that uncertainties were higher than 1 x GSD and propagated through the workflow to cause DEM deformations. These uncertainties reflect translational and/or rotational offsets that remained unresolved from the SfM-MVS workflow that even the ICP algorithm could not remove (Sections 5.3.2 and 6.2.2). The cause possibly stems from a combination of factors: the approximate camera exposure stations derived from the consumer-

grade UAV sensors employed, the imaging network, the unstable SfM-MVS solution of camera distortion parameters and the actual landslide motion integrated into the workflow. Most errors are hidden in the SfM-MVS pipeline and they only become apparent as DEM deformations (Sections 3.2.5 and 3.2.6, also noted by Carbonneau and Dietrich (2016)). Because of this, to generate a budget per error source is a rather challenging task. However, the sensitivity estimation (Section 3.5) constitutes a quality index of the MBR workflow and accounts for all possible errors. The analysis in Chapters 5 and 6 supported the understanding of the error sources that influenced the MBR outcomes.

Firstly, consumer-grade UAVs generally incorporate low-cost single frequency GNSS receivers and inertial navigation sensors that are capable of m-level positioning. In addition, the Quest-300 UAV used in this research did not provide reliable synchronisation of the camera triggering time which might have caused additional positional systematic offsets to the camera exposure stations (Rehak and Skaloud, 2017b), as discussed in Section 2.3.1. The camera exposure stations were used for coarse alignment in the MBR workflow (Section 3.4.2). Associated systematic errors could cause a suboptimal imaging network, adversely affecting the SfM-MVS results. For example, in the case of the E0-E2 epoch pair in the MBR-UAV experiment (see Section 5.2.2), significant rotational variations in the coarse absolute coordinates of the two epochs were observed. Even though multiple pseudo GCPs were generated across the site for both epochs, the SfM-MVS bundle adjustment could not resolve these rotations. A possible solution to this issue would be the post-processing of raw phase observations from the on-board GNSS receiver, in a similar manner to a real-time precise point positioning (e.g. Rehak and Skaloud (2017a) and Shi et al. (2017)). This post-process could refine the UAV trajectory, thereby improving the precision of the camera exposure stations. However, as the Quest-300 UAV was manufactured by a commercial company, raw sensor observations were unavailable for post-processing. An alternative solution to refine the coarse alignment could be the manual identification of at least three conjugate features appearing in E0 and E2 orthophotomosaics. Such a solution would require human intervention and would be impractical over unstable and/or grassy terrain. Nevertheless, the MBR workflow achieved the co-registration of the E0-E1 epoch pairs in the absence of GCPs with an adequate relative error ratio (see Table 7.1) as the two coarse alignments did not differ as significantly as the coarse alignment of the E0-E2 epoch.

Apart from imprecise camera exposure stations, inferior imaging networks can be caused by other factors such as a sensor's unstable focal length, low image overlap, parallel flight lines, blur and strong wind gusts, as discussed in Sections 2.3.1, 3.2.6 and 6.2.2. Especially for the

MBR results in E1 at Hollin Hill, large DEM deformations were observed that even the ICP algorithm could not account for. Characteristic is the 0.108 m remaining error computed with the M3C2 comparison after the ICP implementation (Table 6.10). Among all epochs, a few oblique images were acquired only at E1 (Section 6.1.2). DEM deformations occurred at E1 even with the inclusion of GCPs, as discussed in Section 6.2.2. It is noteworthy that, in many cases, DEM deformations exist with small magnitudes and because of that are often not reported in studies, as stated by Woodget et al. (2015). A possible approach to identify the particular cause of these uncertainties in E1 would be an additional investigation that examines systematic errors on each image. For instance, James et al. (2017a) plotted planimetric errors of tie points on each image after bundle adjustment to check for directional patterns. That way problems caused by particular tie points or images could be examined. James et al. (2017a) achieved this through their own dedicated software. However, such tools are still unavailable in *PhotoScan*. Analysis at image-level could be beneficial to the MBR workflow, thereby preventing error propagation in later stages of the monitoring strategy.

In relation to the instability of SfM-MVS self-calibrating solutions, Sections 5.1.2 and 6.5.3 demonstrated discrepancies in determined camera distortion parameters and focal length estimations. Various estimations (e.g. focal length differences exceeding 10 pixels) were observed even with the inclusion of GCPs. Discrepancies were also reported in previous studies (Remondino et al., 2012; Shahbazi et al., 2015). A UAV flying at different heights could reduce these variations, as demonstrated in Section 5.1.2. However, continuous and extensive use of a camera on-board a UAV can increase internal instability, particularly due to repetitive landings. This requires routine inspection, as seen in Section 6.5.3, especially when the camera is used for monitoring studies. The inspection can be carried out, for example, through indoor calibrations performed between UAV surveys. Calibrations with non-SfM-MVS software would be preferable in order to prevent introducing additional inconsistency into the results.

Recent studies (Carbonneau and Dietrich, 2016; James et al., 2017b) suggested analytical approaches to quantifying the precision of the estimated IOPs within SfM processing. These included multiple Monte Carlo tests, either to derive optimal combinations of  $K_1$ - $K_2$  camera distortion coefficients (Carbonneau and Dietrich, 2016), or examination of the optimal SfM software parameters (i.e. marker/tie points accuracies) together with the strengthening of image observations (James et al., 2017b).

#### ***With respect to morphological attributes and algorithms***

The MBR workflow implemented the SIFT algorithm alongside the morphological attribute of *curvature* (Section 3.3.2) to generate pseudo GCPs with *curvature* characteristics that were

invariant through time (Section 3.4.2). This concept overcomes issues associated with optical images, such as illumination variations, shadows etc., thereby increasing the effectiveness of the co-registration. As this co-registration does not rely on the identification of manmade features, it can be applicable to natural environments, as demonstrated in chapter 6, therefore finding favour in the study of remote inaccessible areas. In addition, *curvature* grids of multiple kernel sizes were utilised, providing redundancy to the number of pseudo GCPs. Together with *curvature*, the morphological attribute of *openness* (Section 3.3.2) added reliability in selecting pseudo GCPs only over stable terrain. This was based on the assumption that active landslides deform the surface topography, thereby increasing its roughness (McKean and Roering, 2004; Tarolli, 2014). Candidate pseudo GCPs on hard surface edges were therefore excluded. This indicates that *openness* can support the detection of potential hazards over landslide environments. Apart from *curvature* and *openness*, the DEM standard deviation (Section 3.3.1) was useful for vegetation cleansing, thereby adding value in the workflow's automation.

Analysis presented in Chapters 5 and 6 identified two essential requirements for the MBR workflow: a) the site under investigation should have discrete surface characteristics over stable terrain, and b) a trial and error procedure is necessary for the choice of RANSAC threshold and *curvature* kernel sizes used with the SIFT algorithm (Section 3.4.2). The site dependency requirements limit the transferability of the MBR workflow to any natural environment site. For instance, no points were identified over smooth terrain on the inclined part of the slope at Sandford (Figure 5.6d), nor over the south part of the eastern lobe at Hollin Hill (Figure 6.5). However, the procedure of tuning settings per site in SfM-MVS software is a typical task, as seen in previous studies (Cook, 2017; Dall'Asta et al., 2017).

### **7.1.2 Performance of the image cross-correlation function**

To derive surface deformation, morphological attributes were combined with the image normalised cross-correlation function (Section 3.5.3). Firstly, the comparative analysis of the NCC function with synthetic data (Section 6.4.1) was necessary to tune the function's optimal settings. For example, if small displacements close to the UAV-derived sensitivity level do not fit within the specified window size, they cannot be precisely estimated (e.g. Region A in Figure 6.14.a), as was noted by Fey et al. (2015). Small step and window sizes improved the spatial resolution of the surface displacement magnitude map but increased the computational time and noise. This occurred because features with similar / repetitive patterns within the vicinity of the specified window sizes generated false displacements (Travelletti et al., 2014; Fey et al., 2015). Hence, the choice of the function's parameters is usually based on the required spatial

resolution, the computational effort and the displacement magnitude (Daehne and Corsini, 2013; Travelletti et al., 2014; Fey et al., 2015).

Analysis with synthetic data in Section 6.4.1, alongside that performed with real data in Section 6.4.2, demonstrated that the various morphological attributes generated different displacement estimations and noise levels when used with the NCC function. *Slope*, *openness* and *curvature* outperformed *shaded relief* in terms of noise over stable terrain, even though all attributes are insensitive to illumination variations and shadows (Daehne and Corsini, 2013; Lucieer et al., 2014; Fey et al., 2015). A possible error source could be grass cover, well known to affect the results of image cross-correlation (Lucieer et al., 2014; Stumpf et al., 2017). The additional analysis with various kernel sizes presented in Section 6.4.2, showed that noise levels caused by vegetation were not suppressed.

The production of reliable surface displacements with the image cross correlation functions over vegetated terrain constitutes a significant challenge. As vegetation covers surface features, the NCC function generates additional noise. Conversely, grassy surfaces produce images with low texture and without distinctive surface features which can also affect the NCC function's performance (Travelletti et al., 2014), as seen in Figures 6.17 and 6.19 around the eastern lobe.

Independentl of the NCC function's sensitivity to displacement magnitude and vegetation presence, analysis presented in Section 6.4 also revealed other limitations, already well reported in previous studies (Daehne and Corsini, 2013; Lucieer et al., 2014; Travelletti et al., 2014; Fey et al., 2015; Stumpf et al., 2017). A priori knowledge of the displacement magnitude is required for tuning the function's settings, therefore somewhat limiting the automated fashion of the workflow. In addition, decorrelation occurs when a surface has significantly changed between two consecutive epochs, with implications for rapidly changing slopes. Finally, image cross-correlation functions generate unreliable estimates over regions with rotational failures, creating spurious vectors or voids, whereas performance is much better over translational earth flow slides (Figure 6.19).

This discussion revealed that the performance of image cross-correlation clearly depends on the site. However, the usage of UAV-derived *slope* and *openness* with image cross-correlation can offer an alternative solution compared to the standard use of *shaded relief*, or orthophotomosaics that other studies previously explored (Lucieer et al., 2014; Turner et al., 2015). In addition, the analysis in Section 6.4 constitutes a fundamental basis for further research as image cross-correlation implementation with UAV-based surface derivatives has not previously been investigated. The potential of generating continuous multi-epoch surface

displacements (Figure 6.19) with directions (Figure B.12 in Appendix B) to provide higher spatial resolution than that obtained with point-based techniques, has been demonstrated. Moreover, a comparative analysis of other image cross-correlation functions than the NCC function (e.g in Rosu et al. (2015) and Dall'Asta et al. (2017)) could reveal extended capabilities of the UAV-derived morphological attributes.

### ***7.1.3 Implications for landslide monitoring***

In relation to the artificial surface change at Sandford (Section 5.3), a  $\pm 0.120$  m sensitivity level was detected independently of the presence of GCPs. This corresponds to  $2.7 \times$  GSD, setting the uncertainty level of the MBR solution. The volume of change was quantified with  $\pm 2$  % difference to the TLS datasets. In relation to the Hollin Hill landslide (Sections 6.3 and 6.5), a  $\pm 0.221$  m minimum detectable change was estimated with the MBR-GCP workflow and the volume of change was quantified with  $\pm 8.5$  % from the GCP-based solutions. The discrepancies between the two sites are mostly attributable to the uncertainties discussed in the previous section. Moreover, the setup at Sandford was ideally designed to simulate change in the middle of a site surrounded by known stable terrain with little vegetation and acquire data with short revisit time. In comparison, the Hollin Hill landslide constitutes a real world scenario with vegetation producing additional noise. This has been documented as a problematic factor in other SfM-MVS workflows (Woodget et al., 2015; Carbonneau and Dietrich, 2016; Cook, 2017). Perhaps a higher temporal frequency of UAV acquisitions could reassure the stability of the smooth terrain. However, to generate optimal results with the least amount of noise possible, accounting for the vegetation variation, winter would constitute the optimal annual period to conduct UAV surveys.

In relation to the derivation of surface change time-series, six components were involved in the monitoring strategy, namely the morphological surface attributes of *slope*, *openness* and DEM standard deviation, the image cross-correlation function implemented in COSI-Corr and CIAS tools, the DEM differencing and the UAV-derived orthophotomosaics. The use of *slope* and *openness*, together with the COSI-Corr tool supported the quantification of movement over the whole site (Figure 6.19). The CIAS tool applied to *openness* tracked the evolution of discernible surface patterns in a semi-automated fashion (Figure 6.21). The exploitation of available image cross-correlation tools (COSI-Corr and CIAS) with *openness* decreased the intensive task of manual feature tracking. However, this task is still essential for cross-validation, especially in cases where ground truth observations are lacking over the monitoring period. DEM differencing was also applied to quantify the episodic surface ruptures and interpret the generated voids on displacement maps (Section 6.3.2). The DEM standard deviations used for

vegetation filtering (Section 6.1.3) and the orthomosaics supported the cross-validation of the results (Sections 6.4.2 and 6.5.2). The multiple uses of morphological attributes at different stages of the strategy facilitated the quantification of landslide kinematics and offered additional insight to understanding the landslide behaviour.

Heterogeneous landslide deformations were observed at Hollin Hill over the eighteen-month monitoring period. The morphology-based strategy estimated that the eastern lobe has surged forward 0.85 m/yr and the head at the back scarp have moved downwards 0.15 m/yr (Figure 6.22d). Characteristic surface features over both regions were observed to have displaced more than 1.5 m in total since December 2014 (Figure 6.21). The comparison with rainfall datasets, presented in Section 6.5.2, supported the understanding of acceleration/deceleration periods. Hollin Hill landslide has been characterised by BGS investigations (Chambers et al., 2011) as a very slow moving multiple earth slide-earth flow (Table 1.1). It can be concluded that for such a complex landslide type, the morphology-based strategy can provide acceptable annual displacement rates with optimal results over winter periods.

Overall, a UAV-based strategy without reliance on GCPs has been established, constituting a potential practical low-cost approach for monitoring hazardous terrain. This research has also offered a quantitative framework for time-series morphological surface changes with cm-level spatial resolution and dm-level minimum detectable change.

## **7.2 Revisiting research objectives**

This research aimed *to develop a strategy for handling UAV imagery that can provide multi-temporal surface morphological information for landslide monitoring*. The aim was achieved through the accomplishment of the original five objectives, as follows:

*Objective One:* To evaluate the suitability of current UAV-based approaches for morphological monitoring.

This objective was addressed in Chapters 2 and 3 through the critical literature review of emerging UAV-based approaches. These were compared against conventional geomatics and classical photogrammetric techniques in relation to accuracies, spatial resolution and logistics. Through examples from recent morphological studies (d'Oleire-Oltmanns et al., 2012; Niethammer et al., 2012; Lucieer et al., 2014; Eltner et al., 2015; Turner et al., 2015; Woodget et al., 2015; Carbonneau and Dietrich, 2016; Dall'Asta et al., 2017; James et al., 2017a), it was demonstrated that UAV-based approaches can produce DEMs, orthophotomosaics of high

spatial and temporal resolution. These can provide time-efficient and cost-effective morphological monitoring at inaccessible areas.

*Objective Two:* To investigate the uncertainties associated with SfM-MVS processing of UAV imagery.

Firstly, a description of the SfM-MVS pipeline, which constitutes the core workflow for post-processing of UAV images, was addressed in Chapters 2 and 3. Further, an investigation of errors at various stages of the SfM-MVS pipeline was achieved in Chapter 3 through the review of previous research. In Section 5.1, a better understanding of a consumer-grade UAV system was gained through data acquisition and processing at Cockle Park. Additional analysis of the SfM-MVS uncertainties was demonstrated through the results of the presented work in Chapters 5 and 6. It was found that a series of errors stemming from various sources such as imaging network configurations, GCP and site characteristics etc., typically result in DEM deformations and unstable estimations of camera IOPs. In the context of landslide monitoring, these errors should be taken into consideration in order to derive actual terrain change.

*Objective Three:* To propose and develop a monitoring strategy that establishes the rigorous alignment of spatio-temporal UAV-derived observations and quantifies landslide kinematics.

This objective was reported in Chapter 3, which details the development of the morphology-based monitoring strategy and its implementation through the description of relevant algorithms. The monitoring strategy consists of four main components, namely, the SfM-MVS pipeline, the morphological attributes of *curvature* and *openness*, the SIFT algorithm and the NCC function. The proposed strategy generates pseudo GCPs to co-register multi-temporal SfM-MVS products and then produces subsequent elevation differences and planimetric surface displacements. Uncertainties, investigated through the Objective Two are quantified with statistical tests deriving a global sensitivity threshold of the proposed strategy.

*Objective Four:* To implement the monitoring strategy at appropriate test sites and undertake quantitative evaluation with the aid of benchmark observations.

In Sections 5.2 and 5.3 the morphology-based monitoring strategy was tested at Sandford, an experimental site with artificial surface change. In Chapter 6 the strategy was applied to an active landslide at Hollin Hill BGS observatory using two different cameras. Experimental tests at Sandford supported the strategy development and tests at Hollin Hill investigated its effectiveness to derive landslide motion. The quantitative evaluation was achieved with the aid of TLS, GNSS and total station observations at each stage of the monitoring strategy.

*Objective Five:* To evaluate the capabilities and uncertainties of the strategy, thereby ensuring its applicability for landslide monitoring.

This objective was achieved through the analysis of results reported in Chapters 5 and 6. Various experiments, both with and without the inclusion of GCPs, analysed the strategy's capabilities and uncertainties. It was shown that the proposed strategy could achieve acceptable accuracies with the inclusion of only five GCPs in the reference epoch, thereby retaining low operational costs. The discussion in Section 7.1 compared the strategy's results with results from previous studies and demonstrated the merits and limitations with implications for the wider investigation of landslide motion.

### 7.3 Future work and outlook

The core aspect of the developed monitoring strategy is the morphology-based co-registration workflow. This is based on the implementation of the SIFT algorithm with the morphological attribute of *curvature* to derive candidate pseudo GCPs in 2D. This concept relies on DEM generation from the SfM-MVS point cloud (Section 3.2.2). An interesting extension of this development would be the implementation of a 3D-SIFT algorithm to extract points of similar characteristics from subsequent point clouds, thereby minimising errors introduced by interpolation. A 3D-SIFT algorithm (e.g. that developed by Rusu (2009)) can identify points at surface edges or with specific geometric attributes (Hänsch et al., 2014). These attributes could include, for example, *curvature* values to match points of invariant *curvature* structures within subsequent point clouds. This processing would require high computational effort when applying to SfM-MVS point clouds of high density. However, relevant research has already been established within the computer vision community (Krig, 2014). Implementation with point clouds of the natural environment is yet to be explored. Integrating such algorithms within SfM-MVS software would further expand the potential of multi-temporal point cloud co-registration and eliminate the requirement of GCP inclusion. In addition, monitoring investigation with co-registered 3D point clouds would potentially derive true 3D landslide information, linking each morphological structure with a 3D motion vector. By adding a fourth component, the time, this could expand to a 4D point cloud landslide information.

With regard to transferability, the MBR workflow could be implemented with multi/hyperspectral UAV images, thereby extending its potential to the wider community of natural hazards and remote sensing. Specifically, near-infrared and thermal satellite/airborne images have long been used for soil water content and surface temperature mapping (Quattrochi and Luvall, 2004; Xiao et al., 2005), which are vital parameters for landslide investigation (Lee, 2004). With the emerging technology of compact sensors, UAVs can carry small thermal and multi-spectral cameras, data from which can be post-processed using the SfM-MVS pipeline (Laliberte et al., 2011; Jensen et al., 2012). Further investigations to merge multiple datasets in the absence of GCPs with the MBR workflow could offer significant potential to accelerating assessment of hazardous environments.

Interpreting a landslide mechanism is a challenging task, as it requires the integration of multiple surface/subsurface datasets, the understanding of errors associated with various techniques and expertise in geology, geomorphology and other environmental sciences. To that end, this research has established a quantitative basis of morphological information that can complement ground-based geotechnical and geophysical investigations. This basis appeals to

scientists who can utilise the outputs of this research and extract additional landslide information. For instance, co-registered UAV-derived surface displacements can serve as input for strain field estimations (an example with TLS-derived displacements is demonstrated in Travelletti et al. (2014)). The strain field reveal characteristics of ground material, such as extension/compression behavior that is caused by the landslide forces (Teza et al., 2008; Travelletti et al., 2014). The morphology-based monitoring strategy delivered SfM-MVS point clouds, DEMs, orthophotomosaics and other morphological attributes (*curvature, openness, slope* etc.) of cm-level spatial resolution (e.g. 0.02 m GSD from images captured with Sony A6000). This facilitates the derivation of length and width of surface of rupture and other dimensions of a slope failure, which are essential metrics for landslide assessment (Lee, 2004). The research deliverables can also contribute to the delineation and measurement of landslide fissures and surface openings that indicate slope instability. Previous studies (Barazzetti and Scaioni, 2009; Stumpf et al., 2013) investigated automatic solutions for detection of surface openings with the aid of optical images. Further implementations of these solutions with morphological attributes could assist in automated geomorphological map production.

With regard to large-scale landslide assessment, the morphology-based monitoring strategy could be suitable for wider areas than those presented in this research. UAVs are easily deployable enabling multiple surveys per day that can cover areas of km<sup>2</sup>-level. In addition, this potential could be further extended with the integration of other type of observations than UAV imagery. For instance, a DEM derived from TLS or ground-based photogrammetry could be utilised for reference whereby the MBR workflow could extract pseudo GCPs to co-register this DEM with subsequent UAV DEMs. Similarly, DEMs derived from satellite remote sensing could be aligned with the UAV DEMs, offering the opportunity for upscaling. To that end, the morphology-based monitoring strategy could potentially bring together time-series of surface morphological information observed with various spatial resolutions and sensors.



# Appendix A

---

## Python script to extract the approximate 3D camera exposure stations from UAV log file (Section 3.4.2)

```
# -*- coding: utf-8 -*-
"""
Sources:
https://pypi.python.org/pypi/ExifRead#downloads
http://twigstechtips.blogspot.co.uk/2014/06/python-reading-exif-and-iptc-tags-from.html
"""
import numpy as np
import exifread
import ntpath
startTime=time.time()
inpath='C:\\b3059651\\Sandford_industrial_site\\RGB\\Epoch1\\tiffs'
outpath='C:\\b3059651\\Sandford_industrial_site\\Logfiles'
outfile=outpath+'\\'+Epoch1_Exif_time.txt'

def get_filelist(path):
    return [os.path.join(path,f) for f in os.listdir(path) if (f.endswith('.tif'))]

def get_exif(file):
    exif = exifread.process_file(file)

    if 'EXIF DateTimeOriginal' in exif:
        #print "DatetimeTaken", exif['EXIF DateTimeOriginal'].values
        exifInfo=exif['EXIF DateTimeOriginal'].values
        return exifInfo

def name_leaf(path):
    head, tail = ntpath.split(path)
    return tail or ntpath.basename(head)

Flist=get_filelist(inpath)
nbr=len(Flist) #number of files

with open(outfile,"w") as file:
    for input_file in Flist:

        f=open(input_file,'rb')
        exifInfo=get_exif(f)

        h = int(exifInfo[11]+exifInfo[12])
        m = int(exifInfo[14]+exifInfo[15])
        s = int(exifInfo[17]+exifInfo[18])
        #to = datetime.time(h, m, s)
        #tt=str(h)+':'+str(m)+':' +str(s)
        tsec=h*3600+m*60+s
        #print tt
        outname=name_leaf(input_file)
        file.write(outname+' '+str(tsec)+'\n')
```

## Python script to generate the candidate pseudo GCPs (Section 3.4.2)

```
# -*- coding: utf-8 -*-
"""
Created on Mon Jan 04 17:04:40 2016,
Sources:
http://opencv-python-tutroals.readthedocs.org/en/latest/py\_tutorials/py\_feature2d/py\_matcher/py\_matcher.html#matcher
http://docs.opencv.org/master/da/de9/tutorial\_py\_epipolar\_geometry.html#gsc.tab=0
http://www.shogun-toolbox.org/static/notebook/current/Scene\_classification.html
http://docs.opencv.org/3.0-beta/modules/calib3d/doc/camera\_calibration\_and\_3d\_reconstruction.html#decomposehomographymat
In order to work the tif should have 4 bit depth
"""
import cv2, os
import numpy as np
from matplotlib import pyplot as plt
import gdal

clear = lambda: os.system('cls')
clear()

def get_Imsize(filepath):
    ds=gdal.Open(filepath, gdal.GA_ReadOnly)
    width= ds.RasterXSize # number of pixels in x
    height = ds.RasterYSize
    return width,height

# get the list of all images from the path provided
def get_imlist(path):
    return [os.path.join(path,f) for f in os.listdir(path) if (f.endswith('Sift.tif'))]

def image_pairMatch(kp1,kp2,des1,des2,ratio_threshold,ransac_threshold):
    pts1=[]
    pts2=[]
    good=[]
    matches_final=[]
    matches = bf.knnMatch(des1,des2,k=2)

    for m,n in matches:
        if m.distance <= ratio_threshold*n.distance: # Apply ratio test
            good.append([m])
            pts1.append(kp1[m.queryIdx].pt)
            pts2.append(kp2[m.trainIdx].pt)
    pts111=np.float32(pts1).reshape(-1,1,2)
    pts222=np.float32(pts2).reshape(-1,1,2)

    H, mask = cv2.findHomography(pts111, pts222, cv2.RANSAC, ransac_threshold) ##Homography+RANSAC
    matchesMask = mask.ravel().tolist()
    x=np.ma.make_mask(matchesMask)
    x1=x.nonzero()
    for i in range(np.size(x1)):
        matches_final.append(good[x1[0][i]])
    # We select only inlier points
    pts1_final = pts111[mask.ravel()==1]
    pts2_final = pts222[mask.ravel()==1]
    return(matches,good,matches_final,H,pts1_final,pts2_final)

def Pixel2World(geoMatrix,x,y):
    ulX=geoMatrix[0]
    ulY=geoMatrix[3]
    xDist=geoMatrix[1]
    yDist=geoMatrix[5]
    coorX=(ulX+(x*xDist))
    coorY=(ulY+(y*yDist))
    coords=coorX,coorY
    return coords

def get_geoTrans(img):
```

```

gdal.AllRegister()
src=gdal.Open(img)
#get the GeoTransform object from the image
geoTrans=src.GetGeoTransform()
return geoTrans

def xy2coords(geoTrans,pts): # I have to input the list of final points after matching
    pix=[]
    piy=[]
    plist=pts.tolist()
    for i in range(len(plist)):
        p1=plist[i]
        #pp1=p1[0]
        #pp2=p1[1]
        pp1=np.float(np.asarray(zip(*p1)[0]))
        pp2=np.float(np.asarray(zip(*p1)[1]))
        pix.append(pp1)
        piy.append(pp2)
    pix1=np.asarray(pix)
    piy1=np.asarray(piy)
    #perform the conversion
    p2w=Pixel2World(geoTrans,pix1,piy1)
    return p2w, pix1, piy1

def get_error(pix1,piy1,pix2,piy2,H):
    #Apply homography to correspondences and
    #return the error for each transformed point
    #from points (make homogeneous coords first)
    fp=(np.vstack((pix1,piy1,np.ones(len(pix1)))))
    #To points
    tp=(np.vstack((pix2,piy2,np.ones(len(pix1)))))
    #transform fp
    fp_transformed=np.dot(H,fp)
    # normalize hom. coordinates
    for i in range(3):
        fp_transformed[i] /= fp_transformed[2]
    # return average error from all point
    dist = tp-fp_transformed
    dist2 = np.multiply(dist, dist)
    err = np.sum(dist2)
    rmse = np.sqrt(err/len(pix1));

    # return error per point
    error_per_point=np.sqrt(np.sum((tp-fp_transformed)**2,axis=0) )
    return rmse, error_per_point

# initialise OpenCV's SIFT
sift=cv2.xfeatures2d.SIFT_create()
# BFMatcher with default params
bf = cv2.BFMatcher()
imlistname=["Dec14","May16"]
imlistdummy=[0,1]
ratio_threshold=0.8
ransac_threshold=0.9
K_curv=35
path='C:\\b3059651\\SIFT_Curvature\\Sony_Feb16_Reference_20161005\\4_Curvature_update\\K'+str(K_curv)
print path
imlist=get_imlist(path)
nbr_images=len(imlist) #number of images
matchscores=np.zeros((nbr_images,nbr_images))

##pairwise matching of all image combinations
for i in range(nbr_images):
    for j in range(i+1,nbr_images):
        print"-----"
        ##pairwise matching of all image combinations
        print "comparing:",imlistdummy[i], imlistdummy[j]
        img1 = cv2.imread(imlist[i])
        img2 = cv2.imread(imlist[j])
        #detect the SIFT keypoints and the descriptors.

```

```

kp1, des1=sift.detectAndCompute(img1,None)
kp2, des2=sift.detectAndCompute(img2,None)
matches,good,matches_final,H,pts1_final,pts2_final=image_pairMatch(kp1,kp2,des1,des2,...
ratio_threshold,ransac_threshold)
nbr_matches=len(matches_final)
matchscores[i,j]=nbr_matches

#to convert the points per pair from pixel to world coordinates
geoTrans1=get_geoTrans(imlist[i])
p2w_ref,pix1,piy1=xy2coords(geoTrans1,pts1_final) #reference image1
geoTrans2=get_geoTrans(imlist[j])
p2w_match,pix2,piy2=xy2coords(geoTrans2,pts2_final) #matching image2

rmse1,error_per_point1=get_error(pix1,piy1,pix2,piy2,H)
p2w=np.vstack((p2w_ref,p2w_match,error_per_point1))
pixels_points=np.vstack((pix1,piy1,pix2,piy2,error_per_point1))

scale=np.sqrt(H[0][0]**2+H[0][1]**2)
theta=np.degrees(np.arctan2(H[0][1],H[0][0]))
r11=np.cos(np.arctan2(H[0][1],H[0][0]))
r12=np.sin(np.arctan2(H[0][1],H[0][0]))
Rot=([r11,-r12],[r12,r11])
print "initial matches=", str(len(matches))
print "matches after test ratio=",str(len(good))
print "final matches after ransac=", str(len(matches_final))
print "final number pair-point inliers= " + str(len(pts1_final))
print "Overall rms error of the matching= " + str(rmse1)

#save it as a txt

np.savetxt(path+"\pair'+str(i)+str(j)+'K'+str(K_curv)+'_Ransac'+str(ransac_threshold)+'_Points_from_ref_to_match.csv',
np.transpose(p2w), delimiter=',', fmt='% .10f')
np.savetxt(path+"\pair'+str(i)+str(j)+'K'+str(K_curv)+'_Ransac'+str(ransac_threshold)+'_Points_from_to_pixels.csv',
np.transpose(pixels_points), delimiter=',', fmt='% .10f')

with open(path+"\pair'+str(i)+str(j)+'K'+str(K_curv)+'_Ransac'+str(ransac_threshold)+'_matches_masked.txt','w')as file:
file.write('initial matches=' +str(len(matches))+'\n'+matches after test ratio=' +str(len(good))+'\n'+_final matches after
ransac=' +str(len(matches_final))+'\n'+final number pair-point inliers= ' +str(len(pts1_final))+'\n'+Overall rms error of the
matching=' + str(rmse1))

np.savetxt(path+"\pair'+str(i)+str(j)+'K'+str(K_curv)+'_Ransac'+str(ransac_threshold)+'_Homography_matrix.csv', H,
delimiter=',', fmt='% .10f')

np.savetxt(path+"\pair'+str(i)+str(j)+'K'+str(K_curv)+'_Ransac'+str(ransac_threshold)+'_Angle.csv',np.vstack((scale,theta)),d
elimiter=',', fmt='% .5f')
np.savetxt(path+"\pair'+str(i)+str(j)+'K'+str(K_curv)+'_Ransac'+str(ransac_threshold)+'_Rotation.csv',Rot,delimiter=',',
fmt='% .5f')

#Save a picture for every matching result
P=plt.figure(1)
img3 = cv2.drawMatchesKnn(img1,kp1,img2,kp2,matches_final,None,(255,0,0),2)
plt.imshow(img3),plt.show()
P.savefig(path+"\pair'+str(i)+str(j)+'K'+str(K_curv)+'_Ransac'+str(ransac_threshold)+'_matching_pic.png',dpi=200,
format='png')
plt.close(P)

```

---

## 2D similarity transformation (Section 3.2.4)

The mathematical expression of the 2D similarity transformation is

$$X = x(S\cos\theta) - y(S\sin\theta) + T_x$$

$$Y = x(S\sin\theta) + y(S\cos\theta) + T_y$$

where  $X$ ,  $Y$  the coordinates of SIFT key-points of epoch  $i$  ( $E_i$ ) *curvature* grid,  $x$ ,  $y$  the corresponding points of  $E_j$  *curvature* grid, with  $S$  the scale factor,  $\theta$  the rotation about X-axis and  $T_x$ ,  $T_y$  the two translations between  $E_i$  and  $E_j$  *curvature* grids. After substitution

$$a = S\cos\theta, \quad b = S\sin\theta$$

a system of linear equations can be formulated as:

$$X = ax - by + T_x$$

$$Y = bx + ay + T_y$$

## Python script for statistical outlier detection of Stage 2c (Section 3.4.2)

```
# -*- coding: utf-8 -*-
"""
Created on Fri Jun 19 14:06:36 2015
Sources:
http://stackoverflow.com/questions/28242593/correct-way-to-obtain-confidence-interval-with-scipy
"""
import os
import numpy as np
import matplotlib.pyplot as plt
from scipy import stats

clear = lambda: os.system('cls')
clear()

start = time.time()
os.chdir(r'C:\b3059651\SIFT_Curvature\FINAL_Dec14_Ref\2_Curvature\PseudoGCPs')

def pdn(x,mu,sigma):
    f= (1/(sigma * np.sqrt(2 * np.pi)))*(np.exp( - (x - mu)**2 / (2 * sigma**2) ))
    return f

%% Import the csv for calculations from PhotoScan
input_file='E5_errorsGCPs5_strictmasks11.txt'
data=np.genfromtxt(input_file, dtype=float,delimiter=',',skiprows=2)
label=data[:,0]
XYZerr=data[:,4]
Xerr=data[:,5]
Yerr=data[:,6]
Zerr=data[:,7]
#planerror=np.sqrt(Xerr**2+Yerr**2)

%% Histograms
H1=plt.figure(1)
n, bins, patches = plt.hist(Xerr,15,weights=np.ones_like(Xerr)*100/Xerr.size,facecolor='green')
# statistics
Xmean, Xsigma = Xerr.mean(), Xerr.std(ddof=1)
```

```

Xconf_int68 = stats.norm.interval(0.68, loc=Xmean, scale=Xsigma)
Xconf_int95 = stats.norm.interval(0.95, loc=Xmean, scale=Xsigma)
Xconf_int99 = stats.norm.interval(0.99, loc=Xmean, scale=Xsigma)
# add a 'best fit' line
bw=bins[1]-bins[0]
bins1 = np.linspace(bins.min(),bins.max(),300) #to smooth the curv I create more bins
f = plt.plot(bins1,pdn(bins1,Xmean,Xsigma)*bw*100,'r-', linewidth=1)
plt.axvline(Xmean, color='b', linestyle='dashed', linewidth=2)
plt.axvline(Xconf_int68[0], color='k', linestyle='dashed', linewidth=2)
plt.axvline(Xconf_int68[1], color='k', linestyle='dashed', linewidth=2)
#textstr1 = '$\sigma=%.2f$'%(Xsigma)
#plt.annotate(textstr1, xy=(0.02,12.3),fontsize = 16, color='black')

#plt.annotate('-1sigma='+str(round(Xconf_int68[0],3)),xy=(Xconf_int68[0]-0.1,2.8),fontsize = 15, color='black',rotation=90)
#plt.annotate('+1sigma='+str(round(Xconf_int68[1],3)),xy=(Xconf_int68[1]+0.03,2.8),fontsize = 15,
color='black',rotation=90)
plt.xlabel( 'Residual in Easting [m]' )
plt.ylabel( 'Relative frequency [%]' )

plt.xlim(-0.2,0.2)
plt.ylim(0,15.1)
plt.grid(True)
plt.tight_layout()
plt.show()

H2=plt.figure(2)
n, bins, patches = plt.hist(Yerr,18,weights=np.ones_like(Yerr)*100/Yerr.size,facecolor='green')
# statistics
Ymean, Ysigma = Yerr.mean(), Yerr.std(ddof=1)
Yconf_int68 = stats.norm.interval(0.68, loc=Ymean, scale=Ysigma)
Yconf_int95 = stats.norm.interval(0.95, loc=Ymean, scale=Ysigma)
Yconf_int99 = stats.norm.interval(0.99, loc=Ymean, scale=Ysigma)
# add a 'best fit' line
bw=bins[1]-bins[0]
bins1 = np.linspace(bins.min(),bins.max(),300) #to smooth the curv I create more bins
f = plt.plot(bins1,pdn(bins1,Ymean,Ysigma)*bw*100,'r-', linewidth=1)
plt.axvline(Ymean, color='b', linestyle='dashed', linewidth=2)
plt.axvline(Yconf_int68[0], color='k', linestyle='dashed', linewidth=2)
plt.axvline(Yconf_int68[1], color='k', linestyle='dashed', linewidth=2)
#textstr1 = '$\sigma=%.2f$'%(Ysigma)
#plt.annotate(textstr1, xy=(0.02,12.3),fontsize = 16, color='black')

#plt.annotate('-1sigma='+str(round(Yconf_int68[0],3)),xy=(Yconf_int68[0]-0.1,2.8),fontsize = 15, color='black',rotation=90)
#plt.annotate('+1sigma='+str(round(Yconf_int68[1],3)),xy=(Yconf_int68[1]+0.03,2.8),fontsize = 15,
color='black',rotation=90)
plt.xlabel( 'Residual in Northing [m]' )
plt.ylabel( 'Relative frequency [%]' )
plt.xlim(-0.2,0.2)
plt.ylim(0,15.1)
plt.grid(True)
plt.tight_layout()
plt.show()

#H1.savefig(os.path.splitext(input_file)[0]+'East_residual_Hist.png',dpi=200, format='png')
#H2.savefig(os.path.splitext(input_file)[0]+'North_residual_Hist.png',dpi=200, format='png')

H3=plt.figure(3)
n, bins, patches = plt.hist(Zerr,18,weights=np.ones_like(Zerr)*100/Zerr.size,facecolor='green')
# statistics
Vmean, Vsigma = Zerr.mean(), Zerr.std(ddof=1)
Vconf_int68 = stats.norm.interval(0.68, loc=Vmean, scale=Vsigma)
Vconf_int95 = stats.norm.interval(0.95, loc=Vmean, scale=Vsigma)
Vconf_int99 = stats.norm.interval(0.99, loc=Vmean, scale=Vsigma)

# add a 'best fit' line
bw=bins[1]-bins[0]
bins1 = np.linspace(bins.min(),bins.max(),300) #to smooth the curv I create more bins
f = plt.plot(bins1,pdn(bins1,Vmean,Vsigma)*bw*100,'r-', linewidth=1)
plt.axvline(Zerr.mean(), color='b', linestyle='dashed', linewidth=2)
plt.axvline(Vconf_int68[0], color='k', linestyle='dashed', linewidth=2)

```

```

plt.axvline(Vconf_int68[1], color='k', linestyle='dashed', linewidth=2)
#textstr1 = '$\sigma=%.2f$'%(Vsigma)
#plt.annotate(textstr1, xy=(0.22,12.3),fontsize = 16, color='black')
#plt.annotate('-1sigma='+str(round(Vconf_int68[0],3)),xy=(Vconf_int68[0]-0.04,6.6),fontsize = 15, color='black',rotation=90)
#plt.annotate('+1sigma='+str(round(Vconf_int68[1],3)),xy=(Vconf_int68[1]+0.01,6.6),fontsize = 15, color='black',rotation=90)
plt.xlabel( 'Residual in Height [m]' )
plt.ylabel( 'Relative frequency [%]' )
plt.xlim(-0.2,0.2)
plt.ylim(0,15.1)
plt.grid(True)
plt.tight_layout()
plt.show()

#H3.savefig(os.path.splitext(input_file)[0]+'Height_residual_Hist.png',dpi=200, format='png')
def outlier_detection(Xerr, Yerr, Zerr, Xconf, Yconf, Vconf):
    #Find the indeces with values larger than the confidence level
    X1idx=[i for i, val in enumerate(Xerr) if val>Xconf[1]]
    X2idx=[i for i, val in enumerate(Xerr) if val<Xconf[0]]

    Y1idx=[i for i, val in enumerate(Yerr) if val>Yconf[1]]
    Y2idx=[i for i, val in enumerate(Yerr) if val<Yconf[0]]

    V1idx=[i for i, val in enumerate(Zerr) if val>Vconf[1]]
    V2idx=[i for i, val in enumerate(Zerr) if val<Vconf[0]]
    label1=[]
    label2=[]
    label3=[]
    label4=[]
    label5=[]
    label6=[]
    for i in range(0,len(X1idx)):
        l1=label[X1idx[i]]
        label1.append([l1])
    for i in range(0,len(X2idx)):
        l2=label[X2idx[i]]
        label2.append([l2])

    for i in range(0,len(Y1idx)):
        l3=label[Y1idx[i]]
        label3.append([l3])

    for i in range(0,len(Y2idx)):
        l4=label[Y2idx[i]]
        label4.append([l4])

    for i in range(0,len(V1idx)):
        l5=label[V1idx[i]]
        label5.append([l5])

    for i in range(0,len(V2idx)):
        l6=label[V2idx[i]]
        label6.append([l6])

    label1.extend(label2)
    label1.extend(label3)
    label1.extend(label4)
    label1.extend(label5)
    label1.extend(label6)
    label1.sort()
    labels=[ii for n,ii in enumerate(label1) if ii not in label1[:n]] # to remove duplicates and keep the order
    return labels

# confidence level
label68=outlier_detection(Xerr,Yerr,Zerr,Xconf_int68,Yconf_int68,Vconf_int68)
label95=outlier_detection(Xerr,Yerr,Zerr,Xconf_int95,Yconf_int95,Vconf_int95)
label99=outlier_detection(Xerr,Yerr,Zerr,Xconf_int99,Yconf_int99,Vconf_int99)

print "For 68% confidence level the number of outliers are:"+ str(len(label68))
print "For 95% confidence level the number of outliers are:"+ str(len(label95))

```

```

print "For 99% confidence level the number of outliers are:"+ str(len(label99))

print "Xmean="+str(Xmean)+" Xsigma="+str(Xsigma)
print "Ymean="+str(Ymean)+" Ysigma="+str(Ysigma)
print "Vmean="+str(Vmean)+" Vsigma="+str(Vsigma)
print"....."
rmsX=np.sqrt(np.mean(np.square(Xerr)),dtype=np.float64)
rmsY=np.sqrt(np.mean(np.square(Yerr)),dtype=np.float64)
rmsPlan=np.sqrt(rmsX**2+rmsY**2)
rmsZ=np.sqrt(np.mean(np.square(Zerr)),dtype=np.float64)
print "RMSE Easting="+str(rmsX)
print "RMSE Northing="+str(rmsY)
print "RMSE plan="+str(rmsPlan)+" RMSE vertical="+str(rmsZ)
print "Std Plan="+str(np.sqrt(Xsigma**2+Ysigma**2))+ " Std vertical="+str(Vsigma)

#np.savetxt(os.path.splitext(input_file)[0]+'_2sigma_outliers.txt', label95, delimiter=',', fmt='% .0f')

#Final check of normal distribution outlier detection
#for 95% t=1.96
to=1.96
Thres=(-to,to)
#normalised residual
Xres_norm=(Xerr-Xmean)/Xsigma
Yres_norm=(Yerr-Ymean)/Ysigma
Zres_norm=(Zerr-Vmean)/Vsigma
label_normalised=outlier_detection(Xres_norm,Yres_norm,Zres_norm,Thres,Thres,Thres)
len(label_normalised)

np.savetxt(os.path.splitext(input_file)[0]+'_2sigma_outliers.txt', label_normalised, delimiter=',', fmt='% .0f')

```

---

## Examples of analysis from experiment in Cockle Park (Section 5.1.2)

Table A.1: Mean RMSEs at CPs after post processing with 0, 5, 10 and 15 GCPs.

No of GCPs	Project id (ft)	RMSE in Plan [m]	RMSE in Elevation [m]	3D RMSE [m]
0	1(250)	8.134	2.338	8.667
0	2(300)	8.951	0.926	8.998
0	3(350)	28.310	1.240	28.337
0	4(combined)	15.527	12.483	19.923
5	1(250)	0.048	0.040	0.062
5	2(300)	0.041	0.066	0.078
5	3(350)	0.060	0.098	0.115
5	4(combined)	0.038	0.046	0.060
10	1(250)	0.040	0.046	0.061
10	2(300)	0.037	0.046	0.059
10	3(350)	0.051	0.064	0.082
10	4(combined)	0.032	0.040	0.051
15	1(250)	0.034	0.060	0.069
15	2(300)	0.032	0.029	0.044
15	3(350)	0.037	0.043	0.057
15	4(combined)	0.025	0.035	0.043

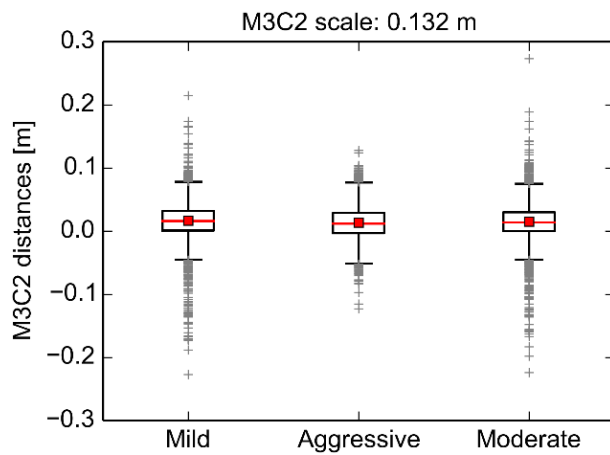


Figure A.1: Boxplots of M3C2 comparison of three different disparity settings for dense point cloud reconstruction. Median is shown by the red rectangle and outliers by grey crosses.

**Examples of analysis from experiments at Sandford Industrial Park (Section 5.2.2)**

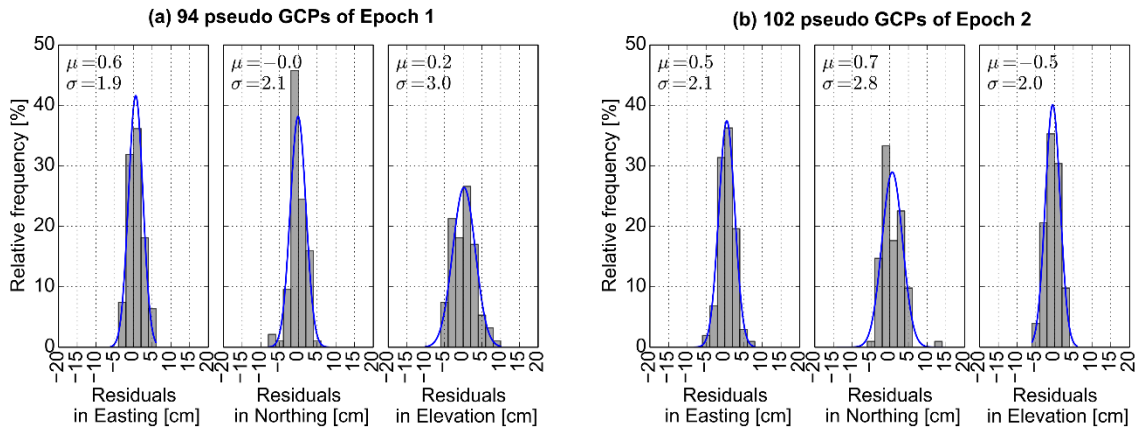


Figure A.2: Histograms of final selected pseudo GCPs after bias removal in the MBR-GCP based experiment.

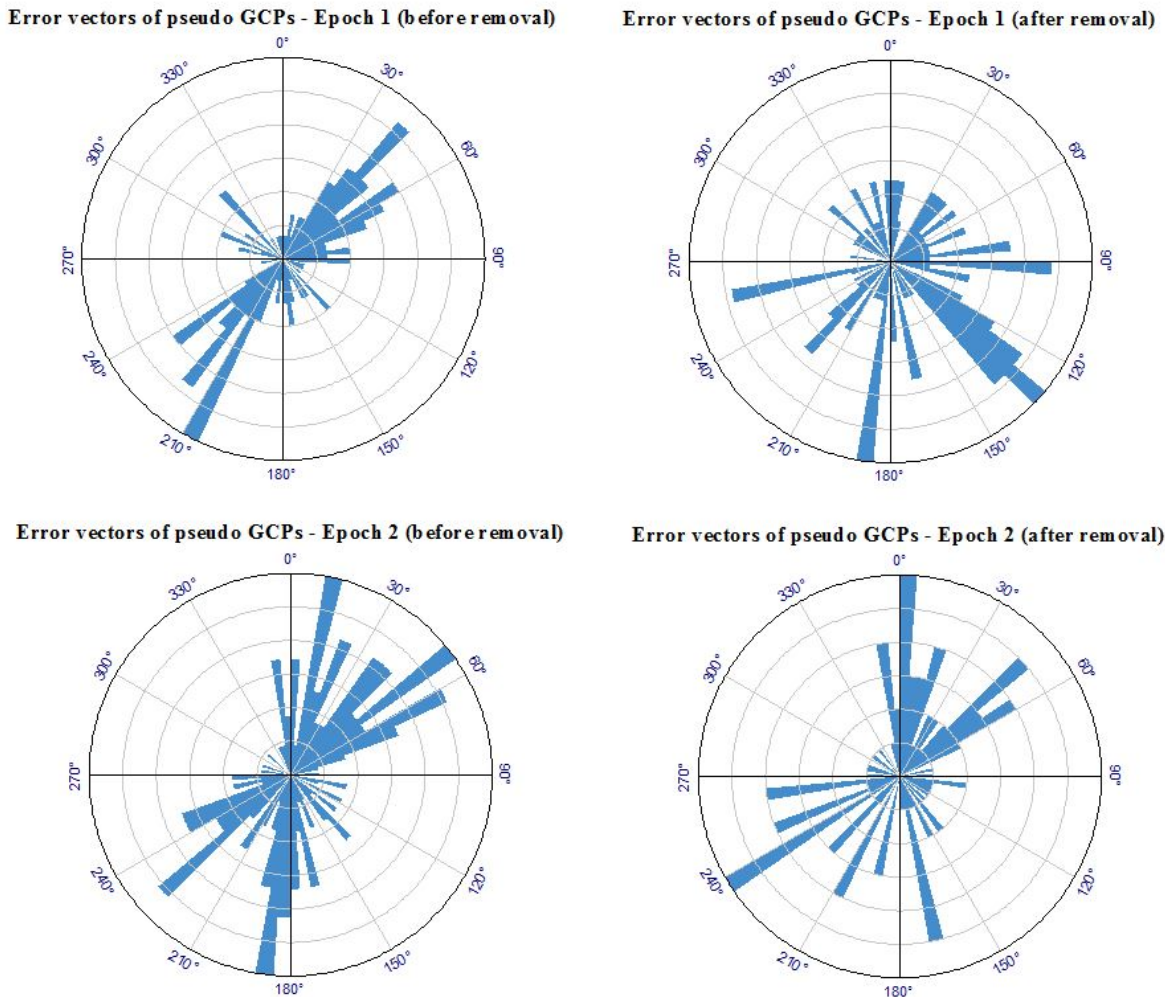


Figure A.3: Polar plots of pseudo GCPs residuals before and after bias removal in the MBR-GCP based experiment for both epochs.

# Appendix B

---

## DPC Pre-processing and vegetation cleaning (Section 6.1.3)

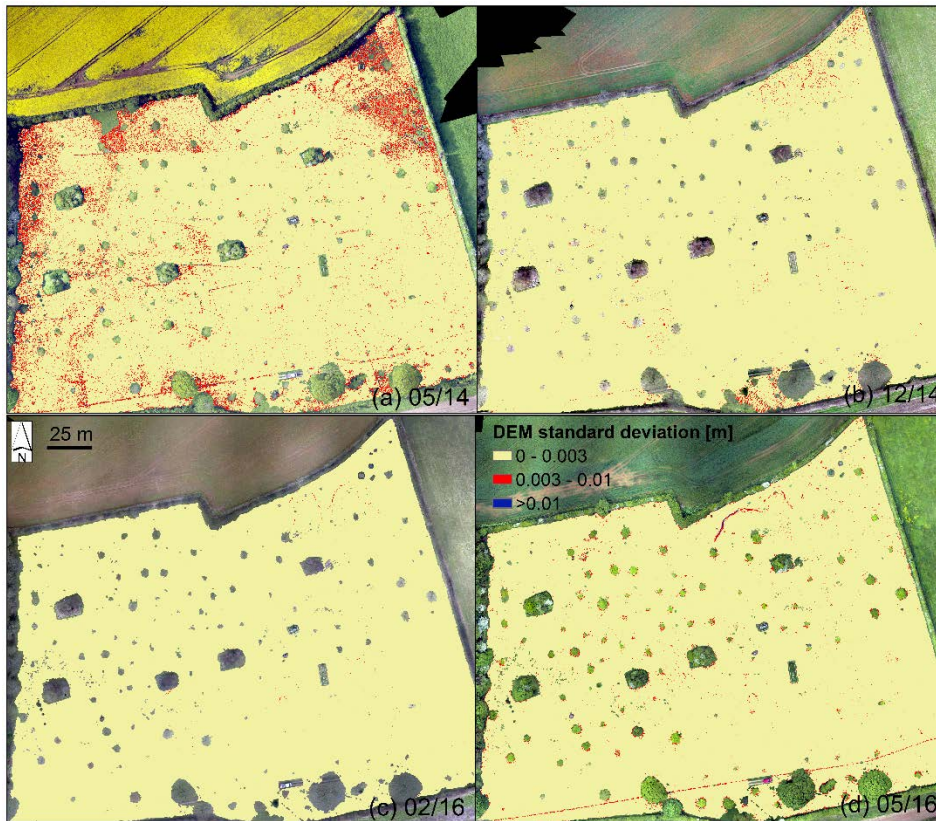


Figure B.1: GCP-based Panasonic experiment: DEM standard deviations for (a) 05/14, (b) 12/14, (c) 02/16 and (d) 05/16 datasets. Linear artefacts were observed in 05/14 due to low image overlap.

**MBR-based implementation and analysis (Section 6.2.1)**

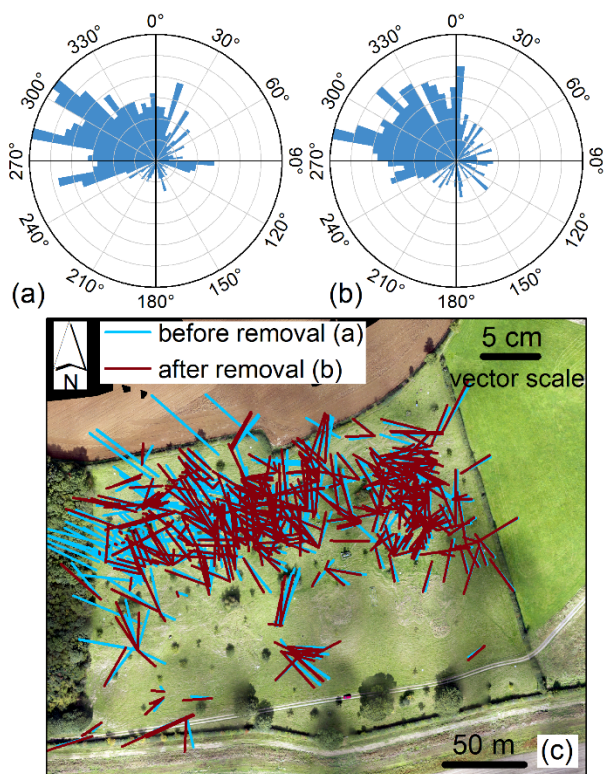


Figure B.2: MBR-GCP Panasonic experiment: Polar plots of E3 pseudo GCPs.

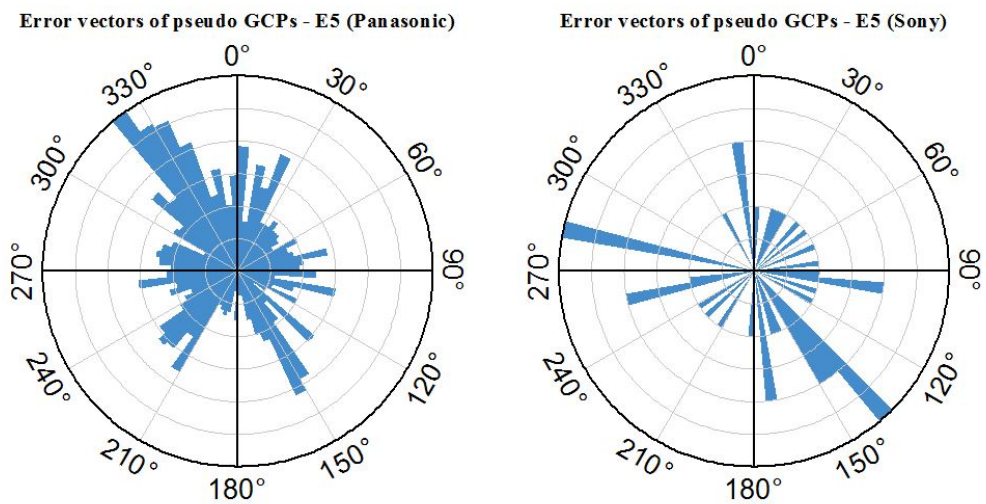


Figure B.3: Polar plots of E5 pseudo GCPs error vectors resulted from Panasonic and Sony MBR-GCP based experiments.

## Assessment of co-registration solutions (Section 6.2.2)



Figure B.4: Panasonic image acquired in 09/15 (E3) over GP15 target showing how sun glare degraded black and white contrast of the target.



Figure B.5: Panasonic image acquired in 06/15 (E2), over CP02 target. Blur altered the circular shape.

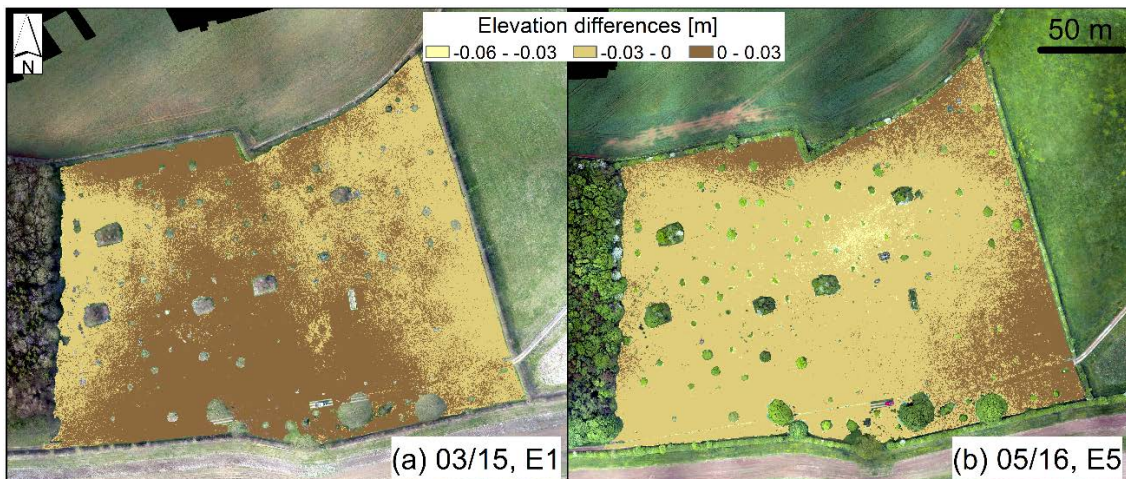


Figure B.6: GCP-based Panasonic experiment: Elevation differences from DEM obtained with all available GCPs.

### Estimation of elevation and volume change (Section 6.3.2)

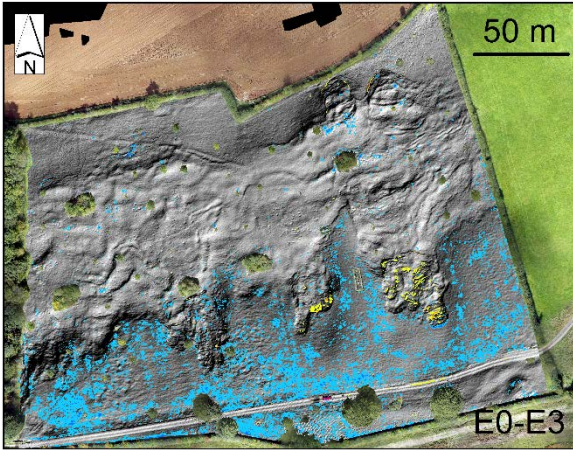


Figure B.7: GCP-based Panasonic experiment: Elevation differences between E0-E3 epoch pair showing vegetation changes mixed into the actual landslide deformation. This map shares the same colour scheme shown in Figure 6.13.

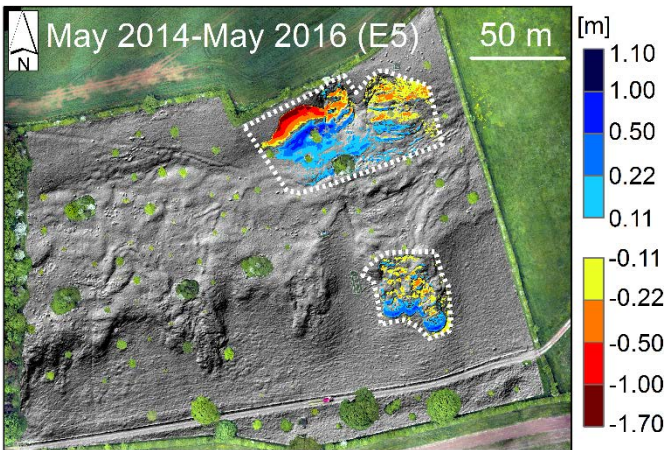


Figure B.8: Elevation differences between May 2014 – May 2016 over back scarp and eastern lobe from GCP-based observations.

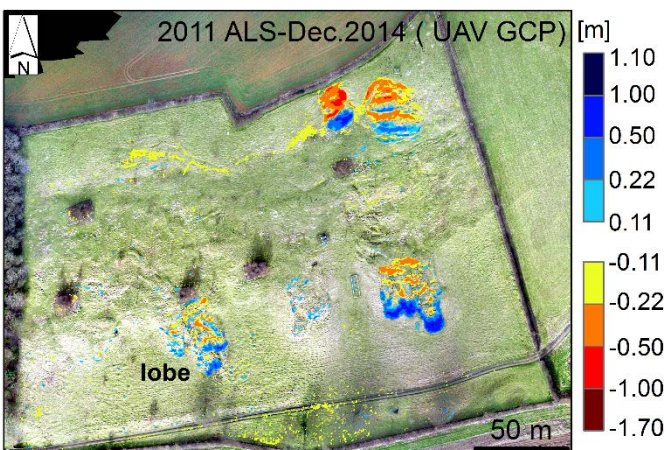


Figure B.9: Elevation differences between ALS 2011 DEM and UAV GCP-based E0 DEM.

## NCC implementation with synthetic datasets (Section 6.4.1)

Table B.1: Statistics of SNR values derived from morphological attributes over Region A and B and outside those constituting stable terrain of the synthetic datasets.

Morphological attributes	dE [m]				dN [m]			
	$\mu$	$\sigma$	min	max	$\mu$	$\sigma$	min	max
stable terrain								
<i>Shaded relief</i>	0.000	0.037	-1.145	1.169	0.000	0.055	-1.074	1.155
<i>Slope</i>	0.000	0.018	-0.783	0.903	-0.000	0.039	-1.084	1.021
<i>Positive openness</i>	0.000	0.030	-0.991	1.143	0.000	0.054	-1.163	1.144
<i>Curvature</i>	0.000	0.025	-1.078	0.958	-0.000	0.053	-1.149	1.026
region A								
<i>Shaded relief</i>	0.029	0.029	-0.022	0.085	-0.056	0.030	-0.111	-0.003
<i>Slope</i>	0.036	0.032	-0.026	0.098	-0.053	0.028	-0.109	0.010
<i>Positive openness</i>	0.024	0.029	-0.029	0.085	-0.052	0.036	-0.109	0.002
<i>Curvature</i>	0.034	0.020	-0.008	0.064	-0.055	0.025	-0.108	-0.007
region B								
<i>Shaded relief</i>	0.427	0.114	-0.068	0.505	-0.528	0.131	-0.706	0.012
<i>Slope</i>	0.433	0.141	-0.047	0.707	-0.505	0.156	-0.707	0.111
<i>Positive openness</i>	0.435	0.145	-0.059	0.848	-0.493	0.182	-0.697	0.537
<i>Curvature</i>	0.432	0.115	-0.012	0.508	-0.513	0.140	-0.690	0.033

## Sensitivity analysis of the NCC function with real datasets (Section 6.4.2)

Table B.2: RMSEs computed between the NCC estimations and manual observations.

Epoch pairs	RMSEs [m]	
	<i>slope</i>	<i>openness</i>
E0-E1	0.087	0.042
E1-E4	0.185	0.142
E4-E5	0.185	0.372

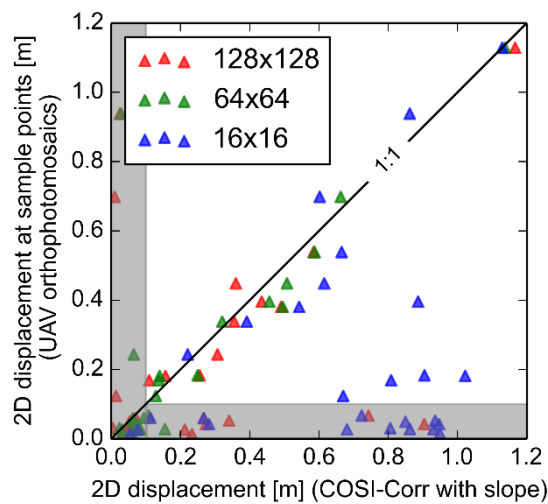


Figure B.10: COSI-Corr surface displacements with *slope* plotted against manual observations.

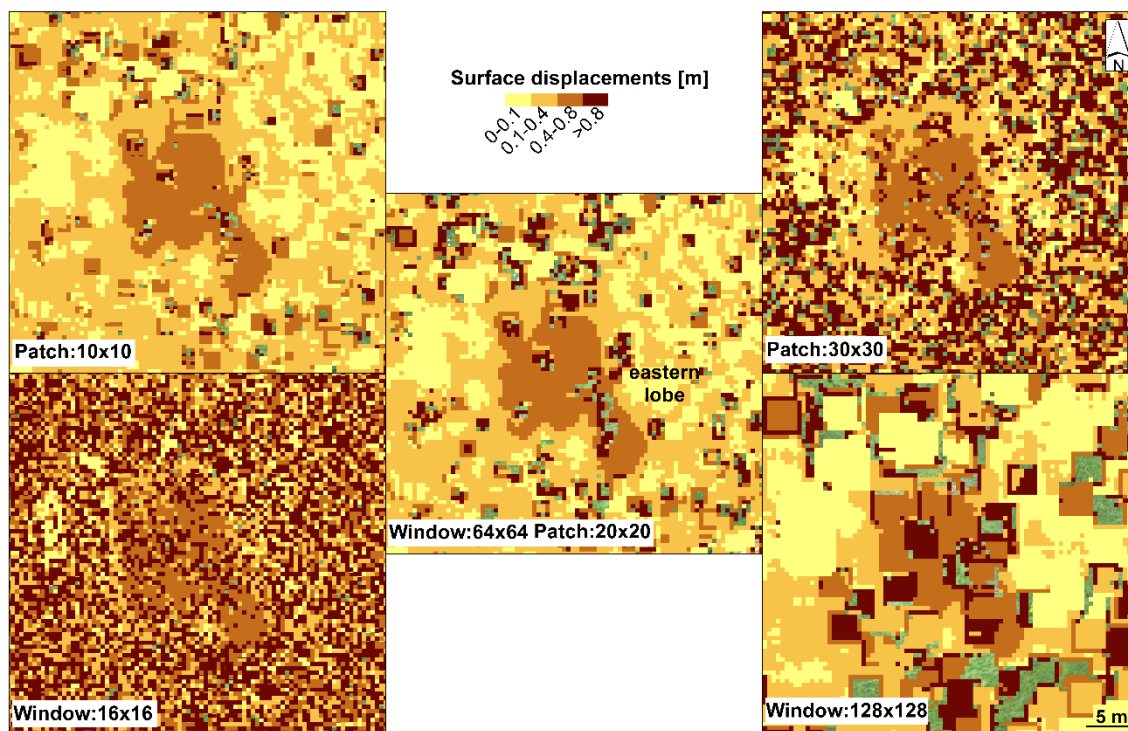


Figure B.11: COSI-Corr surface displacements with positive *openness* under various settings.

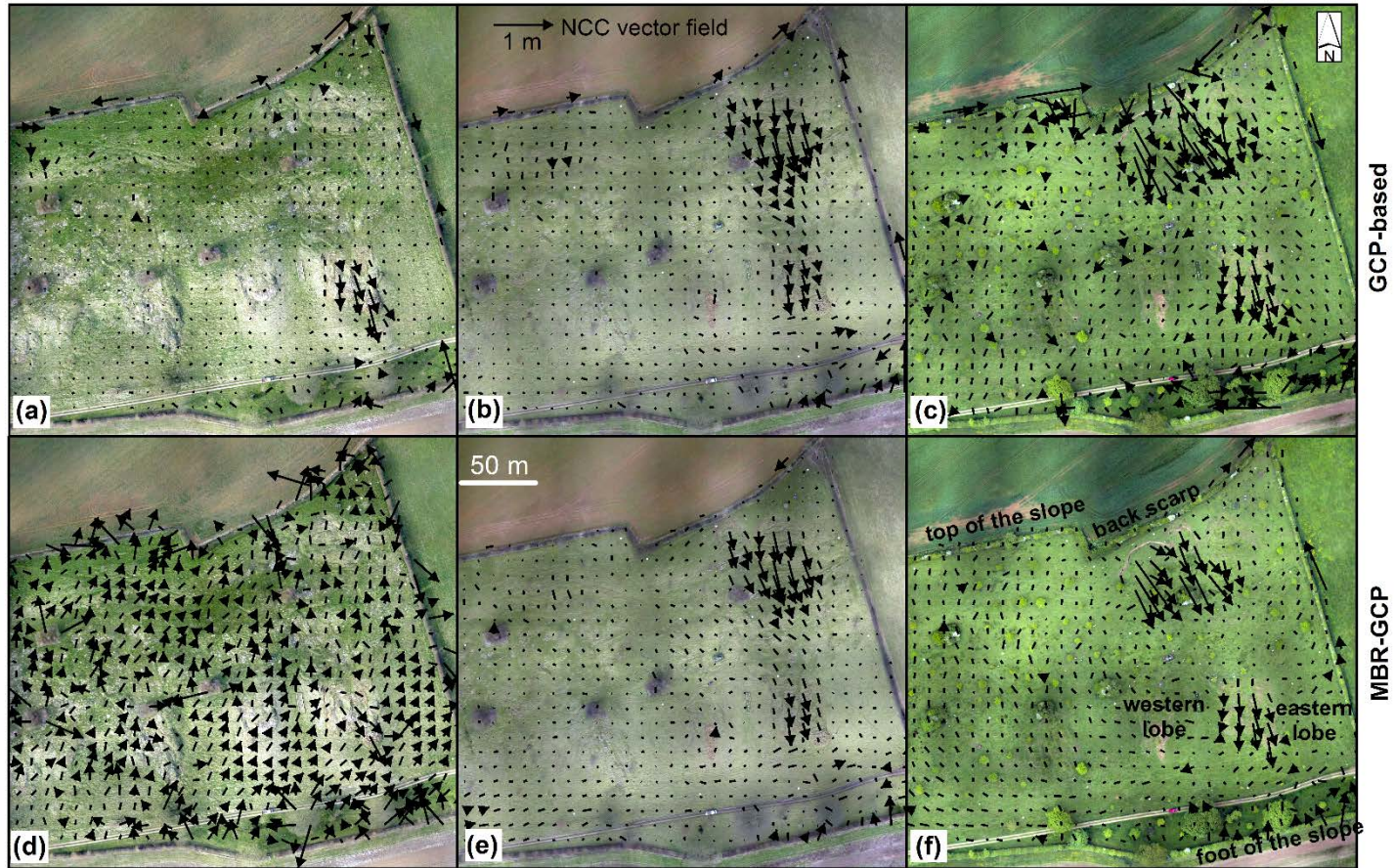


Figure B.12: Vector fields estimated from the NCC function in COSI-Corr (see Figure 6.21).

### Camera stability checks (Section 6.5.3)

Table B.3: Calibration results post UAV flights for Panasonic DMC-LX5 and Sony A6000, as derived from DBAT (see Section 4.4.2 for description).

Determined parameters	Panasonic DMC-LX5- Calibration 22/07/2017		Sony A6000- Calibration 22/07/2017	
	Value	$\sigma$	Value	$\sigma$
f-focal length [mm]	5.071	$4.28 \times 10^{-04}$	16.200	$1.11 \times 10^{-03}$
$x_p$ -principal point [mm]	3.540	$2.96 \times 10^{-04}$	11.998	$7.01 \times 10^{-03}$
$y_p$ -principal point [mm]	2.718	$4.00 \times 10^{-04}$	7.873	$6.26 \times 10^{-04}$
$F_w$ -format width [mm]	7.143	$1.40 \times 10^{-04}$	23.997	-
$F_h$ -format height [mm]	5.358	-	16.000	-
$K_1$ -radial distortion 1	$2.53 \times 10^{-04}$	$1.80 \times 10^{-05}$	$2.95 \times 10^{-4}$	$1.62 \times 10^{-03}$
$K_2$ - radial distortion 2	$-6.52 \times 10^{-05}$	$2.39 \times 10^{-06}$	$-1.45 \times 10^{-6}$	$2.02 \times 10^{-08}$
$K_3$ - radial distortion 3	$2.12 \times 10^{-06}$	-	$-2.11 \times 10^{-10}$	$8.55 \times 10^{-11}$
$P_1$ - decentering distortion 1	$2.98 \times 10^{-04}$	$4.00 \times 10^{-06}$	$4.07 \times 10^{-5}$	$8.94 \times 10^{-07}$
$P_2$ - decentering distortion 2	$-8.77 \times 10^{-05}$	$3.63 \times 10^{-06}$	$3.04 \times 10^{-5}$	$7.91 \times 10^{-07}$

# References

---

- Abbate, E. & Lovisolo, M. (2010). Geotechnical Ground-based Monitoring Systems. *In the Deliverable 4.1 of the European project SAFELAND: Review of Techniques for Landslide Detection, Fast Characterisation, Rapid Mapping and Long-Term Monitoring*
- Abdullah, Q., Maune, D. & Smith, D. (2015). New standard for new era: Overview of the 2015 ASPRS positional accuracy standards for digital geospatial data. *Photogrammetric Engineering and Remote Sensing*, 81(3), 173-176, doi:10.14358/Pers.81.3.173.
- Abellán, A., Jaboyedoff, M., Oppikofer, T. & Vilaplana, J. M. (2009). Detection of millimetric deformation using a terrestrial laser scanner: Experiment and application to a rockfall event. *Natural Hazards and Earth System Science*, 9(2), 365-372, doi:10.5194/nhess-9-365-2009.
- Achilli, V., Carrubba, P., Fabris, M., Menin, A. & Pavanello, P. (2015). An archival geomatics approach in the study of a landslide. *Applied Geomatics*, 7(4), 263-273, doi:10.1007/s12518-015-0153-4.
- Ackermann, F. (1984). Digital image correlation: performance and potential application in photogrammetry. *The Photogrammetric Record*, 11(64), 429-439, doi:10.1111/j.1477-9730.1984.tb00505.x.
- Ackermann, F. (1999). Airborne laser scanning - Present status and future expectations. *ISPRS Journal of Photogrammetry and Remote Sensing*, 54(2-3), 64-67, doi:10.1016/S0924-2716(99)00009-X.
- Aguilar, F. J., Agüera, F., Aguilar, M. A. & Carvajal, F. (2005). Effects of terrain morphology, sampling density, and interpolation methods on grid DEM accuracy. *Photogrammetric Engineering and Remote Sensing*, 71(7), 805-816, doi:10.14358/PERS.71.7.805.
- Aguilar, F. J., Mills, J. P., Delgado, J., Aguilar, M. A., Negreiros, J. G. & Pérez, J. L. (2010). Modelling vertical error in LiDAR-derived digital elevation models. *ISPRS Journal of Photogrammetry and Remote Sensing*, 65(1), 103-110, doi:10.1016/j.isprsjprs.2009.09.003.
- Aiger, D., Mitra, N. J. & Cohen-Or, D. (2008). 4-Points congruent sets for robust pairwise surface registration. *ACM Transactions on Graphics*, 27(3), doi:10.1145/1360612.1360684.
- Al-Rawabdeh, A., Al-Gurrani, H., Al-Durgham, K., Detchev, I., He, F., El-Sheimy, N. & Habib, A. (2016a). A robust registration algorithm for point clouds from UAV images for change detection. *The International Archives of the Photogrammetry, Remote Sensing and Spatial Information Sciences*, 2016a. 765-772.
- Al-Rawabdeh, A., He, F., Moussa, A., El-Sheimy, N. & Habib, A. (2016b). Using an unmanned aerial vehicle-based digital imaging system to derive a 3D point cloud for landslide scarp recognition. *Remote Sensing*, 8(2), doi:10.3390/rs8020095.
- Ang, K. & Mitchell, H. L. (2010). Non-rigid surface matching and its application to scoliosis modelling. *The Photogrammetric Record*, 25(130), 105-118, doi:10.1111/j.1477-9730.2010.00581.x.
- Aryal, A., Brooks, B. A., Reid, M. E., Bawden, G. W. & Pawlak, G. R. (2012). Displacement fields from point cloud data: Application of particle imaging velocimetry to landslide geodesy. *Journal of Geophysical Research: Earth Surface*, 117(1), doi:10.1029/2011jf002161.
- Autodesk. (2017). Open-source software Autodesk 123D Catch. Available: <https://autodesk-123d-catch.en.softonic.com/> [Accessed 13th June 2017].
- Ayoub, F., Leprince, S. & Avouac, J. P. (2009a). Co-registration and correlation of aerial photographs for ground deformation measurements. *ISPRS Journal of Photogrammetry and Remote Sensing*, 64(6), 551-560, doi:10.1016/j.isprsjprs.2009.03.005.
- Ayoub, F., Leprince, S. & Keene, L. (2009b). User's guide to COSI-Corr: Co-registration of optically sensed images and correlation. Available from the Caltech Tectonics Observatory <http://www.tectonics.caltech.edu>.

- Baek, M. H. & Kim, T. H. (2015). A study on the use of planarity for quick identification of potential landslide hazard. *Natural Hazards and Earth System Sciences*, 15(5), 997-1009, doi:10.5194/nhess-15-997-2015.
- Baldi, P., Cenni, N., Fabris, M. & Zanutta, A. (2008). Kinematics of a landslide derived from archival photogrammetry and GPS data. *Geomorphology*, 102(3-4), 435-444, doi:10.1016/j.geomorph.2008.04.027.
- Baltsavias, E. P. (1999). A comparison between photogrammetry and laser scanning. *ISPRS Journal of Photogrammetry and Remote Sensing*, 54(2-3), 83-94, doi:10.1016/S0924-2716(99)00014-3.
- Barazzetti, L. & Scaioni, M. (2009). Crack measurement: Development, testing and applications of an automatic image-based algorithm. *ISPRS Journal of Photogrammetry and Remote Sensing*, 64(3), 285-296, doi:10.1016/j.isprsjprs.2009.02.004.
- Barazzetti, L., Scaioni, M. & Gianinetto, M. (2014). Automatic co-registration of satellite time series via least squares adjustment. *European Journal of Remote Sensing*, 47(1), 55-74, doi:10.5721/EuJRS20144705.
- Barazzetti, L., Scaioni, M. & Remondino, F. (2010). Orientation and 3D modelling from markerless terrestrial images: Combining accuracy with automation. *The Photogrammetric Record*, 25(132), 356-381, doi:10.1111/j.1477-9730.2010.00599.x.
- Barbarella, M., Fiani, M. & Lugli, A. (2017). Uncertainty in terrestrial laser scanner surveys of landslides. *Remote Sensing*, 9(2), doi:10.3390/rs90201013.
- Barnea, S. & Filin, S. (2008). Keypoint based autonomous registration of terrestrial laser point-clouds. *ISPRS Journal of Photogrammetry and Remote Sensing*, 63(1), 19-35, doi:10.1016/j.isprsjprs.2007.05.005.
- Barnhart, T. B. & Crosby, B. T. (2013). Comparing two methods of surface change detection on an evolving thermokarst using high-temporal-frequency terrestrial laser scanning, Selawik River, Alaska. *Remote Sensing*, 5(6), 2813-2837, doi:10.3390/rs5062813.
- Bater, C. W. & Coops, N. C. (2009). Evaluating error associated with lidar-derived DEM interpolation. *Computers and Geosciences*, 35(2), 289-300, doi:10.1016/j.cageo.2008.09.001.
- Baum, R. L. & Reid, M. E. (1995). Geology, hydrology, and mechanics of a slow-moving, clay-rich landslide, Honolulu, Hawaii. In: HANEBERG, W. C. & ANDERSON, S. A. (eds.) *Clay and Shale Slope Instability*. Geological Society of America.
- Bay, H., Ess, A., Tuytelaars, T. & Van Gool, L. (2008). Speeded-Up Robust Features (SURF). *Computer Vision and Image Understanding*, 110(3), 346-359, doi:10.1016/j.cviu.2007.09.014.
- Benassi, F., Dall'Asta, E., Diotri, F., Forlani, G., Cella, U. M., Roncella, R. & Santise, M. (2017). Testing accuracy and repeatability of UAV blocks oriented with gnss-supported aerial triangulation. *Remote Sensing*, 9(2), doi:10.3390/rs9020172.
- Berti, M., Corsini, A. & Daehne, A. (2013). Comparative analysis of surface roughness algorithms for the identification of active landslides. *Geomorphology*, 182, 1-18, doi:10.1016/j.geomorph.2012.10.022.
- Besl, P. J. & McKay, N. D. (1992). A method for registration of 3-D shapes. *IEEE Transactions on Pattern Analysis and Machine Intelligence*, 14(2), 239-256, doi:10.1109/34.121791.
- BGS, (2017). *How does BGS classify landslides?* [Online]. BGS. Available: [http://www.bgs.ac.uk/research/engineeringGeology/shallowGeohazardsAndRisks/landslides/How\\_does\\_BGS\\_classify\\_landslides.html](http://www.bgs.ac.uk/research/engineeringGeology/shallowGeohazardsAndRisks/landslides/How_does_BGS_classify_landslides.html) [Accessed 3rd September 2017].
- BGS Landslides Team, (2013). *Increased incidence of landslides in 2012* [Online]. British Geological Survey (BGS). Available: <http://www.bgs.ac.uk/landslides/November2012.html> [Accessed 19th December 2013].
- Birchfield, S. & Tomasi, C. (1999). Depth discontinuities by pixel-to-pixel stereo. *International Journal of Computer Vision*, 35(3), 269-293, doi:10.1023/A:1008160311296.

- Booth, A. M., Roering, J. J. & Perron, J. T. (2009). Automated landslide mapping using spectral analysis and high-resolution topographic data: Puget Sound lowlands, Washington, and Portland Hills, Oregon. *Geomorphology*, 109(3-4), 132-147, doi:10.1016/j.geomorph.2009.02.027.
- Borgatti, L., Vittuari, L. & Zanutta, A. (2010). Geomatic methods for punctual and areal control of surface changes due to landslide phenomena. In: WERNER, E. D. & FRIEDMAN, H. P. (eds.) *Landslides: Causes, Types and Effects*. New York: Nova Science Publishers, Inc. 133-176.
- Börlin, N. & Grussenmeyer, P. (2013). Bundle adjustment with and without damping. *The Photogrammetric Record*, 28(144), 396-415, doi:10.1111/phor.12037.
- Börlin, N. & Grussenmeyer, P. (2016). External verification of the bundle adjustment in photogrammetric software using the damped bundle adjustment toolbox. *The International Archives of the Photogrammetry, Remote Sensing and Spatial Information Sciences*, 2016. 7-14.
- Brasington, J., Langham, J. & Rumsby, B. (2003). Methodological sensitivity of morphometric estimates of coarse fluvial sediment transport. *Geomorphology*, 53(3-4), 299-316, doi:10.1016/S0169-555X(02)00320-3.
- Brasington, J., Vericat, D. & Rychkov, I. (2012). Modeling river bed morphology, roughness, and surface sedimentology using high resolution terrestrial laser scanning. *Water Resources Research*, 48(11), doi:10.1029/2012WR012223.
- Brown, D. C. (1971). Close-range camera calibration. *Photogrammetric Engineering*, 37(8), 855-866.
- Brückl, E., Brunner, F. K. & Kraus, K. (2006). Kinematics of a deep-seated landslide derived from photogrammetric, GPS and geophysical data. *Engineering Geology*, 88(3-4), 149-159, doi:10.1016/j.enggeo.2006.09.004.
- Buckley, S. J. (2003). *A geomatics data fusion technique for change monitoring*. PhD, Newcastle University, Newcastle upon Tyne, UK.
- Buckley, S. J. & Mitchell, H. L. (2004). Integration, validation and point spacing optimisation of digital elevation models. *Photogrammetric Record*, 19(108), 277-295, doi:10.1111/j.0031-868X.2004.00287.x.
- Buscombe, D. (2016). Spatially explicit spectral analysis of point clouds and geospatial data. *Computers and Geosciences*, 86, 92-108, doi:10.1016/j.cageo.2015.10.004.
- CAP (2012). *Unmanned Aircraft System Operations in UK Airspace – Guidance CAP 722*. UK: Civil Aviation Authority, Safety Regulation Group.
- Carbonneau, P. E. & Dietrich, J. T. (2016). Cost-effective non-metric photogrammetry from consumer-grade sUAS: Implications for direct georeferencing of structure from motion photogrammetry. *Earth Surface Processes and Landforms*, doi:10.1002/esp.4012.
- Chambers, J. E., Wilkinson, P. B., Kuras, O., Ford, J. R., Gunn, D. A., Meldrum, P. I., Pennington, C. V. L., Weller, A. L., Hobbs, P. R. N. & Ogilvy, R. D. (2011). Three-dimensional geophysical anatomy of an active landslide in Lias Group mudrocks, Cleveland Basin, UK. *Geomorphology*, 125(4), 472-484, doi:10.1016/j.geomorph.2010.09.017.
- Chandler, J. H. & Brunsten, D. (1995). Steady state behaviour of the black ven mudslide: The application of archival analytical photogrammetry to studies of landform change. *Earth Surface Processes and Landforms*, 20(3), 255-275, doi:10.1002/esp.3290200307.
- Chaplot, V., Darboux, F., Bourennane, H., Leguédou, S., Silvera, N. & Phachomphon, K. (2006). Accuracy of interpolation techniques for the derivation of digital elevation models in relation to landform types and data density. *Geomorphology*, 77(1-2), 126-141, doi:10.1016/j.geomorph.2005.12.010.
- Chaulagain, H., Rodrigues, H., Silva, V., Spacone, E. & Varum, H. (2016). Earthquake loss estimation for the Kathmandu Valley. *Bulletin of Earthquake Engineering*, 14(1), 59-88, doi:10.1007/s10518-015-9811-5.

- Chen, R. F., Lin, C. W., Chen, Y. H., He, T. C. & Fei, L. Y. (2015). Detecting and characterizing active thrust fault and deep-seated landslides in dense forest areas of southern Taiwan using airborne LiDAR DEM. *Remote Sensing*, 7(11), 15443-15466, doi:10.3390/rs71115443.
- Chen, Y. & Medioni, G. (1991). Object modeling by registration of multiple range images. Proceedings - IEEE International Conference on Robotics and Automation, 1991. 2724-2729.
- Chiang, K. W., Tsai, M. L. & Chu, C. H. (2012). The development of an UAV borne direct georeferenced photogrammetric platform for Ground Control Point free applications. *Sensors*, 12(7), 9161-80, doi:10.3390/s120709161.
- Chidburee, P., Mills, J. P., Miller, P. E. & Fieber, K. D. (2016). Towards a low-cost, real-time photogrammetric landslide monitoring system utilising mobile and cloud computing technology. The International Archives of the Photogrammetry, Remote Sensing and Spatial Information Sciences, 2016. 791-797.
- CIAS (2012). Image correlation software (<http://www.mn.uio.no/geo/english/research/projects/icemass/cias/>) University of Oslo.
- Clague, J. J. & Stead, D. (2012). *Landslides types, mechanisms and modeling*, Cambridge, New York, Cambridge University Press.
- Clarke, T. A. & Fryer, J. G. (1998). The development of camera calibration methods and models. *Photogrammetric Record*, 16(91), 51-66.
- Colesanti, C. & Wasowski, J. (2006). Investigating landslides with space-borne Synthetic Aperture Radar (SAR) interferometry. *Engineering Geology*, 88(3-4), 173-199, doi:10.1016/j.enggeo.2006.09.013.
- Collins, R. T. (1996). A space-sweep approach to true multi-image matching. Proceedings CVPR IEEE Computer Society Conference on Computer Vision and Pattern Recognition, 18-20 June 1996. 358-363.
- Colomina, I. & Molina, P. (2014). Unmanned aerial systems for photogrammetry and remote sensing: A review. *ISPRS Journal of Photogrammetry and Remote Sensing*, 92(0), 79-97, doi:10.1016/j.isprsjprs.2014.02.013.
- Cook, K. L. (2017). An evaluation of the effectiveness of low-cost UAVs and structure from motion for geomorphic change detection. *Geomorphology*, 278, 195-208, doi:10.1016/j.geomorph.2016.11.009.
- Corominas, J., Moya, J., Lloret, A., Gili, J. A., Angeli, M. G., Pasuto, A. & Silvano, S. (2000). Measurement of landslide displacements using a wire extensometer. *Engineering Geology*, 55(3), 149-166, doi:10.1016/S0013-7952(99)00086-1.
- Cruden, D. M. (1991). A simple definition of a landslide. *Bulletin of the International Association of Engineering Geology - Bulletin de l'Association Internationale de Géologie de l'Ingénieur*, 43(1), 27-29, doi:10.1007/BF02590167.
- Cruden, D. M. & Varnes, D. J. (1996). Landslide types and processes. In: TURNER AK, S. R. (ed.) *Landslides, investigation and mitigation*. Washington, DC. 36-75.
- d'Oleire-Oltmanns, S., Marzoff, I., Peter, K. D. & Ries, J. B. (2012). Unmanned Aerial Vehicle (UAV) for monitoring soil erosion in Morocco. *Remote Sensing*, 4(12), 3390-3416, doi:10.3390/rs4113390.
- Daehne, A. & Corsini, A. (2013). Kinematics of active earthflows revealed by digital image correlation and DEM subtraction techniques applied to multi-temporal LiDAR data. *Earth Surface Processes and Landforms*, 38(6), 640-654, doi:10.1002/esp.3351.
- Dall'Asta, E., Forlani, G., Roncella, R., Santise, M., Diotri, F. & Morra di Cella, U. (2017). Unmanned Aerial Systems and DSM matching for rock glacier monitoring. *ISPRS Journal of Photogrammetry and Remote Sensing*, 127(1), doi:10.1016/j.isprsjprs.2016.10.003.
- Dall'Asta, E. & Roncella, R. (2014). A comparison of semiglobal and local dense matching algorithms for surface reconstruction. *The International Archives of the Photogrammetry, Remote Sensing and Spatial Information Sciences*, XL-5, 187-194, doi:10.5194/isprsarchives-XL-5-187-2014.

- Dawson, E. M., Roth, W. H. & Drescher, A. (1999). Slope stability analysis by strength reduction. *Geotechnique*, 49(6), 835-840, doi:10.1680/geot.1999.49.6.835.
- de Smith, M. J., Goodchild, M. F. & Longley, P. A., (2015). *Geospatial Analysis A comprehensive Guide to Principles, Techniques and Software Tools* [Online]. The Winchelsea Press Available: <http://www.spatialanalysisonline.com/> [Accessed 15th June 2016].
- Debella-Gilo, M. & Kääh, A. (2011). Sub-pixel precision image matching for measuring surface displacements on mass movements using normalized cross-correlation. *Remote Sensing of Environment*, 115(1), 130-142, doi:10.1016/j.rse.2010.08.012.
- Delacourt, C., Allemand, P., Jaud, M., Grandjean, P., Deschamps, A., Ammann, J., Cuq, V. & Suanez, S. (2009). DRELIO: An unmanned helicopter for imaging coastal areas. *Journal of Coastal Research*, (SPEC. ISSUE 56), 1489-1493.
- Dellinger, F., Delon, J., Gousseau, Y., Michel, J. & Tupin, F. (2015). SAR-SIFT: A SIFT-like algorithm for SAR images. *IEEE Transactions on Geoscience and Remote Sensing*, 53(1), 453-466, doi:10.1109/TGRS.2014.2323552.
- Dermanis, A. (1994). The photogrammetric inner constraints. *ISPRS Journal of Photogrammetry and Remote Sensing*, 49(1), 25-39, doi:10.1016/0924-2716(94)90053-1.
- Dewitte, O., Jasselette, J. C., Cornet, Y., Van Den Eeckhaut, M., Collignon, A., Poesen, J. & Demoulin, A. (2008). Tracking landslide displacements by multi-temporal DTMs: A combined aerial stereophotogrammetric and LIDAR approach in western Belgium. *Engineering Geology*, 99(1-2), 11-22, doi:10.1016/j.enggeo.2008.02.006.
- Dietrich, J. T. (2016). Riverscape mapping with helicopter-based Structure-from-Motion photogrammetry. *Geomorphology*, 252, 144-157, doi:10.1016/j.geomorph.2015.05.008.
- Dominguez, S., Avouac, J. P. & Michel, R. (2003). Horizontal coseismic deformation of the 1999 Chi-Chi earthquake measured from SPOT satellite images: Implications for the seismic cycle along the western foothills of central Taiwan. *Journal of Geophysical Research: Solid Earth*, 108(2), ESE 8-1 - 8-19, doi:10.1029/2001jb000951.
- Dunnicliff, J. (1988). *Geotechnical instrumentation for monitoring field performance*, New York, Wiley, 608.
- Dyn, N., Iske, A. & Wendland, H. (2008). Meshfree thinning of 3D point clouds. *Foundations of Computational Mathematics*, 8(4), 409-425, doi:10.1007/s10208-007-9008-7.
- Eisenbeiß, H. (2009). *UAV photogrammetry*. PhD Thesis, Swiss Federal Institute of Technology (ETH).
- Eisenbeiss, H. & Sauerbier, M. (2011). Investigation of UAV systems and flight modes for photogrammetric applications. *The Photogrammetric Record*, 26(136), 400-421, doi:10.1111/j.1477-9730.2011.00657.x.
- Eltner, A., Baumgart, P., Maas, H. G. & Faust, D. (2015). Multi-temporal UAV data for automatic measurement of rill and interrill erosion on loess soil. *Earth Surface Processes and Landforms*, 40(6), 741-755, doi:10.1002/esp.3673.
- Eltner, A., Kaiser, A., Castillo, C., Rock, G., Neugirg, F. & Abellán, A. (2016). Image-based surface reconstruction in geomorphometry-merits, limits and developments. *Earth Surface Dynamics*, 4(2), 359-389, doi:10.5194/esurf-4-359-2016.
- Eltner, A. & Schneider, D. (2015). Analysis of different methods for 3D reconstruction of natural surfaces from parallel-axes UAV images. *The Photogrammetric Record*, 30(151), 279-299, doi:10.1111/phor.12115.
- Evans, I. S. (1972). General Geomorphometry, derivatives of altitude and descriptive statistics. In: CHORLEY, R. J. (ed.) *Spatial Analysis in Geomorphology*. London, UK: Methuen & Co Ltd. 17-90.
- Evans, I. S. (1979). *An Integrated System of Terrain Analysis and Slope Mapping. Final Report (Report 6) on Grant DA-ERO-591-73-G0040*, Department of Geography, University of Durham, 192.

- Evans, I. S. (1980). An integrated system of terrain analysis and slope mapping. *Zeitschrift für Geomorphologie, Supplementband*, 36, 274-295.
- Fan, L. & Atkinson, P. M. (2015). Accuracy of Digital Elevation Models Derived From Terrestrial Laser Scanning Data. *IEEE Geoscience and Remote Sensing Letters*, doi:10.1109/LGRS.2015.2438394.
- Favalli, M. & Fornaciai, A. (2017). Visualization and comparison of DEM-derived parameters. Application to volcanic areas. *Geomorphology*, 290, 69-84, doi:10.1016/j.geomorph.2017.02.029.
- Ferraz, A., Mallet, C. & Chehata, N. (2016). Large-scale road detection in forested mountainous areas using airborne topographic lidar data. *ISPRS Journal of Photogrammetry and Remote Sensing*, 112, 23-36, doi:10.1016/j.isprsjprs.2015.12.002.
- Fey, C., Rutzinger, M., Wichmann, V., Prager, C., Bremer, M. & Zangerl, C. (2015). Deriving 3D displacement vectors from multi-temporal airborne laser scanning data for landslide activity analyses. *GIScience & Remote Sensing*, 52(4), 437-461, doi:10.1080/15481603.2015.1045278.
- Fischler, M. A. & Bolles, R. C. (1981). Random sample consensus: a paradigm for model fitting with applications to image analysis and automated cartography. *Communications of the ACM*, 24(6), 381-395, doi:10.1145/358669.358692.
- Fonstad, M. A., Dietrich, J. T., Courville, B. C., Jensen, J. L. & Carbonneau, P. E. (2013). Topographic structure from motion: A new development in photogrammetric measurement. *Earth Surface Processes and Landforms*, 38(4), 421-430, doi:10.1002/esp.3366.
- Förstner, W. (1982). On the geometric precision of digital correlation. *The International Archives of the Photogrammetry, Remote Sensing and Spatial Information Sciences*, 24(3), 176-189.
- Förstner, W. (1986). A Feature Based Correspondence Algorithm for Image Matching. *The International Archives of the Photogrammetry, Remote Sensing and Spatial Information Sciences*, 26(3), 150-166.
- Förstner, W. (1993). Feature extraction in Digital Photogrammetry. *The Photogrammetric Record*, 14(82), 595-611, doi:10.1111/j.1477-9730.1993.tb00771.x.
- Förstner, W. & Gülch, E. (1987). A Fast Operator for Detection and Precise Location of Distinct Points, Corners and Centers of Circular Features. ISPRS Intercommission Workshop, 1987.
- Frankel, K. L. & Dolan, J. F. (2007). Characterizing arid region alluvial fan surface roughness with airborne laser swath mapping digital topographic data. *Journal of Geophysical Research: Earth Surface*, 112(2), doi:10.1029/2006JF000644.
- Franklin, J. A. (1984). Slope instrumentation and monitoring. In: BRUNSDEN, D. & PRIOR, D. B. (eds.) *Slope Instability*. Wiley, Chichester. 143-169.
- Fraser, C. S. (1982). Optimization of precision in close-range photogrammetry. *Photogrammetric Engineering and Remote Sensing*, 48(4), 561-570.
- Fraser, C. S. (1997). Digital camera self-calibration. *ISPRS Journal of Photogrammetry and Remote Sensing*, 52(4), 149-159, doi:10.1016/S0924-2716(97)00005-1.
- Furukawa, Y. & Ponce, J. (2010). Accurate, dense, and robust multiview stereopsis. *IEEE Transactions on Pattern Analysis and Machine Intelligence*, 32(8), 1362-1376, doi:10.1109/TPAMI.2009.161.
- Gance, J., Malet, J. P., Dewez, T. & Travelletti, J. (2014). Target Detection and Tracking of moving objects for characterizing landslide displacements from time-lapse terrestrial optical images. *Engineering Geology*, 172, 26-40, doi:10.1016/j.enggeo.2014.01.003.
- Gariano, S. L. & Guzzetti, F. (2016). Landslides in a changing climate. *Earth-Science Reviews*, 162, 227-252, doi:10.1016/j.earscirev.2016.08.011.
- Gehrke, S., Morin, K., Downey, M., Boehrer, N. & Fuchs, T. (2010). Semi-global matching: An alternative to lidar for DSM generation? *The International Archives of the Photogrammetry, Remote Sensing and Spatial Information Sciences*, 2010.

- Gerke, M. & Przybilla, H. J. (2016). Accuracy analysis of photogrammetric UAV image blocks: Influence of onboard RTK-GNSS and cross flight patterns. *Photogrammetrie, Fernerkundung, Geoinformation*, 2016(1), 17-30, doi:10.1127/pfg/2016/0284.
- Ghuffar, S., Székely, B., Roncat, A. & Pfeifer, N. (2013). Landslide displacement monitoring using 3D range flow on airborne and terrestrial LiDAR data. *Remote Sensing*, 5(6), 2720-2745, doi:10.3390/rs5062720.
- Gili, J. A., Corominas, J. & Rius, J. (2000). Using Global Positioning System techniques in landslide monitoring. *Engineering Geology*, 55(3), 167-192, doi:10.1016/S0013-7952(99)00127-1.
- Giordan, D., Allasia, P., Manconi, A., Baldo, M., Santangelo, M., Cardinali, M., Corazza, A., Albanese, V., Lollino, G. & Guzzetti, F. (2013). Morphological and kinematic evolution of a large earthflow: The Montaguto landslide, southern Italy. *Geomorphology*, 187, 61-79, doi:10.1016/j.geomorph.2012.12.035.
- Glenn, N. F., Streutker, D. R., Chadwick, D. J., Thackray, G. D. & Dorsch, S. J. (2006). Analysis of LiDAR-derived topographic information for characterizing and differentiating landslide morphology and activity. *Geomorphology*, 73(1-2), 131-148, doi:10.1016/j.geomorph.2005.07.006.
- Glira, P., Pfeifer, N., Briese, C. & Ressel, C. (2015). A correspondence framework for ALS strip adjustments based on variants of the ICP algorithm. *Photogrammetrie, Fernerkundung, Geoinformation*, 2015(4), 275-289, doi:10.1127/pfg/2015/0270.
- Gneeniss, A. S., Mills, J. P. & Miller, P. E. (2015). In-flight photogrammetric camera calibration and validation via complementary lidar. *ISPRS Journal of Photogrammetry and Remote Sensing*, 100, 3-13, doi:10.1016/j.isprsjprs.2014.04.019.
- Godone, D. & Garnero, G. (2013). The role of morphometric parameters in Digital Terrain Models interpolation accuracy: a case study. *European Journal of Remote Sensing*, 46(1), 198-214, doi:10.5721/EuJRS20134611.
- Gonçalves, J. A. & Henriques, R. (2015). UAV photogrammetry for topographic monitoring of coastal areas. *ISPRS Journal of Photogrammetry and Remote Sensing*, 104, 101-111, doi:10.1016/j.isprsjprs.2015.02.009.
- Graham, R. W. (1988). SMALL FORMAT AERIAL SURVEYS FROM LIGHT AND MICROLIGHT AIRCRAFT. *The Photogrammetric Record*, 12(71), 561-573, doi:10.1111/j.1477-9730.1988.tb00605.x.
- Granshaw, S. I. (1980). Bundle adjustment methods in Engineering Photogrammetry *The Photogrammetric Record*, 10(56), 181-207, doi:10.1111/j.1477-9730.1980.tb00020.x.
- Granshaw, S. I. (2016a). Photogrammetric Terminology: Third Edition. *The Photogrammetric Record*, 31(154), 210-252, doi:10.1111/phor.12146.
- Granshaw, S. I. (2016b). Terminological Dichotomies. *The Photogrammetric Record*, 31(154), 116-120, doi:10.1111/phor.12148.
- Granshaw, S. I. & Fraser, C. S. (2015). Editorial: Computer Vision and Photogrammetry: Interaction or Introspection? *The Photogrammetric Record*, 30(149), 3-7, doi:10.1111/phor.12092.
- Gray, A. (1997). The Three Fundamental Forms. *Modern Differential Geometry of Curves and Surfaces with Mathematica*. 2nd ed.: CRC Press, Inc. 1056.
- Grohmann, C. H., Smith, M. J. & Riccomini, C. (2011). Multiscale analysis of topographic surface roughness in the Midland Valley, Scotland. *IEEE Transactions on Geoscience and Remote Sensing*, 49(4), 1200-1213, doi:10.1109/TGRS.2010.2053546.
- Groves, P. D. (2013). *Principles of GNSS, Inertial, and multisensor integrated navigation systems*, Artech House GNSS Library.
- Gruen, A. (2012). Development and Status of Image Matching in Photogrammetry. *The Photogrammetric Record*, 27(137), 36-57, doi:10.1111/j.1477-9730.2011.00671.x.

- Gruen, A. & Akca, D. (2005). Least squares 3D surface and curve matching. *ISPRS Journal of Photogrammetry and Remote Sensing*, 59(3), 151-174, doi:10.1016/j.isprsjprs.2005.02.006.
- Gruen, A. & Baltsavias, E. P. (1988). Geometrically Constrained Multiphoto Matching. *Photogrammetric Engineering and Remote Sensing*, 54(5), 633-641.
- Gruen, A. W. (1985). Adaptive Least Squares Correlation: A Powerful Image Matching Technique. *South African Journal of Photogrammetry, Remote Sensing, and Cartography*, 14.
- Gunn, D. A., Chambers, J. E., Hobbs, P. R. N., Ford, J. R., Wilkinson, P. B., Jenkins, G. O. & Merritt, A. (2013). Rapid observations to guide the design of systems for long-term monitoring of a complex landslide in the Upper Lias clays of North Yorkshire, UK. *Quarterly Journal of Engineering Geology and Hydrogeology*, 46(3), 323-336, doi:10.1144/qjegh2011-028.
- Guo, Q., Li, W., Yu, H. & Alvarez, O. (2010). Effects of topographic variability and lidar sampling density on several DEM interpolation methods. *Photogrammetric Engineering and Remote Sensing*, 76(6), 701-712, doi:10.14358/PERS.76.6.701.
- Haala, N. & Rothemel, M. (2012). Dense multi-stereo matching for high quality Digital Elevation Models. *Photogrammetrie, Fernerkundung, Geoinformation*, 2012(4), 331-343, doi:10.1127/1432-8364/2012/0121.
- Habib, A., Pullivelli, A., Mitishita, E., Ghanma, M. & Kim, E. M. (2006). Stability analysis of low-cost digital cameras for aerial mapping using different georeferencing techniques. *The Photogrammetric Record*, 21(113), 29-+, doi:10.1111/j.1477-9730.2006.00352.x.
- Hajiyev, C. & Soken, H. E. (2013). Robust Adaptive Kalman Filter for estimation of UAV dynamics in the presence of sensor/actuator faults. *Aerospace Science and Technology*, 28(1), 376-383, doi:10.1016/j.ast.2012.12.003.
- Hänsch, R., Weber, T. & Hellwich, O. (2014). Comparison of 3D interest point detectors and descriptors for point cloud fusion. *ISPRS Ann. Photogramm. Remote Sens. Spatial Inf. Sci.*, II-3, 57-64, doi:10.5194/isprsannals-II-3-57-2014.
- Haque, U., Blum, P., da Silva, P. F., Andersen, P., Pilz, J., Chalov, S. R., Malet, J. P., Auflič, M. J., Andres, N., Poyiadji, E., Lamas, P. C., Zhang, W., Peshevski, I., Pétursson, H. G., Kurt, T., Dobrev, N., García-Davalillo, J. C., Halkia, M., Ferri, S., Gaprindashvili, G., Engström, J. & Keellings, D. (2016). Fatal landslides in Europe. *Landslides*, 13(6), 1545-1554, doi:10.1007/s10346-016-0689-3.
- Harris, C. & Stephens, M. (1988). A combined corner and edge detector. Proceedings of the fourth Alvey Vision Conference, 1988. 147-151.
- Hartley, R. I. & Zisserman, A. (2004). *Multiple View Geometry in Computer Vision*, Second ed, Cambridge University Press, 673.
- Harwin, S., Lucieer, A. & Osborn, J. (2015). The impact of the calibration method on the accuracy of point clouds derived using unmanned aerial vehicle multi-view stereopsis. *Remote Sensing*, 7(9), 11933-11953, doi:10.3390/rs70911933.
- Heid, T. & Kääh, A. (2012). Evaluation of existing image matching methods for deriving glacier surface displacements globally from optical satellite imagery. *Remote Sensing of Environment*, 118, 339-355, doi:10.1016/j.rse.2011.11.024.
- Heipke, C. (1992). A global approach for least-squares image matching and surface reconstruction in object space. *Photogrammetric Engineering and Remote Sensing*, 58(3), 317-323.
- Helava, U. V. (1978). Digital correlation in photogrammetric instruments. *Photogrammetria*, 34(1), 19-41, doi:10.1016/0031-8663(78)90020-0.
- Heritage, G. L., Milan, D. J., Large, A. R. G. & Fuller, I. C. (2009). Influence of survey strategy and interpolation model on DEM quality. *Geomorphology*, 112(3-4), 334-344, doi:10.1016/j.geomorph.2009.06.024.
- Hiller, J. K. & Smith, M. (2008). Residual relief separation: Digital elevation model enhancement for geomorphological mapping. *Earth Surface Processes and Landforms*, 33(14), 2266-2276.

- Hirschmüller, H. (2008). Stereo processing by semiglobal matching and mutual information. *IEEE Transactions on Pattern Analysis and Machine Intelligence*, 30(2), 328-341, doi:10.1109/TPAMI.2007.1166.
- Hobrough, G. L. (1959). Automatic stereo plotting. *Photogrammetric Engineering*, 25(5), 763-769.
- Hobson, R. D. (1972). Surface roughness in topography: quantitative approach. In: CHORLEY, R. J. (ed.) *Spatial Analysis in Geomorphology*. Methuen, London. 221-245.
- Hofmann-Wellenhof, B. (2008). *GNSS - Global Navigation Satellite Systems: GPS, GLONASS, Galileo, and more*, Wien; New York: Springer, 516.
- Hollaus, M., Mandlbürger, G., Pfeifer, N. & Mücke, W. (2010). Land cover dependent derivation of digital surface models from airborne laser scanning data. *The International Archives of the Photogrammetry, Remote Sensing and Spatial Information Sciences*, 2010. 221-226.
- Horn, B. K. P. (1981). Hill Shading and the Reflectance Map. *Proceedings of the IEEE*, 69(1), 14-47, doi:10.1109/PROC.1981.11918.
- Hungr, O., Leroueil, S. & Picarelli, L. (2014). The Varnes classification of landslide types, an update. *Landslides*, 11(2), 167-194, doi:10.1007/s10346-013-0436-y.
- Immerzeel, W. W., Kraaijenbrink, P. D. A., Shea, J. M., Shrestha, A. B., Pellicciotti, F., Bierkens, M. F. P. & De Jong, S. M. (2014). High-resolution monitoring of Himalayan glacier dynamics using unmanned aerial vehicles. *Remote Sensing of Environment*, 150, 93-103, doi:10.1016/j.rse.2014.04.025.
- Ives, R.-O. & Delbracio, M. (2014). Anatomy of the SIFT Method. *Image Processing On Line*, 4, 370-396, doi:10.5201/ipol.2014.82.
- Iwahashi, J., Watanabe, S. & Furuya, T. (2003). Mean slope-angle frequency distribution and size frequency distribution of landslide masses in Higashikubiki area, Japan. *Geomorphology*, 50(4), 349-364, doi:10.1016/S0169-555X(02)00222-2.
- Jaboyedoff, M., Oppikofer, T., Abellán, A., Derron, M. H., Loye, A., Metzger, R. & Pedrazzini, A. (2012). Use of LIDAR in landslide investigations: A review. *Natural Hazards*, 61(1), 5-28, doi:10.1007/s11069-010-9634-2.
- James, M. R. & Robson, S. (2012). Straightforward reconstruction of 3D surfaces and topography with a camera: Accuracy and geoscience application. *Journal of Geophysical Research: Earth Surface*, 117(3), doi:10.1029/2011jf002289.
- James, M. R. & Robson, S. (2014). Mitigating systematic error in topographic models derived from UAV and ground-based image networks. *Earth Surface Processes and Landforms*, 39(10), 1413-1420, doi:10.1002/esp.3609.
- James, M. R., Robson, S., d'Oleire-Oltmanns, S. & Niethammer, U. (2017a). Optimising UAV topographic surveys processed with structure-from-motion: Ground control quality, quantity and bundle adjustment. *Geomorphology*, 280, 51-66, doi:10.1016/j.geomorph.2016.11.021.
- James, M. R., Robson, S. & Smith, M. W. (2017b). 3-D uncertainty-based topographic change detection with structure-from-motion photogrammetry: precision maps for ground control and directly georeferenced surveys [in press]. *Earth Surface Processes and Landforms* doi:10.1002/esp.4125.
- Javernick, L., Brasington, J. & Caruso, B. (2014). Modeling the topography of shallow braided rivers using Structure-from-Motion photogrammetry. *Geomorphology*, 213, 166-182, doi:10.1016/j.geomorph.2014.01.006.
- Jazayeri, I. & Fraser, C. S. (2010). Interest operators for feature-based matching in close range photogrammetry. *The Photogrammetric Record*, 25(129), 24-41, doi:10.1111/j.1477-9730.2009.00559.x.
- Jensen, A. M., Neilson, B. T., McKee, M. & Chen, Y. (2012). Thermal remote sensing with an autonomous unmanned aerial remote sensing platform for surface stream temperatures. *International Geoscience and Remote Sensing Symposium (IGARSS)*, 2012. 5049-5052.

- Jongmans, D. & Garambois, S. (2007). Geophysical investigation of landslides: A review. *Bulletin de la Societe Geologique de France*, 178(2), 101-112, doi:10.2113/gssgfbull.178.2.101.
- Kääb, A. & Vollmer, M. (2000). Surface geometry, thickness changes and flow fields on creeping mountain permafrost: Automatic extraction by digital image analysis. *Permafrost and Periglacial Processes*, 11(4), 315-326, doi:10.1002/1099-1530(200012)11:4<315::AID-PPP365>3.0.CO;2-J.
- Karras, G. E. & Petsa, E. (1993). DEM matching and detection of deformation in close-range photogrammetry without control. *Photogrammetric Engineering and Remote Sensing*, 59(9), 1419-1424.
- Kasai, M., Ikeda, M., Asahina, T. & Fujisawa, K. (2009). LiDAR-derived DEM evaluation of deep-seated landslides in a steep and rocky region of Japan. *Geomorphology*, 113(1-2), 57-69, doi:10.1016/j.geomorph.2009.06.004.
- Ke, Y. & Sukthankar, R. (2004). PCA-SIFT: A more distinctive representation for local image descriptors. *Computer Vision and Pattern Recognition, 2004. CVPR 2004. Proceedings of the 2004 IEEE Computer Society Conference on, 2004. IEEE*, II-506-II-513.
- Kehl, C., Buckley, S. J., Viseur, S., Gawthorpe, R. L. & Howell, J. A. (2017). Automatic Illumination-Invariant Image-to-Geometry Registration in Outdoor Environments. *The Photogrammetric Record*, 32(158), 93-118, doi:10.1111/phor.12188.
- Kenner, R., Bühler, Y., Delaloye, R., Ginzler, C. & Phillips, M. (2014). Monitoring of high alpine mass movements combining laser scanning with digital airborne photogrammetry. *Geomorphology*, 206, 492-504, doi:10.1016/j.geomorph.2013.10.020.
- Klose, M., Highland, L., Damm, B. & Terhorst, B. (2014). Estimation of direct landslide costs in industrialized countries: Challenges, concepts, and case study. *Landslide Science for a Safer Geoenvironment: Volume 2: Methods of Landslide Studies*. 661-667.
- Koch, A. & Heipke, C. (2006). Semantically correct 2.5D GIS data - The integration of a DTM and topographic vector data. *ISPRS Journal of Photogrammetry and Remote Sensing*, 61(1), 23-32, doi:10.1016/j.isprsjprs.2006.07.005.
- Kraus, K. (2007). *Photogrammetry: geometry from images and laser scans*, 2nd ed, Berlin; New York, Walter De Gruyter, 476.
- Kraus, K., Karel, W., Briese, C. & Mandlbürger, G. (2006). Local accuracy measures for digital terrain models. *The Photogrammetric Record*, 21(116), 342-354, doi:10.1111/j.1477-9730.2006.00400.x.
- Krig, S. (2014). *Computer vision metrics: Survey, taxonomy, and analysis*, 1-472. 10.1007/978-1-4302-5930-5
- Kunz, M., King, M. A., Mills, J. P., Miller, P. E., Fox, A. J., Vaughan, D. G. & Marsh, S. H. (2012). Multi-decadal glacier surface lowering in the Antarctic Peninsula. *Geophysical Research Letters*, 39(19), L19502, doi:10.1029/2012gl052823.
- Lague, D., Brodu, N. & Leroux, J. (2013). Accurate 3D comparison of complex topography with terrestrial laser scanner: Application to the Rangitikei canyon (N-Z). *ISPRS Journal of Photogrammetry and Remote Sensing*, 82, 10-26, doi:10.1016/j.isprsjprs.2013.04.009.
- Laliberte, A. S., Goforth, M. A., Steele, C. M. & Rango, A. (2011). Multispectral remote sensing from unmanned aircraft: Image processing workflows and applications for rangeland environments. *Remote Sensing*, 3(11), 2529-2551, doi:10.3390/rs3112529.
- Lancaster, P. & Salkauskas, K. (1981). Surfaces generated by moving least squares methods. *Mathematics of computation*, 37(155), 141-158, doi:10.2307/2007507.
- Lane, S. N., James, T. D. & Crowell, M. D. (2000). Application of digital photogrammetry to complex topography for geomorphological research. *The Photogrammetric Record*, 16(95), 793-821, doi:10.1111/0031-868x.00152.
- Lane, S. N., Richards, K. S. & Chandler, J. H. (1998). *Landform monitoring, modelling, and analysis*, Chichester, J. Wiley & Sons, 454.

- Lane, S. N., Westaway, R. M. & Hicks, D. M. (2003). Estimation of erosion and deposition volumes in a large, gravel-bed, braided river using synoptic remote sensing. *Earth Surface Processes and Landforms*, 28(3), 249-271, doi:10.1002/esp.483.
- Lecomte, I., Grandjean, G. & Michoud, C. (2010). Ground-Based Geophysical Investigations. *In the Deliverable 4.1 of the European project SAFELAND: Review of Techniques for Landslide Detection, Fast Characterisation, Rapid Mapping and Long-Term Monitoring*
- Lee, E. M. (2004). *Landslide risk assessment*, London, Thomas Telford, 410.
- Lee, S. & Min, K. (2001). Statistical analysis of landslide susceptibility at Yongin, Korea. *Environmental Geology*, 40(9), 1095-1113, doi:10.1007/s002540100310.
- Leprince, S., Ayoub, F., Klinger, Y. & Avouac, J. P. (2007a). Co-Registration of Optically Sensed Images and Correlation (COSI-Corr): an Operational Methodology for Ground Deformation Measurements. *IEEE International Geoscience and Remote Sensing Symposium (IGARSS 2007)*.
- Leprince, S., Barbot, S., Ayoub, F. & Avouac, J. P. (2007b). Automatic and precise orthorectification, coregistration, and subpixel correlation of satellite images, application to ground deformation measurements. *IEEE Transactions on Geoscience and Remote Sensing*, 45(6), 1529-1558, doi:10.1109/TGRS.2006.888937.
- Lewis, J. P. (1995). Fast Normalized Cross-Correlation. *Vision Interface*, 10 (1), 120-123.
- Lichti, D. D. & Jamtsho, S. (2006). Angular resolution of terrestrial laser scanners. *The Photogrammetric Record*, 21(114), 141-160, doi:10.1111/j.1477-9730.2006.00367.x.
- LIME, (2018). *Visualisation and Interpretation Software* [Online]. Virtual Outcrop Geology Group, Uni Research CIPR, Bergen, Norway Available: <http://virtualoutcrop.com/lime> [Accessed 15th January 2018].
- Liu, J.-G. & Mason, P. J. (2016). *Essential image processing and GIS for remote sensing*, 2nd ed, Oxford: Wiley-Blackwell., 456.
- Liu, S., Tong, X., Chen, J., Liu, X., Sun, W., Xie, H., Chen, P., Jin, Y. & Ye, Z. (2016). A linear feature-based approach for the registration of unmanned aerial vehicle remotely-sensed images and airborne LiDAR data. *Remote Sensing*, 8(2), doi:10.3390/rs8020082.
- Lloyd, C. D. & Atkinson, P. M. (2002). Deriving DSMs from LiDAR data with kriging. *International Journal of Remote Sensing*, 23(12), 2519-2524, doi:10.1080/01431160110097998.
- Longuet-Higgins, H. C. (1981). A computer algorithm for reconstructing a scene from two projections. *Nature*, 293(5828), 133-135.
- Lourakis, M. I. A. & Argyros, A. A. (2009). SBA: A software package for generic sparse bundle adjustment. *ACM Transactions on Mathematical Software*, 36(1), doi:10.1145/1486525.1486527.
- Lowe, D. G. (2004). Distinctive image features from scale-invariant keypoints. *International Journal of Computer Vision*, 60(2), 91-110, doi:10.1023/B:VISI.0000029664.99615.94.
- Lu, D., Mausel, P., Brondízio, E. & Moran, E. (2004). Change detection techniques. *International Journal of Remote Sensing*, 25(12), 2365-2407, doi:10.1080/0143116031000139863.
- Lucas, B., D. & Kanade, T. (1981). An Iterative Image Registration Technique with an Application to Stereo Vision (IJCAI). Proceedings of the 7th International Joint Conference on Artificial Intelligence (IJCAI '81), 1981. 674-679.
- Lucieer, A., Jong, S. M. & Turner, D. (2014). Mapping landslide displacements using Structure from Motion (SfM) and image correlation of multi-temporal UAV photography. *Progress in Physical Geography*, 38(1), 97-116, doi:10.1177/0309133313515293.
- Luhmann, T., Fraser, C. & Maas, H. G. (2016). Sensor modelling and camera calibration for close-range photogrammetry. *ISPRS Journal of Photogrammetry and Remote Sensing*, 115, 37-46, doi:10.1016/j.isprsjprs.2015.10.006.

- Maas, H.-G. (1996). Automatic DEM generation by multi-image feature based matching. *The International Archives of the Photogrammetry, Remote Sensing and Spatial Information Sciences*, 31(3), 484-489.
- Malet, J. P., Maquaire, O. & Calais, E. (2002). The use of Global Positioning System techniques for the continuous monitoring of landslides: application to the Super-Sauze earth flow (Alpes-de-Haute-Provence, France). *Geomorphology*, 43(1), 33-54, doi:10.1016/S0169-555X(01)00098-8.
- Mancini, F., Dubbini, M., Gattelli, M., Stecchi, F., Fabbri, S. & Gabbianelli, G. (2013). Using unmanned aerial vehicles (UAV) for high-resolution reconstruction of topography: The structure from motion approach on coastal environments. *Remote Sensing*, 5(12), 6880-6898, doi:10.3390/rs5126880.
- Mantovani, F., Soeters, R. & Van Westen, C. J. (1996). Remote sensing techniques for landslide studies and hazard zonation in Europe. *Geomorphology*, 15(3-4 SPEC. ISS.), 213-225, doi:10.1016/0169-555x(95)00071-C.
- Marr, D. & Poggio, T. (1976). Cooperative computation of stereo disparity. *Science*, 194(4262), 283-287, doi:10.1126/science.968482.
- Maune, D. F., American Society for, P. & Remote, S. (2007). Digital elevation model technologies and applications: the DEM users manual. *DEM users manual*. 2nd ed. Bethesda, MD: Bethesda, MD : American Society for Photogrammetry and Remote Sensing.
- McKean, J. & Roering, J. (2004). Objective landslide detection and surface morphology mapping using high-resolution airborne laser altimetry. *Geomorphology*, 57(3-4), 331-351, doi:10.1016/S0169-555X(03)00164-8.
- Merritt, A. J., Chambers, J. E., Murphy, W., Wilkinson, P. B., West, L. J., Gunn, D. A., Meldrum, P. I., Kirkham, M. & Dixon, N. (2014). 3D ground model development for an active landslide in Lias mudrocks using geophysical, remote sensing and geotechnical methods. *Landslides*, 11(4), 537-550, doi:10.1007/s10346-013-0409-1.
- Messerli, A. & Grinsted, A. (2015). Image georectification and feature tracking toolbox: ImGRAFT. *Geoscientific Instrumentation, Methods and Data Systems*, 4(1), 23-34, doi:10.5194/gi-4-23-2015.
- Michael, S. L. & Heinrich, H. B. (2000). Depth Discrimination from Shading under Diffuse Lighting. *Perception*, 29(6), 649-660, doi:10.1068/p3060.
- Micheletti, N., Chandler, J. H. & Lane, S. N. (2015). Investigating the geomorphological potential of freely available and accessible structure-from-motion photogrammetry using a smartphone. *Earth Surface Processes and Landforms*, 40(4), 473-486, doi:10.1002/esp.3648.
- Mikhail, E., M., Bethel, S. J. & McGlone, J. C. (2001). *Introduction to Modern Photogrammetry*, John Wiley & Sons, Inc., 479.
- Mikolajczyk, K. & Schmid, C. (2005). A performance evaluation of local descriptors. *IEEE Transactions on Pattern Analysis and Machine Intelligence*, 27(10), 1615-1630, doi:10.1109/TPAMI.2005.188.
- Milan, D. J., Heritage, G. L., Large, A. R. G. & Fuller, I. C. (2011). Filtering spatial error from DEMs: Implications for morphological change estimation. *Geomorphology*, 125(1), 160-171, doi:10.1016/j.geomorph.2010.09.012.
- Milenković, M., Karel, W., Ressler, C. & Pfeifer, N. (2016). A Comparison of UAV and TLS data for soil roughness assessment. *ISPRS Annals of the Photogrammetry, Remote Sensing and Spatial Information Sciences*, III-5, 145-152, doi:10.5194/isprs-annals-III-5-145-2016.
- Milenkovic, M., Pfeifer, N. & Glira, P. (2015). Applying terrestrial laser scanning for soil surface roughness assessment. *Remote Sensing*, 7(2), 2007-2045, doi:10.3390/rs70202007.
- Milledge, D. G., Lane, S. N. & Warburton, J. (2009). The potential of digital filtering of generic topographic data for geomorphological research. *Earth Surface Processes and Landforms*, 34(1), 63-74, doi:10.1002/esp.1691.

- Miller, P., Mills, J., Edwards, S., Bryan, P., Marsh, S., Mitchell, H. & Hobbs, P. (2008). A robust surface matching technique for coastal geohazard assessment and management. *ISPRS Journal of Photogrammetry and Remote Sensing*, 63(5), 529-542, doi:10.1016/j.isprsjprs.2008.02.003.
- Mills, J. P., Buckley, S. J. & Mitchell, H. L. (2003a). Synergistic fusion of GPS and photogrammetrically generated elevation models. *Photogrammetric Engineering and Remote Sensing*, 69(4), 341-349.
- Mills, J. P., Buckley, S. J., Mitchell, H. L., Clarke, P. J. & Edwards, S. J. (2005). A geomatics data integration technique for coastal change monitoring. *Earth Surface Processes and Landforms*, 30(6), 651-664, doi:10.1002/esp.1165.
- Mills, J. P., Newton, I. & Graham, R. W. (1996). Aerial photography for survey purposes with a high resolution, small format, digital camera. *Photogrammetric Record*, 15(88), 575-587.
- Mills, J. P., Schneider, D., Barber, D. M. & Bryan, P. G. (2003b). Geometric assessment of the kodak DCS Pro back. *The Photogrammetric Record*, 18(103), 193-208, doi:10.1111/0031-868X.t011-00019.
- Mills, S. & McLeod, P. (2013). Global seamline networks for orthomosaic generation via local search. *ISPRS Journal of Photogrammetry and Remote Sensing*, 75, 101-111, doi:10.1016/j.isprsjprs.2012.11.003.
- Mitchell, H. L. (1994). An approach to digital photogrammetry for body surface measurement. *The International Archives of the Photogrammetry, Remote Sensing and Spatial Information Sciences*, 30(5), 265-272.
- Monserrat, O. & Crosetto, M. (2008). Deformation measurement using terrestrial laser scanning data and least squares 3D surface matching. *ISPRS Journal of Photogrammetry and Remote Sensing*, 63(1), 142-154, doi:10.1016/j.isprsjprs.2007.07.008.
- Moravec, H. P. (1981). Rover visual obstacle avoidance. *Proceedings of the 7th international joint conference on Artificial intelligence - Volume 2*. Vancouver, BC, Canada: Morgan Kaufmann Publishers Inc.
- Nex, F. & Remondino, F. (2014). UAV for 3D mapping applications: A review. *Applied Geomatics*, 6(1), 1-15, doi:10.1007/s12518-013-0120-x.
- Niethammer, U., James, M. R., Rothmund, S., Travelletti, J. & Joswig, M. (2012). UAV-based remote sensing of the Super-Sauze landslide: Evaluation and results. *Engineering Geology*, 128, 2-11, doi:10.1016/j.enggeo.2011.03.012.
- Nistér, D. (2004). An efficient solution to the five-point relative pose problem. *IEEE Transactions on Pattern Analysis and Machine Intelligence*, 26(6), 756-770, doi:10.1109/TPAMI.2004.17.
- Noh, M. J. & Howat, I. M. (2014). Automated coregistration of repeat digital elevation models for surface elevation change measurement using geometric constraints. *IEEE Transactions on Geoscience and Remote Sensing*, 52(4), 2247-2260.
- O'Connor, J., Smith, M. J. & James, M. R. (2017). Cameras and settings for aerial surveys in the geosciences. *Progress in Physical Geography*, 41(3), 325-344, doi:10.1177/0309133317703092.
- Otto, G. & Chau, T. (1989). 'Region-growing' algorithm for matching of terrain images. *Image and Vision Computing*, 7(2), 83-94, doi:10.1016/0262-8856(89)90001-2.
- Pauly, M., Gross, M. & Kobbelt, L. P. (2002). Efficient simplification of point-sampled surfaces. *IEEE Visualization, VIS*. doi:10.1109/VISUAL.2002.1183771.
- Peppas, M. V., Mills, J. P., Moore, P., Miller, P. E. & Chambers, J. E. (2016). Accuracy assessment of a uav-based landslide monitoring system. *The International Archives of the Photogrammetry, Remote Sensing and Spatial Information Sciences*, 2016. 895-902.
- Peppas, M. V., Mills, J. P., Moore, P., Miller, P. E. & Chambers, J. E. (2017). Brief communication: Landslide motion from cross correlation of UAV-derived morphological attributes. *Nat. Hazards Earth Syst. Sci.*, 17(12), 2143-2150, doi:10.5194/nhess-17-2143-2017.

- Pfeifer, N., Mandlbürger, G., Otepka, J. & Karel, W. (2014). OPALS: A framework for Airborne Laser Scanning data analysis. *Computers, Environment and Urban Systems*, 45, 125-136, doi:10.1016/j.compenvurbysys.2013.11.002.
- PhotoModeler. (2017). Low-cost commercial 3D modelling, SfM and image matching software from Eos Systems (Canada). Available: <http://www.photomodeler.com/index.html> [Accessed 14th June 2017].
- PhotoScan. (2016a). Commercial SfM and image matching software from Russian company Agisoft version 1.2.5 ([www.agisoft.com](http://www.agisoft.com)). Available: User's manual (<http://www.agisoft.com/downloads/user-manuals/>) [Accessed 15th March 2017].
- PhotoScan, (2016b). *PhotoScan's related documentation* [Online]. Available: <http://wiki.agisoft.com/wiki/Links/Articles> [Accessed 18th May 2015].
- Pierrot-Deseilligny, M. & Paparoditis, N. (2006). A multiresolution and optimization-based image matching approach: An application to surface reconstruction from SPOT5-HRS stereo imagery. *The International Archives of the Photogrammetry, Remote Sensing and Spatial Information Sciences*, 36(1/W41).
- Pierrot Deseilligny, M. & Clery, I. (2011). Apero, an open source bundle adjustment software for automatic calibration and orientation of set of images. *The International Archives of the Photogrammetry, Remote Sensing and Spatial Information Sciences*, 2011. 269-276.
- Pix4D (2016). Stand-alone software Pix4D ([www.pix4d.com](http://www.pix4d.com)), Pix4D SA.
- Pomerleau, F., Colas, F., Siegwart, R. & Magnenat, S. (2013). Comparing ICP variants on real-world data sets: Open-source library and experimental protocol. *Autonomous Robots*, 34(3), 133-148, doi:10.1007/s10514-013-9327-2.
- Prescott, W. H., Davis, J. L. & Svarc, J. L. (1989). Global positioning system measurements for crustal deformation: Precision and accuracy. *Science*, 244(4910), 1337-1340, doi:10.1126/science.244.4910.1337.
- Pressley, A. (2010). *Elementary Differential Geometry*. Springer Undergraduate Mathematics Series. Springer London, doi:10.1007/978-1-84882-891-9.
- Prokešová, R., Kardoš, M. & Medved'ová, A. (2010). Landslide dynamics from high-resolution aerial photographs: A case study from the Western Carpathians, Slovakia. *Geomorphology*, 115(1-2), 90-101, doi:10.1016/j.geomorph.2009.09.033.
- Quattrochi, D. A. & Luvall, J. C. (2004). *Thermal remote sensing in land surface processes*, New York, Taylor and Francis, 440.
- Rehak, M., Mabillard, R. & Skaloud, J. (2013). A micro-UAV with the capability of direct georeferencing. *UAV-g2013*. Rostock Germany: The International Archives of the Photogrammetry, Remote Sensing and Spatial Information Sciences.
- Rehak, M. & Skaloud, J. (2017a). Performance assessment of integrated sensor orientation with a low-cost GNSS receiver. *ISPRS Annals of the Photogrammetry, Remote Sensing and Spatial Information Sciences*.
- Rehak, M. & Skaloud, J. (2017b). Time synchronization of consumer cameras on Micro Aerial Vehicles. *ISPRS Journal of Photogrammetry and Remote Sensing*, 123, 114-123, doi:10.1016/j.isprsjprs.2016.11.009.
- Remondino, F., Del Pizzo, S., Kersten, T. P. & Troisi, S. (2012). Low-cost and open-source solutions for automated image orientation - A critical overview. *Lecture Notes in Computer Science (including subseries Lecture Notes in Artificial Intelligence and Lecture Notes in Bioinformatics)*. doi:10.1007/978-3-642-34234-9\_5.
- Remondino, F., Spera, M. G., Nocerino, E., Menna, F. & Nex, F. (2014). State of the art in high density image matching. *The Photogrammetric Record*, 29(146), 144-166, doi:10.1111/phor.12063.

- Reshetyuk, Y. & Mårtensson, S. G. (2016). Generation of Highly Accurate Digital Elevation Models with Unmanned Aerial Vehicles. *The Photogrammetric Record*, 31(154), 143-165, doi:10.1111/phor.12143.
- Rigol-Sanchez, J. P., Stuart, N. & Pulido-Bosch, A. (2015). ArcGeomorphometry: A toolbox for geomorphometric characterisation of DEMs in the ArcGIS environment. *Computers and Geosciences*, 85, 155-163, doi:10.1016/j.cageo.2015.09.020.
- Rosenfeld, A. & Kak, A., C. (1982). *Digital Picture Processing: Volume 1*, 2nd ed, Elsevier, 435
- Rosnell, T. & Honkavaara, E. (2012). Point cloud generation from aerial image data acquired by a quadcopter type micro unmanned aerial vehicle and a digital still camera. *Sensors*, 12(1), 453-480, doi:10.3390/s120100453.
- Rosten, E. & Drummond, T. (2006). Machine Learning for High-Speed Corner Detection. In: LEONARDIS, A., BISCHOF, H. & PINZ, A. (eds.) *Computer Vision – ECCV 2006: 9th European Conference on Computer Vision, Graz, Austria, May 7-13, 2006. Proceedings, Part I*. Springer Berlin Heidelberg. 430-443.
- Rosu, A. M., Pierrot-Deseilligny, M., Delorme, A., Binet, R. & Klinger, Y. (2015). Measurement of ground displacement from optical satellite image correlation using the free open-source software MicMac. *ISPRS Journal of Photogrammetry and Remote Sensing*, 100, 48-59, doi:10.1016/j.isprsjprs.2014.03.002.
- Roy, S. & Cox, I. J. (1998). Maximum-flow formulation of the N-camera stereo correspondence problem. *Proceedings of the IEEE International Conference on Computer Vision*, 1998. 492-499.
- Rupnik, E., Nex, F., Toschi, I. & Remondino, F. (2015). Aerial multi-camera systems: Accuracy and block triangulation issues. *ISPRS Journal of Photogrammetry and Remote Sensing*, 101(0), 233-246, doi:10.1016/j.isprsjprs.2014.12.020.
- Rusu, R. B. (2009). *Semantic 3D Object Maps for Everyday Manipulation in Human Living Environments*. PhD Thesis, Technical University of Munich, Germany.
- Rychkov, I., Brasington, J. & Vericat, D. (2012). Computational and methodological aspects of terrestrial surface analysis based on point clouds. *Computers and Geosciences*, 42, 64-70, doi:10.1016/j.cageo.2012.02.011.
- SafeLand. (2011). Deliverable D4.4: Guidelines for the selection of appropriate remote sensing technologies for monitoring different types of landslides. *Living with landslide risk in Europe: Assessment, effects of global change, and risk management strategies*. [Online]. Available: <https://www.ngi.no/download/file/6014> [Accessed 30th October 2013].
- Salvini, R., Vanneschi, C., Riccucci, S., Francioni, M. & Gullì, D. (2015). Application of an integrated geotechnical and topographic monitoring system in the Lorano marble quarry (Apuan Alps, Italy). *Geomorphology*, 241, 209-223, doi:10.1016/j.geomorph.2015.04.009.
- Sarma, D. D. (2009). *Geostatistics with applications in earth sciences*, 2nd ed.. ed, Springer Netherlands, 10.1007/978-1-4020-9380-7
- Scaioni, M., Feng, T., Barazzetti, L., Previtali, M. & Roncella, R. (2015). Image-based deformation measurement. *Applied Geomatics*, 7(2), 75-90, doi:10.1007/s12518-014-0152-x.
- Scaioni, M., Longoni, L., Melillo, V. & Papini, M. (2014). Remote sensing for landslide investigations: An overview of recent achievements and perspectives. *Remote Sensing*, 6(10), 9600-9652, doi:10.3390/rs6109600.
- Scambos, T. A., Dutkiewicz, M. J., Wilson, J. C. & Bindschadler, R. A. (1992). Application of image cross-correlation to the measurement of glacier velocity using satellite image data. *Remote Sensing of Environment*, 42(3), 177-186, doi:10.1016/0034-4257(92)90101-O.
- Schenk, T. (1997). Towards automatic aerial triangulation. *ISPRS Journal of Photogrammetry and Remote Sensing*, 52(3), 110-121, doi:10.1016/s0924-2716(97)00007-5.
- Schmidt, J., Evans, I. S. & Brinkmann, J. (2003). Comparison of polynomial models for land surface curvature calculation. *International Journal of Geographical Information Science*, 17(8), 797-814.

- Schuster, R. L. (1996). Socioeconomic significance of landslides. *Special Report - National Research Council, Transportation Research Board*, 247, 12-35.
- Seitz, S. M., Curless, B., Diebel, J., Scharstein, D. & Szeliski, R. (2006). A Comparison and Evaluation of Multi-View Stereo Reconstruction Algorithms. 2006 IEEE Computer Society Conference on Computer Vision and Pattern Recognition (CVPR'06), 17-22 June 2006 2006. 519-528.
- Shahbazi, M., Sohn, G., Théau, J. & Menard, P. (2015). Development and evaluation of a UAV-photogrammetry system for precise 3D environmental modeling. *Sensors*, 15(11), 27493-27524, doi:10.3390/s151127493.
- Shary, P. A. (1995). Land surface in gravity points classification by a complete system of curvatures. *Mathematical Geology*, 27(3), 373-390, doi:10.1007/BF02084608.
- Shaw, E. M., (1999). *Hydrology in Practice* [Online]. Cheltenham: CRC Press. Available: <http://search.ebscohost.com/login.aspx?direct=true&db=nlebk&AN=142758&site=ehost-live> [Accessed 30th August 2017].
- Shepard, M. K., Campbell, B. A., Bulmer, M. H., Farr, T. G., Gaddis, L. R. & Plaut, J. J. (2001). The roughness of natural terrain: A planetary and remote sensing perspective. *Journal of Geophysical Research: Planets*, 106(E12), 32777-32795, doi:10.1029/2000je001429.
- Shi, J. & Tomasi, C. (1994). Good features to track. Proceedings of IEEE Conference on Computer Vision and Pattern Recognition, 21-23 Jun 1994. 593-600.
- Shi, J., Yuan, X., Cai, Y. & Wang, G. (2017). GPS real-time precise point positioning for aerial triangulation. *GPS Solutions*, 21(2), 405-414, doi:10.1007/s10291-016-0532-2.
- Shortis, M. R., Robson, S. & Beyer, H. A. (1998). Principal point behaviour and calibration parameter models for kodak DCS cameras. *Photogrammetric Record*, 16(92), 165-186.
- Sibson, R. (1981). A brief description of natural neighbor interpolation (Chapter 2) *In*: BARNETT, V. (ed.) *Interpolating Multivariate Data*. John Wiley. 21-36.
- Sieberth, T., Wackrow, R. & Chandler, J. H. (2014). Motion blur disturbs - the influence of motion-blurred images in photogrammetry. *The Photogrammetric Record*, 29(148), 434-453, doi:10.1111/phor.12082.
- Sima, A. & Buckley, S. (2013). Optimizing SIFT for Matching of Short Wave Infrared and Visible Wavelength Images. *Remote Sensing*, 5(5), 2037-2056, doi:10.3390/rs5052037.
- Sima, A. A., Buckley, S. J., Kurz, T. H. & Schneider, D. (2014). Semi-automated registration of close-range hyperspectral scans using oriented digital camera imagery and a 3D model. *The Photogrammetric Record*, 29(145), 10-29, doi:10.1111/phor.12049.
- Sjöberg, L. E., Pan, M., Asenjo, E. & Erlingsson, S. (2000). Glacial rebound near Vatnajökull, Iceland, studied by GPS campaigns in 1992 and 1996. *Journal of Geodynamics*, 29(1-2), 63-70, doi:10.1016/S0264-3707(99)00061-7.
- Smith, M. J. & Clark, C. D. (2005). Methods for the visualization of digital elevation models for landform mapping. *Earth Surface Processes and Landforms*, 30(7), 885-900, doi:10.1002/esp.1210.
- Smith, M. W. & Vericat, D. (2015). From experimental plots to experimental landscapes: Topography, erosion and deposition in sub-humid badlands from Structure-from-Motion photogrammetry. *Earth Surface Processes and Landforms*, 40(12), 1656-1671, doi:10.1002/esp.3747.
- Snively, N., Seitz, S. M. & Szeliski, R. (2008). Modeling the world from Internet photo collections. *International Journal of Computer Vision*, 80(2), 189-210, doi:10.1007/s11263-007-0107-3.
- Spetsakis, M. & Aloimonos, J. Y. (1991). A multi-frame approach to visual motion perception. *International Journal of Computer Vision*, 6(3), 245-255, doi:10.1007/BF00115698.
- Stöcker, C., Eltner, A. & Karrasch, P. (2015). Measuring gullies by synergetic application of UAV and close range photogrammetry - A case study from Andalusia, Spain. *Catena*, 132, 1-11, doi:10.1016/j.catena.2015.04.004.

- Stumpf, A., Kerle, N. & Malet, J. P. (2011). Deliverable D4.4: Guidelines for the selection of appropriate remote sensing technologies for monitoring different types of landslides. *SAFELAND-Living with landslide risk in Europe: Assessment, effects of global change, and risk management strategies* 7th Framework Programme: Cooperation Theme 6 Environment (including climate change): Sub-Activity 6.1.3 Natural Hazards
- Stumpf, A., Malet, J.-P. & Delacourt, C. (2017). Correlation of satellite image time-series for the detection and monitoring of slow-moving landslides. *Remote Sensing of Environment*, 189, 40-55, doi:10.1016/j.rse.2016.11.007.
- Stumpf, A., Malet, J.-P., Kerle, N., Niethammer, U. & Rothmund, S. (2013). Image-based mapping of surface fissures for the investigation of landslide dynamics. *Geomorphology*, 186, 12-27, doi:10.1016/j.geomorph.2012.12.010.
- Stumpf, A., Malet, J. P., Allemand, P., Pierrot-Deseilligny, M. & Skupinski, G. (2015). Ground-based multi-view photogrammetry for the monitoring of landslide deformation and erosion. *Geomorphology*, 231, 130-145, doi:10.1016/j.geomorph.2014.10.039.
- Szeliski, R. (2011). *Computer Vision - Algorithms and Applications*, Heidelberg, Germany, Springer, 812.
- Tarolli, P. (2014). High-resolution topography for understanding Earth surface processes: Opportunities and challenges. *Geomorphology*, 216, 295-312, doi:10.1016/j.geomorph.2014.03.008.
- Tarolli, P., Sofia, G. & Dalla Fontana, G. (2012). Geomorphic features extraction from high-resolution topography: Landslide crowns and bank erosion. *Natural Hazards*, 61(1), 65-83, doi:10.1007/s11069-010-9695-2.
- Teatini, P., Tosi, L., Strozzi, T., Carbognin, L., Wegmüller, U. & Rizzetto, F. (2005). Mapping regional land displacements in the Venice coastland by an integrated monitoring system. *Remote Sensing of Environment*, 98(4), 403-413, doi:10.1016/j.rse.2005.08.002.
- TerraScan. (2016). Toolset for point cloud processing embedded into Microstation software. Available: <http://www.terrasolid.com/products/terrascanpage.php>.
- Teza, G., Galgaro, A., Zaltron, N. & Genevois, R. (2007). Terrestrial laser scanner to detect landslide displacement fields: a new approach. *International Journal of Remote Sensing*, 28(16), 3425-3446, doi:10.1080/01431160601024234.
- Teza, G., Pesci, A., Genevois, R. & Galgaro, A. (2008). Characterization of landslide ground surface kinematics from terrestrial laser scanning and strain field computation. *Geomorphology*, 97(3-4), 424-437, doi:10.1016/j.geomorph.2007.09.003.
- Tobler, W. R. (1970). A computer movie simulating urban growth in the Detroit region. *Economic Geography*, 46(2), 234-240, doi:10.2307/143141.
- Tomasi, C. & Kanade, T. (1992). Shape and motion from image streams under orthography: a factorization method. *International Journal of Computer Vision*, 9(2), 137-154, doi:10.1007/bf00129684.
- Tonkin, T. N., Midgley, N. G., Graham, D. J. & Labadz, J. C. (2014). The potential of small unmanned aircraft systems and structure-from-motion for topographic surveys: A test of emerging integrated approaches at Cwm Idwal, North Wales. *Geomorphology*, 226, 35-43, doi:10.1016/j.geomorph.2014.07.021.
- Toth, C. & Jóźków, G. (2016). Remote sensing platforms and sensors: A survey. *ISPRS Journal of Photogrammetry and Remote Sensing*, 115, 22-36, doi:10.1016/j.isprsjprs.2015.10.004.
- Tournadre, V., Pierrot-Deseilligny, M. & Faure, P. H. (2015). UAV linear photogrammetry. *The International Archives of the Photogrammetry, Remote Sensing and Spatial Information Sciences*, 2015. 327-333.
- Travelletti, J., Delacourt, C., Allemand, P., Malet, J. P., Schmittbuhl, J., Toussaint, R. & Bastard, M. (2012). Correlation of multi-temporal ground-based optical images for landslide monitoring:

- Application, potential and limitations. *ISPRS Journal of Photogrammetry and Remote Sensing*, 70, 39-55, doi:10.1016/j.isprsjprs.2012.03.007.
- Travelletti, J., Malet, J.-P. & Delacourt, C. (2014). Image-based correlation of Laser Scanning point cloud time series for landslide monitoring. *International Journal of Applied Earth Observation and Geoinformation*, 32(0), 1-18, doi:10.1016/j.jag.2014.03.022.
- Triggs, B., McLauchlan, P. F., Hartley, R. I. & Fitzgibbon, A. W. (2000). Bundle adjustment – a modern synthesis. *Lecture Notes in Computer Science (including subseries Lecture Notes in Artificial Intelligence and Lecture Notes in Bioinformatics)*.
- Tsai, Z. X., You, G. J. Y., Lee, H. Y. & Chiu, Y. J. (2012). Use of a total station to monitor post-failure sediment yields in landslide sites of the Shihmen reservoir watershed, Taiwan. *Geomorphology*, 139-140, 438-451, doi:10.1016/j.geomorph.2011.11.008.
- Turner, D., Lucieer, A. & de Jong, S. M. (2015). Time series analysis of landslide dynamics using an Unmanned Aerial Vehicle (UAV). *Remote Sensing*, 7(2), 1736-1757, doi:10.3390/rs70201736.
- Turner, D., Lucieer, A. & Wallance, L. (2013). Direct Georeferencing of Ultrahigh-Resolution UAV Imagery. *IEEE Transactions on Geoscience and Remote Sensing* doi:10.1109/TGRS.2013.2265295.
- Turner, I. L., Harley, M. D. & Drummond, C. D. (2016). UAVs for coastal surveying. *Coastal Engineering*, 114, 19-24, doi:10.1016/j.coastaleng.2016.03.011.
- Turner, K. A. (1997). What's the difference among 2-D, 2.5-D, 3-D and 4-D. *Applied Geoscience Forum* [Online]. Available: [http://dusk.geo.orst.edu/gis/gis\\_world\\_article.pdf](http://dusk.geo.orst.edu/gis/gis_world_article.pdf) [Accessed 20th June 2017].
- Uhlemann, S., Chambers, J., Wilkinson, P., Maurer, H., Merritt, A., Meldrum, P., Kuras, O., Gunn, D., Smith, A. & Dijkstra, T. (2017). Four-dimensional imaging of moisture dynamics during landslide reactivation. *Journal of Geophysical Research: Earth Surface*, 122(1), 398-418, doi:10.1002/2016JF003983.
- Uhlemann, S., Smith, A., Chambers, J., Dixon, N., Dijkstra, T., Haslam, E., Meldrum, P., Merritt, A., Gunn, D. & Mackay, J. (2016). Assessment of ground-based monitoring techniques applied to landslide investigations. *Geomorphology*, 253, 438-451, doi:10.1016/j.geomorph.2015.10.027.
- Uhlemann, S., Wilkinson, P. B., Chambers, J. E., Maurer, H., Merritt, A. J., Gunn, D. A. & Meldrum, P. I. (2015). Interpolation of landslide movements to improve the accuracy of 4D geoelectrical monitoring. *Journal of Applied Geophysics*, 121, 93-105, doi:10.1016/j.jappgeo.2015.07.003.
- Ullman, S. (1979). The interpretation of structure from motion. *Proceeding of Royal Society of London*, 1979. B-203, 405-442.
- USGS, (2016). *Landslides Hazards Program* [Online]. Available: <https://www.usgs.gov/news/reflecting-2015-natural-hazards> [Accessed 3rd September, 2017].
- Van Westen, C. J., Rengers, N. & Soeters, R. (2003). Use of geomorphological information in indirect landslide susceptibility assessment. *Natural Hazards*, 30(3), 399-419, doi:10.1023/B:NHAZ.0000007097.42735.9e.
- Varnes, D. J. (1978). Slope movement types and processes. *Special Report 176: Landslides: Analysis and Control*. Washington, D.C.: Transportation Research Board.
- Veitinger, J., Sovilla, B. & Purves, R. S. (2014). Influence of snow depth distribution on surface roughness in alpine terrain: a multi-scale approach. *The Cryosphere*, 8(2), 547-569, doi:10.5194/tc-8-547-2014.
- Ventura, G., Vilardo, G., Terranova, C. & Sessa, E. B. (2011). Tracking and evolution of complex active landslides by multi-temporal airborne LiDAR data: The Montaguto landslide (Southern Italy). *Remote Sensing of Environment*, 115(12), 3237-3248, doi:10.1016/j.rse.2011.07.007.
- Verhoeven, G., Doneus, M., Briese, C. & Vermeulen, F. (2012). Mapping by matching: a computer vision-based approach to fast and accurate georeferencing of archaeological aerial photographs. *Journal of Archaeological Science*, 39(7), 2060-2070, doi:10.1016/j.jas.2012.02.022.

- Verhoeven, G. J. J. (2010). It's all about the format – unleashing the power of RAW aerial photography. *International Journal of Remote Sensing*, 31(8), 2009-2042, doi:10.1080/01431160902929271.
- Vogiatzis, G., Hernández Esteban, C., Torr, P. H. S. & Cipolla, R. (2007). Multiview Stereo via Volumetric Graph-Cuts and Occlusion Robust Photo-Consistency. *IEEE Transactions on Pattern Analysis and Machine Intelligence*, 29(12), 2241-2246, doi:10.1109/TPAMI.2007.70712.
- Vu, H. H., Labatut, P., Pons, J. P. & Keriven, R. (2012). High Accuracy and Visibility-Consistent Dense Multiview Stereo. *IEEE Transactions on Pattern Analysis and Machine Intelligence*, 34(5), 889-901, doi:10.1109/TPAMI.2011.172.
- Wackrow, R., Chandler, J. H. & Bryan, P. (2007). Geometric consistency and stability of consumer-grade digital cameras for accurate spatial measurement. *The Photogrammetric Record*, 22(118), 121-134, doi:10.1111/j.1477-9730.2007.00436.x.
- Walstra, J., Dixon, N. & Chandler, J. H. (2007). Historical aerial photographs for landslide assessment: Two case histories. *Quarterly Journal of Engineering Geology and Hydrogeology*, 40(4), 315-332, doi:10.1144/1470-9236/07-011.
- Wang, L., Niu, Z., Wu, C., Xie, R. & Huang, H. (2012). A robust multisource image automatic registration system based on the SIFT descriptor. *International Journal of Remote Sensing*, 33(12), 3850-3869, doi:10.1080/01431161.2011.636079.
- Watson, G. S. (1966). Statistics of Orientation Data. *Journal of Geology*, 74, 786-795, doi:10.1086/627211.
- Watts, A. C., Ambrosia, V. G. & Hinkley, E. A. (2012). Unmanned aircraft systems in remote sensing and scientific research: Classification and considerations of use. *Remote Sensing*, 4(6), 1671-1692, doi:10.3390/rs4061671.
- Weiss, S. & Siegwart, R. (2011). Real-Time Metric State Estimation for Modular Vision-Inertial Systems. *2011 IEEE International Conference on Robotics and Automation*.
- Westoby, M. J., Brasington, J., Glasser, N. F., Hambrey, M. J. & Reynolds, J. M. (2012). 'Structure-from-Motion' photogrammetry: A low-cost, effective tool for geoscience applications. *Geomorphology*, 179, 300-314, doi:10.1016/j.geomorph.2012.08.021.
- Wheaton, J. M., Brasington, J., Darby, S. E. & Sear, D. A. (2010). Accounting for uncertainty in DEMs from repeat topographic surveys: Improved sediment budgets. *Earth Surface Processes and Landforms*, 35(2), 136-156, doi:10.1002/esp.1886.
- Whitehead, K. & Hugenholtz, C. H. (2015). Applying ASPRS accuracy standards to surveys from small unmanned aircraft systems (UAS). *Photogrammetric Engineering and Remote Sensing*, 81(10), 787-794, doi:10.14358/PERS.81.10.787.
- Wolf, P. R., Dewitt, B. A. & Wilkinson, B. E. (2014). *Elements of Photogrammetry with applications in GIS*, 4th ed, USA, McGraw-Hill Education, 676.
- Wolf, P. R. & Ghilani, C. D. (2010). *Adjustment Computations: Statistics and Least Squares in Surveying and GIS*, 5th ed, New York John Wiley & Sons, 611.
- Wood, J. D. (1996). *The geomorphological characterisation of digital elevation models*. PhD Thesis, University of Leicester, Available from: <http://www soi.city.ac.uk/~jwo/phd/>.
- Woodcock, N. H. (1977). Specification of Fabric Shapes Using an Eigenvalue Method. *Geological Society of America Bulletin*, 88, 1231-1236, doi:10.1130/0016-7606(1977)88<1231:SOFSUA>2.0.CO;2.
- Woodget, A. S., Carbonneau, P. E., Visser, F. & Maddock, I. P. (2015). Quantifying submerged fluvial topography using hyperspatial resolution UAS imagery and structure from motion photogrammetry. *Earth Surface Processes and Landforms*, 40(1), 47-64, doi:10.1002/esp.3613.
- Woodman, J. O. (2007). Technical Report (UCAM-CL-TR-696): An introduction to inertial navigation. University of Cambridge.

- Wrobel, B. P. (1987). Digital image matching by facets using object space models. *Proceedings of SPIE - The International Society for Optical Engineering*, 804, 325-333, doi:10.1117/12.941331.
- Wu, C. (2017). VisualSFM: A Visual Structure from Motion System. Available: <http://ccwu.me/vsfm/> [Accessed 13th June 2017].
- Wujanz, D., Krueger, D. & Neitzel, F. (2016). Identification of Stable Areas in Unreferenced Laser Scans for Deformation Measurement. *The Photogrammetric Record*, 31(155), 261-280, doi:10.1111/phor.12152.
- Xiao, X., Boles, S., Liu, J., Zhuang, D., Frolking, S., Li, C., Salas, W. & Moore III, B. (2005). Mapping paddy rice agriculture in southern China using multi-temporal MODIS images. *Remote Sensing of Environment*, 95(4), 480-492, doi:10.1016/j.rse.2004.12.009.
- Yang, B. & Zang, Y. (2014). Automated registration of dense terrestrial laser-scanning point clouds using curves. *ISPRS Journal of Photogrammetry and Remote Sensing*, 95, 109-121, doi:10.1016/j.isprsjprs.2014.05.012.
- Yokoyama, R., Shirasawa, M. & Pike, R. J. (2002). Visualizing topography by openness: A new application of image processing to digital elevation models. *Photogrammetric Engineering and Remote Sensing*, 68(3), 257-265.
- Zakšek, K., Oštir, K. & Kokalj, Ž. (2011). Sky-View Factor as a Relief Visualization Technique. *Remote Sensing*, 3(12), 398-415, doi:10.3390/rs3020398.
- Zevenbergen, L. W. & Thorne, C. R. (1987). Quantitative analysis of land surface topography. *Earth Surface Processes and Landforms*, 12(1), 47-56, doi:10.1002/esp.3290120107.
- Zhang, T. & Cen, M. (2008). Robust DEM co-registration method for terrain changes assessment using least trimmed squares estimator. *Advances in Space Research*, 41(11), 1827-1835, doi:10.1016/j.asr.2007.06.035.
- Zhang, Z. (1996). On the epipolar geometry between two images with lens distortion. *Proceedings - International Conference on Pattern Recognition*, 1996. 407-411.